SHEAR RESPONSE OF ROCK DISCONTINUITIES: THROUGH THE

LENS OF GEOPHYSICS

by

Hala El Fil

A Dissertation

Submitted to the Faculty of Purdue University

In Partial Fulfillment of the Requirements for the degree of

Doctor of Philosophy

Lyles School of Civil Engineering

West Lafayette, Indiana

August 2021

THE PURDUE UNIVERSITY GRADUATE SCHOOL
STATEMENT OF COMMITTEE APPROVAL

Dr. Antonio Bobet, co-chair

Lyles School of Civil Engineering

Dr. Laura J. Pyrak-Nolte, co-chair

Department of Physics and Astronomy

Dr. Maria Caterina Santagata

Lyles School of Civil Engineering

Dr. Pablo D. Zavattieri

Lyles School of Civil Engineering

Approved by:

Dr. Dulcy M. Abraham

Dedicated to my parents: Ola and Khaled
and my siblings Bachir and Farah

ACKNOWLEDGMENTS

First and foremost, I would like to express my deepest gratitude to my advisors: Prof. Antonio Bobet and Prof. Laura J. Pyrak-Nolte, for their patience, support, and excellent advice throughout my Ph.D. journey. The work presented in this thesis would have far been possible without your support and guidance. I would like to thank you for the scientific challenge; it made me grow as a researcher and as a professional. Your technical and personal support throughout my time at Purdue has been invaluable—bottom line, I am very blessed that I got the chance to work with and learn from both of you. Thank you for nurturing my scientific curiosity!

I would like to thank my Ph.D. committee members Prof. Pablo Zavattieri and Prof. Maria Caterina Santagata, for their kind advice and support and for serving on my Ph.D. committee. Prof. Santagata: I am very happy that I got the chance to take my first course at Purdue with you and to get to know you—our interactions in the office (especially during my first couple of months at Purdue) have helped me so much with adapting to the lifestyle at Purdue. Thank you for all the support you provided me with; I will dearly miss the good times!

I would like to thank my friends, Kike and Amy; you guys have been an immense source of support to me; I will miss our laughs and the good times we had. I would also like to thank Kyungsoo: you have been a great lab mate; I wish you a future as bright as you deserve, i.e., as hard as you work! Liyang: thank you for the help in my experiments and for being a good friend; I will miss the good times we had in New York and our laughs. I would also like to thank Dr. Anahita Modiriasari for her help and support in the lab during my first months at Purdue. Dr. Osvaldo Vitali and Yu-Chung Lin, thank you for the great times and laughs. Prof. Khasawneh— our time at Purdue did not coincide, but your support and help have been invaluable.

The most special people to my heart: my mom, dad, brother, and sister: your selfless love and unconditional support–even if we were miles apart—helped me a lot during this journey; I am truly blessed to have a selfless and supporting family. Dad and mom: I appreciate all the sacrifices you made to provide us with the best education and life; I hope to always make you proud. Bachir and Farah: thank you for being my backbone and for being great role models. Mohamad: thank you for being a loving, supporting, and motivating partner and best friend during the lows and highs of this journey.

TABLE OF CONTENTS

LIST OF TABLES

LIST OF FIGURES

ABSTRACT

Failure along rock discontinuities can result in economic losses as well as loss of life. It is essential to develop methods that monitor the response of these discontinuities to shear loading to enable prediction of failure. Laboratory experiments are performed to investigate geophysical techniques to monitor shear failure of a pre-existing discontinuity to detect signatures of impending failure. Previous studies have detected precursors to shear failure in the form of maxima of transmitted waves across a discontinuity under shear. However, those experiments focused on well-matched discontinuities. However, in nature, rock discontinuities are not always perfectly matched because the asperities may be weathered by chemical, physical or mechanical processes. Further, the specific shear mechanism of mismatched discontinuities is still poorly understood. In this thesis, the ability to detect seismic precursors to shear failure for various discontinuity conditions—well-matched (rough and saw-tooth), mismatched (rough), and nonplanar (discontinuity profile with a half-cycle sine wave (HCS))—was assessed. The investigation was carried out through a coupled geophysical and mechanical experimental program that integrated detailed laboratory observations at the micro- and meso-scales. Shear experiments on gypsum discontinuities were conducted to observe changes in compressional (P) and shear (S) waves transmitted across the discontinuity. Digital Image Correlation (DIC) was used to quantify the vertical and horizontal displacements along the discontinuity during shearing to relate the location and magnitude of slip with the measured wave amplitudes.

Results from the experiments conducted on planar, well-matched rough discontinuities (grit 36 sandpaper roughness) showed that seismic precursors to failure took the form of peaks in the normalized transmitted amplitude prior to the peak shear stress. Seismic wave transmission detected non-uniform dilation and closure of the discontinuity at a normal stress of 1 MPa. The results showed that large-scale roughness (presence of a HCS) could mask the generation of precursors, as it can cause non-uniform closure/dilation along the fracture plane at low normal stress.

The experiments on idealized saw-toothed gypsum discontinuities showed that seismic precursors to failure appeared as maxima in the transmitted wave amplitude and conversely as minima in the

reflected amplitudes. Converted waves (S to P & P to S) were also detected, and their amplitudes reached a maximum prior to shear failure. DIC results showed that slip occurred first at the top of the specimen, where the load was applied, and then progressed along the joint as the shear stress increased. This process was consistent with the order of emergence of precursors, i.e., precursors were first recorded near the top and later at the center, and finally at the bottom of the specimen.

Direct shear experiments conducted on specimens with a mismatched discontinuity did not show any precursors (in the transmitted amplitude) to failure at low normal stresses (2 MPa), while those precursors appeared at higher normal stresses (5 MPa). The interplay between wave transmission, the degree of mismatch, and the discontinuity's micro-physical, -chemical and -mechanical properties was assessed through: (1) 3D CT in-situ Xray scans to quantify the degree of mismatch at various normal stresses; (2) micro-indentation testing, to measure the micro-strength of the asperities; and (3) Scanning Electron Microscopy (SEM) and Electron Xray Diffraction (EDX), to study the micro-structure and chemical composition of the discontinuity. The X-ray results showed that contact between asperities increased with normal stress, even when the discontinuity was mismatched. The results indicated that: (1) at 2 MPa, the void aperture was large, so significant shear displacement was needed to interlock and damage the asperities; and (2) the micro-hardness of the asperities of the mismatched discontinuity was larger than that of the well-matched discontinuity, which points to inducing less damage for the same shear displacement. Both mechanisms contribute to the need for larger shear displacements to the mismatched discontinuity asperities to cause damage, which is consistent with the inability to detect seismic precursors to failure. The experimental results suggest that monitoring changes in transmitted wave amplitude across a discontinuity is a promising method for predicting impending failure for well-matched rock discontinuities. Precursor monitoring for mismatched rock discontinuities seems only possible when there is sufficient contact between the two rock surfaces, which occurs at large normal stresses.

1   INTRODUCTION

1.1   Motivation

Rocks are unique engineering materials because of their discontinuous nature; they are composed of interlocking rock matrices and joints. The presence of discontinuities governs the strength of rock masses (Barton, 1973; Hoek et al., 2002; Nakagawa et al., 2000; Patton, 1966). Discontinuities may cause failures in excavations and slopes, leading to the loss of life and significant economic losses. Therefore, it is essential to monitor the evolution of failure along pre-existing discontinuities and study the shear strength of rock discontinuities. A considerable amount of research has been conducted to investigate the shear strength of rock discontinuities (Barton & Choubey, 1977; Barton, 1973; Byerlee, 1978; Jaeger et al., 2007; Zhao, 1997; Indraratna et al., 2008). From these studies, researchers observed that the mechanical behavior of a discontinuity is influenced by many factors such as joint roughness and trace, weathering, normal stress applied on the joint, whether it is filled (type and thickness of the infill) or not, and environmental conditions (Byerlee, 1978; Jaeger et al., 2007).

The roughness of a rock discontinuity has a significant effect on its shear strength. Patton (1966) conducted experiments to study the impact of irregularities/asperities on shear strength. He concluded that different modes of shear failure occur for different rock surfaces, i.e., failure may occur by sliding along a rock surface, shearing through rock, or both depending on the joint roughness and strength of the material. Joint surface roughness was studied by Barton (1973) using the joint roughness coefficient criterion (JCR), which led to the development of various roughness joint profiles (Barton & Choubey, 1977) that are among the most commonly used tools to characterize a discontinuity's surface roughness.

Moreover, rock discontinuities are often filled with various materials such as sand, debris, and clayey deposits transported by weathering, chemical processes, and fluids in the field. The most pronounced effect of fill on the shear strength is either a reduction or increase in friction and shear strength. The nature of the fill plays an essential role in determining the discontinuity's shear strength; for example, rock joints containing fine infill materials—that exhibit low friction properties—are expected to be the weakest elements in a rock mass (de Toledo & de Freitas, 1993;

16

Ladanyi & Archambault, 1977). On the other hand, some infilled discontinuities can gain strength over time because of bonding and consolidation, yet the strength of such discontinuities can be reduced if subjected to successive movements (Indraratna et al., 2005; 2008). Another essential factor to consider is the degree mismatch of rock discontinuities, as it affects the shear strength and behavior of the rock mass. In nature, discontinuities may not be perfectly matched due to erosion or chemical and physical processes that alter one or both fracture surfaces. Zhao (1997) conducted shear experiments on natural granite samples (mismatched) and on freshly induced (well-matched) granite joints and found that a mismatched discontinuity generally results in a decrease in shear strength.

The mechanical understanding of rock discontinuities is crucial and gives insight into the macroscopic behavior of discontinuities subjected to shear. However, it is also essential to determine the current stress conditions of the joint and to detect impending slip or failure. Geophysical methods such as seismic wave propagation are promising tools to remotely measure the stress variation subjected to different types of loading. Pyrak-Nolte et al. (1990) measured waves transmitted across a single fracture under normal stress and determined the change in shear and normal stiffness of the fracture with changes in stress. Other studies successfully used active seismic monitoring and observed precursors slip along pre-existing discontinuities (Hedayat et al., 2014b; Scuderi et al., 2016), detected the formation of shear cracks (Modiriasari et al., 2018; 2020), and were able to extract information about a discontinuity's engineering properties such as its stiffness (Choi et al., 2013; Pyrak-Nolte, 2018) and compliance (Worthington et al., 2007).

Earthquake prediction has been a long-lasting goal for scientists, which was considered achievable in the 1970s based on recorded laboratory changes in elastic wave speeds before fault rupture (Scholz et al., 1973). A precursory event in the form of a change in the compressional to shear velocity ratio (V_p/V_s) was recorded before the 1971 San Fernando earthquake in California with a magnitude of 6.4 (Whitcomb et al., 1973). In 1975, seismologists successfully predicted the Haicheng earthquake (M=7.3) in China because a high-gain seismograph station was located around 20 km from the epicenter. Researchers observed distinct characteristics in the recorded foreshocks, such as the accelerating rate of occurrence, the high proximity of epicenters, and P to S amplitudes (Xu et al., 1981).

From laboratory studies, precursors to slip along existing discontinuities have been observed in the transmitted and reflected wave amplitudes (Hedayat et al., 2014b) and frequency attenuation of transmitted signals (Hedayat & Hinton, 2017) while shearing a rock discontinuity. The precursory events (at laboratory-scale) cited above were recorded for clean (no fill) and well-matched planar discontinuities. Other studies also successfully applied machine learning to predict the time remaining before slip took place for laboratory earthquakes, using experimental acoustic emission data recorded by running double direct shear experiments on fault gouges (Rouet-Leduc et al., 2017; Johnson et al., 2021). Hulbert et al. (2019) applied machine learning to acoustic emission data obtained from shearing experiments on quartz fault gouge. They were able to predict the time and magnitude of laboratory earthquakes retrospectively. Interesting research questions are raised: Are these seismic precursors present in all signal modes, i.e., transmitted, reflected, and converted signals? What discontinuity conditions would mask the presence of these seismic precursors to failure? What are the geophysical signatures of shearing mismatched rock discontinuities?

1.2 Research Objectives and Scope

This interdisciplinary research aims to investigate the geophysical and mechanical response of rock discontinuities undergoing shear and to understand when seismic precursors to failure could be recorded and when not. Active seismic monitoring is employed to study the shear behavior of well-matched (with various discontinuity profiles) and mismatched discontinuities at the microscopic level. The following tasks are performed to complete the objectives of this study:

a. Investigate the geophysical signature of shearing a discontinuity with different surface profiles. Active seismic monitoring has the potential to detect dilation and closure of discontinuities subjected to shear stress, which is crucial in evaluating key processes such as the evolution of joint permeability during shearing.

b. Explore the seismic signals on an idealized saw-tooth discontinuity. The aim is to provide further insight into how precursors occur and the differences among precursors detected from transmitted, reflected, and converted waves.

c. Examine the effect of joint mismatch on shearing behavior and analyze its corresponding mechanical and geophysical response. Previous work (Hedayat et al., 2014b) shows that active seismic monitoring has the potential to detect precursors to failure when shearing a well-matched pre-existing discontinuity. However, discontinuities are not always well-matched in the field and may be mismatched due to weather and chemical or physical processes in nature. The goal is to investigate whether the mismatch of a discontinuity masks seismic precursors and identify the geophysical signatures of a mismatched discontinuity under shear. 3D X-ray tomography imaging is employed to understand the changes of the aperture of well-matched and mismatched fractures at various normal stresses.

1.3   Organization of the Thesis

This thesis is organized as follows:

Chapter 2 presents a review of past studies that examined the shear strength of rock discontinuities. Also, a theoretical review of the Displacement Discontinuity theory and its extended form is presented. Finally, studies that examine the effect of discontinuity characteristics (roughness), fill, and degree of mismatch on mechanical and geophysical responses are presented.

Chapter 3 describes the experimental work and setup employed in this research study. The chapter describes the coupled seismic and mechanical measurements made, together with surface observations using digital image correlation (DIC) to study the shearing behavior of discontinuities.

Chapter 4 includes the results from direct shear experiments conducted on a discontinuity with ideal saw-tooth asperities. The goals of the research are to (1) observe the shearing process of an ideal discontinuity, to compare signatures of failure in transmitted, reflected, and converted elastic waves, and (2) analyze the propagation of slip as the discontinuity is driven to failure.

Chapter 5 provides an in-depth understanding of the behavior of a well-matched versus a mismatched rock discontinuity subjected to various normal stresses using 3D CT X-ray scans. Direct shear experiments are also presented on mismatched discontinuities and are compared with

the results of well-matched discontinuities to study whether the precursors are masked due to discontinuity mismatch.

Chapter 6 presents the main findings of this research and suggests future work that may contribute to further understanding of the subject.

2 LITERATURE REVIEW

2.1 Introduction

A review of previous studies is presented to understand factors that affect the shear strength of rock discontinuities. In addition, a theoretical review of the Displacement Discontinuity Theory (DDT) and its extended form is discussed to provide a theoretical understanding of seismic waves transmitted across a discontinuity. Finally, relevant studies that couple geophysical and mechanical approaches to study the behavior of pre-existing discontinuities subjected to shear loading are included.

2.2 Shear Behavior of Rock Discontinuities

This section presents studies on the factors that affect the shear strength of rock discontinuities.

2.2.1 Factors affecting the shear strength of rock discontinuities (no infill material)

Several factors affect the shear strength of clean (unfilled) rock discontinuities; the most important factors include joint roughness, shearing rate, normal stress applied, and the boundary conditions; (Constant Normal Load (CNL) or Constant Normal Stiffness (CNS)). (Crawford & Curran, 1981; Barton, 1973; Goodman & Ohnishi, 1973). The following subsections will briefly describe how these factors after the shear strength of rock discontinuities.

2.2.1.1 *Joint surface roughness*

Patton (1966) and Ladanyi & Archambault (1970) defined a discontinuity roughness as a parameter determined by the average inclination angle, i_0, of asperities. Barton & Choubey (1977) introduced the Joint Roughness Coefficient (JRC) to quantify the discontinuity's profile. The JRC ranges from [0-20], 0 being smooth and 20 corresponding to a very rough discontinuity surface. The shear strength of discontinuities with large JRC values exhibited higher shear strength and dilation than discontinuities with lower JRC values (Barton & Choubey, 1977; Skinas et al., 1990; Kodikara & Johnston, 1994).

2.2.1.2 Rate of shearing

Crawford & Curran (1981) found that the shear strength of soft rock discontinuities tends to increase with an increase in shearing rate, up to a critical point after which it remains unaffected. They also found that the shear strength of hard rock discontinuities tends to decrease with an increase in shearing rate. So, soft and hard rock discontinuities behave differently when subjected to higher shearing rates. They mention that the actual mechanism of why soft and hard rocks behave differently when subjected to higher shearing rates is not completely understood. However, they mention that factors such as the contact area, asperities, mineralogy, and hardness could possibly affect the observed behavior.

2.2.1.3 Boundary conditions

The boundary conditions of a rock discontinuity are a function of its location in the field, i.e., if the rock surrounding the discontinuity is deformable—giving the discontinuity chance to dilate—then constant normal load conditions prevail. According to Thirukumaran & Indraratna (2016), a practical example that illustrates CNL conditions is a slope stability situation, as the discontinuity slides across the slope with no constraints. Conversely, if the surrounding rock is stiff, the discontinuity will not dilate, and constant normal stiffness conditions are applicable, e.g., reinforced rock wedges sliding across a rock slope, movement of vertical concrete piles (Thirukumaran, & Indraratna, (2016). Skinas et al. (1990), Indraratna & Haque (1997) conducted direct shear laboratory experiments under CNS conditions. They observed that experimental data obtained under CNS conditions exhibited an increase in shear stress while dilation decreased in comparison with CNL conditions. They attributed this increase in shear stress to the increase in normal stress required to suppress dilation.

Furthermore, Indraratna et al. (1999) conducted direct shear experiments on idealized sawtooth discontinuities. They observed that the linearity of the normal stress–shear stress failure envelopes was affected by the normal boundary condition applied to the discontinuity. They found that direct shear experiments conducted with CNS conditions resulted in a higher nonlinearity of the failure envelopes, as shown in Figure 2.1. Figure 2.1 represents the shear stress vs. normal stress failure envelope curves obtained by Indraratna & Haque, 1997 for three types of saw-toothed joints and shows the nonlinearity of the failure envelopes obtained under CNS conditions.
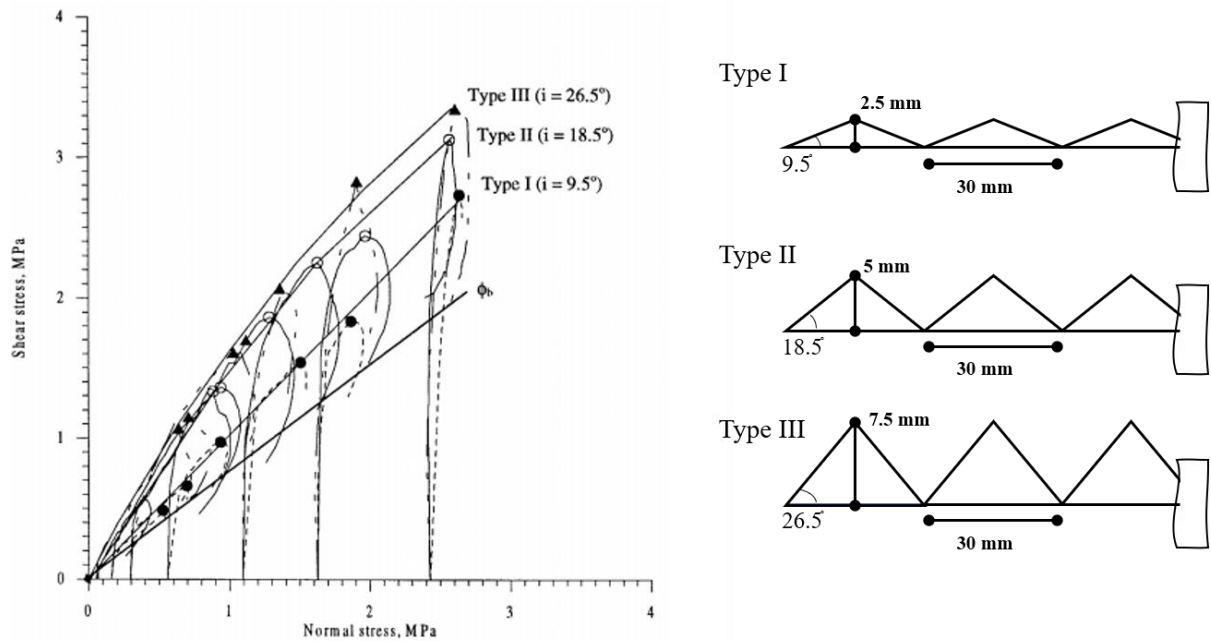
Figure 2.1. Failure envelope of sawtooth rock discontinuities under CNS conditions (adapted from Indraratna & Haque, 1997)

2.2.1.4 Normal stress

Researchers have examined how the applied normal stress affects the shearing behavior of rock discontinuities (Leichnitz, 1985; Indraratna et al., 1999). As expected, these studies indicated that a discontinuity with low normal stress exhibited a dilative behavior. The asperities were significantly damaged at higher normal stress and resulted in lower dilation and higher peak strength.

2.2.1.5 Pore water pressure and moisture

In the field, discontinuities may exist below the water table. Thus, it is essential to examine the influence of the pore water pressure on rock discontinuities. The water pressure in rock discontinuities may increase or decrease, depending on the discontinuity behavior during shearing. If the discontinuity aperture decreases due to confinement, the water pressure will increase since flow would be restrained with aperture closure for a disconnected discontinuity; conversely, if the aperture increases (asperity overriding), the water pressure tends to decrease, that depends on the

source of water supply. Goodman & Ohnishi (1973) found that the "effective normal stress" controls the shear strength of rock discontinuities subjected to pore pressure, as these discontinuities (saturated) exhibited a lower shear strength than dry rocks when subjected to the same normal stress. Moisture also affects the shear strength of discontinuities; Barton (1973) studied the effect of water on the shear strength of a discontinuity and found that when a smooth discontinuity was slightly wet, the shear strength remained either unaffected or exhibited a slight increase, whereas the strength of rough discontinuities decreased with the presence of water (moisture); this might be attributed to the effect of moisture on the compressive strength of the rock, which influences the shear strength of rough discontinuities.

2.2.1.6   *Scale effect*

The size of the rock discontinuity affects its corresponding shear strength. Various studies report that for discontinuities with larger lengths, a reduction in shear strength is expected. This reduction in shear strength is attributed to a decrease in effective joint roughness (Fecker & Rengers, 1971). Bandis et al. (1981) conducted direct shear experiments on laboratory-fabricated plaster rocks prepared with molds that have the shape of natural rock discontinuities at various scales. They found that an increase in length of a discontinuity results in a reduction in peak shear stress; this is due to a reduction in asperity failure and dilation component of the larger discontinuity. They also found that smooth rock discontinuities are not affected by the scale effects as much as the rougher rock discontinuities; this is due to differences in the asperity size of both types of discontinuities. While other studies concluded the opposite behavior (Swan & Zongqi, 1985), in which they argued that the strength of a discontinuity increases with an increase in the joint area. They reached this conclusion by numerically investigating the roughness scale effects of two surface profiles, fitting a least squared line in each profile (Swan 1983).

2.3   Shear Behavior of Infilled-Rock Discontinuities

Some discontinuities in the field are filled with debris and soils, affecting their shear strength and behavior. The fill may reduce the rock-to-rock contact and thus result in a reduction in shear strength. However, some infill may consolidate or solidify and increase shear strength (Indraratna et al., 2005; 2008).

2.3.1 Factors affecting the shear strength of infilled rock joints

Various factors influence the shear strength of infilled rock discontinuities; the most important factors include the type and thickness of the fill, discontinuity's surface profile, and boundary conditions (Goodman, 1970; Phien-Wej et al., 1991; Papaliangas et al., 1990; de Toledo & de Freitas, 1993; Jahanian & Sadaghiani, 2015).

2.3.1.1 Type and thickness of infill material

Several researchers have examined the effect of fill type and thickness on the shear strength of discontinuities; relevant studies are reviewed in this section. Goodman (1970) investigated the effect of crushed mica as an infill material in an idealized sawtooth discontinuity. Figure 2.2 shows results adopted from Goodman (1970). He found that the shear strength of the infilled discontinuity was higher than that of the infill for discontinuities with fill thickness to mean asperity ratio (t/a)<1.25 (125% to which joint is filled with mica). Whereas discontinuities with $t/a \geq 1.25$ exhibit a shear strength that is similar to that of the infill material.
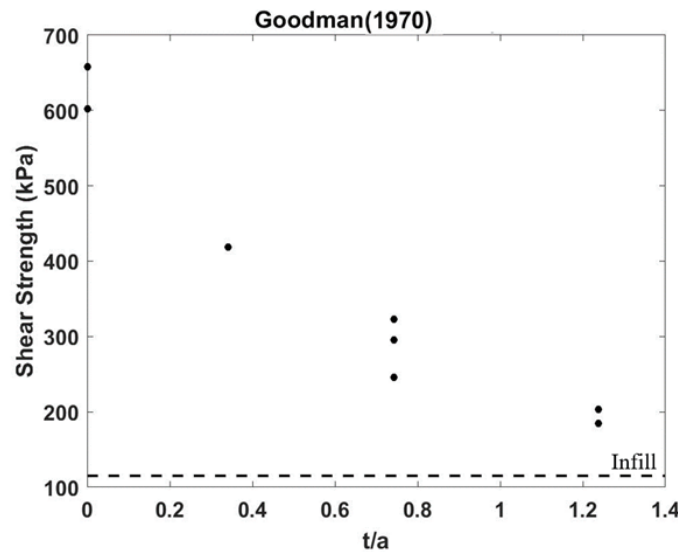
Figure 2.2. Shear strength vs. t/a, after Goodman (1970)

In a study conducted by Phien-Wej et al. (1991) on the effect of oven-dried bentonite as an infill material for a gypsum sawtooth discontinuity, they found that as *t/a* approached 2, the shear

strength of the infilled discontinuity was similar to that of the infill, for three normal stresses they used: 0.5, 0.75, and 1 MPa.

Direct shear experiments on cement discontinuities with different types of infill were conducted by Papaliangas et al. (1990). They investigated three types of fill materials: kaolin, marble dust on a joint with a joint roughness coefficient (JCR) of 8, and pulverized fuel ash in a joint with a JCR of 10. Marble dust was used as a denser frictional material, and the particles were angular, kaolin had a moisture content of 50% and was used as a non-frictional infill, and finally, the pulverized fly ash was used to represent a fine-grained infill. According to their results, the shear strength of discontinuities with kaolin reached a constant value (similar to the infill shear strength) for t/a=0.6. Tests on infilled discontinuities with marble dust and fuel show that the shear strength of the discontinuity reached a constant value when t/a approached [1.25-1.5]. The authors do not mention why a discontinuity with kaolin as an infill material reached a constant shear strength as low t/a value, but it could be due to the effect of moisture content which may result in cohesion and thus lower shear strengths at t/a as low as 0.2.

2.3.1.2 *Boundary conditions*

In general, and under CNL conditions, the shear strength of infilled discontinuities increases as the normal stress increases, and dilation decreases due to compaction and asperity damage (Lama, 1978; Phien-Wej et al., 1991; Papaliangas et al., 1993; de Toledo and de Freitas, 1993)—this depends on the ability of the infill material to be compacted. Cheng & Haberfield (1998), Indraratna et al. (1999), and Indraratna & Jayanathan (2005) stated that under CNS conditions, the effect of stiffness was reduced with an increase in fill thickness because there was no more rock-to-rock contact across the discontinuity.

2.3.1.3 *Fill-rock interaction*

To investigate fill-rock interaction, de Toledo and de Freitas (1993) studied how the roughness of the discontinuity affects the rolling mechanism of sand grains. They used granite with rough and smooth discontinuities, as shown in Figure 2.3 (a-b). They found that the extent of influence of surface roughness was a function of particle size. The rolling mechanism of a particle is associated

with smaller frictional strength than sliding. Thus, for a smooth discontinuity (Figure. 2.3 (b)), particle rolling is the governing mechanism that is consistent with the researchers' observation of a reduction in shear strength because of the presence of infill. On the other hand, the discontinuity in Figure 2.3(a) has a roughness that would prevent the sand grains from moving easily (freely); the governing mechanism is asperity crushing and sliding; thus, the sliding shear strength must be reached for failure to take place and could result in a similar shear strength to an unfilled rock discontinuity.
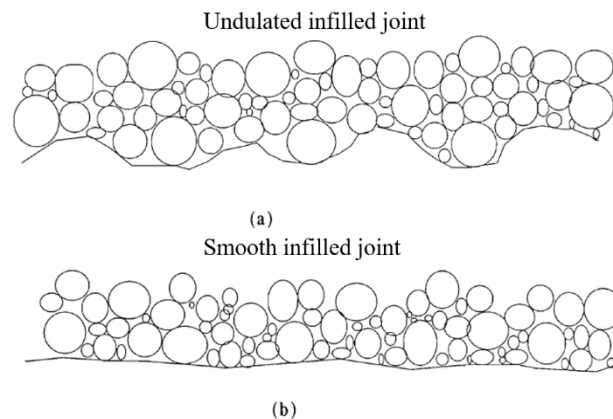
Figure 2.3. Rock-fill interaction: (a) rough/undulated infilled discontinuity; (b) smooth infilled discontinuity (adapted from de Toledo and de Freitas (1993))

2.4   Shear Behavior of Mismatched Rock Discontinuities

A joint surface in nature may undergo physical and chemical changes due to erosion, shearing, and fluid transport across the discontinuity that can result in a mismatch between the surface roughness of the discontinuity. A "mismatched" discontinuity is a discontinuity in which the two rock surfaces are not mirrored across the discontinuity and thus cannot fully interlock, and voids exist. The effect of discontinuity matching on shear strength was studied by Zhao (1997), who found that the peak shear strength of a mismatched discontinuity was much lower than that of a perfectly matched discontinuity. He proposed the Joint Matching Coefficient (JMC) to describe the degree of discontinuity matching; JMC=1 corresponds to a perfectly matched discontinuity and JMC ~0 to a completely mismatched discontinuity. Zhao (1997) also found that the degree of discontinuity matching is a function of the discontinuity shape and thus has a significant effect on the mechanical

and hydraulic properties of the discontinuity, i.e., a large discontinuity mismatch could result in larger apertures and, therefore, easier fluid flow. He also observed that the stiffness of a mismatched discontinuity was lower than that of a perfectly matched discontinuity because the asperities were not fully interlocked.

2.5 Predicting the shear strength of rock discontinuities: state-of-the-art:

With the emergence of new Artificial Intelligence (AI) techniques in the field of geotechnical engineering, researchers are employing machine learning methods such as Artificial Neural Networks (ANN) to predict the shear strength of rock discontinuities. Dantas Neto et al. (2017) developed an ANN model that predicts the shear strength of clean rock discontinuities. The input variables of their model were JRC, boundary conditions, uniaxial compressive strength, basic friction angle of intact rock, and horizontal displacement. The outputs of their model were the shear strength and dilation of the discontinuity. After training and validating their model, they obtained a correlation coefficient between training and tests of 0.99. They proved that their model was able to predict the shear strength of clean rock discontinuities accurately. They found that the most important parameter, i.e., the parameter that affected their ANN results, was the uniaxial compressive strength. They also showed how each input parameter affected the outputs of their model. They concluded that their ANN results fitted the experimental data more accurately than other analytical models in the literature, as shown in Figure 2.4.
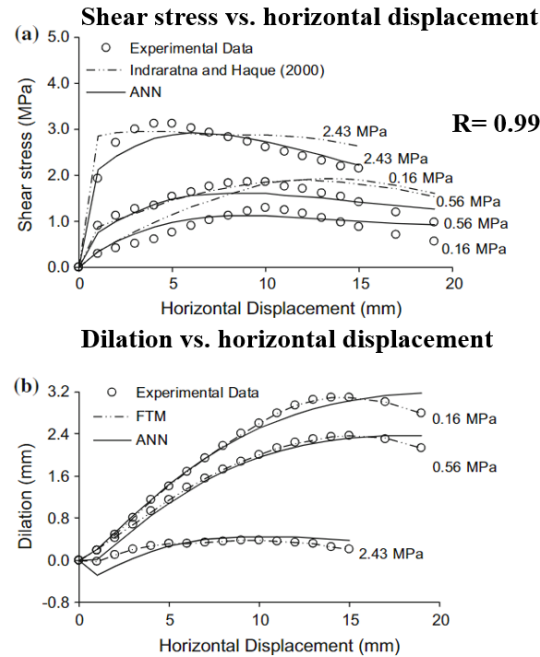
Figure 2.4 Results of ANN model, experimental data, and analytical model of Indraratna and Haque 2000 (adapted from Dantas Neto et al. 2017)

Figure 2.4 shows a comparison between the predicted and experimental results of direct shear experiments conducted by Skinas et al. (1990) on clean hard rock discontinuities. For comparison, the analytical model of Indraranta & Haque (2000) was included. The ANN model was able to accurately predict the shear strength and the horizontal displacement of the discontinuities. Even though the ANN model delivered successful outcomes, it has some drawbacks. For example, more than 75% of the input uniaxial compressive strength data was in the range of 8-16 MPa. Such limitation of the range of data could make the model less robust because it only learned within such a specific range of data [8-16 MPa].

Previous studies have extensively studied the shear behavior and strength of rock discontinuities under different conditions. All the studies mentioned above provide insight into the factors that may affect the shear strength of rock discontinuities, and in more recent studies, researchers also successfully predicted the shear strength of rock discontinuities using machine learning. A mechanical understanding of the shear strength of rock discontinuities is crucial and gives insight into the macroscopic behavior of failure, but it is important to also monitor for impending shear failure. Geophysical techniques such as active seismic monitoring may provide information on the

microscopic behavior of shearing rock discontinuities, and thus it is important to have a multi-modal (mechanical and geophysical) monitoring process of rock discontinuities subjected to shear stress. In the following paragraphs, the displacement discontinuity theory and its extended form are discussed.

2.6 The Displacement Discontinuity Theory

Seismic wave propagation across discontinuities is among the most successful techniques employed to probe the condition of a discontinuity, i.e., open, closed, or partially closed. This section provides a review of seismic wave propagation and, in particular, of the displacement discontinuity theory (DDT) (Schoenberg, 1980; Pyrak-Nolte et al., 1990). According to the DDT, a discontinuity is modeled as a non-welded interface where the stresses across the discontinuity are continuous, and the displacements are discontinuous. Various researchers used the DDT to study waves propagating across rock discontinuities. Schoenberg (1980) derived a complete solution of the DDT for shear and compressional waves propagating at incident angles oblique to the discontinuity. Pyrak-Nolte et al. (1990) derived a closed form solution for seismic waves propagating across a single discontinuity and determined the stiffness of the fracture by matching experimental and theoretical wave spectra at different normal stresses. For a wave transmitted normally across a fracture located in the x-y plane (see schematic in Figure 2.5), with elastic uniform material in the half-space, the transmission and reflection coefficients for normally incident P, SV, and SH waves are (for complete solutions, readers can refer to Pyrak-Nolte et al., 1990):

$$T_p(\omega) = 1/(1 - i\omega Z_{p1}/2\kappa_z) \tag{2.1}$$

$$R_p(\omega) = (i\omega Z_{p1}/2\kappa_z)/(1 - i\omega Z_{p1}/2\kappa_z) \tag{2.2}$$

$$T_{Sv}(\omega) = 1/(1 - i\omega Z_{s1}/2\kappa_x) \tag{2.3}$$

$$R_{Sv}(\omega) = (i\omega Z_{s1}/2\kappa_x)/(1 - i\omega Z_{s1}/2\kappa_x) \tag{2.4}$$

$$T_{SH}(\omega) = 1/(1 - i\omega Z_{s1}/2\kappa_y) \tag{2.5}$$

$$R_{SH}(\omega) = (i\omega Z_{s1}/2\kappa_y)/(1 - i\omega Z_{s1}/2\kappa_y) \tag{2.6}$$

T_p, R_p, T_{Sv}, R_{Sv}, T_{SH}, and R_{SH} are transmitted and reflected coefficients of incident P, SV, and SH waves, respectively. Z_{s1}, Z_{p1} are the shear and compressional seismic impedances, i.e., the product of the shear and compressional wave speeds (respectively) and density of the material. κ_x, κ_y, and κ_z are the tangential (x and y) and normal (z) fracture stiffnesses, and ω is the signal frequency.
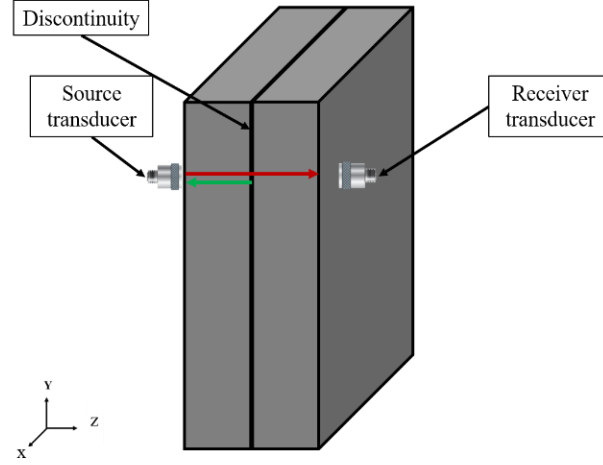
Figure 2.5. Schematic of a seismic transducer transmitting a normally incident wave

Figure 2.6 shows the transmitted and reflected coefficients as a function of normalized frequency obtained from the DDT (Pyrak-Nolte et al., 1990).
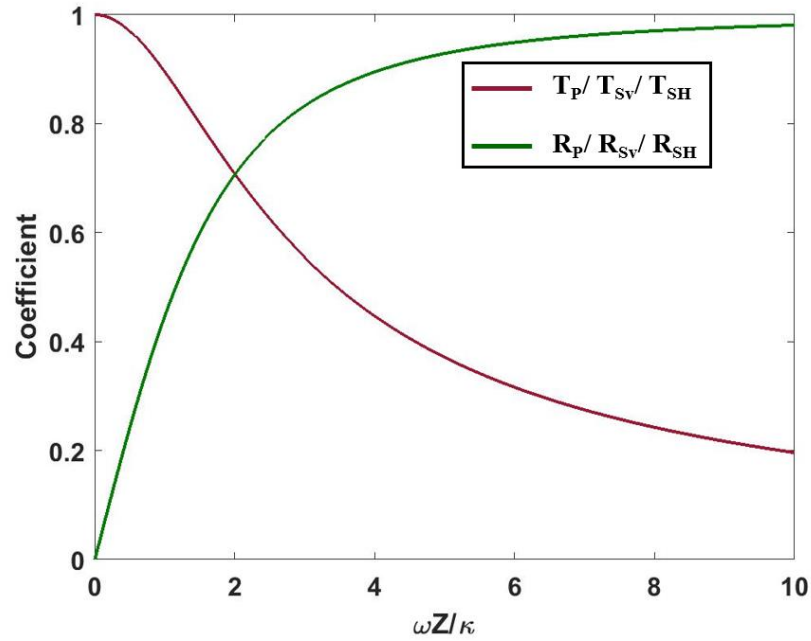
Figure 2.6 Transmitted and Reflected coefficients derived from DDT (after Pyrak-Nolte et al. 1990)

As shown in Figure 2.6, for a normally incident wave, as the specific stiffness of the fracture κ approaches zero, i.e., increase in normalized frequency, the transmission coefficient decreases, and the reflection coefficient increases, implying that the discontinuity behaves like a "free" surface. On the other hand, when the fracture-specific stiffness κ approaches infinity—low normalized frequency, the transmission coefficient approaches 1, and the reflection coefficient approaches 0. In that case, the fracture behaves as a welded contact (Pyrak-Nolte et al., 1990).

2.6.1 Extended-displacement discontinuity theory:

Nakagawa et al. (2000) studied elastic wave propagation on a discontinuity containing oriented microcracks under shear stress. They were able to detect seismic wave conversion as they sheared their samples, i.e., considering a transmitted P-wave, as it impinges a discontinuity (with certain characteristics, which will be discussed in this section), it gets converted to a shear wave and vice versa for an incident S-wave. A discontinuity with oriented micro-cracks or voids would result in wave conversion. In their study, Nakagawa et al. (2000) attributed wave conversion to cross-coupling stiffnesses generated along the fracture as it was sheared. Considering an incident P-wave propagating across a fracture subjected to shear stress, normal and tangential displacements are

caused by shearing. In the extended displacement discontinuity theory, the cross-coupling stiffnesses in the fracture stiffness matrix are included in addition to the fracture normal k_{zz} and shear k_{xx} stiffnesses. The cross-coupling stiffnesses (κ_{xz} and κ_{zx}) are the ratios between the tangential and normal stresses applied to the fracture and the normal and tangential displacements incurred, respectively. Based on Nakagawa et al. (2000), for a fracture located in the x-y plane (see Figure 2.7 for the coordinate system), the specific stiffness is:

$$k_{xz} = \sigma_{zx}/(u_{2z} - u_{1z}) \tag{2.7}$$

$$k_{zx} = \sigma_{zz}/(u_{2x} - u_{1x}) \tag{2.8}$$
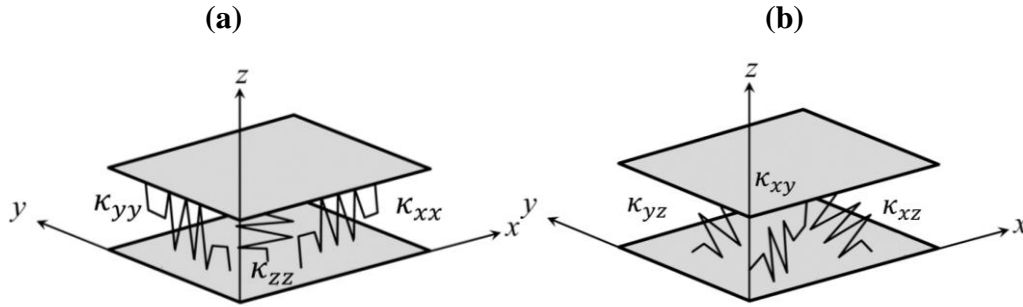
Figure 2.7 (a) axial fracture stiffnesses; (b) cross-coupling fracture stiffnesses (after Nakagawa et al. 2000)

Nakagawa et al. (2000) defined a new parameter **R**, as is the relative magnitude of the coupling stiffnesses:

$$R = \sqrt{\frac{\kappa_{zx}.\kappa_{xz}}{\kappa_{xx}.\kappa_{zz}}} \tag{2.7}$$

The magnitude of R ranges between 0 and 1; a crack inclination of 0° corresponds to R=0, and a crack inclination of ~63° corresponds to R=1, where fracture stiffnesses become infinitely large. Figure 2.8 shows the transmitted (red), reflected (green), and converted (purple) coefficients for a normally incident P-wave impinging on a fracture for R=0, 0.5, 0.7, and 0.9. For the case of R=0, i.e., no cross-coupling stiffnesses, so the wave energy is either reflected or transmitted. At low normalized frequencies and for R=0, the fracture stiffness k is large; thus, most of the energy is

transmitted, and as explained earlier (Figure 2.5), the fracture behaves as a welded surface. As R increases, the amplitude of the converted wave increases, as shown in Figure 2.8. The increase in converted waves is not monotonic. It peaks at a normalized frequency [0.2-1] for all cases (R=0.5, 0.7, and 0.9), while the reflection and transmission coefficient monotonically increase and decrease (respectively) with an increase in normalized frequency.
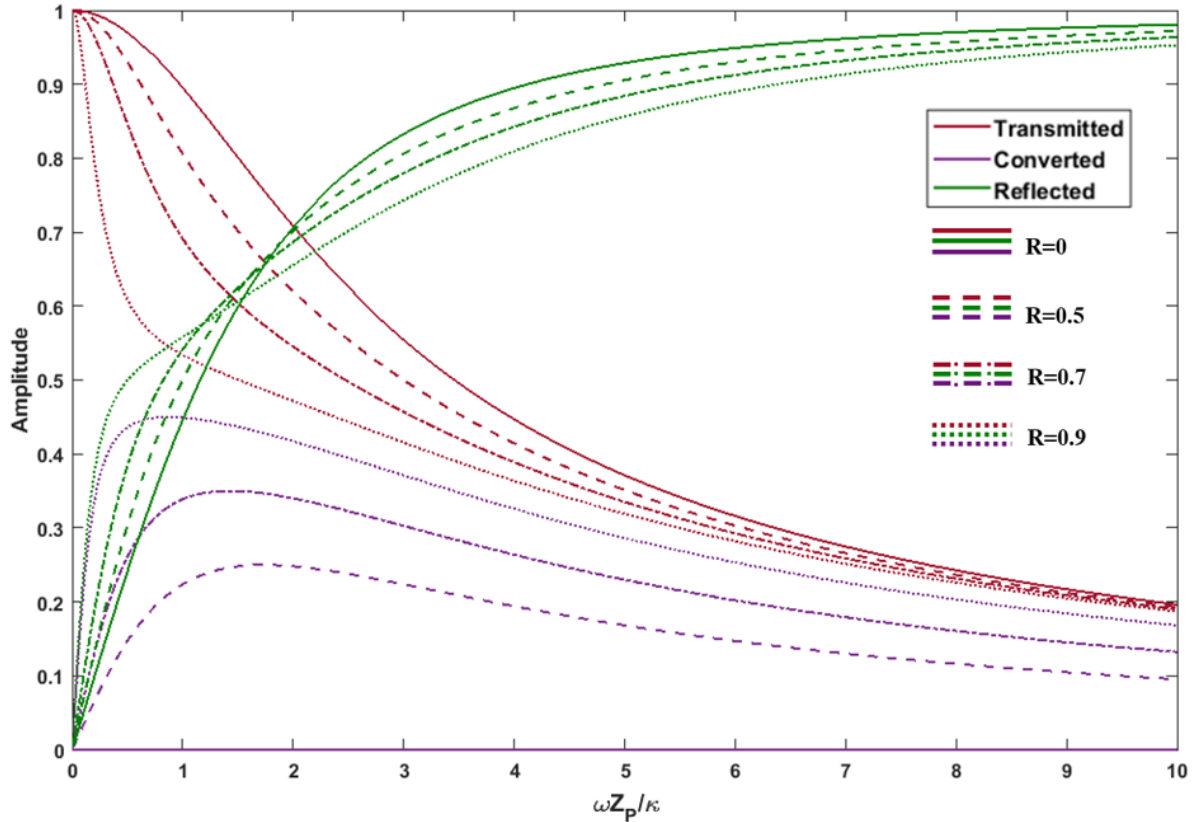
Figure 2.8. Transmitted (red), reflected (green), and converted (purple) coefficients for a P-wave, at normal incidence, for R= 0, 0.5, 0.7, and 0.9

To gain additional insight into how the extended displacement discontinuity theory coefficients vary with the relative coupling stiffness, R, the amplitudes of a normal incident SV wave are plotted in Figure 2.9. The normal and shear stiffnesses are assumed to be equal ($\kappa_{xx} = \kappa_{zz}$). The material properties used are: ρ=1560 kg/m^3, V$_s$=2005 m/s, frequency=800 kHz. Figure 2.9 shows the transmitted (maroon), reflected (green), and converted (purple) coefficients at two normalized frequencies: $\omega Z_s/\kappa$=0.1 (solid lines) and 0.9 (dashed lines). The relative coupling stiffness R is a function of the orientation of microcracks and cross-coupling stiffnesses. Thus, R increases due to

34

an increase in microcrack inclination angle and/or an increased cross-coupling stiffness. As R increases, energy partitioning takes place, an increase in the converted-mode coefficient is occurs. For normalized frequencies of 0.1 –large fracture stiffness (k); solid lines—the increase in converted amplitude occurs for R≥ 0.2. The plot presented in Figure 2.9 implies that at low normalized frequencies –high fracture stiffness (k)— larger relative coupling stiffness (R) is required to observe an increase in converted and reflected wave amplitude. Physically this means that fractures with high stiffness (k) behave as welded surfaces; thus, most of the energy is transmitted even at R~0.8. For the case of high normalized frequencies –low fracture stiffness (k)— there exists a transmitted, reflected, and converted signal; the converted signal is observed for low values of R (0.2).
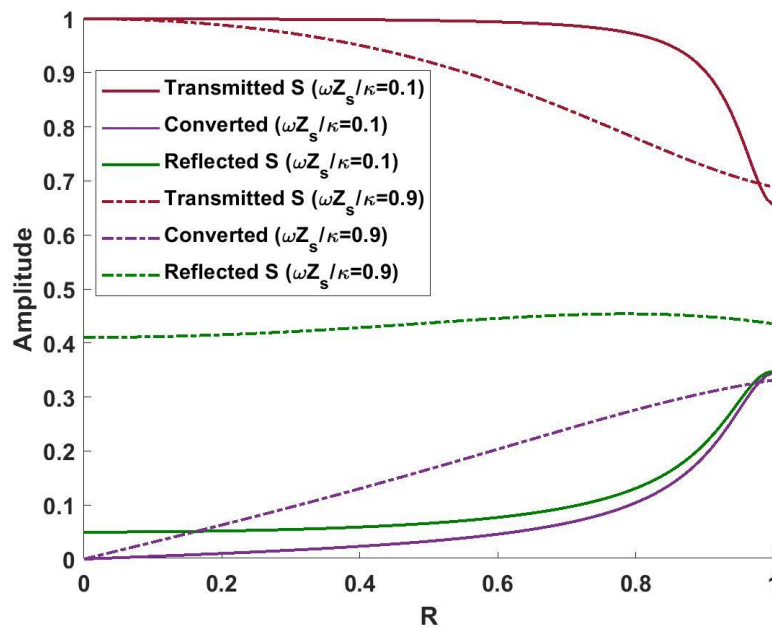
Figure 2.9 Transmitted converted and reflected coefficients for $\omega Z_s/\kappa$=0.1 (solid lines) and 0.9 (dashed lines)

2.7   Geophysical methods to study shearing of discontinuities

This section provides a brief review of relevant studies that used geophysical methods to investigate rocks subjected to shear loading.

Chen et al. (1993) investigated the shearing of granite samples with pre-existing discontinuities. They employed active seismic monitoring by transmitting shear waves across the discontinuity while subjecting it to shear stress. They were able to distinguish between a discontinuity undergoing stable sliding and a discontinuity exhibiting a stick-slip behavior. They observed that the shear wave amplitudes decreased gradually during stable sliding, whereas during stick-slip, the shear wave amplitude recorded a rapid decrease prior to or at slip. They attributed these changes in amplitude to changes in specific stiffness of the discontinuity.

Hedayat et al. (2014b) used active seismic monitoring to examine rough discontinuities in gypsum and Indiana limestone subjected to shear stress. They found that the amplitudes of the transmitted waves across the discontinuity increased as the shear stress increased until the peak shear strength was reached; afterward, the amplitudes decreased. The peak of the transmitted amplitudes occurred prior to the peak of the shear stress. This observation was used as a seismic precursor to failure. Hedayat et al. (2014b) attributed the decrease in transmitted amplitude (after the peak amplitude) to damage incurred on the asperities before slip took place. They also recorded reflected signals, where the opposite behavior was observed. The reflected amplitude decreased as the shear stress increased, reaching a minimum at the point of maximum transmission. After the peak, the amplitude of the transmitted waves decreased (while that of the transmitted waves decreased, as discussed).

Scuderi et al. (2016) conducted shear experiments on quartz powder, as a fault gouge, placed between steel plates. They observed precursors in the form of changes in compressional wave velocities for slow and fast stick-slip events. A reduction in the sample's seismic velocity and elastic moduli before failure was observed, indicating that active monitoring of active faults could detect precursors to earthquakes.

Rouet-Leduc et al. (2017) applied Machine Learning (ML) to experimental acoustic emission data obtained from double direct shear experiments on fault gouge to predict slip time. They found that

their ML model could predict the time remaining before a slip happened with high accuracy. Their study's interesting and helpful outcome was that their model could be applied to predict different types of failures such as landslides, avalanches, etc.

Hulbert et al. (2019) also applied ML to acoustic emissions data recorded during shearing of quartz fault gouge to predict the timing, duration, and magnitude of "laboratory earthquakes." They found that ML could predict the time, duration, and magnitude of laboratory earthquakes, whether slow or fast.

Previous studies show that monitoring the geophysical response of rock discontinuities is a promising tool to retrospectively predict the shear failure of pre-existing discontinuities. Studies from the literature show that it is possible to detect shear failure of pre-existing discontinuities at the laboratory scale (Hedayat et al., 2014b; Chen et al., 1993). Despite these crucial findings, it is still unclear whether we would be able to detect seismic precursors to failure on rock discontinuities with different characteristics. These characteristics could be similar to what would be present in the field, i.e., mismatched discontinuities or infilled discontinuities. It is also important to study different seismic precursory modes (transmitted, converted, and reflected) and analyze the information from each precursory mode. One of the objectives of this work is to study idealized sawtooth discontinuities subjected to shear and extract the information provided by the transmitted, reflected, and converted seismic signals. Which seismic mode is more sensitive to shear failure? Another goal is to investigate whether the mismatch of a discontinuity masks seismic precursors and identify the geophysical signatures of a mismatched discontinuity under shear.

3 GEOPHYSICAL RESPONSE OF SHEARING A ROCK DISCONTINUITY

3.1 Introduction

In the field, there is a range of types of rock slope failure, namely, planar, wedge, toppling, and circular failures. What all these types have in common is that they involve discontinuities within the rock. The failure along discontinuities can result in economic losses as well as the loss of life. Thus, it is important to develop methods to monitor the evolution of failure along pre-existing discontinuities to enable the prediction of failure, a very challenging problem. One step towards meeting this challenge is to perform laboratory experiments that use geophysical techniques to monitor shear failure of a pre-existing discontinuity to detect signatures of impending shear failure. In this chapter, the sample preparation protocol and the experimental setup adopted to perform such experiments and results from the experiments are described in detail.

3.2 Sample Preparation and Experimental Setup

All of the specimens used for this research were made of gypsum that is often used as a rock-model material (e.g., Bobet & Einstein, 1998; Mutlu & Bobet, 2006). A sample was composed of two independent prismatic gypsum blocks (length = 152.4 mm, width = 127 mm, and thickness = 25.4 mm) fabricated in the laboratory following a previously documented protocol (Bobet, 1997; Hedayat, 2013; Choi, 2013). In this protocol, first, 11.43 g of diatomaceous earth and 400 cc of water were mixed at a low speed (54 rpm) for 30 seconds. Next, a 1000 g of gypsum Hydrocal B11 powder was added to the mixture and blended at a low speed (54 rpm) for 30 seconds and then at high speed (180 rpm) for 4.5 minutes. The mixture was then poured into a mold that had grit 36 sandpaper (483 µm grain size) at the bottom. After filling the mold, it was vibrated at high speed (100 rpm) for 5 minutes to enable air bubbles to float to the surface. After an hour, the hardened sample was turned over, and a second gypsum mixture was poured over the rough surface of the first block. Before pouring, care was taken to apply a thin layer of a mold release agent to the rough surface of the first block to enable the separation of the blocks after curing. The nature of the mold release agent and the amount of mold release agent used was crucial as it caused variability in the rock surfaces (more on this in Chapter 5). For the experiments presented in this

chapter, a water-based Dow corning 2418 release emulsion agent was used. As mentioned earlier, it is essential to note that the amount of mold release agent applied plays a critical role in generating well-matched discontinuities; the amount of mold release agent used must be sufficient to separate the two blocks, but at the same time not excessive as this would result in mismatched rock discontinuities (more details on this topic are presented in chapter 5). All samples (both blocks) were left to cure at room temperature for 24 hours, followed by 4 days of curing in an oven with a temperature of 40°C. Figure 3.1 (a) shows a single block in the mold, and Figure 3.1 (b) shows a schematic of a sample with dimensions.
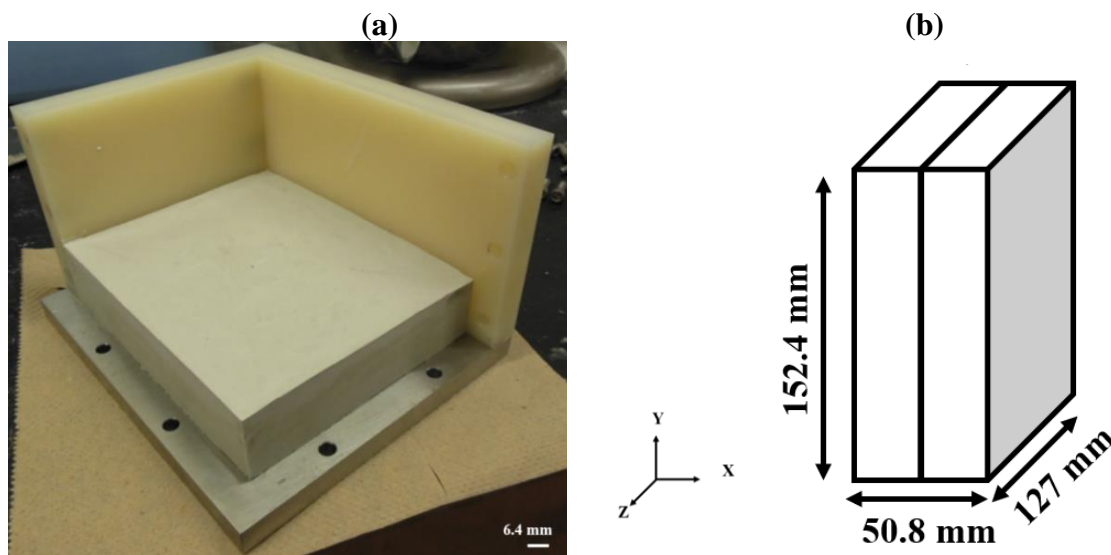
Figure 3.1. (a) Sample preparation; (b) schematic of the sample

After curing, the outside surfaces of the sample (those parallel to the fracture plane) were polished in the Physics machine shop at Purdue University using a Kennametal SVJBRF-062D fly cutter with a cutter angle of $35^{\circ}$and a Wells index milling machine, as shown in Figure 3.2. The polishing process involves mounting the sample on two steel parallels to ensure that the asperities do not get damaged throughout the polishing process, as these parallels are only in contact with the edges of the specimen. It is essential to polish the surfaces of the samples at the lowest speed –speed <1 in the Well's machine—to ensure smooth polished surfaces. Polishing at higher speeds produces rough surfaces that cause poor transducer-rock coupling (the coupling process is discussed in this section below). This step is also important to ensure that the normal load (while running the direct shear experiments) is uniformly applied to the sample.
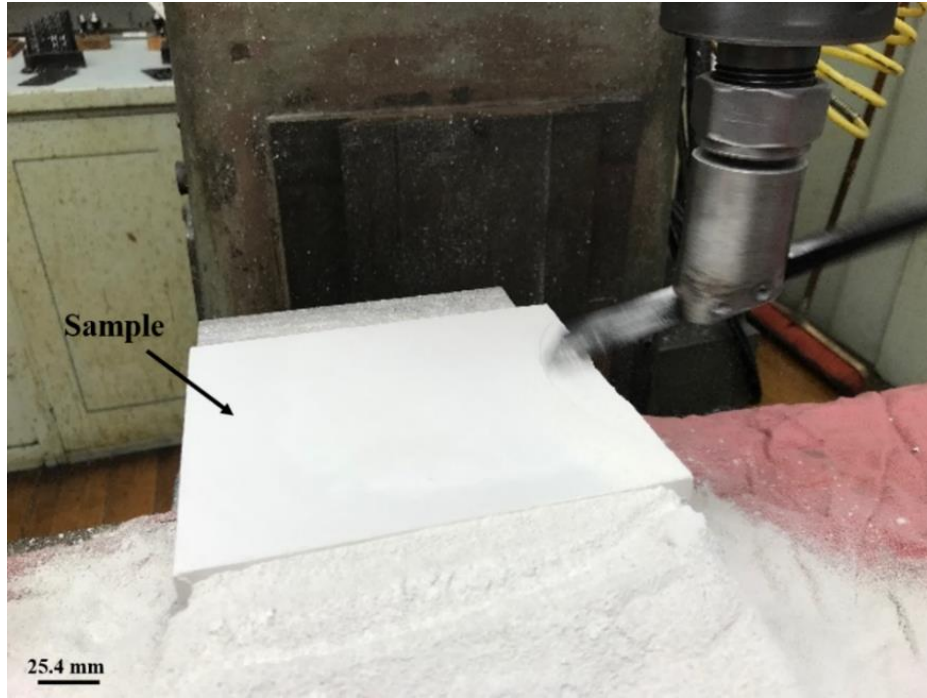
Figure 3.2. The polishing process by a fly cutter

After fabrication, curing, and polishing, the gypsum block assembly was ready to be tested. The experimental setup –shown in Figure 3.3(a-b), includes a biaxial apparatus composed of steel rods, rollers, and plates. The apparatus also includes a flat jack (ENERPAC RSM500) that is used to apply the normal stress. The flat-jack pressure was controlled using an electronic feedback control loop (CC8 multi-test control machine) to ensure that the normal load applied was constant throughout the experiment.

The experimental setup also includes a synced ultrasonic seismic system composed of a chassis National Instruments (NI) PXI-1042 with two multiplexer switches (NI TB-2630) to record several waveforms simultaneously and a 68-pin NI TB terminal block that connects the chassis with the relay switch to switch between source and receiver transducers; a simplified schematic of the seismic system is presented in Figure 3.4. Ultrasonic transducers (Olympus V153RM for shear & V103RM for compression) with a diameter of 11 mm with a central frequency of 1 MHz were used in this research. These transducers were adopted because their behavior under mechanical load—whether normal or shear stress—has been well-documented and established by previous researchers (Savic, 1995; de Pater et al., 2001; Pyrak-Nolte et al., 2005; Li et al., 2009; Li, 2011;

40

Hedayat et al., 2014b; Choi et al., 2014). Square wave pulses with an amplitude of 100 V and a repetition rate of 1 kHz were used to excite the piezoelectric transducers using an Olympus 5077PR pulse generator. A LabVIEW program was used to record the seismic data. The program enables the user to choose the number of channels, i.e., transducers desired for each experiment, and stores the collected full waveforms in an ASCII file. The sensor housing was composed of two arrays (Figure 3.3 (b)), each with 9 embedded ultrasonic transducers. Figure 3.3 (c) presents the layout of the transducers. The same layout was used for all of the experiments reported in this thesis. The sample was placed between the transducer housing in the biaxial apparatus and compressional, and shear seismic signals were transmitted across the specimens during the experiment at a sampling rate of 100 MSamples/second, i.e., 10,000 data points, yielding 0.01 microseconds per point.

(a)

LVDT

Sample

Transducer housing

Flatjack

Biaxial apparatus

(b)

(c)

Source

Receiver

2S
4P
5S
7S
9P
8S
6S
3P
1S
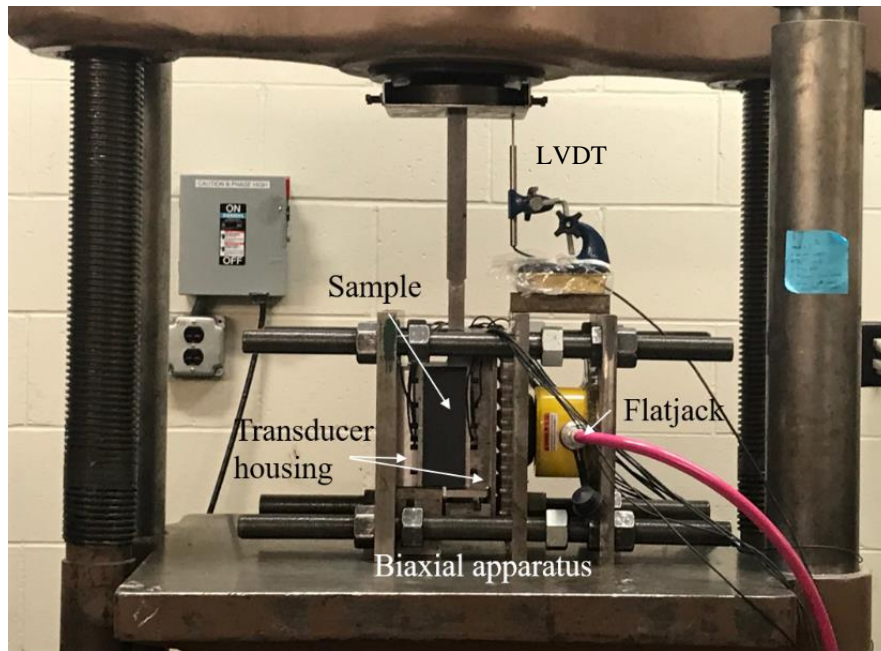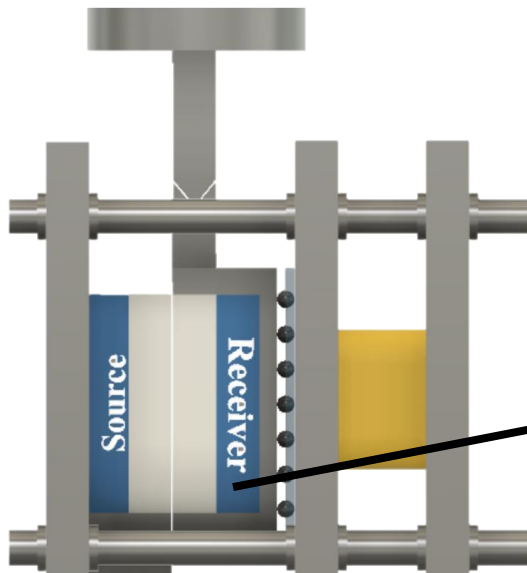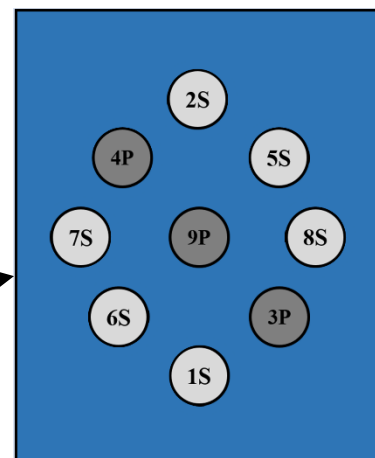
Figure 3.3. (a) Direct shear experimental setup; (b) schematic of the direct shear experiment; (c) transducers' layout
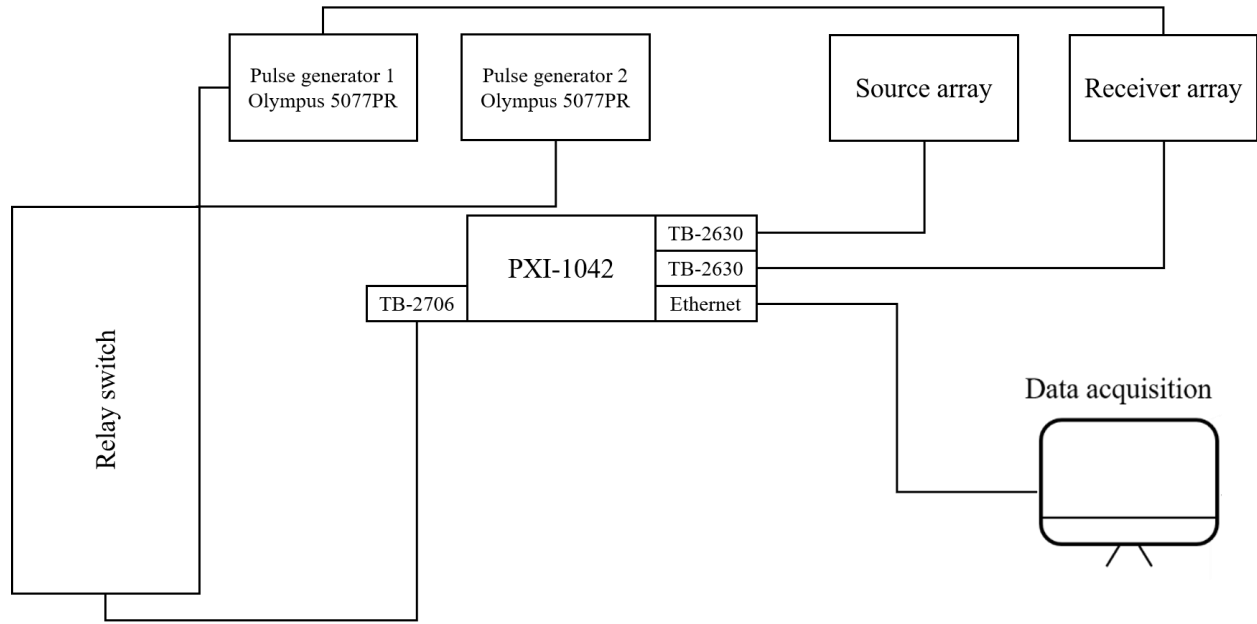
Figure 3.4. Schematic of the seismic system

The direct shear experiments were conducted with a shearing rate of 8 μm/s using the biaxial apparatus shown in Figure 3.3. The seismic transducers were coupled with the sample by applying a thin layer of baked honey. The honey was baked at 90ºC for 90 minutes (Modiriasari et al., 2017). It is important to note that before coupling the transducers, a thin layer of transparent tape was applied to the polished surfaces of the sample to make sure that the honey did not infiltrate into the sample. The coupling process involved applying a 1 MPa normal stress to the specimen, and platens housed the transducers. The load was maintained for 4 hours before testing to obtain stable transducer-rock coupling. After 4 hours, the specimen was loaded to the desired normal stress, and then the shear load was applied. Monitoring of the experiments also included recording digital images of the sample's surface while shearing, i.e., Digital Image Correlation (DIC), which will be discussed in the following subsection.

3.2.1 Digital Image Correlation

Digital image correlation was employed to record and analyze the sample's surface displacements during shearing. A Grasshopper (Point Grey) CCD camera with 2448×2048 square pixels resolution with a Fujinon lens (focal length=75 mm; Model HF75SA-1) was used to record images during the experiment at a rate of 4 frames/sec and was placed perpendicular to the surface of the

specimen, as shown in Figure 3.6. The FlyCapture® SDK software was used to control the camera and to record and save the images. Before recording DIC images, a random grey speckle spray (Rust-Oleum multicolor textured) was applied to the surface of the specimen., i.e., the surface being probed by the DIC camera. DIC operates as follows: first, a reference image is identified, i.e., the first collected image during an experiment. The image is then divided into a square subset composed of unique pixels (the uniqueness of the pixels is obtained from the grey speckle spray paint) (Sutton et al., 2009; Pan et al., 2009), as shown in Figure 3.5 (for clarity, only four subsets are shown). Figure 3.5 (a) presents a schematic of a reference image divided into four subsets with dimensions of 2M+1 pixels each, M represents half of the size of the subset, and a point of interest in the figure is denoted by the red dot in each subset, i.e., *f(xᵢ,yᵢ)* *(T)*. The deformed image is presented in Figure 3.5 (b), where the points of interest —*f(xᵢ,yᵢ)* *(T)* in the reference image—are now *g(xᵢ,yᵢ)* *(S)* in the deformed image. Figure 3.5 (c) presents the deformed image overlaid on top of the reference image. A degree of similarity is defined by a correlation criterion created between the reference subset and the deformed images. Raw DIC images were post-processed using DaVis LaVision software that employs the zero normalized form (ZNCC) to analyze surface displacements from DIC images (Pan et al., 2009). Equation 3.1 was used to measure the similarity and differences between the referenced and deformed images (Pan et al., 2009).

$$C_{ZNCC(d)} = \sum_{i=-M}^{M} \sum_{j=-M}^{M} \frac{(f(x_i,y_j)-f_m)(g(x_i',y_j')-g_m)}{\Delta f \Delta g} \tag{3.1}$$

Where,

$$f_m = \frac{1}{(2M+1)^2} \sum_{i=-M}^{M} \sum_{j=-M}^{M} f(x_i,y_j) \tag{3.2}$$

$$g_m = \frac{1}{(2M+1)^2} \sum_{i=-M}^{M} \sum_{j=-M}^{M} g(x_i',y_j') \tag{3.3}$$

$$\Delta f = \sqrt{\sum_{i=-M}^{M} \sum_{j=-M}^{M} (f(x_i,y_j) - f_m)^2} \tag{3.4}$$

$$\Delta f = \sqrt{\sum_{i=-M}^{M} \sum_{j=-M}^{M} (g(x_i',y_j') - g_m)^2} \tag{3.5}$$

The ZNCC varies between 0 and 1. A value of 1 is associated with no difference in intensity of pixels between the reference and the deformed subset; that is, it indicates that points *S* and *T* are the same. Thus, the change in the location of the center point between the reference (point *T*) and

the deformed subset (point S) defines the displacement vector d, as shown in Figure 3.5(c). For more information on the ZNCC statistical analysis method and on 2D-DIC, readers can refer to Sutton et al. (2009), Hedayat (2013), and Hedayat et al. (2014a).
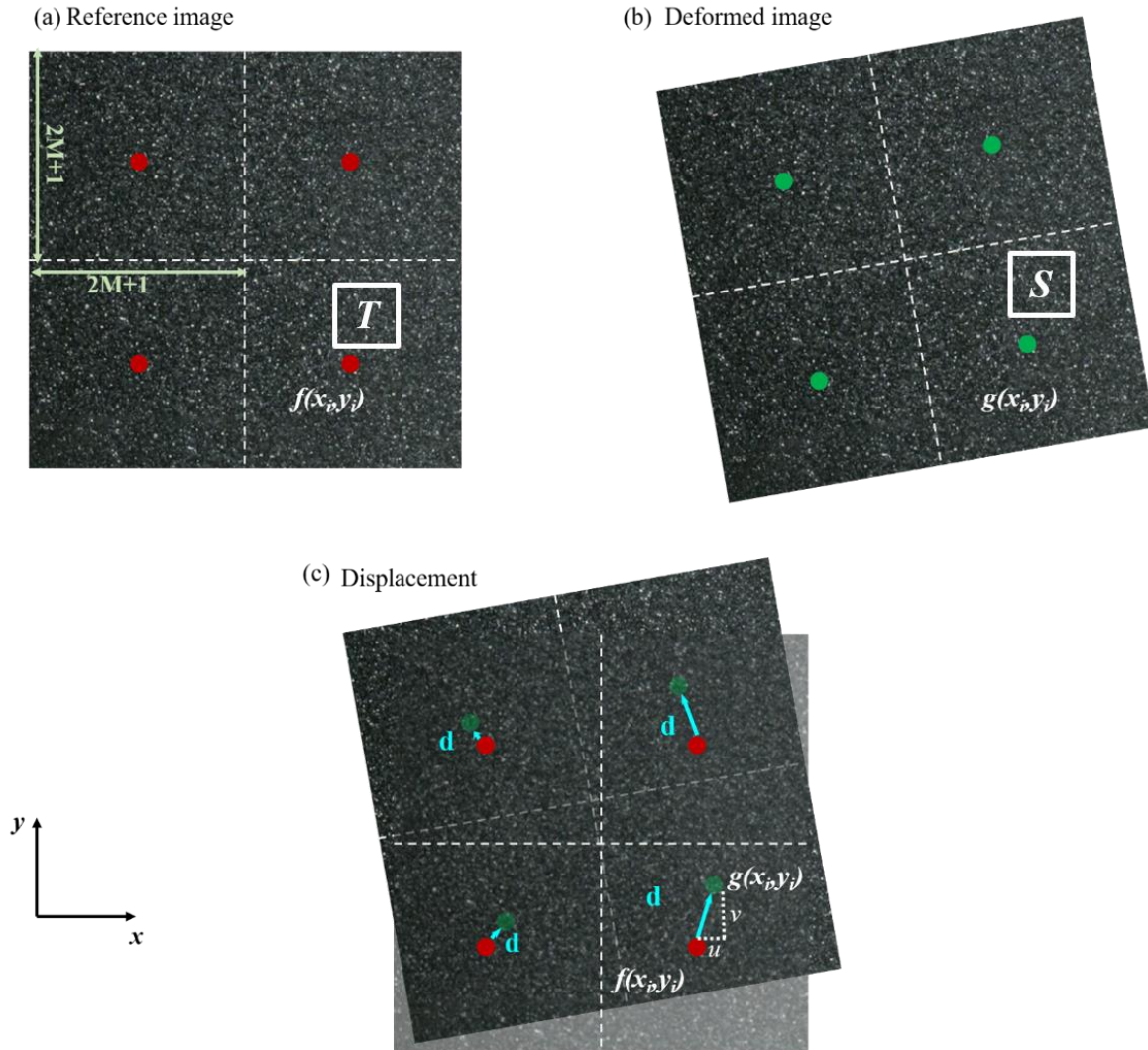
Figure 3.5. DIC reference and deformed schematics

(a)

(b)

Loading frame

Loading piston

Sample

Biaxial apparatus

Rollers

Hydraulic pump cable

Hydraulic pump

Loading frame

Biaxial apparatus

Data acquisition

CCD camera

Loading piston

90°
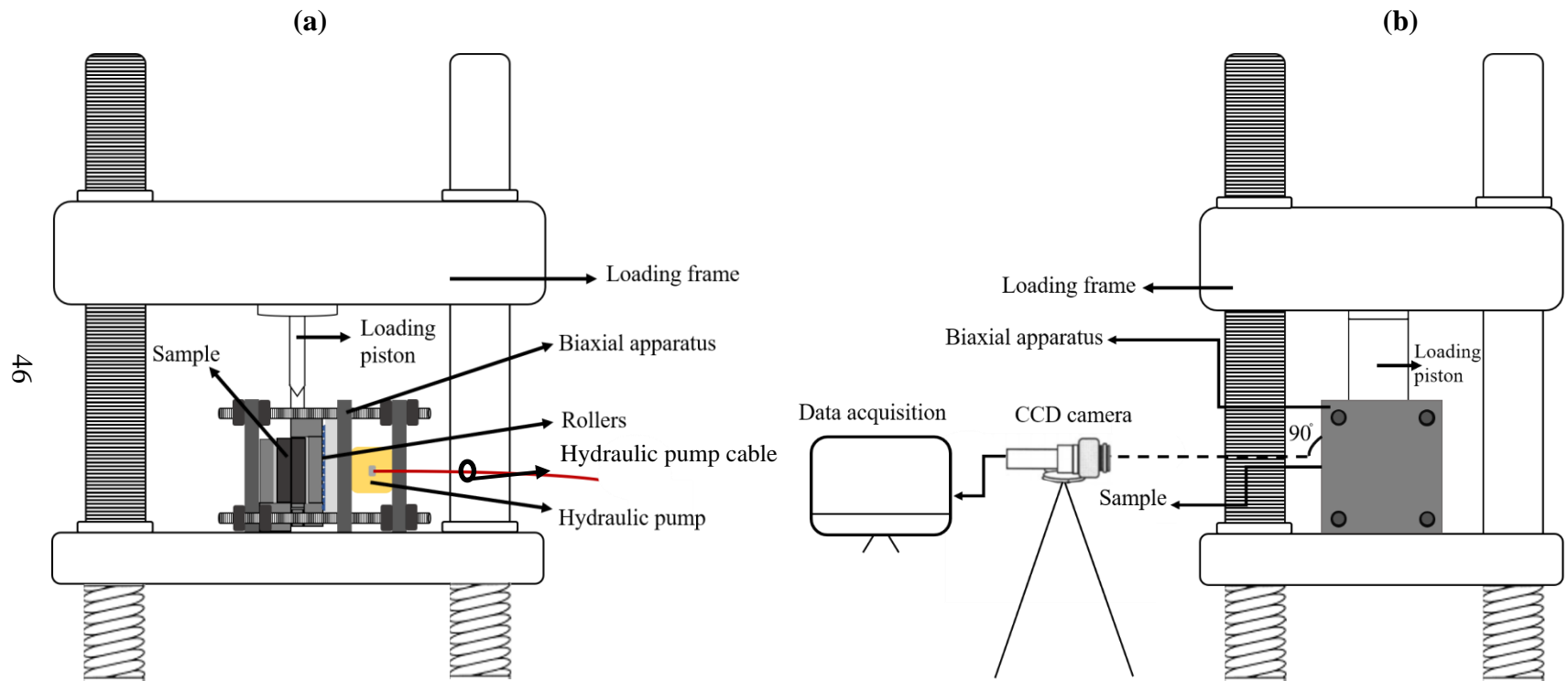
Sample

Figure 3.6. Schematic of the experimental setup (a) front-view; (b) side-view showing the digital camera position with respect to the sample

3.2.2   Normal Stress Distribution Across a Discontinuity

A pressure-sensitive film (FujiFilm Prescale Sensor Film) was placed between the two blocks to determine whether the normal stress applied to the discontinuity was uniform (along the rough interface, see Figure 3.7 (a)). Then the sample was subjected to normal stress of 5 MPa for ~20 minutes (as shown in Figure 3.7 (b)). Figure 3.8 is an image of the film placed between the two grit 36 rough surfaces.

(a)   **(b)**
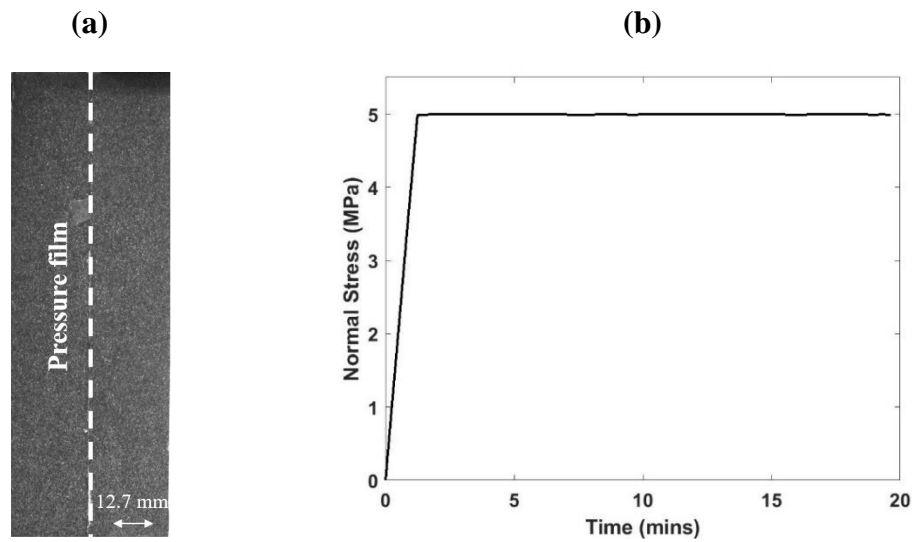
Figure 3.7. (a) Sample indicating the pressure film's position;(b) normal stress applied for pressure film experiments
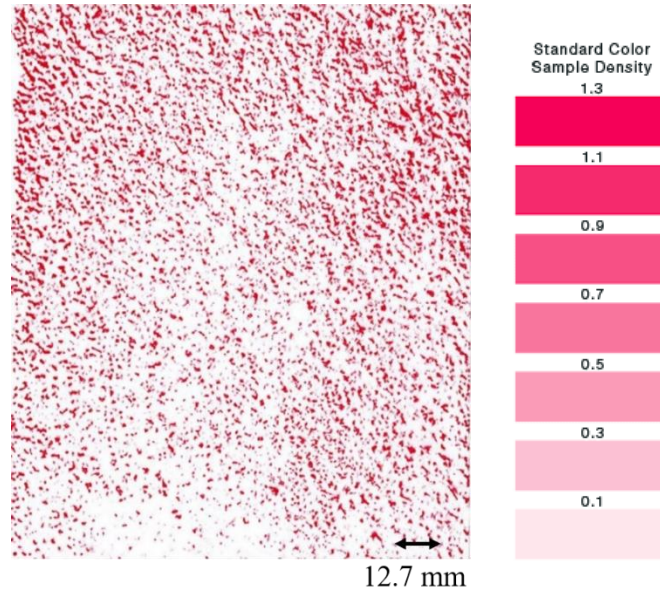
Figure 3.8. Scanned pressure film for a rough discontinuity

Image analysis was performed on the scanned film to quantify the pressure exerted on the discontinuity and assess its uniformity. The intensities of the red pixels in Figure 3.8 were converted to quantitative pressure values based on a calibration chart provided by the manufacturer (Figure 3.9). Figure 3.9 (a) shows the corresponding pressure values in Megapascals for selected red color densities. The calibration chart was first converted to a Hue, Saturation, and Value (HSV) model. The saturation is equivalent to the density of the red color on the pressure film. Then, the graph in Figure 3.9 (b) was used to obtain the corresponding pressure for each recorded intensity. One of the curves (A, B, C, or D) would be selected based on the temperature and humidity recorded when conducting the experiment (Figure 3.9 (c)). Curve D was chosen for this analysis because the laboratory temperature was assumed to be closest to ~20ºC with a Relative Humidity (RH) of 55%.
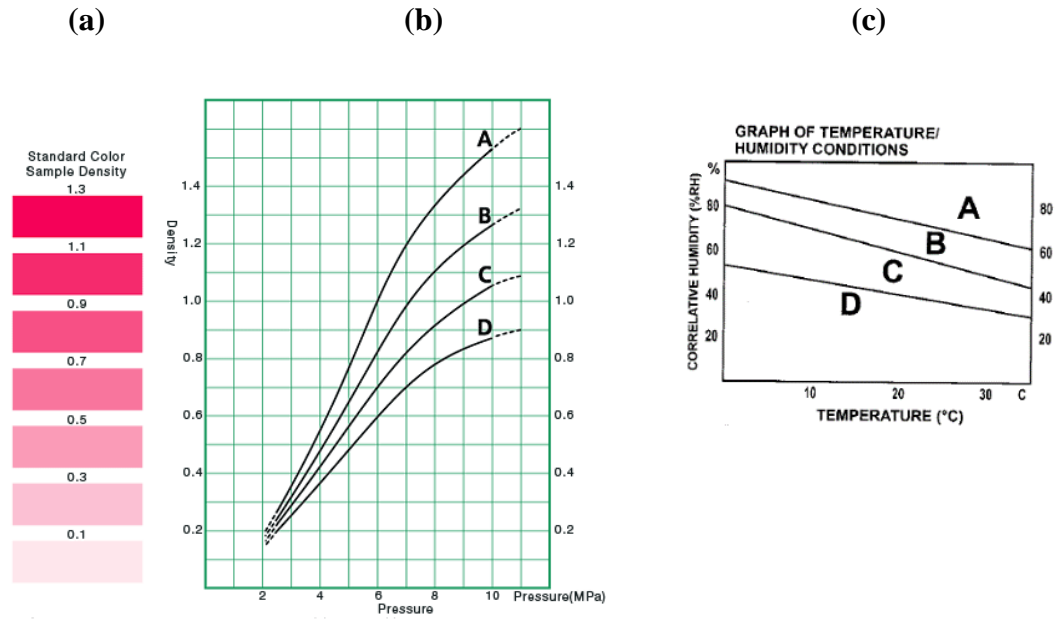
Figure 3.9. (a) Pressure film calibration chart; (b) pressure film density as a function of pressure; (c) humidity and temperature correlation

Figure 3.10 shows the stress distribution along the discontinuity.
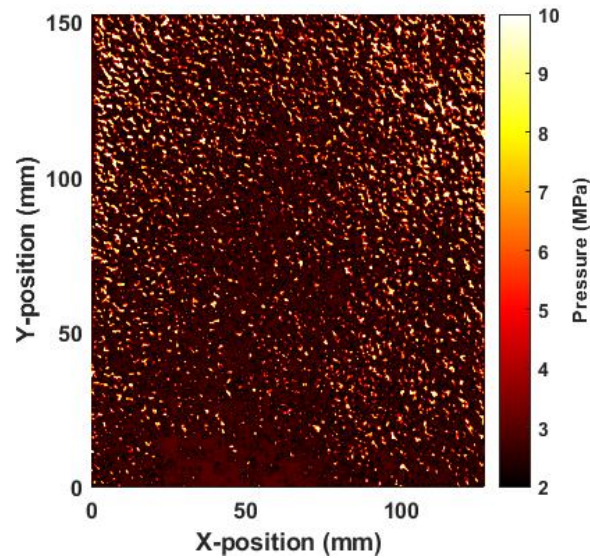
Figure 3.10. Quantified stress along a rough discontinuity

Table 3.1 presents a statistical summary of the pressure. The average pressure was 3.41 MPa, and the minimum and maximum pressures were 2.43 and 9.65 MPa, respectively.

49

Table 3.1. Statistical summary for the stress distribution

Average pressure	3.41 MPa
Minimum pressure	2.43 MPa
Maximum pressure	9.65 MPa

Figure 3.11 shows the distribution of pressures that appear to follow a lognormal distribution. The magnitude of the pressure applied may not be accurate due to, e.g., calibration or sensitivity errors or because only one pressure experiment was conducted. The outcome of this test should be viewed in terms of uniformity of the pressure applied, but the test may not result in an accurate magnitude of stress.
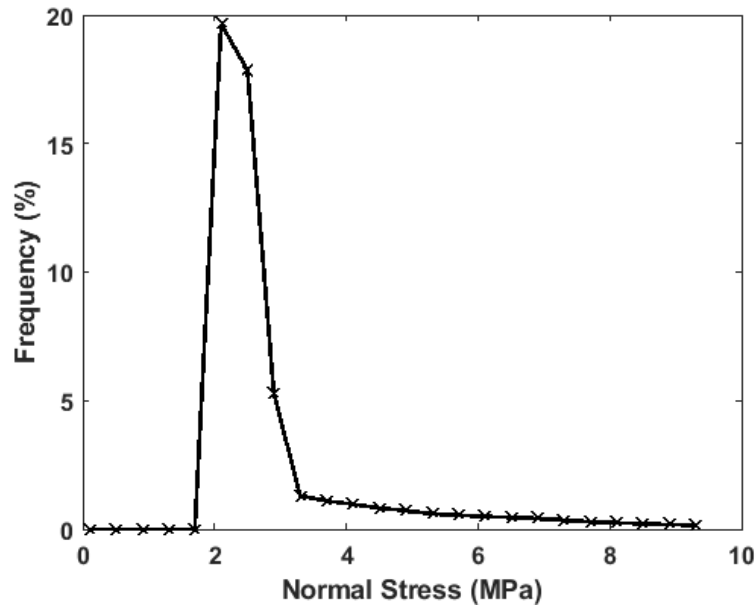
Figure 3.11. Normal stress distribution from pressure film

3.3   Results and Discussion

3.3.1   Direct shear experiments on a planar discontinuity

This section includes the geophysical results obtained from shearing planar gypsum discontinuities. Figure 3.12 shows the normalized transmitted amplitude from waves propagated across the top, middle, and bottom transducers as a function of shear displacement (see Figure 3.3 (c) for

transducer layout location). The normalized transmitted amplitudes were obtained by performing a wavelet analysis (Combes et al., 1989; Nolte et al., 2000) and plotting the peak amplitudes at ~682 kHz frequency (for all the data presented in this chapter for consistency). On the secondary y-axis, the shear stress is also presented as a function of shear displacement for a sample sheared at 1 MPa normal stress. The shear stress plot shows the data after seating deformation. The dashed line represents the displacement at which the peak shear stress was recorded.
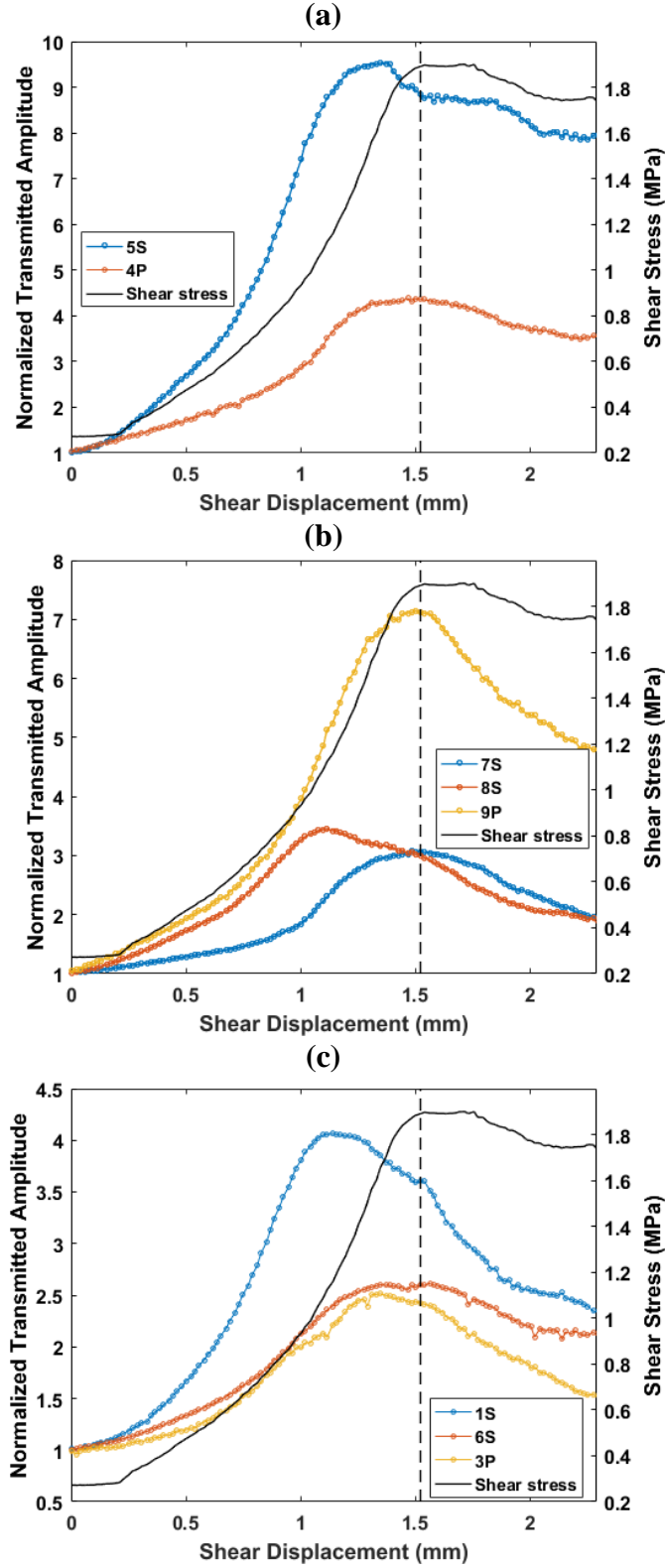
Figure 3.12. Normalized transmitted amplitude recorded by (a) top, (b) middle, and (c) bottom transducers as a function of shear displacement at a normal stress of 1 MPa; the secondary y-axis plots the shear stress

Initially, as the shear stress increases, the normalized transmitted amplitude measured by all of the transducers increases (Figure 3.12 (a-c)). This increase is caused by an increase in both normal and shear fracture-specific stiffnesses which has been shown to enhance the transmission (Pyrak-Nolte al. 1990, Choi et al., 2014). A peak in the transmitted amplitude is reached prior to the occurrence of peak shear stress, representing a seismic precursor to failure, the same as that identified by Hedayat et al. (2014b). The normalized transmitted amplitudes then decrease because of damage incurred by the asperities, resulting in a reduction in fracture stiffness and, in turn, a decrease in transmission.

DIC images were analyzed to study how slip –across the discontinuity—occurred as the shear stress was applied. Figure 3.13 (a) shows a contour plot of the vertical displacement at a shear stress of ~1 MPa (~56% of peak shear stress). The vertical displacements at three horizontal cross-sections are plotted in Figure 3.13 (b) to gain better insight into how and when slip initiates along the fracture. A vertical displacement discontinuity is observed when slip between the two blocks of the discontinuity occurs. Figure 3.13 (b) shows that a vertical displacement discontinuity takes place first at the top portion of the specimen—where the load was applied—and as the shear stress increases, it progresses across the middle and bottom parts of the discontinuity. It is essential to mention that, in general, slip along a discontinuity initiates from an area with low frictional resistance and then extends to areas with higher frictional resistance (Mutlu and Bobet, 2006; Hedayat et al. 2014a). Since the sample has a homogenous rough surface, it could either slip at the top or bottom portion of the specimen, depending on local frictional conditions and where the load was applied. Hedayat et al. (2014a) conducted similar direct shear experiments on non-homogeneous gypsum rock discontinuities (smooth & rough). They showed that slip initiated first along the smoother portion of the interface—whether the smooth portion of the specimen was placed at the top or the bottom in the biaxial apparatus. Figure 3.13 (c) shows a contour plot of the vertical displacements recorded at ~1.8 MPa (peak shear stress), and similarly, Figure 3.13 (d) shows the vertical displacement cross-sections at the same three cross-sections. As Figure 3.13 (d) shows, the displacement discontinuity is recorded at the three portions of the specimen and seems to progress from the top to the bottom portion of the specimen.
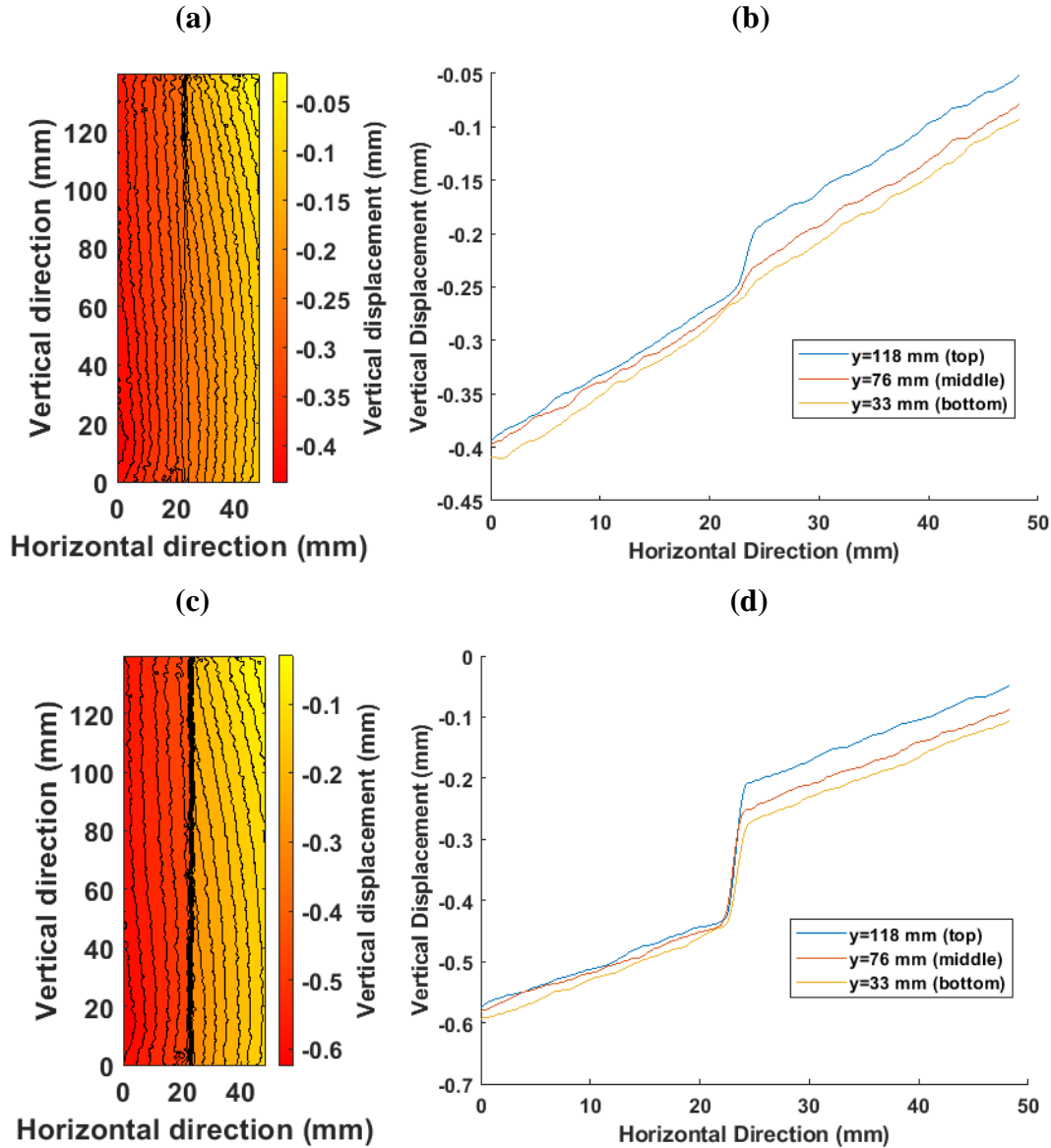
Figure 3.13. Contour plot of vertical displacements recorded by DIC at (a) 1 MPa and (c) 1.8 MPa; vertical displacements at three horizontal cross-sections from top (y=118 mm; blue), middle (y=76 mm; orange), and bottom (y=33 mm; yellow) portions of the specimen at (b) 1 MPa and (d) 1.8 MPa

Horizontal displacements from DIC were also analyzed and are presented in Figure 3.14 to examine whether the sample exhibited any dilation or horizontal displacements at a shear stress of 1.8 MPa. Horizontal displacements at three horizontal cross-sections (top=118 mm; middle=76 mm; and bottom=33 mm) along the discontinuity are also presented. The data shows that the specimen with a planar discontinuity does not exhibit any dilation. For the resolution of the

measurements (2 micrometers), no horizontal displacement discontinuity is observed between the two blocks of the specimen for all three cross-sections.

(a)   **(b)**
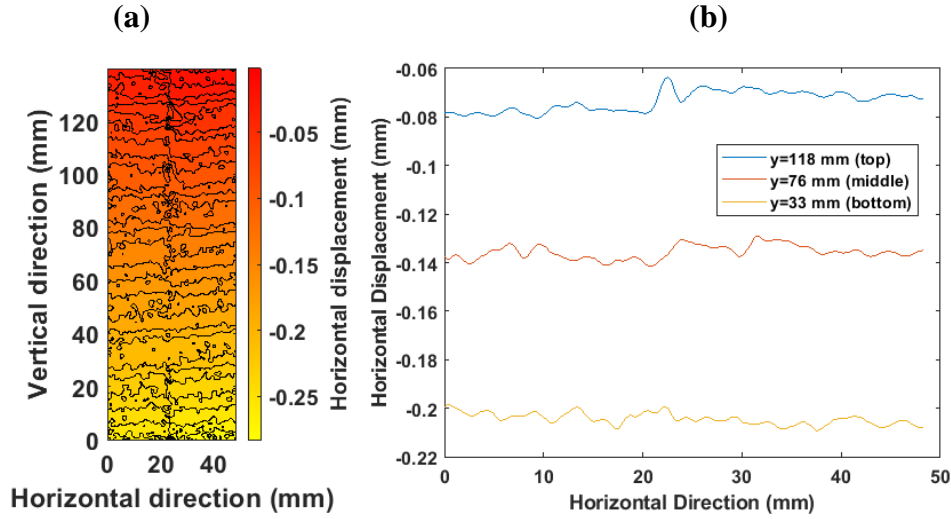
Figure 3.14. Horizontal displacement (a) contour plot; (b) cross-sectional displacements at top (y=118 mm, blue), middle (y=76 mm, orange) and bottom (y=33 mm, yellow) at shear stress = 1.8 MPa

3.3.2 Direct shear experiments on a nonplanar discontinuity

Direct shear experiments on a nonplanar discontinuity with a half-cycle sine wave that spanned the central 1/3 of the discontinuity length (see Figure 3.16 and Figure 3.17) were performed to determine the effect of the fracture profile on joint dilation during shearing. Before preparing gypsum discontinuities with nonplanar profiles, laser profilometry was employed to quantify the surface roughness of a planar discontinuity prepared with a grit 36 sandpaper (section 3.2). Laser profilometry was used to scan the rough planar surface (with grit 36 roughness) generated by the sandpaper. A Keyence LK-G152 laser with a spot size of 120 µm was used with a step size of 0.25 mm to scan the rough surface of a specimen, which was mounted on a motion-controlled (Newport MTM250PP1) translation stage. The obtained scan was corrected for possible sample positioning errors by subtracting the gradients obtained from performing a 2D plane fitting from the asperity height matrix. Figure 3.15 (a) shows a frequency distribution of asperity heights with a minimum of -0.35 mm and a maximum of 0.32 mm. A reconstruction of the surface is shown in Figure 3.15 (b).
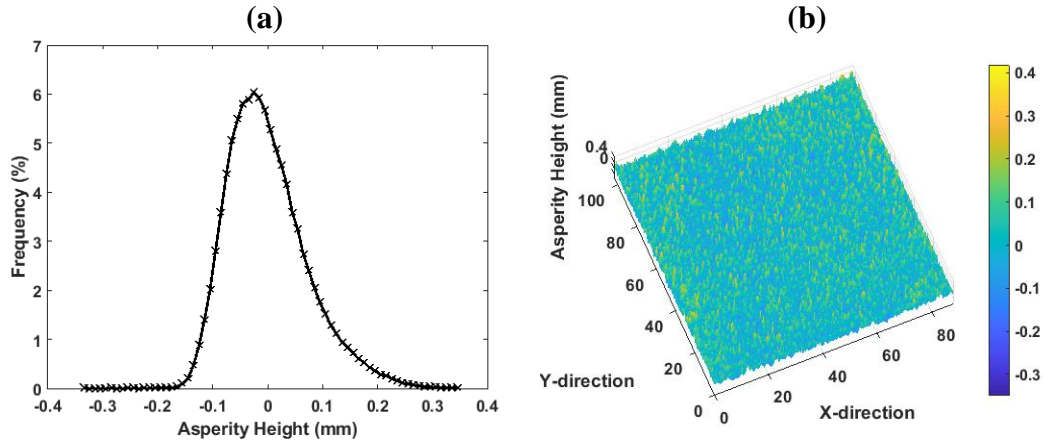
Figure 3.15. (a) Frequency distribution of the height of the asperities; (b) 3D reconstruction of the spatial distribution of asperities height. The color scale represents the asperity height in mm.

3D printing was used to create a sample with a nonplanar discontinuity. A plastic prismatic block with a surface profile was printed with a central half-cycle sine (HCS) wave with an amplitude of 3.2 mm, as shown in Figure 3.16 (10 times greater than the maximum asperity height created by the sandpaper as shown in Figure 3.15).

Figure 3.16. 3D-printed mold base

The profile consisted of two planar portions adjacent to a centrally located half-cycle sine wave (Figure 3.17). A frit 36 sandpaper was taped over the 3D printed mold to create roughness on the fabricated discontinuity—resulting in 1st order and 2nd order asperities. The first-order asperities correspond to the HCS, and the second-order asperities correspond to the asperities generated from the sandpaper.

Planar
_____

Amplitude =3.2 mm
_____
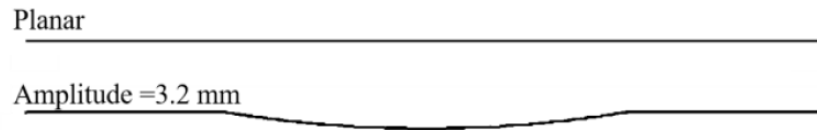
Figure 3.17. Schematic of discontinuity surface profile examined

Figure 3.18 shows the peak shear stress as a function of normal stress for planar samples (blue squares) and samples with an HCS in magenta squares. The graph also shows data obtained by previous researchers who conducted similar direct shear experiments on planar rough (grit 36 roughness) gypsum discontinuities (Mutlu, 2006; Hedayat, 2013).
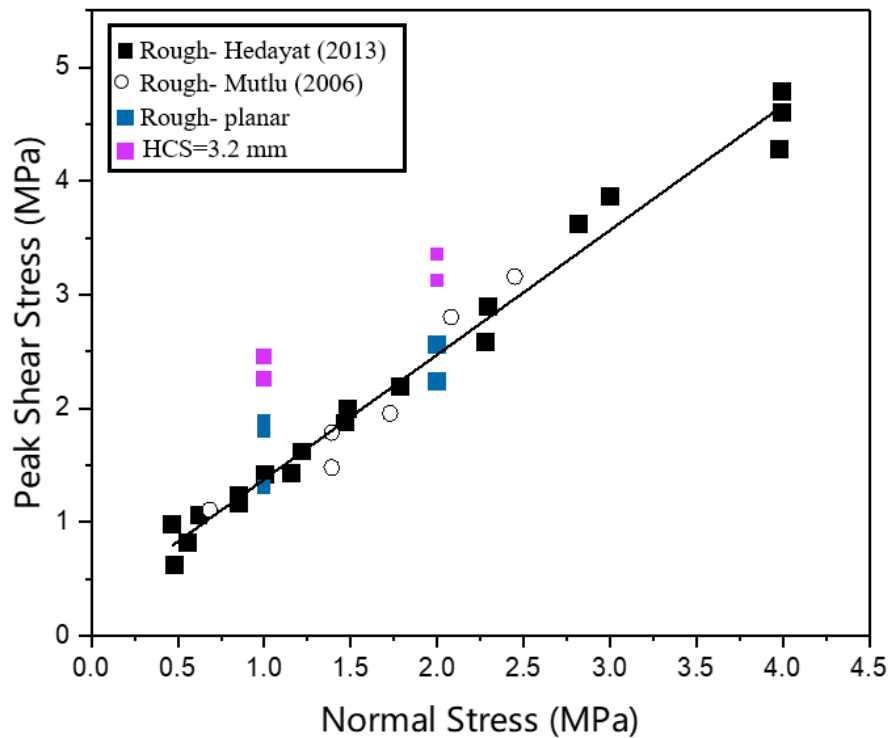
Figure 3.18. Peak shear stress versus normal stress with data from previous researchers (Hedayat, 2013; Mutlu, 2006)

When the amplitude of half-cycle sine wave surface is an order of magnitude larger than the mean asperity height the roughness obtained from the sandpaper, a higher peak shear strength is observed relative to that from a planar discontinuity for both normal stresses of 1 and 2 MPa. The average

peak shear strength for a specimen with an HCS is ~ 1.4 times the average peak shear stress obtained for planar discontinuities at both normal stresses (1 and 2 MPa).

Two samples with a half-cycle sine wave with an amplitude of 3.2 mm (i.e., 10 times the maximum asperity height) were sheared under constant normal stress of 1 MPa (repeatability experiments are presented in Appendix A). Figure 3.19 shows the normalized transmitted amplitude for (a) top, (b) middle, and (c) bottom transducers probing the sample. The results of the planar discontinuity sample were presented in section 3.3.1. The secondary y-axis is the shear stress as a function of shear displacement. As the shear stress increased, the normalized transmitted amplitude increased for all of the transducers. In Figure 3.19, the normalized transmitted amplitude from the top transducers (2S, 5S, and 4P) exhibited a continuous increase even after the peak shear stress was reached. This trend was not observed in those transducers located at the middle or the bottom of the sample (7S, 8S, 9P, 6S, and 1S). A plausible interpretation is that there seems to be enhanced contact at the top portion of the specimen—thus a continuous transmission recorded by top transducers even after the peak shear stress, and a loss of contact at the bottom portion of the specimen—thus a decrease in transmission after peak shear stress. This interpretation could apply if the sample undergoes rotation, resulting in better contact at one portion of the specimen and a loss of contact at another. This mechanism is explained in more detail below when discussing the DIC results. Precursors to failure, in the form of peaks in the normalized transmitted amplitudes, were not observed in any of the wave amplitudes. However, some transducers showed a change in transmitted amplitude before the peak shear stress, namely, 5S, 2S, 4P, and 9P, and could be interpreted as a precursor to shear failure. As shown in Figure 3.19, the peaks of the normalized transmitted amplitude of transducers 1S, 3P, 6S, 7S, and 8S did not occur before the peak shear strength. To investigate the differences, DIC images were analyzed to examine the displacements along and across the fracture.

Figure 3.19. Normalized transmitted amplitude for the sample with HCS=3.2 mm at normal stress of 1 MPa, for transducers from (a) top, (b) middle, and (c) bottom portion of the specimen; the secondary y-axis plots the shear stress

DIC data were examined to gain more insight into the displacement behavior of nonplanar discontinues. Figure 3.20 (a) shows a contour graph of horizontal displacement obtained from DIC at the peak load (shear stress= 2.25 MPa; peak shear stress). Figure 3.20 (b) shows the displacements for three different three cross-sections of the sample: top (y=118 mm, blue), middle (y=76 mm, orange), and bottom (y=33 mm, yellow). Figure 3.20 (b) shows that dilation—horizontal displacement discontinuity between the two blocks—occurred at all three locations; however, the discontinuity in horizontal displacement at the top (y=118 mm, blue curve) was less than that recorded at the middle and bottom of the sample (y=76 mm and 33 mm, respectively). These differences in horizontal displacement discontinuities resulted from a rotation of the two blocks that caused the blocks to separate/unload at the bottom. This mechanism helps explain the observations in transmitted wave amplitude in Figure 3.19. It is hypothesized that the following mechanism occurred: at the top, the normal stress between the two blocks increases due to the rotation, which in turn increases the normal and shear stiffness of the discontinuity, thus increasing the amplitude of the transmitted waves. At the bottom of the specimen, the effect is the opposite: the normal stress decreases because of the rotation, which induces an additional reduction in transmitted wave amplitude. Figure 3.20 (c) shows the aperture of the fracture as the sample dilates at a post-peak shear stress of ~1.8 MPa, and it demonstrates that according to DIC data, the aperture is larger (~0.3 mm) at the bottom portion of the sample compared to the top portion of the specimen that was still in good contact. Thus, the rotation of the specimen, by affecting the normal local stresses, resulted in no observations of precursors to failure.

Figure 3.20. Horizontal displacement for a sample with HCS=3.2 mm at a normal stress of 1 MPa (a) contour plot; (b) cross-sectional displacements at top (y=118 mm, blue), middle (y=76 mm, orange) and bottom (y=33 mm, yellow); (c) discontinuity aperture (post failure)

Two samples with the same half-cycle sine wave discontinuity profile were sheared at a normal stress of 2 MPa (the repeatability experiment is presented in Appendix A) to investigate whether the seismic precursors could be observed and whether dilation was suppressed. An increase in normal stress may suppress dilation due to higher confinement application across the discontinuity. The normalized transmitted amplitudes are shown in Figure 3.21. Similar to previous figures, the shear stress is graphed on the vertical y-axis. In Figure 3.21, the normalized amplitudes of the signals increased as the shear stress increased, then reached a peak, and then decreased prior to peak shear load. The trend in the normalized transmitted amplitude is similar to that described earlier in section 3.3.1 for the planar fractures, namely, as the shear stress increases, the fracture stiffness increases, and in turn, results in an increase in transmitted amplitude. The transmitted

amplitudes then peaked, after which transmission decreased. This decrease in the transmission is caused by damage sustained by the asperities from the shear stress applied. Almost all of the transducers recorded seismic precursors to failure, i.e., recorded a peak in transmission prior to the peak shear stress, which, as discussed later, was the result of dilation suppression due to higher confinement. Sharp drops in transmission are observed in the normalized transmitted amplitudes of transducers 5S (at a shear displacement of ~1.41 mm) and 8S (at a shear displacement of ~1.38 mm) in Figure 3.21 (a-b). Such sharp drops when a crack is generated (on a plane that is perpendicular to the discontinuity) during the shearing process of a sample. Such sharp drops in transmission were also recorded in other samples with planar discontinuities (Appendix A), so it is not necessarily an outcome of the half-cycle sine wave discontinuity

While this is a complex phenomenon and requires structured experiments to understand further how and why the crack was initiated, a couple of qualitative observations are worth mentioning. An interesting observation is that the generated crack was detected by transducers 5S and 8S— which are adjacent to each other, as shown in Figure 3.22. At the same shear displacement (1.41 mm), transducer 3P recorded a sharp increase in transmission coincides with the initiation of this crack (on a plane orthogonal to the discontinuity). Data from transducers 5S, 8S, and 3P are presented in Figure 3.22. The cause of the crack initiation can be attributed to several reasons: (1) there exists a mismatch between the contact surface of the discontinuity (at the asperity level), so some asperities may act as pressure concentrators, thus resulting in high-pressure points, which may lead to a crack—the pressure film presented in Figure 3.10 (pressure film data) supports this interpretation as some asperities recorded pressures as high as 9.6 MPa—while the average recorded stress was ~3.41 MPa—when the discontinuity was subjected to normal stress of 5 MPa—, (2) uneven polishing: even with a fly cutter, the polishing is only as good as the tolerance of the steel parallels used to hold the specimen while polishing its surfaces, and (3) due to both, i.e., mismatch and uneven polishing. These observations further shed light on the potential of using seismic tools to detect impending shear failure and cracks generated orthogonal to a pre-existing discontinuity when subjected to shear stress.
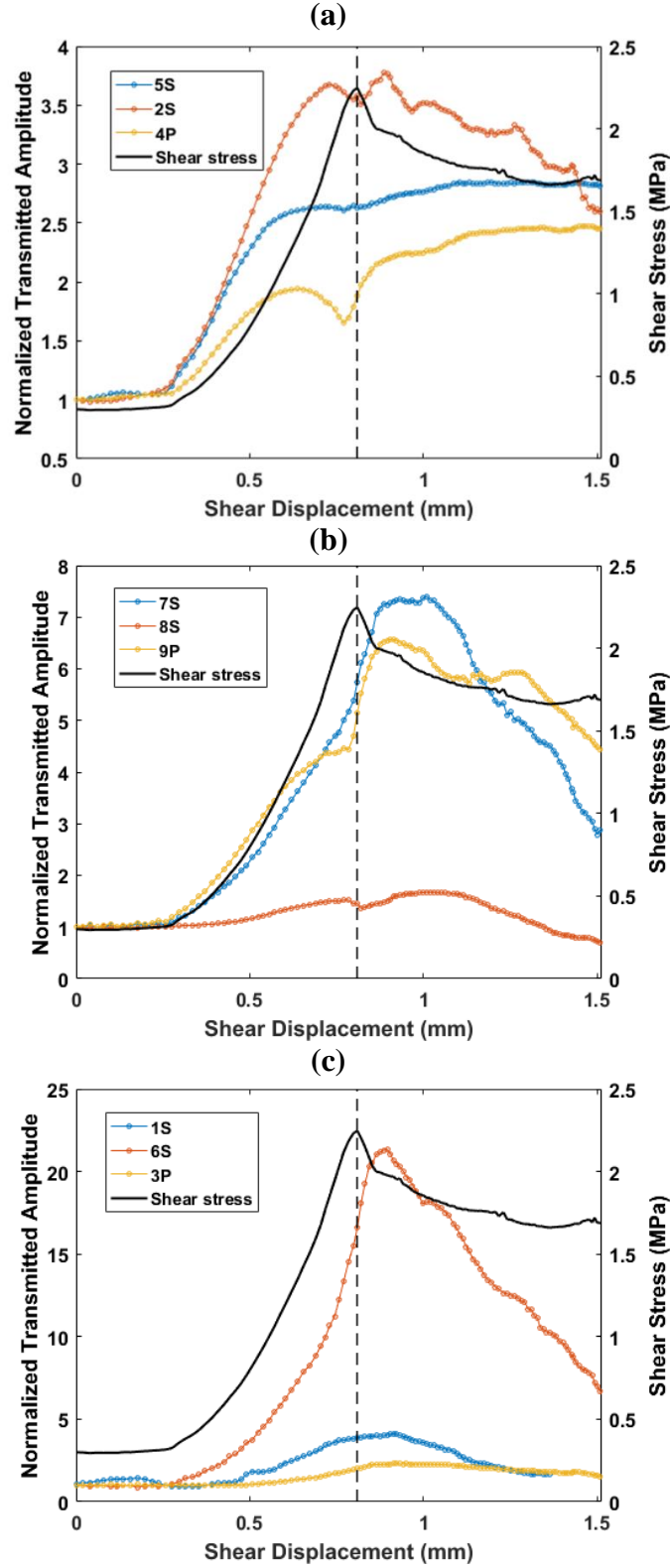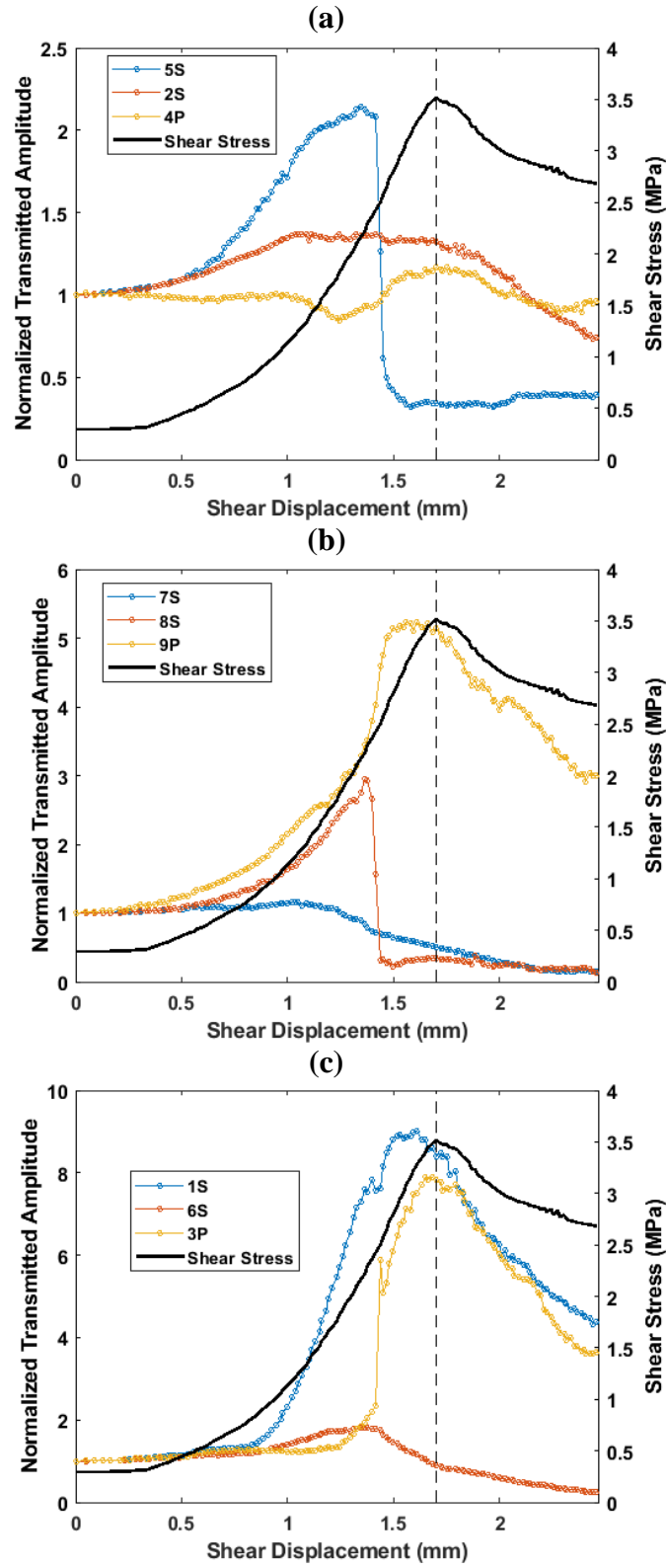
Figure 3.21. Normalized transmitted amplitude for a sample with HCS= 3.2 mm at a normal stress of 2 MPa for (a) top, (b) middle, and (c) bottom transducers; the secondary y-axis plots the shear stress
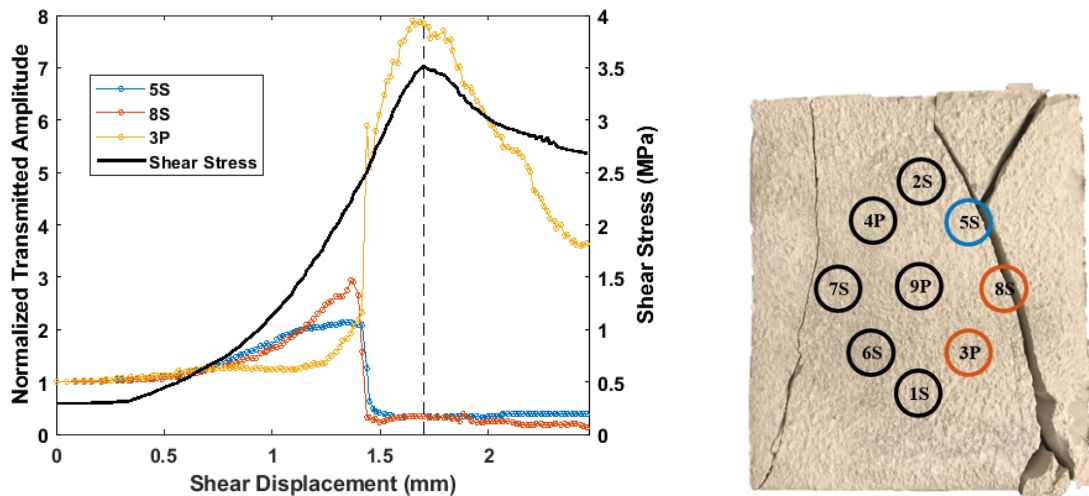
Figure 3.22. Normalized transmitted amplitude for 5S, 8S transducers recording a sharp drop and 3P recording a sharp increase in transmission; the secondary y-axis plots the shear stress—HSC=3.2 mm sample at a normal stress of 2 MPa

Horizontal surface displacements obtained from DIC, at peak load for a sample with an HCS sheared at 2 MPa, are shown in Figure 3.23. Dilation, i.e., a discontinuity in horizontal displacement between the two blocks, occurred almost uniformly along the contact surface, which is quite different than what was observed for the same sample under lower confinement (Figure 3.20 (b)). No significant rotation of the blocks was observed under higher confinement. Thus, no re-distribution of the normal stress occurred during shear, and, therefore, the transducers captured –through the precursors—the damage to the asperities as they were sheared.
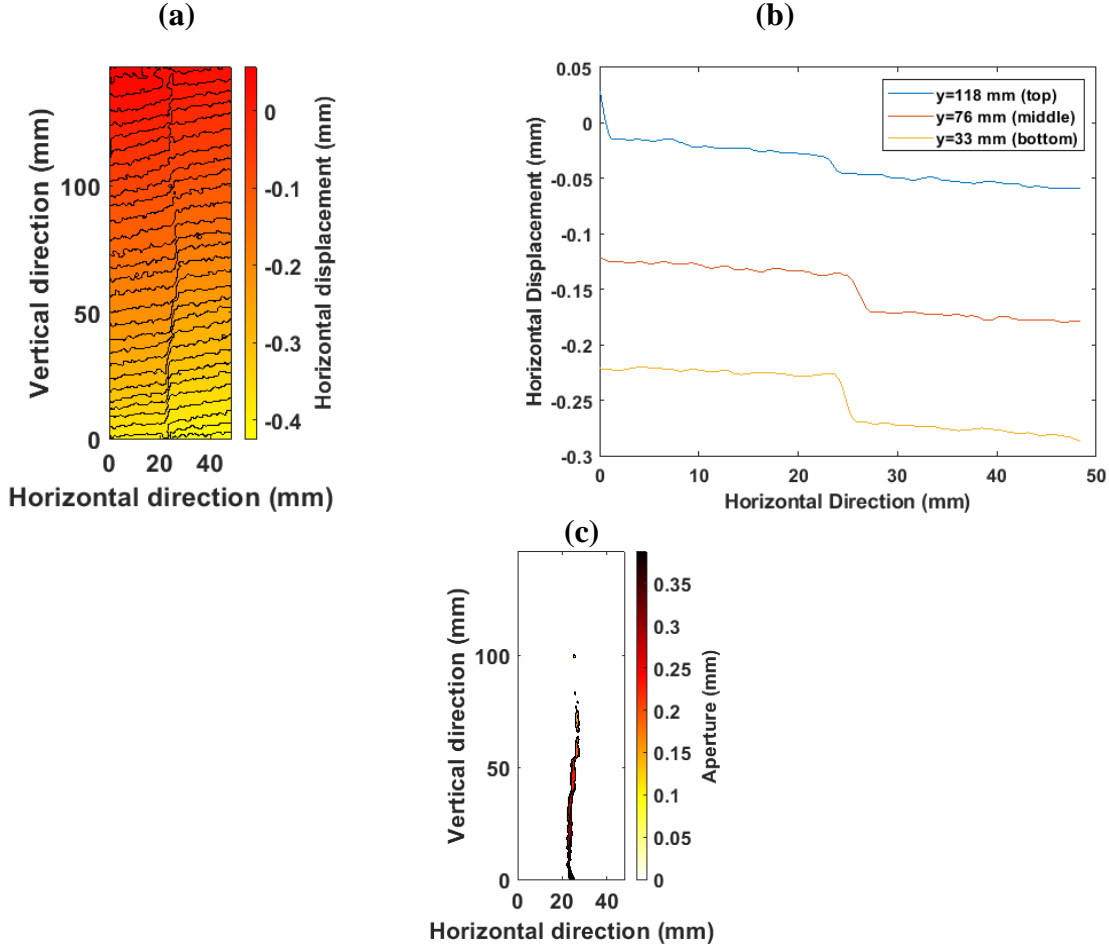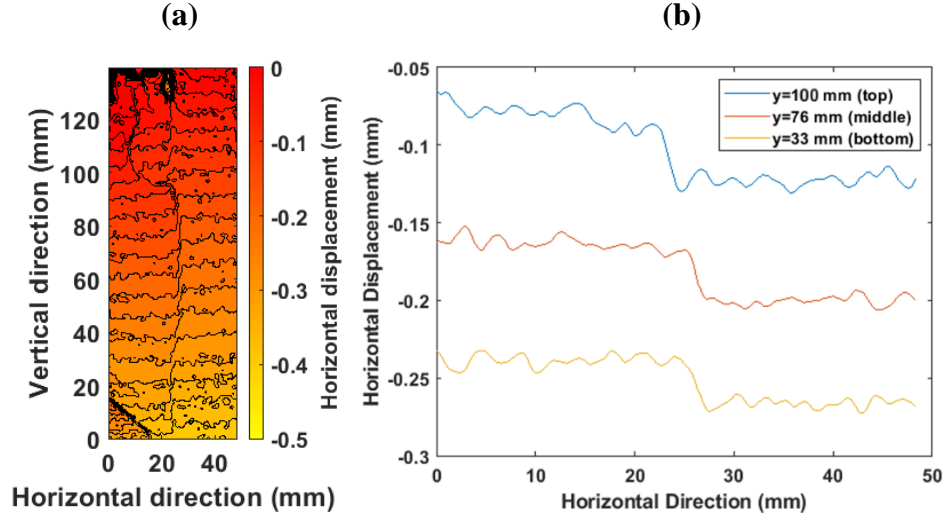
Figure 3.23. Horizontal displacement for sample with HCS= 3.2 mm (a) contour plot; (b) cross-sectional displacements at top (y=100 mm, blue), middle (y=76 mm, orange) and bottom (y=33 mm, yellow)

3.4   Summary

The experiments presented in this chapter show that active seismic monitoring has the potential to detect impending shear failure—peaks in the normalized transmitted amplitude happened before the peak shear stress for planar gypsum discontinuities. For the case of a sample with a half-cycle sine wave that spans the central 1/3rd of the discontinuity (at a normal stress of 1 MPa), sample dilation was detected in the form of continuous transmission recorded by the top transducers even after peak shear stress; the continuous transmission was due to a closure at the top portion of the specimen and an opening at the bottom portion, which was later confirmed by DIC. These observations suggest that changes in compressional and shear amplitudes of transmitted waves during shearing are sensitive to the conditions of the joint interface. In addition, the sensitivity to shearing depends on the amount of dilatation that occurs along the interface, which is affected by the normal stress applied to the joint. The experimental results showed that changes in transmitted seismic waves could provide a method to detect dilation (and closure) along rock discontinuities, which may prove helpful in assessing key mechanical processes such as the evolution of joint permeability during shearing. Seismic transducers could also capture crack initiation –orthogonal to the plane of the pre-existing discontinuity—marked by a sharp drop in transmission by some transducers (8S and 5S) and conversely a sharp increase in transmission by another transducer (3P).

This observation—even though only qualitative—highlights the potential of using geophysical techniques to monitor impending shear failure on pre-existing discontinuities and detect possible crack initiation due to discontinuity shearing.

4 TRANSMITTED, REFLECTED, AND CONVERTED MODES OF SEISMIC PRECURSORS TO SHEAR FAILURE OF ROCK DISCONTINUITIES

Contents of this chapter were presented at the American Rock Mechanics Association (ARMA) in June 2021; permission was granted for reprint.

Hala El Fil, Laura J. Pyrak-Nolte, and Antonio Bobet

4.1 Introduction

Seismic monitoring has been successfully employed to quantify a rock discontinuity's shear and compressional fracture-specific stiffness for different loading conditions (Pyrak-Nolte et al., 1990; Choi et al., 2014; Pyrak-Nolte, 2018). According to Nakagawa et al. (2000), the transmitted and reflected compressional and shear waves do not provide enough insight into the state of stress of a discontinuity undergoing shear because it is difficult to separate the effect of normal stress from that of shear stress during an experiment. They conducted laboratory direct shear experiments on granite samples and were able to detect, at normal incidence to the fracture, converted waves, namely, compressional (P) to shear (S) and shear (S) to compressional (P) waves. The experimentally observed converted modes occurred because of oriented voids along the fracture plane caused by shearing of the fracture plane. They showed numerically and theoretically that the converted mode is attributed to a cross-coupling stiffness during shearing.

Here, results from a series of direct shear experiments conducted on a discontinuity with ideal sawtooth asperities are presented to provide further insight into how precursors occur and the differences among precursors observed from transmitted, reflected, and converted waves. The goals of the research were to: (1) monitor the shearing process of an ideal discontinuity, to compare signatures of failure in transmitted, reflected, and converted elastic waves, and (2) examine the propagation of slip as the discontinuity was driven to failure.

4.2   Methodology

4.2.1   Sample Preparation and Experimental Setup

The specimen was composed of two independent gypsum blocks prepared following the same procedure described in section 3.2 in Chapter 3. A resin mold base (Figure 4.1 (a)) with a sawtooth surface was designed and 3D-printed using a Formlabs Form 2 printer. The sawtooth had a height of 1.5 mm and an angle of 45°, as shown in Figure 4.1 (b). The 3D printed mold base was used to cast the first block of gypsum.
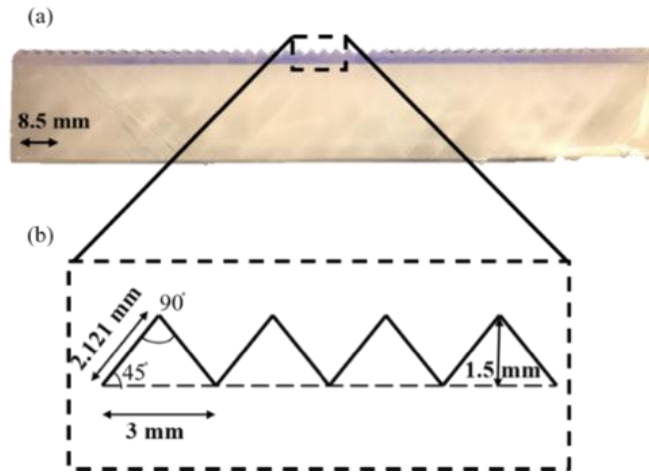
Figure 4.1. (a) 3D-printed resin mold base; (b) schematic of the sawtooth geometry

The experimental setup is the same as the one discussed in section 3.2 in Chapter 3. Two independent experiments were conducted at a constant normal stress of 2 MPa. The data corresponding to the repeatability experiment is presented in Appendix B.

4.3   Results

In this section, first, the results from the ultrasonic measurements during shearing are presented, followed by a discussion of precursors as a function of slip initiation.

4.3.1 Transmitted and Reflected Signals

The normalized transmitted amplitudes from three representative transducers, namely top (2S), middle (9P), and bottom (1S), as a function of shear displacement, are shown in Figure 4.2(a); these amplitudes are obtained by performing a wavelet analysis (Combes et al., 1989; Nolte et al., 2000) and plotting the peak amplitudes each transducer's dominant frequency. The data from these transducers were chosen for clarity. The complete data set that includes measurements made with the other transducers is presented in Appendix B. In Figure 4.2 (a), the applied shear stress is shown on the secondary y-axis. As the shear stress increased, the normalized transmitted amplitudes recorded by all three representative transducers were observed to increase. The increase in transmitted wave amplitude is consistent with an increase in the contact area between the two fracture surfaces caused by the application of shear stress that, in turn, causes an increase in fracture-specific stiffness. However, before failure, the transmitted amplitude decreased. Therefore, the peak in normalized amplitude was reached prior to the peak shear stress, representing a precursor to failure similar to that observed by Hedayat et al. (2014).

As expected, the data from the reflected-wave measurements exhibited the opposite behavior. The normalized reflected amplitudes of signals from the same three representative transducers are displayed in Figure 4.2 (b). As the shear stress increased, the normalized amplitude from the reflected signals decreased and then reached a minimum before reaching the peak shear stress. This type of minimum represents a seismic precursor to failure as manifested in reflected waves monitored over time.

After the precursory maxima (transmitted) or minima (reflected) are reached, a decrease in transmitted wave amplitude or an increase in reflected wave amplitude occurs because of damage to the asperities that reduces the specific shear stiffness of the joint. Note also in Figures 4.2 (a) and 4.2 (b) that the maxima of normalized transmitted amplitudes and the minima of the normalized reflected amplitudes occur close to one another, but not at the same time, i.e., at the same shear displacement. The data show that the precursors observed in the reflected signal data arrive slightly earlier than the precursors of the transmitted signals. For example, for data from transducer 9P, the maximum of the normalized transmitted signal occurs at a shear displacement

of 1.12 mm. In contrast, the minimum in the normalized reflected signal occurs at a shear displacement of 1.06 mm. Additional discussion on this topic is presented in section 4.3.3.

4.3.2   Converted Signals

The normalized amplitude of converted modes (P-to-S and S-to-P) captured by the same three representative transducers, 2S (top), 9P (middle), and 1S (bottom), are shown in Figure 4.2 (c). The figure also shows the applied shear stress as a function of shear displacement. As the shear stress increased, the normalized converted wave amplitudes measured by the representative transducers increased. A maximum in the amplitude was observed prior to the peak of the shear stress. Then the amplitude was observed to decrease with the continued application of shear stress. This maximum in the converted wave amplitude also represents a seismic precursor to failure. As shown by Nakagawa et al. (2000), converted modes exist when a discontinuity contains oriented voids. The saw-toothed samples used in this study were designed to create oriented voids with angles of 45°. As the shear stress was applied to the saw-toothed joint, the shear displacements caused a stiffening of the contact regions on one side of a tooth and a relaxed or no contact on the other side, thereby generating oriented voids. The magnitude of the converted waves is a function of the cross-coupling stiffness of the interface and the orientation of the microcracks. As the shear stress increases, the contact area increases between the asperities from the two fracture surfaces on one side of the tooth and relaxes on the other side, which in turn increases the cross-coupling stiffness of the joint, and thus increases the amplitude of the converted waves. With the continued application of shear stress, the asperities are eventually damaged, which results in a reduction in the converted wave amplitude.
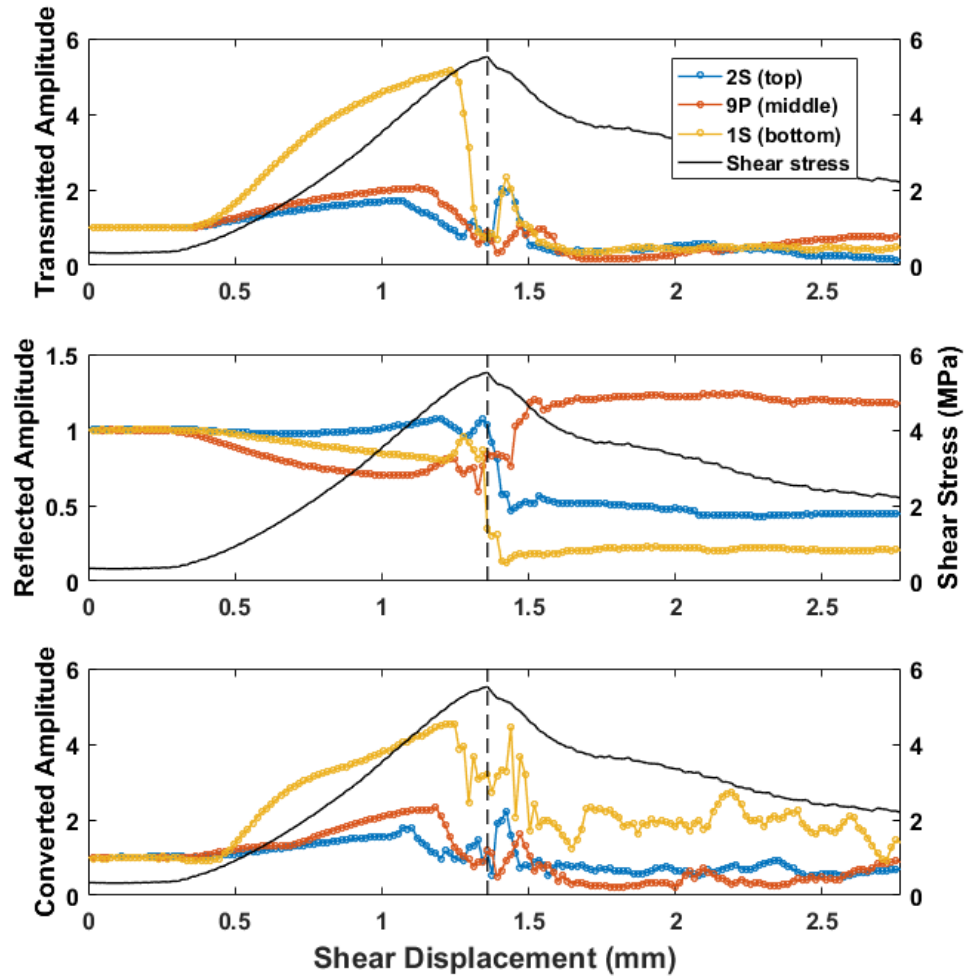
Figure 4.2. Normalized (a) transmitted, (b) reflected, and (c) converted wave amplitudes for three representative transducers: 2S (at the top of the specimen), 9P (middle), and 1S (at the bottom of the specimen) as a function of shear displacement. The secondary y-axis represents the shear stress

4.3.3 Precursory Modes and Slip Initiation

The precursors from the normalized transmitted (maxima), converted (maxima), and reflected (minima) wave amplitudes are shown as a function of shear displacement in Figure 4.3 for the three representative transducers indicated by different symbols. The top transducer (2S) was the first transducer to record all three precursors, i.e., from the transmitted, converted, and reflected waves, followed by the middle transducer (9P), and then by the bottom transducer (1S). The order here refers to the shear displacement at which a precursor was recorded, i.e., the transmitted

71

precursor for transducer 2S was recorded at a shear displacement of 1.06 mm, which took place earlier than the transmitted precursor recorded by transducer 9P; at a shear displacement of 1.12 mm.

As discussed in chapter 3, section 3.3.1, the precursors indicate the onset of damage to the asperities along the joint surfaces. The results suggested that damage occurred first at the top of the specimen, followed by the middle and bottom. It was expected that slip along the discontinuity would start first at the top because the shear load was applied at the top of the specimen. This hypothesis was confirmed by monitoring slip along the discontinuity using DIC data. Figure 4.3 includes snapshots of the relative vertical displacements recorded by the CCD camera at three elevations, at the top (y=118 m), middle (y=76 mm), and bottom (y=33 mm), for different shear stresses. At shear stress of 3.88 MPa (70% of peak shear stress), the snapshot shows that a relative vertical displacement discontinuity of ~15 µm was recorded at y= 118 mm (top portion). At the same time, no significant movement was observed at y= 76 mm and 33 mm (middle and bottom portions). This was when the first precursor was observed (transducer 2S) in the transmitted wave signal.

As the shear stress increased, the magnitude of slip at y=118 mm increased and, at the peak shear stress (shear stress = 5.52 MPa), discontinuities in the displacement of ~78, 43, and 41 µm, at the top, middle, and bottom of the specimen, respectively, were observed, indicating an increase in slip, and thus the propagation of slip, from the top to the bottom of the discontinuity. Finally, at a post-peak shear stress of 4.12 MPa, a large discontinuity in displacement (~ 0.53 mm) was recorded at all three locations. Thus, the DIC data indicated that slip initiated from the top portion of the specimen and progressed along the discontinuity with additional shear loading. This mechanism can be thought of as a slow-motion cascade of slip failure and explains why precursory events took place progressively from the top to the middle and finally to the bottom of the discontinuity.

An interesting aspect is that the precursors from the reflected signals emerged first followed by those from transmitted, and finally from converted signals, indicating that reflected signals are more sensitive to the damage incurred on the discontinuity (see triangular markers in Figure 4.3

72

shows the location and mode of precursor) and to impending failure—this was observed to be the case for top transducers. Based on the extended displacement discontinuity theory (Nakagawa et al., 2000), the change in transmitted, reflected, or converted wave amplitude is a function of early conditions normalized frequency (before shearing), i.e., fracture-specific stiffness. Thus, depending on the normalized frequency, the sensitivity of a particular mode (transmitted or reflected) will prevail; this is further discussed in section 4.4. In addition, the difference in displacements between the appearance of each of the three precursory modes for a given transducer is not constant since the reflected, transmitted, and converted precursors from transducer 2S occurred at shear displacements of 0.99, 1.06, and 1.11 mm, respectively, while they were at 1.07, 1.12, and 1.14 mm, respectively, from transducer 9P and almost at the same displacement for transducer 1S (more on this in section 4.4).
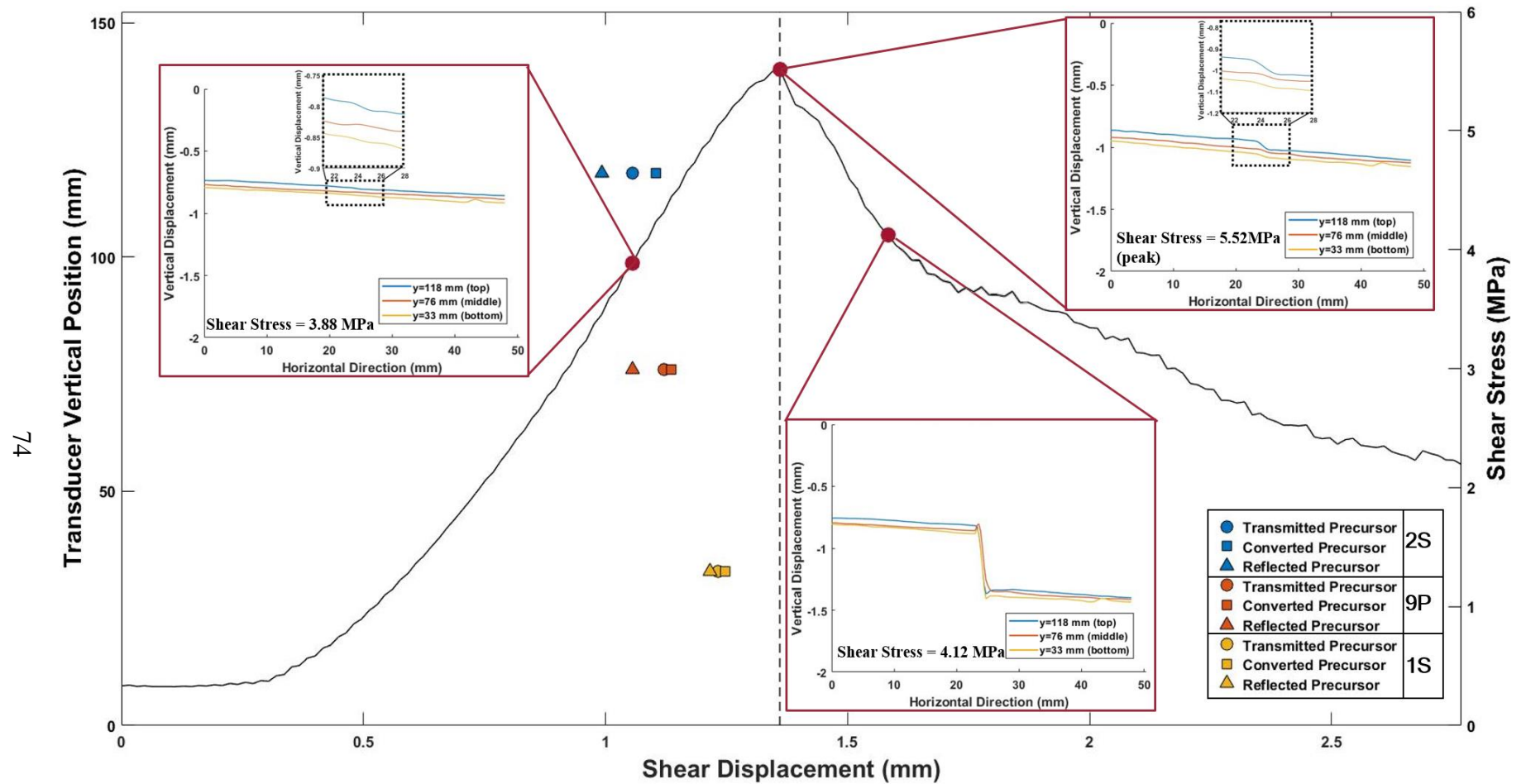
Figure 4.3. Transmitted (circles), reflected (triangles), and converted (squares) seismic precursors for the three representative transducers: 2S (at the top of the specimen), 9P (middle), and 1S (at the bottom of the specimen) as a function of shear displacement; also, snapshots of cross-sections of relative vertical displacements at various shearing stages [at 3.88, 5.52, and 4.12 MPa]

4.4 Extended displacement discontinuity theory

The extended displacement discontinuity theory (Nakagawa et al., 2000) –discussed in Chapter 2 section 2.6.1—was used to compare trends in transmitted, reflected, and converted signals. The corresponding **R** (Equation 4.1)**,** i.e., relative coupling stiffness, for a crack inclination of 45⁰ (sawtooth angle) is 0.9.

$$R = \sqrt{\frac{\kappa_{zx}.\kappa_{xz}}{\kappa_{xx}.\kappa_{zz}}} \tag{4.1}$$

The transmitted reflected and converted amplitudes (at normal incidence) as a function of normalized frequency (logarithmic scale) are derived from the extended displacement discontinuity theory for the case of no coupling stiffnesses of 0 (solid line) and 0.9 (dashed line) for 45° (Figure 4.4).
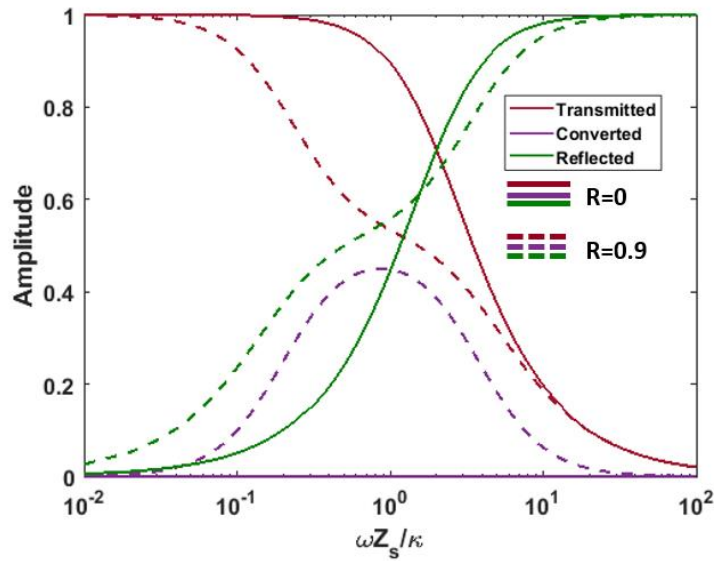
Figure 4.4. Change in transmitted reflected and converted amplitudes as a function of normalized frequency for relative coupling stiffnesses of 0 and 0.9, derived from the extended displacement discontinuity theory. Note: No converted wave exists when the cross-coupling stiffness R = 0.

As shown in Figure 4.4, for a relative coupling stiffness of 0.9 (dashed lines) and at low normalized frequencies, the reflected wave amplitude starts to increase prior to any significant decrease in transmitted wave amplitude as the normalized frequency increases. Thus, observing the precursor in the reflected wave signal before the transmitted in this data set is consistent with the interpretation provided by the extended displacement discontinuity theory—provided that such an observation occurs at lower normalized frequencies. It is important to note that observation of the precursor first in the reflected wave depends on the signal's frequency and the starting condition (i.e., fracture-specific stiffness) of the fracture. For $0.5 < \omega Z_s/\kappa < 5$, the precursors to failure would occur together (transmitted & reflected). However, for $\omega Z_s/\kappa < 0.5$, the precursors would appear first in the reflected signal, while for $\omega Z_s/\kappa > 5$, the precursors would appear first in the transmitted signal. Additional experimental data is required to confirm the theoretical predictions.

4.5   Summary

Direct shear experiments on a discontinuity with ideal sawtooth asperities were conducted to investigate the occurrence and the mode of elastic wave precursors to shear failure. The most important outcome of the study is that seismic precursors to failure can be detected from measurements of transmitted and reflected waves as well as from converted seismic waves. The data also show that the reflected seismic precursors emerged first, followed by the transmitted and converted precursors. The extended displacement discontinuity theory can predict which mode will first exhibit the precursor, which depends on the frequency of the signal and the initial fracture-specific stiffness.

Also, precursors were observed first at the top of the specimen and then were progressively observed farther down the length of the discontinuity, with increasing shear load. Such observation is consistent with the expectation of slip occurring first at the top of the specimen, where the load was applied and then propagating downwards with increasing load. The DIC results confirmed such a relation between the first precursor, the location of the onset of slip, and the progression of precursors and slip along the discontinuity. The tests also showed that the energy partitioned between reflected, transmitted, and converted signals changed with location along the discontinuity. Larger differences in time of occurrences between the three modes of precursors

were observed near the top portion of the specimen, where slip first occurred, than at the bottom. The results suggest that monitoring the moment when precursors are first observed may provide information about how slip propagates along a discontinuity and how close the discontinuity is to failure.

5 MISMATCHED DISCONTINUITIES: DIRECT SHEAR EXPERIMENTS AND CHARACTERIZATION

5.1 Introduction

Previous studies have investigated the shear behavior of well-matched discontinuities by conducting direct shear experiments that employ geophysical tools like active seismic monitoring to assess changes in the properties of a discontinuity (Chen et al., 1993, Hedayat et al., 2014b Hedayat et al., 2018). However, in nature, rock discontinuities are not always perfectly matched because chemical and/or physical processes can weather the fracture surfaces (Singh and Basu, 2016) or due to nearby earthquakes or excavations that may cause movements in the pre-existing discontinuities (Tang et al. 2016). Despite the extensive research conducted to understand the shearing process and strength of rock discontinuities (Kulatilake et al., 1995; Xia et al., 2014; Singh et al., 2018) and to provide methods to detect impending shear failure (Scuderi et al., 2016; Hedayat et al., 2014; Gheibi et al., 2021), the specific shearing mechanism of mismatched discontinuities is still poorly understood. In this chapter, direct shear experiments were conducted on gypsum samples with two types of frictional discontinuities prepared with two different release agents. As mentioned in chapter 3, section 3.2, a release agent was applied on the rough surface of the first block before casting the second. Here, both water-based and oil-based release agents were used and found to create different contact surfaces and fracture void geometries for gypsum discontinuities cast against a grit 36 sandpaper. The release agents created variability in the microstructure, strength, and degree of matching of gypsum discontinuities. The research presented in this chapter aims to investigate the geophysical response of shearing mismatched discontinuities at low and high normal stress with the objective of exploring if a mismatch in the surfaces of the discontinuity would mask the seismic precursors to shear failure that were observed in well-matched discontinuities.

5.2 Matched vs. Mismatched Discontinuity: Sample preparation

Gypsum specimens were prepared following the same procedure described in section 3.2 of chapter 3. Samples were prepared either with a water-based release agent or an oil-based release agent. The mold release agent was applied on the rough surface of the first block of a specimen

prior to casting the second block. Specimens prepared with a water-based release agent (2418 Dow Corning) are referred to as G_W, while those prepared with an oil-based release agent (Duoguard) are labeled G_O. As mentioned in section 3.2 in chapter 3, the amount of release agent applied played a crucial role in creating well-matched discontinuities. A very thin layer of the water-based release agent was sufficient to separate the two blocks after preparation. Conversely, the oil-based release agent required the application of a larger amount of release agent to separate the two blocks without damaging the asperities. Images of G_O specimens that failed to separate due to insufficient amount of release agent are presented in Appendix D. As will be discussed later in this chapter, specimens prepared with the water-based release agent (G_W) created well-matched discontinuities, while specimens prepared with an oil-based release agent (G_O) resulted in mismatched discontinuities. Table 5.1 provides a summary description provided by the manufacturers of both release agents.

Table 5.1. Summary of active ingredients of release agents

Item	Dow corning (water-based)	Duogard (oil-based)
Action	Forms a thin film of a water-based emulsion of a silicone alkylaryl fluid	Composed of an organic chemical that reacts with the alkali content of the mixture (typically used for concrete) to form a release film that effectively inhibits the bonding of the mixture to the mold and/or to dry gypsum
pH	7	N/A

5.3 Direct Shear Experiments: well-matched vs. mismatched discontinuities

Direct shear experiments were conducted in the laboratory on gypsum discontinuities prepared with both types of release agents (water and oil-based). The experiments were performed using the same setup discussed in chapter 3, section 3.2 presented in Figure 5.1 (a) schematic of the experimental setup and (b) layout of the transducers, at normal stresses of 2 and 5 MPa. The following section presents the mechanical and geophysical results from these experiments. The repeatability experimental program entailed conducting 3 experiments for each type of specimen at each normal stress, i.e., 3 experiments for G_O specimen at normal stress of 2 MPa and another set of 3 at a normal stress of 5 MPa, and similarly for G_W specimen. In this section, results from

representative experiments of each type of specimen at each normal stress (2 and 5 MPa) are presented. The remainder of the repeatability results are presented in Appendix C.
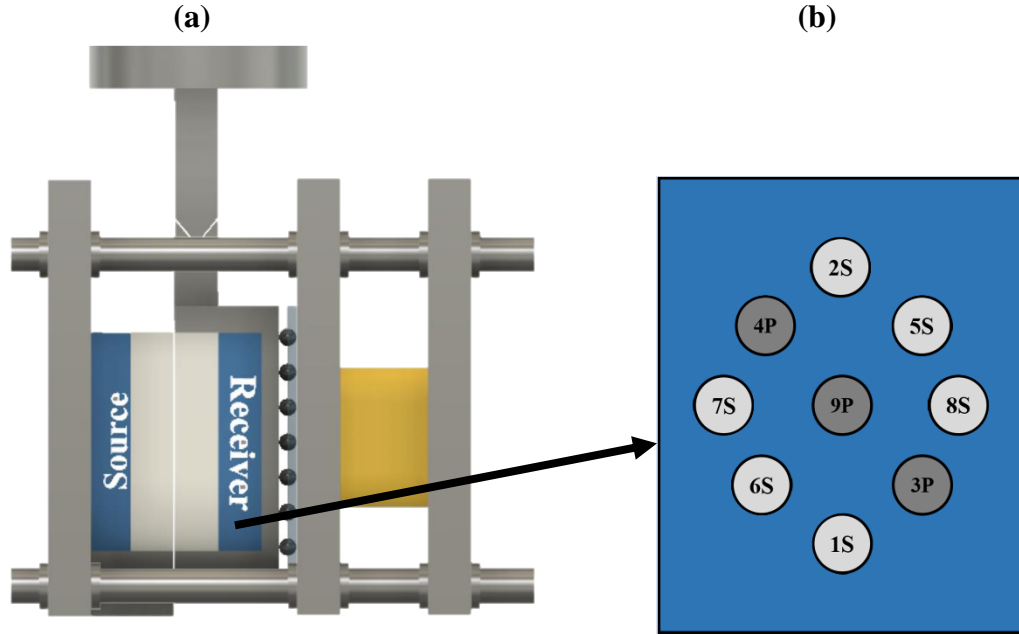
Figure 5.1. (a)Schematic of the direct shear experiment; (b) transducer's layout

5.3.1   Direct shear experiments on G_W and G_O specimens

In this section, the mechanical testing results are presented first and are followed by the results from geophysical measurements made during the direct shear experiments conducted on G_W (prepared with water-based release agent) and G_O (prepared with oil-based release agent) specimens, performed at normal stresses of 2 and 5 MPa.

5.3.1.1   Mechanical response

The peak shear stress obtained from running direct shear experiments on G_W (shades of blue) and G_O (shades of green) specimens at normal stresses of 2 and 5 MPa are compared in Figure 5.2. From Figure 5.2 (a), the mean peak shear stress of G_W specimens at a normal stress of 2 MPa was ~ 2.49 MPa, and that of G_O specimens was ~2.63 MPa, with only a 5.5% difference, indicating that both specimens have a similar peak shear stress at a normal stress of 2 MPa. For

normal stress of 5 MPa, the mean peak shear stress of G_W specimens was ~ 6.27 MPa, and that of G_O specimens was ~ 7.24 MPa. A more significant difference in the peak shear strength of both specimens is observed at the normal stress of 5 MPa, with a difference in the mean peak shear stress of ~ 14.4 %. The cause for the observed differences in mean peak shear stress at 5 MPa was explored by examining the surface properties of the two different types of discontinuities (i.e., G_W and G_O) and the fracture geometry formed by the surface. The findings from these measurements are described in section 5.4. Figure 5.2 (b) shows the peak shear stress versus normal stress for experiments conducted on G_W and G_O specimens. From Figure 5.2 (b), the peak friction angle for a G_O specimen is found to be ~ 56.9º, while that of the G_W specimen had a friction angle of ~ 49.6º. The peak friction angle obtained for a G_W specimen is in good agreement with the peak friction angle obtained by previous researchers who conducted similar direct shear experiments on gypsum specimens (Mutlu and Bobet 2006 & Hedayat 2013).
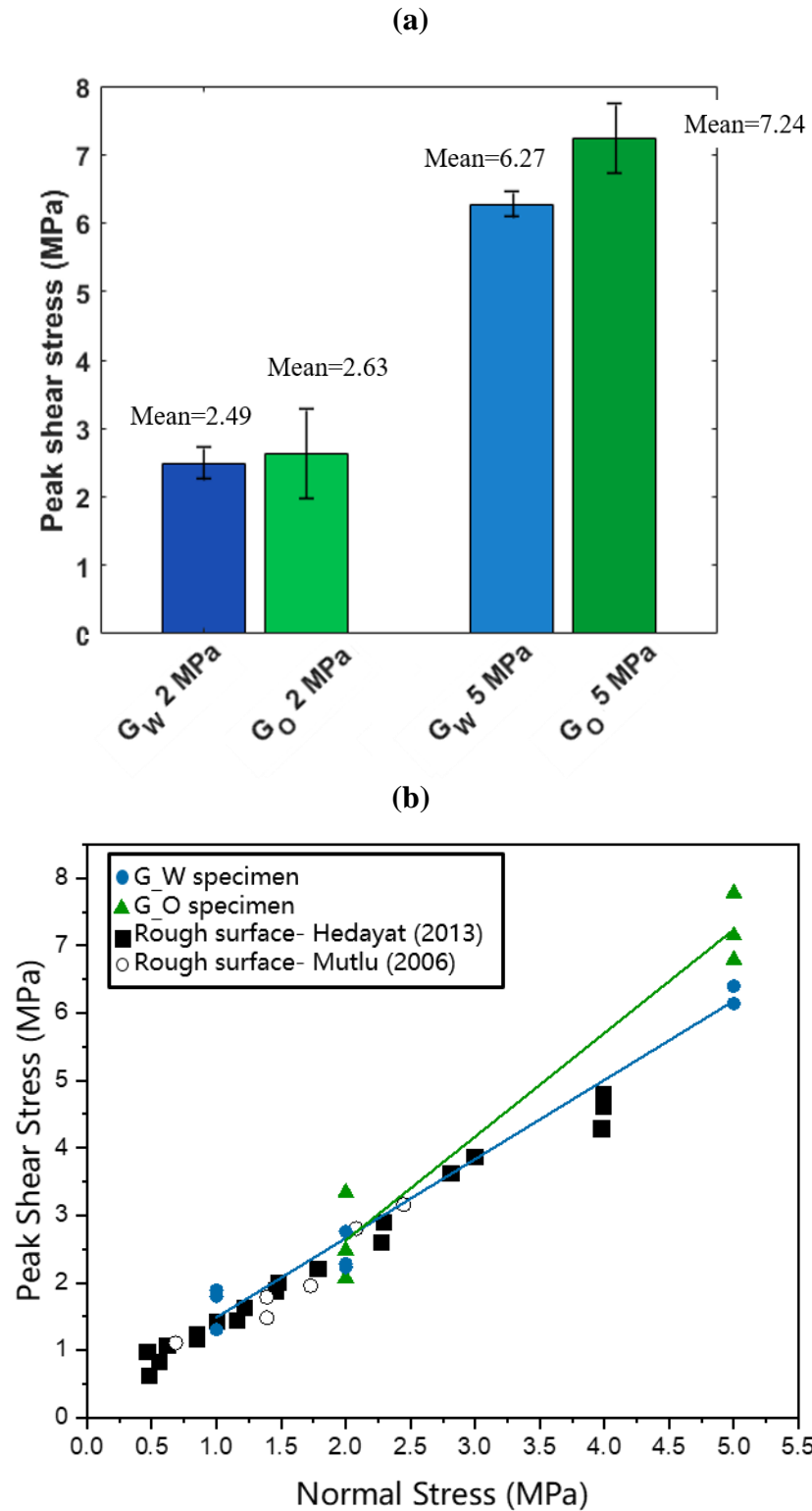
(a)

(b)

Figure 5.2. (a) Peak shear stress of G_W (blue) and G_O (green) specimens at normal stresses of 2 and 5 MPa; the error bars represent the maximum and minimum values for each bar; (b) peak shear stress as a function of normal stress with data from previous researchers (Hedayat, 2013; Mutlu and Bobet, 2006)

5.3.1.2   *Geophysical response*

Figure 5.3 shows the normalized transmitted amplitude as a function of shear displacement for transducers located at (a) top (2S, 5S, and 4P), (b) middle (7S, 8S, and 9P), and (c) bottom (1S, 6S, and 3P) portions of a specimen prepared with a water-based release agent (G_W) and sheared while under applied normal stress of 2 MPa. The shear stress as a function of shear displacement is plotted on the secondary y-axis. Similar to the tests described in section 3.3.1 in chapter 3, as the shear stress increases, the normalized transmitted amplitudes of signals from almost all of the transducers (Figure 5.3 (a-c)) slightly decrease first and then increase due to an increase in normal and shear fracture specific stiffnesses (Pyrak-Nolte et al., 1990; Choi et al., 2014). The normalized transmitted amplitudes then reach peaks that occur before the peak shear stress and then drop. The drop in transmission is caused by damage sustained by the asperities. All transducers recorded seismic precursors to shear failure in the form of peaks in the transmitted amplitude prior to peak shear stress.

Figure 5.3 (d-f) present the normalized transmitted amplitudes as a function of shear displacement for (a) top (2S, 5S, and 4P), (b) middle (7S, 8S, and 9P), and (c) bottom (1S, 6S, and 3P) portion of specimen G_O (prepared with oil-based release agent) and sheared at a normal stress of 2 MPa. Figures 5.3 (d-f) show that the normalized transmitted amplitude of all transducers increases as the shear stress increases and reaches a peak that occurs *after* the peak shear stress. The fact that the peaks in transmitted amplitude take place after the peak shear stress shows that no seismic precursors to failure were recorded in the transmitted signal. Observations of precursors from the G_W specimen are expected (see Section 3.3.1 in Chapter 3), and it has been well-documented in previous research (Hedayat et al., 2014). However, the behavior of the specimen G_O shows no precursors to failure (in the form of peaks of transmitted amplitude before failure). To understand the differences in the behavior of both specimens (G_W and G_O), and to examine if these precursors could be observed with higher confinement, direct shear experiments on both types of contact surfaces were conducted at a higher normal stress of 5 MPa.
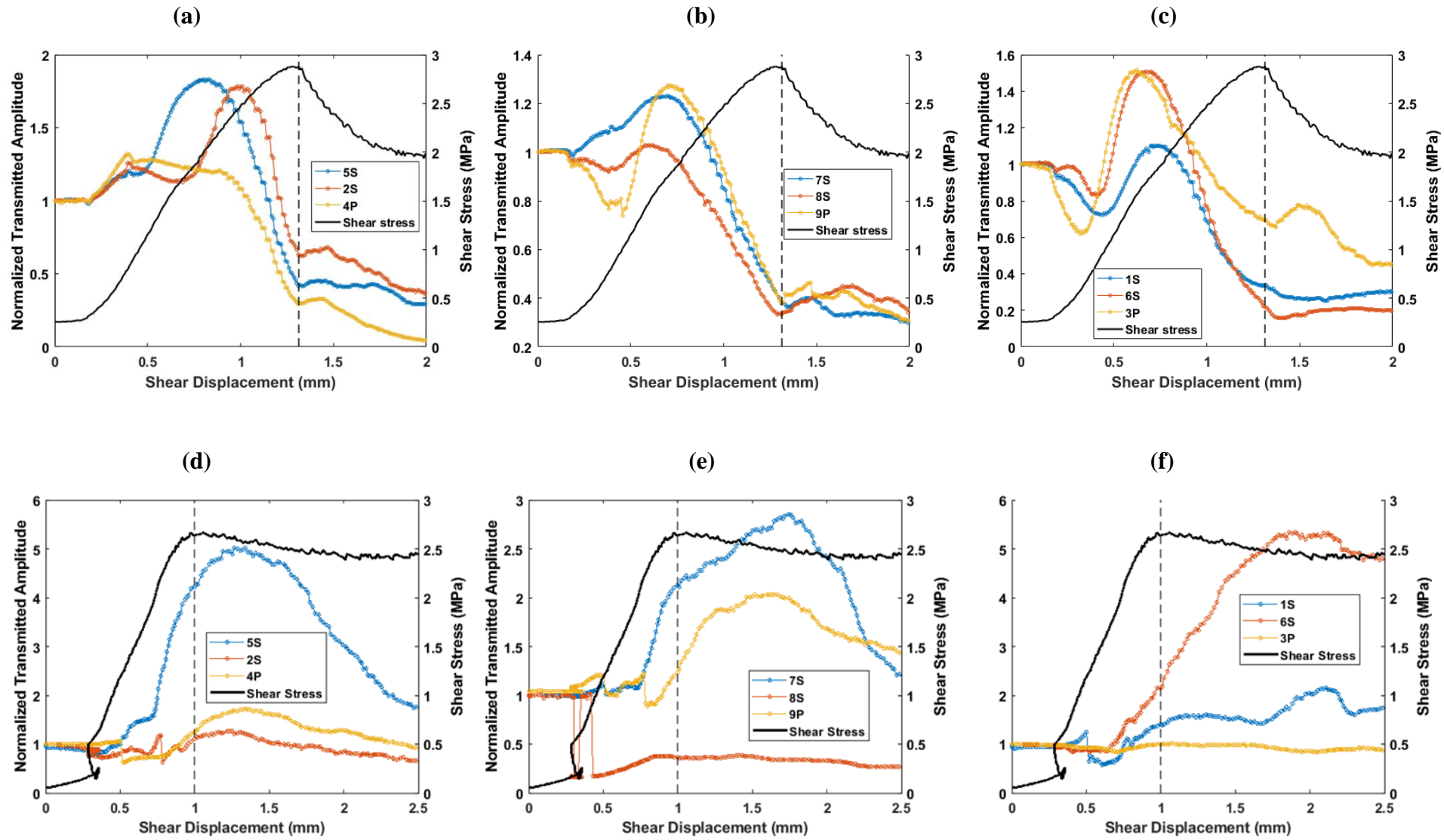
Figure 5.3. Normalized transmitted amplitude for specimens prepared with water (top row) and oil (bottom row)- based release agent for (a & d) top, (b & e) middle, and (c & f) bottom transducers; the secondary y-axis plots the shear stress; at normal stress = 2MPa

Figure 5.4 shows the normalized transmitted amplitude as a function of shear displacement for the top (2S, 5S, and 4P), (b) middle (7S, 8S, and 9P), and (c) bottom (1S, 6S, and 3P) transducers probing specimen G_W, at a normal stress of 5 MPa. Similar to previous Figure 5.3, the secondary y-axis corresponds to the shear stress recorded during the direct shear experiment conducted at a normal stress of 5 MPa. The normalized transmitted amplitudes show a behavior similar to what was discussed earlier (Figure 5.3 (a-c)) for the specimen G_W. As the shear stress increases, the normalized transmitted amplitude increases due to enhanced contact between the asperities caused by an increase in normal and shear fracture-specific stiffnesses. The normalized transmitted amplitude then reaches a peak before the peak shear stress, identified as a seismic precursor to shear failure.

Results from direct shear experiments conducted on G_O specimen at a normal stress of 5 MPa are presented in Figure 5.4 (d-f). As one can see in Figures 5.4 (d-f), as the shear stress increases, the normalized transmitted amplitudes of the signals from all of the transducers increase, then they reach a peak, which takes place before the peak shear stress. Seismic precursors in the form of peaks in the transmitted amplitudes are now observed for the specimen G_O when subjected to higher confinement (note: the normalized transmitted amplitude of transducer 9P was divided by a factor of 10 to enable examination of the change in transmitted amplitudes of transducers 7S and 8S). Sharp drops in the transmitted amplitudes are also observed (around a displacement of ~1mm). As mentioned in section 3.3.2 in Chapter 3, sharp drops in transmission correspond to a crack generated in a plane orthogonal to that of the discontinuity. The results from the G_O specimen sheared under a normal load of 5 MPa differ from those of the specimen G_O sheared under a 2 MPa normal stress for all the repeatability experiments conducted. No precursors to the peak shear stress were observed in the transmitted wave amplitudes for the G_O specimen at a normal stress of 2 MPa, but precursors were observed at a normal stress of 5 MPa.

Based on the results presented in Figures 5.3 and 5.4, it seems that the ability to detect seismic precursors to shear failure in transmitted seismic waves is a function of the joint's condition (i.e., surface properties, void geometry, contact area, etc.) and the normal stress applied. For a G_O specimen, seismic precursors to shear failure were only detected at higher normal stresses, which suggests that a G_O joint requires larger normal stress to induce asperity damage that would result

in seismic precursors (in transmitted signals). Characterization of both surfaces (G_W and G_O) was performed to determine the joint properties and fracture geometry to provide an understanding of how the joint condition affects the observation of seismic precursors to failure.
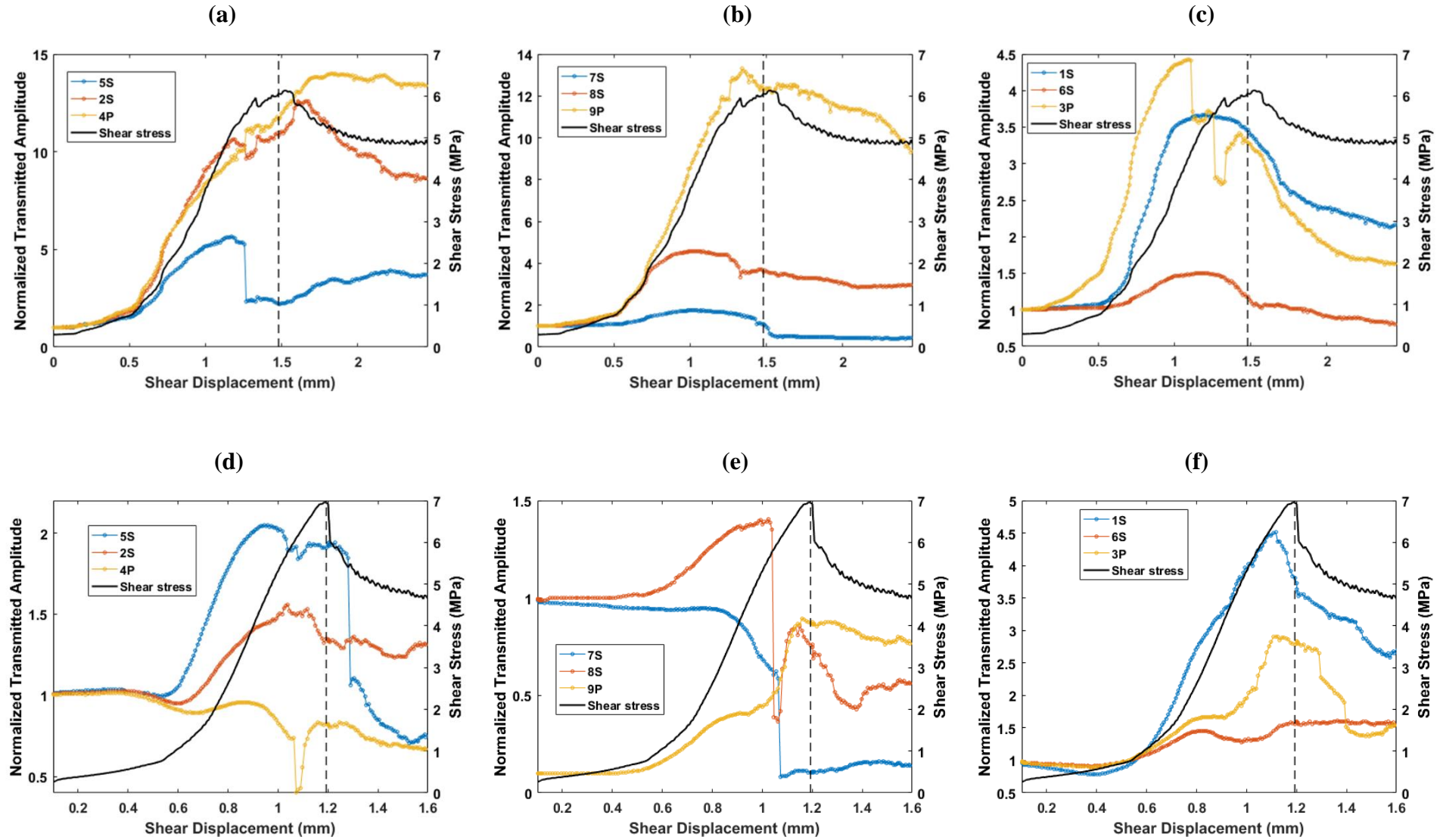
Figure 5.4. Normalized transmitted amplitude for specimens prepared with water-based (top row) and oil-based (bottom row) release agents for (a & d) top, (b & e) middle, and (c & f) bottom transducers; the secondary y-axis plots the shear stress, at normal stress = 5 MPa

5.4 Discontinuity characterization: G_W and G_O specimens

Characterization of joints in G_W and G_O specimens was performed to provide insight into the interplay between wave transmission, the generation of seismic precursors, and the joint condition. That includes the roughness of the surfaces, the strength/mineral/chemical composition of the surfaces, and the fracture geometry, i.e., the contact area and void geometry of the two rough surfaces in contact. The methods used to assess and compare the joints are (1) Scanning Electron Microscopy (SEM) and Electron X-ray Diffraction (EDX), to study the microstructure and chemical composition of the discontinuity, respectively; (2) micro-indentation testing, to measure the micro-strength of the asperities; and (3) 3D CT in-situ uniaxial X-ray scans, to quantify the fracture geometry and to assess the degree of mismatch between the two fracture surfaces.

5.4.1 Microstructure characterization through SEM and chemical composition through EDX

An FEI Nova NanoSEM scanning electron microscope (Life Science Microscopy facility at Purdue University) was used to image a joint surface taken from each type of specimen (G_O and G_W), with a 5 kV voltage, a spot size of 3, a working distance of 5 mm, and a magnification range between 1000x to 7000x (Figure 5.5).
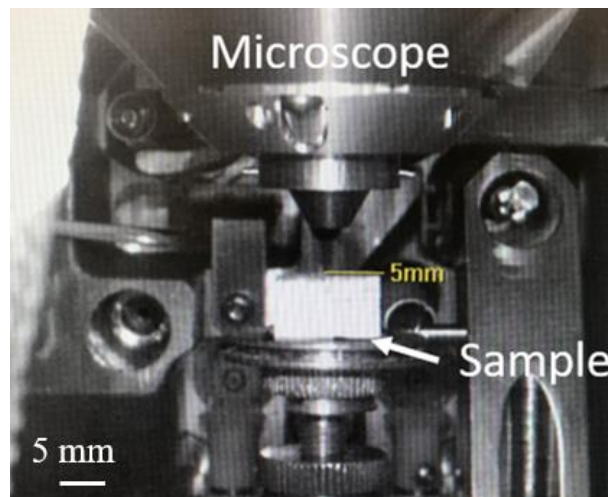

Figure 5.5. SEM set up with a sample

The surfaces of each specimen were prepared by applying a platinum coat using a Cressington turbo-pumped sputter coater that would enable even platinum coating across the specimen surface; the coating thickness usually ranges between 2 to 20 nm. It is essential to coat the specimen's surface before imaging to avoid surface charging and to obtain clear scans.

Figure 5.6 shows SEM images of the rough surface prepared with grit 36 sandpaper for specimens (a) G_W and (b) G_O. These are representative images; additional images can be found in Appendix E. Needle-like microstructures were observed for a surface prepared with the water-based release agent (G_W) with needle lengths that ranged from 0.4 to 15 µm and widths ranging between 0.5 to 3.5 µm, as shown in Figure 5.6 (a). The needles were less distinct and more amorphous for the specimen prepared with an oil-based release agent (G_O), resulting in a somewhat smoother microstructure (Figure 5.6 (b)).

(a)   **(b)**
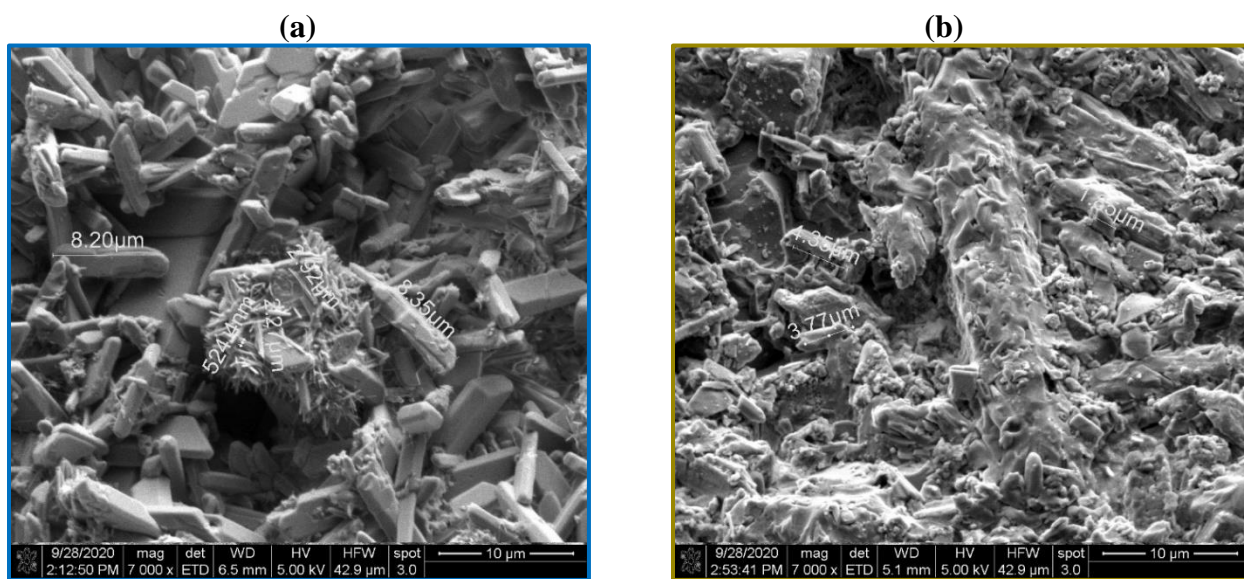
Figure 5.6. SEM images of a rough surface prepared with: (a) water-based release agent (well-matched); and (b) oil-based release agent (mismatched) at a 7000x magnification

From the SEM scans, there is a clear distinction between the microstructure of the surfaces created using the oil-based and the water-based release agents. A chemical composition analysis was performed with Energy-dispersive X-ray spectroscopy (EDX) to determine if the release agent affected the chemical composition of the surfaces. The EDX scans were also conducted using the FEI Nova NanoSEM microscope, and the surfaces were coated with platinum by employing a Cressington turbo-pumped sputter coater to avoid charging the sample surface under the

microscope. The EDX scans were captured at a 10 kV voltage, a spot size of 3, a working distance of 5 mm. A Monte Carlo simulation was conducted to determine the electron trajectory using Winxray (Demers et al., 2002), courtesy of Dr. Christopher J. Gilpin—director of the life science microscopy facility at Purdue University. The output of the Monte Carlo simulations –the trajectory of the transmitted electrons—is presented in Figure 5.7, and it shows that the trajectory has a bell shape, and for a 10 kV, the maximum depth was ~ 1.8 µm and a width of ~ 2.7 µm.
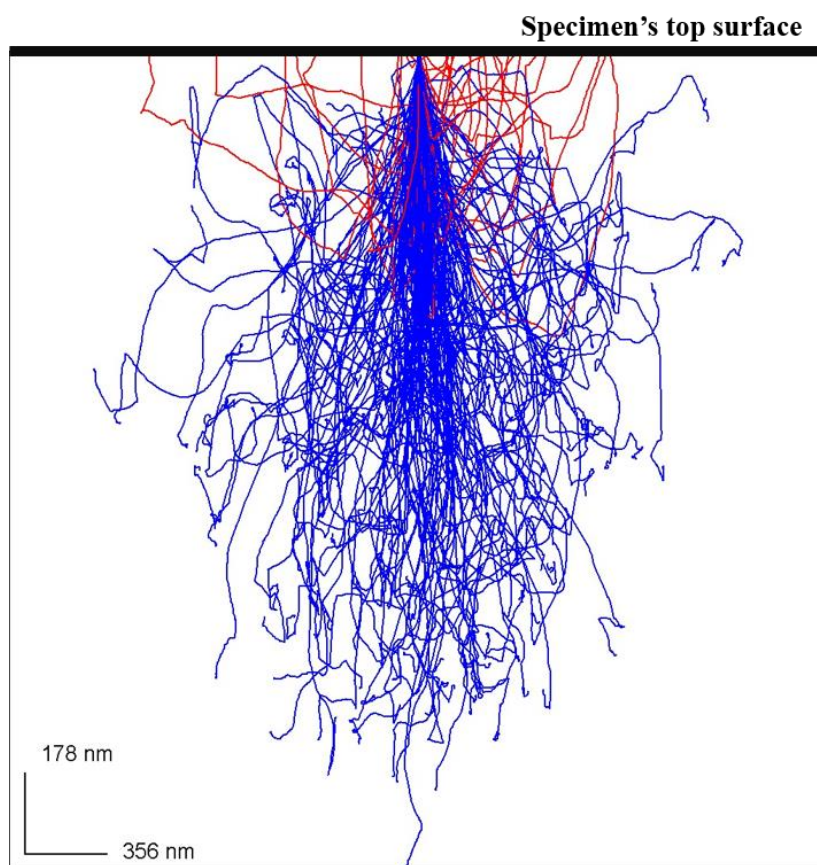

Figure 5.7. Electron trajectory obtained from the Monte Carlo simulations

First, the chemicals in the gypsum specimens (no release agent) were identified and are presented in Table 5.2. The data in the Table were obtained from the manufacturer of the Hydrocal B11 gypsum used in this research.

Table 5.2. Chemical Composition of gypsum obtained from the manufacturer

Material	Weight (%)
Plaster of Paris ($CaSO_4 \cdot H_2O$)	>85
Portland Cement (C_3S, C_2S, C_3A, and C_4AF)	<10
Crystalline Silica	<5

According to Table 5.2, calcium, sulfate, oxygen, hydrogen, carbon, silica, and sulfur are identified as part of the gypsum mixture. Figure 5.8 shows a typical chemical composition spectrum obtained from the EDX analysis, in blue for a G_W specimen and in dark yellow (gold) for a G_O specimen, along with images of the scanned surfaces. The peaks observed in the graph in Figure 5.8 represent distinct X-ray energy, which corresponds to specific chemical elements in the periodic table of elements. The spikes were identified as carbon (C), oxygen (O), silicon (Si), sulfur (S), and calcium (Ca)—the same chemical elements listed in Table 5.2. The same chemical elements were present on the scanned surfaces of both specimens. This is a representative spectrum, with the remainder of the data included in Appendix E.
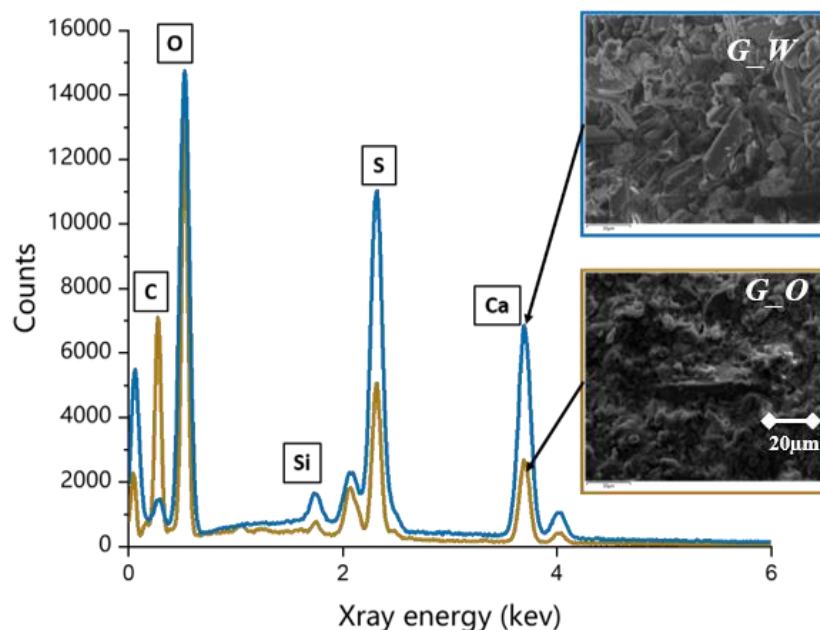
Figure 5.8. A chemical composition spectrum for a surface prepared with water-based release agent (blue) and oil-based release agent (yellow)

Figure 5.9 (a) provides a summary of the chemical composition of the G_O (gold) and G_W (blue) surfaces that is based on all the acquired EDX raw data. The graph shows that almost all chemical elements were present in both scanned surfaces, except for magnesium which was only identified in few G_O specimens but with minimal counts. Figure 5.9 (b) shows the EDX data normalized with respect to oxygen count, which is the element with the highest element count detected. Figure 5.9 (b) shows that, even after normalization, the relative element percentages seem to be the same. Thus, with regards to chemical composition, both specimens did not exhibit significant differences as almost all the chemical elements were present in both spectra.

(a)

(b)

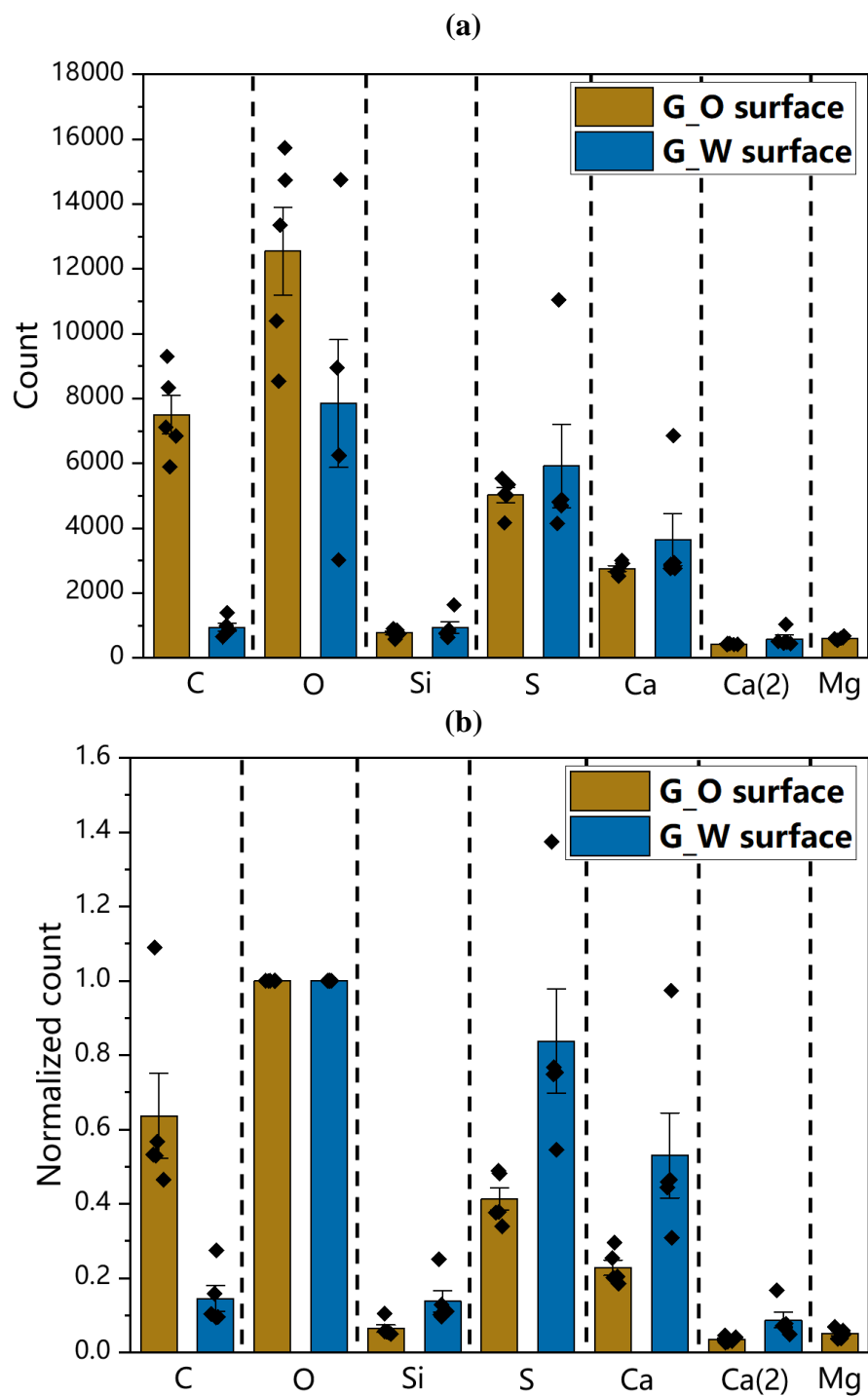
Figure 5.9. Chemical elements summary for surfaces prepared with water-based (blue) and oil-based (yellow/gold) release agents; the diamonds represent counts from the individual spectrum, and the error bars represent the standard error; (a) plots the raw data and (b) plots the normalized data with respect to oxygen

5.4.2 Micro-hardness: via Micro-indentation

From the SEM scans, the appearance of the microstructure of both surfaces differs (Figure 5.6). A question is whether this difference in mineralogy affected the strength of the surface. Thus, it is essential to quantify the micro-strength of each surface. A difference in micro-strength of the asperities would affect the amount and magnitude of the damage incurred to the asperities during shearing, and in turn, would ultimately influence the ability to detect seismic precursors to shear failure in transmitted seismic signals. A Hysitron Tribo-indenter Nano-indenter 950 (load capacity~14,000 N) was employed (Material's engineering laboratory at Purdue University) to characterize the micro-hardness of the asperities prepared with both types of mold release agents.

Figure 5.10 (a) shows the experimental setup of the specimen inside the micro-indenter. Figure 5.10 (b) shows a schematic of the indenter that had a conical tip with a tip diameter of 10 µm and a 62° tip angle. From the SEM scans, the gypsum needles ranged in length from roughly~ 0.4 to 10 µm; thus, the tip diameter was chosen to ensure micro-testing for a representative region and not a single needle or voids in between needles for the surface of the G_W specimen. A tip diameter of 10 µm would typically indent a sample with an indentation diameter larger than 10 µm, which will be discussed later in this section.

(a)   **(b)**

Figure 5.10. (a) Micro-indenter & sample setup; (b) schematic of the micro-indenter employed

The indentations were conducted under displacement-controlled conditions. The displacement pattern adopted is shown in Figure 5.11 (a) that consists of a displacement ramp up to 70 µm for 5 seconds, holding the stage for 10 seconds, and finally, complete unloading for 5 seconds. Figure

5.11 (b) shows a load versus displacement plot for a typical micro-indentation experiment on a smooth gypsum surface. The figure shows the loading and unloading portions of the test and shows contact depth (h_c) which is the intersection of the tangent to the linear portion of the unloading curve with the horizontal axis, and the maximum depth of penetration in the test (h_{max}), which is the maximum depth reached by the indenter.

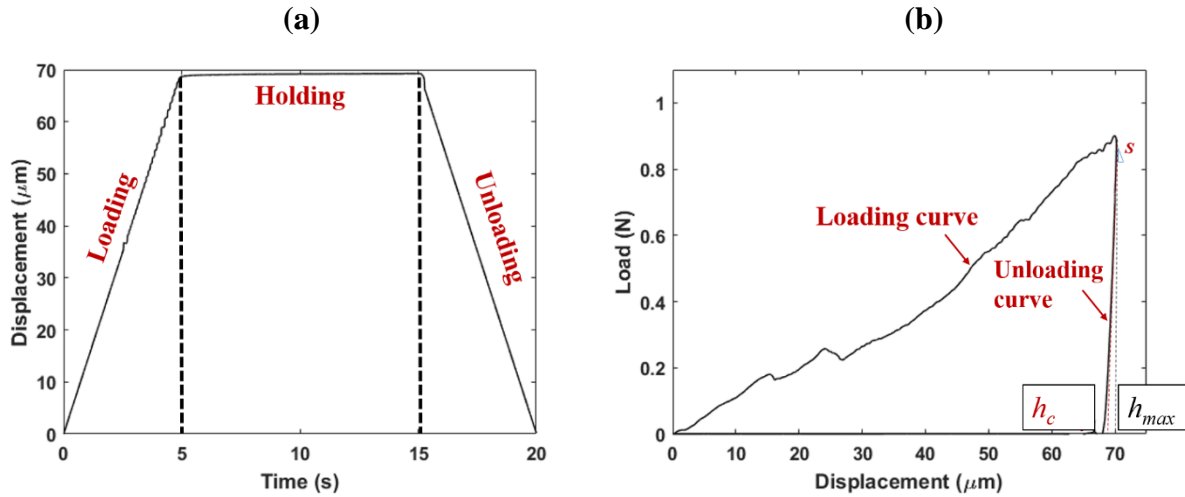**(a)**   **(b)**

Figure 5.11. (a) Loading pattern adopted for micro-indentation experiments; (b) typical load versus displacement plot

Micro-indentation tests were conducted on rough and smooth surfaces (grit 36 sandpaper roughness) prepared with oil and water-based release agents (G_O and G_W specimens). Although it is recommended to conduct indentations on smooth and well-polished samples based on ASTM E384 section 7.1 (ASTM, E384, 2005) and ASTM standard E2546 (2007), a couple of indentations were carried on the rough surfaces in an attempt to quantify the asperity hardness. Indentations on rough surfaces were not easy to perform, and most of the time, the test could not be completed because of the roughness of the surface; for this reason, only five indentations were conducted on each type of specimen. Figure 5.12 shows the rough surface of the G_W specimen under the microscope: (a) before and (b) after indentation. The blurred regions in the figure represent the roughness, i.e., the peaks and troughs of the asperities have different heights; thus, some regions may appear blurry and out of focus. Figure 5.12 (b) shows the indentation performed (blurry region behind the crosshair) that has an indentation diameter of ~ 84 μm, indicating that the indentation

performed was adequate as its diameter was much larger than the gypsum needles observed with SEM in Figure 5.6 (a), i.e., [0.4-15 µm].

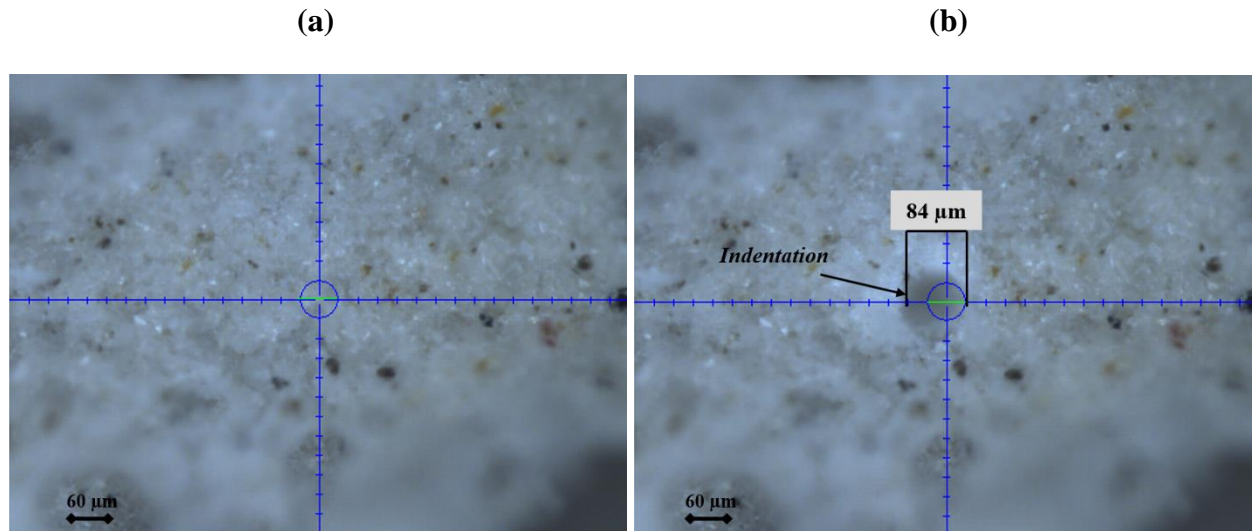**(a)**   **(b)**

Figure 5.12. G_W specimen's rough surface under the microscope: (a) before and (b) after indentation

Figure 5.13 shows the indentation curves obtained from micro-indenting G_W (shades of blue) and G_O (shades of green) rough surfaces (grit 36 sandpaper roughness). Almost all curves exhibit "jumps" similar to a stick-slip behavior during loading. These jumps are associated with the indenter coming in contact with powder produced while indenting the gypsum surface. For almost all indentations, the load required to reach an indentation depth of ~ 70 µm was larger for the G_O (0.7-1.1 N) specimen, indicating a surface harder than the G_W sample (<0.4 N and only one test recorded a load of ~1 N).
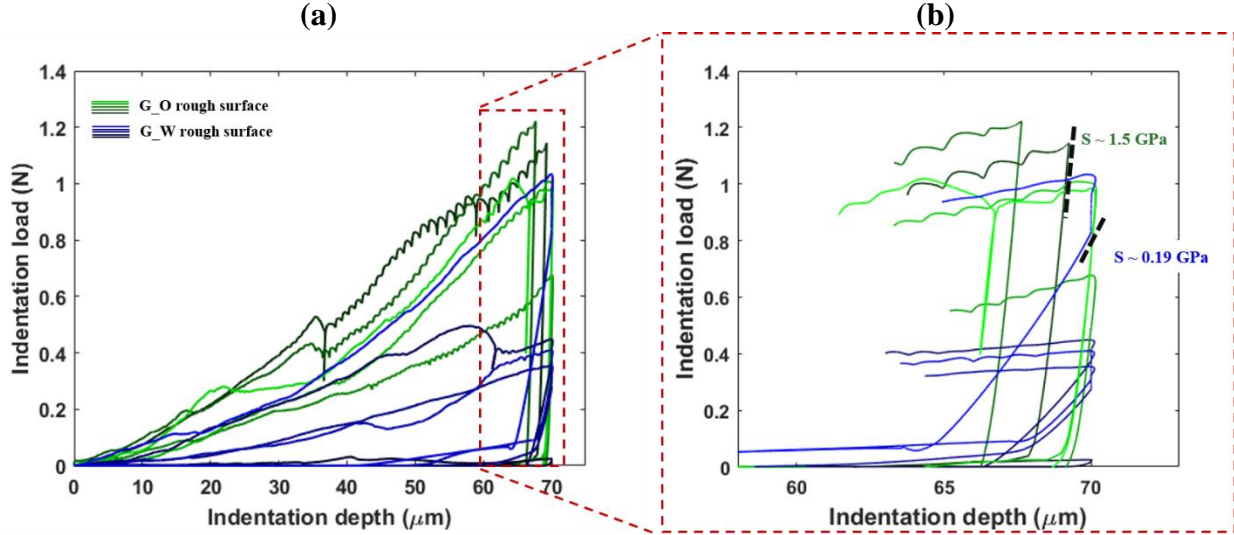
Figure 5.13. Micro-indentation (a) load-displacement curves for rough surfaces of G_W and G_O specimens, (b) enlarged view of the unloading curves

Another important aspect of the micro indentation load-displacement curve is the slope of the unloading curve. The slopes from the G_O specimen were much steeper (~ 1.5 GPa; green curve) than the G_W specimen (~ 0.19 GPa; blue curve), as shown in Figure 5.13 (b). The slope of the linear portion of the unloading curve represents the stiffness.

The micro-hardness for each indentation was computed using the following procedure (Fischer-Cripps, 2011):

- The stiffness "s" during unloading, which is the slope of the linear portion of the unloading curve, was computed using equation 5.1:

$$s = \frac{dLoad}{dDisplacement} \qquad (5.1)$$

The linear portion of the unloading curve is then extended, and the point of its intersection with the x-axis is identified, and it represents h_c (contact depth).

97

- The contact radius (a) and the contact area (A_c) were calculated using equations 5.2 and 5.3, respectively:

$$a = \sqrt{2R_i h_c} \tag{5.2}$$

$$A_c = \pi \times a^2 \tag{5.3}$$

Where R_i is the indenter radius (5 µm).

- The hardness was obtained by dividing the maximum load (P_{max}) by the contact area, as shown in Equation 5.4:

$$Hardness = \frac{P_{max}}{A_c} \tag{5.4}$$

The hardness values computed from the indentations performed on the rough surface of G_W and G_O specimens are presented in the bar plot in Figure 5.14. From the bar plot presented in Figure 5.14, the tests show that G_O specimens exhibit harder surfaces with a mean hardness of ~ 0.40 GPa, and G_W specimens had a mean hardness of ~ 0.17 GPa—indicating that the asperities corresponding to the G_O specimen recorded a mean hardness value more than twice the mean hardness of the G_W specimen. Nevertheless, a limitation to this analysis is the inability to perform many indentations due to the complexity of the rough surface.
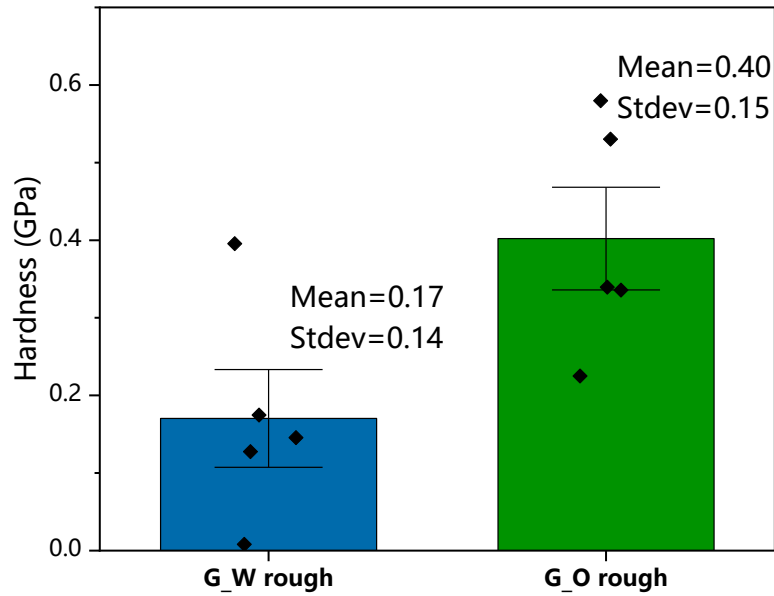
Figure 5.14. Micro-hardness results of G_O and G_W specimens with a rough surface; the diamonds represent the hardness values of individual indentations performed, and the error bars represent the standard error

As mentioned, micro-indentation testing should be performed on smooth surfaces to obtain accurate results (ASTM E384, 2005). For this reason, 25 micro-indentation tests were conducted on the smooth surface of each specimen, G_O, and G_W. The corresponding load-displacement curves from the indentation tests are given in Figure 5.15, where curves with shades of blue correspond to indentations performed on a G_W specimen with a smooth surface and shades of green to indentations performed on a G_O specimen with a smooth surface. Given the number of indentations performed and the noise from the loading portion of the load-displacement curves, it is hard to draw conclusions from the loading portion of the load-displacement plot, thus Figure 5.15 (b) is used to show an enlargement of the unloading portion for clarity. The unloading slopes (which represent the stiffness (s) in Equation 5.1) were ~ 0.75 GPa and ~ 0.52 GPa for G_O and G_W specimens, respectively. The corresponding hardness for each surface was also computed using equation 5.4 and is presented in the bar plot in Figure 5.16. From the micro-indentation tests conducted on smooth surfaces of each specimen, G_W specimen's smooth surface had a mean micro-hardness ~ 0.18 GPa, whereas G_O specimen's smooth surface had a mean micro-hardness was ~ 0.30 GPa, implying that for smooth surfaces, G_O had a ~ 50% harder surface. Thus, the

micro-indentation results show that the G_O specimen's surface has higher micro-hardness values than that of the G_W specimen for both smooth and rough surfaces. The micro-indentation results confirm that a difference in the strength of surface mineralogy exists between the oil-based and the water-based specimens.
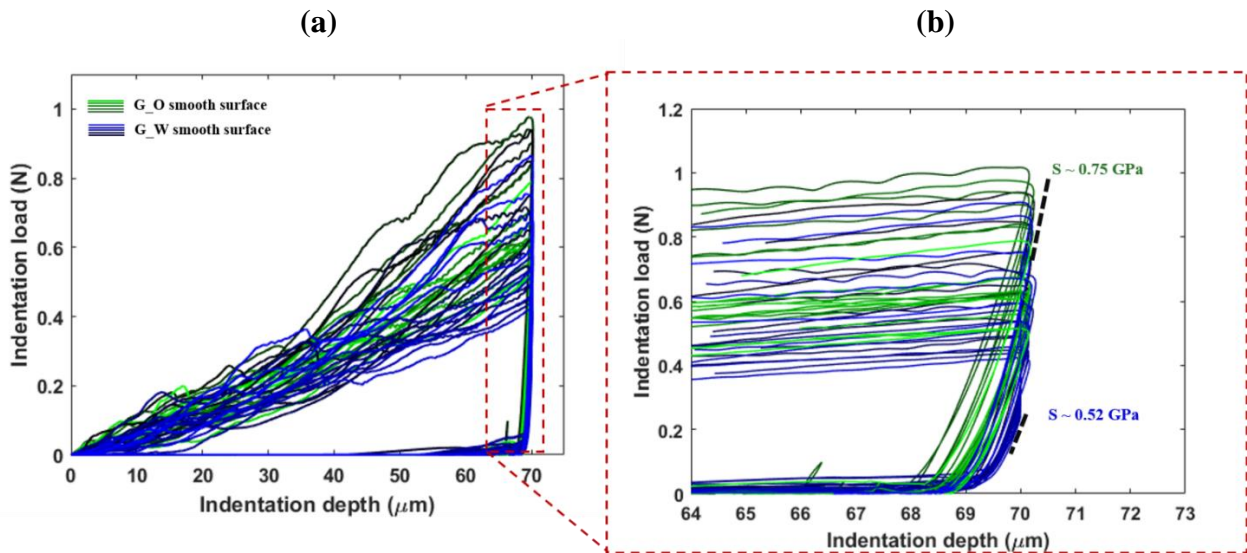

Figure 5.15. Micro-indentation load-displacement curves for smooth surfaces of G_W and G_O specimens
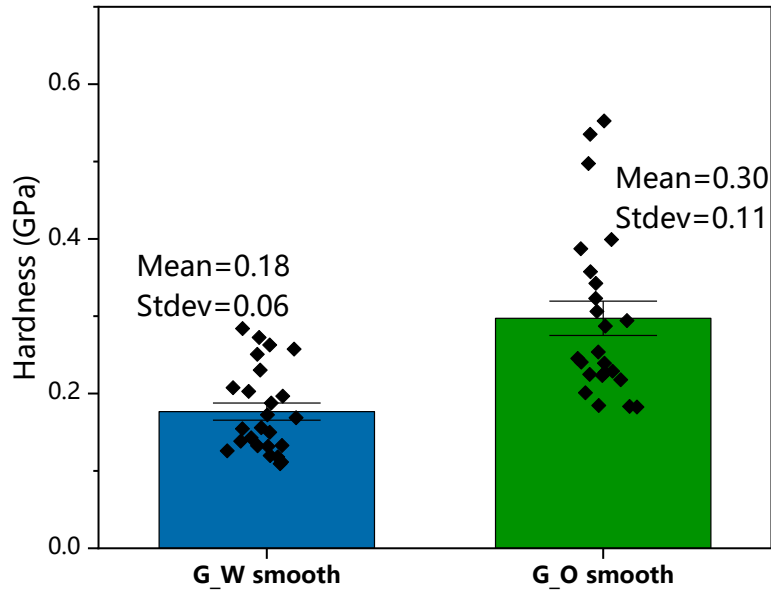
Figure 5.16. Micro-hardness results of G_O (green) and G_W (blue) specimens with a smooth surface; the diamonds represent the hardness values of individual indentations performed, and the error bars represent the standard error

5.4.3 Fracture Geometry Imaging Under Normal Stress

The surface characterization described in section 5.4.2 shows that there is a difference in the micro-mechanical and physical properties of surfaces created using a water-based versus an oil-based release agent. Therefore, it is important to understand how the surface properties affect the fracture response when placed in contact under normal loading. 3D X-ray microscopy on G_W and G_O specimens was performed in an in-situ loading rig to quantify the aperture and to study the change in aperture with the application of normal stress. Each specimen was composed of two independent prismatic blocks with a single discontinuity prepared following the same procedure described in Section 3.2 of Chapter 3. Each gypsum block had the following dimensions: ~ 19 mm in length, 18 mm in width, and 6 mm in height. Figure 5.17 (b) shows the G_W and G_O specimens. The dimensions were such that the specimen could fit inside the X-ray apparatus and still have a representative contact surface. At least three specimens of each type (G_W and G_O) were tested and imaged. The data corresponding to the repeatability of the experiments are presented in Appendix F. The specimen was scanned using a 3D X-ray microscope (XRM), Model Zeiss Xradia

510 Versa. As shown in Figure 5.17 (a), the specimen was placed on a Deben CT5000 loading stage (load capacity of 5000 N), positioned between the X-ray source and the X-ray detector.
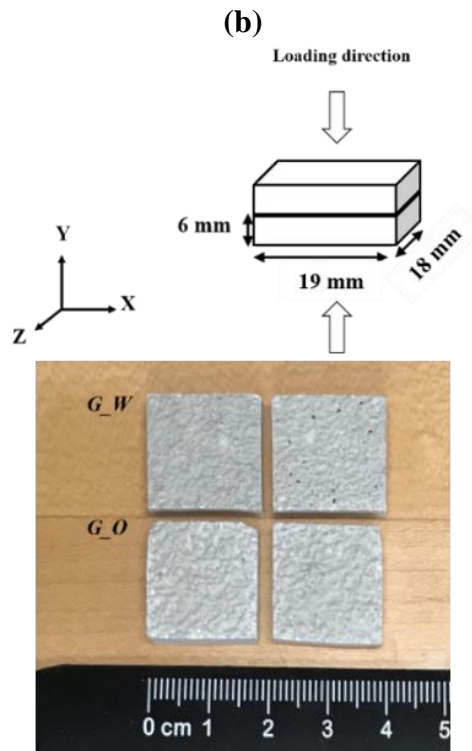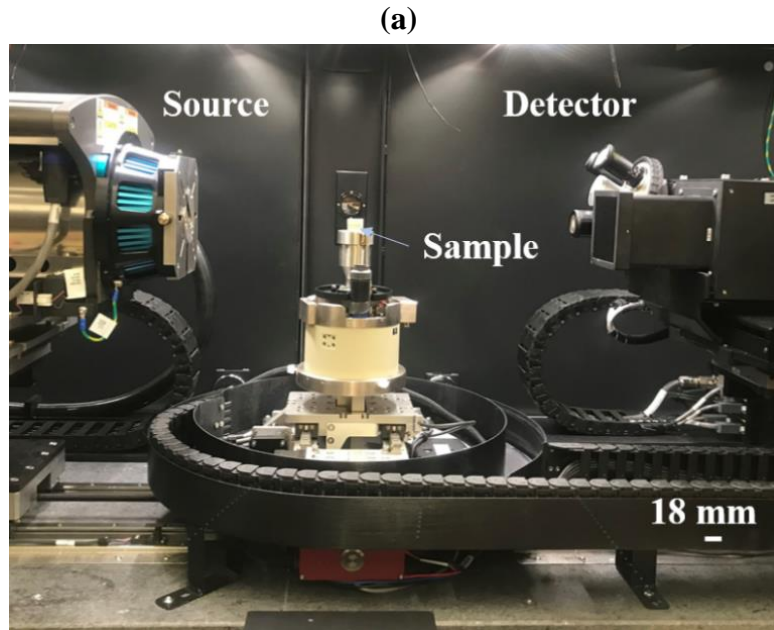
(a)

(b)

Figure 5.17. (a) 3D X-ray in-situ experimental setup; (b) G_W (top) and G_O (bottom) specimens and schematic showing the loading direction

The scans were conducted with a resolution of ~ 23 µm/pixel. The energy and power of the scans were 160 kV and 10W, respectively. Each specimen was placed between the source and the detector with source and detector distances of 100 mm and 200 mm, respectively. The scans had an exposure time of 1 second for 3201 projections, a 0.4x magnification factor, a bin size of 2, and no filter (air) was used. The specimens were loaded in the normal direction (y-direction, as shown in the schematic in Figure 5.17 (b)) at a loading rate of 0.1 mm/min and were scanned at stresses ranging between [1-5 MPa]. After each test, the collected images were post-processed using Objective Research Systems (ORS) Dragonfly 4.0 software to reconstruct the 3D geometry of the specimen. 3D reconstructions for both specimens: (a) G_W; and (b) G_O, for normal stress of 1 MPa are presented in Figure 5.18—the bottom blocks represent the first cast blocks, and the top blocks represent the second cast blocks.
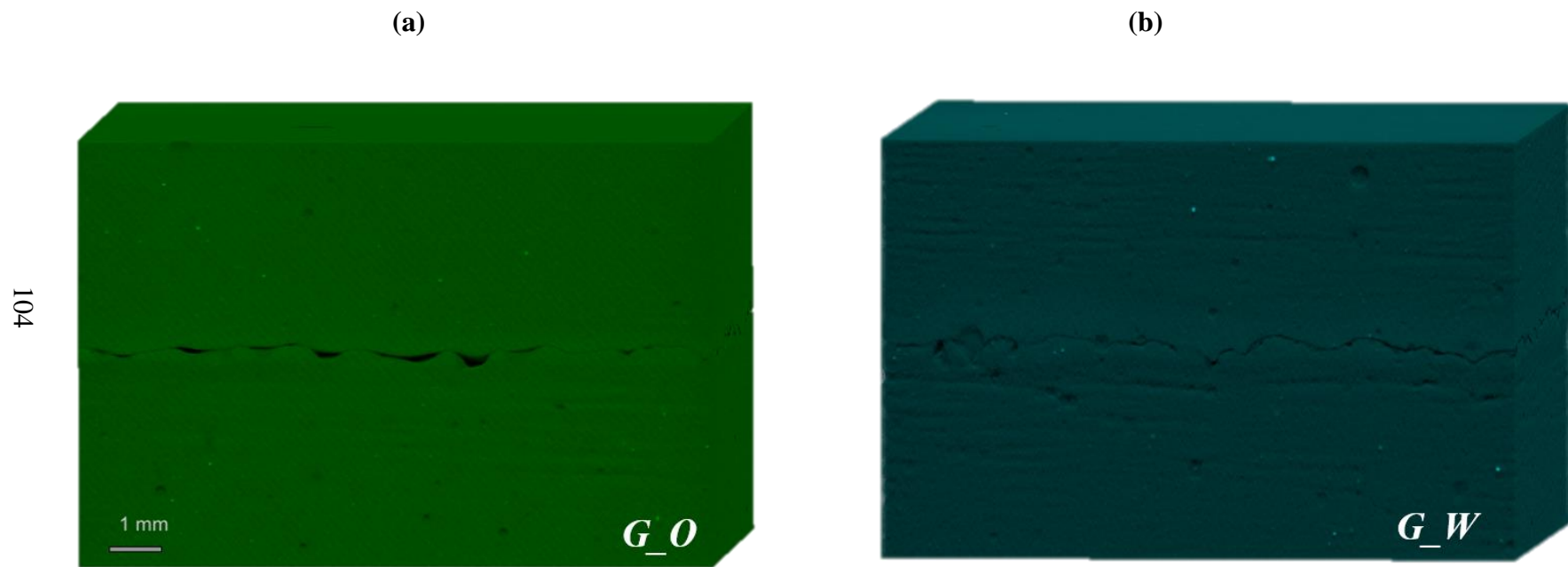
Figure 5.18. 3D reconstructed volumes of: (a) G_O; and (b) G_W specimens, at a normal stress of 1 MPa

5.4.3.1 Image processing

The scanned images were imported into Dragonfly ORS 4.0. The images were first cropped to isolate the specimen and to remove the loading platens of the Deben machine and the surrounding background air from the acquired images. Then, the histogram of the images corresponding to different loading stages was normalized to ensure that an even brightness/contrast was achieved to enable an unbiased image segmentation in later steps. After histogram normalization, the brightness/contrast (via window leveling) of all images was adjusted properly to obtain enough contrast between the areas of low density, i.e., voids, versus areas of higher density, i.e., rock matrix. It is essential to use a fixed window leveling range for all the images obtained at different normal stresses, as this influences the segmentation process discussed in section 5.4.3.2.

Figure 5.19 shows snapshots of slices of a typical (a-e) G_W specimen and (f-j) G_O specimen, at normal stresses of 1-5 MPa, respectively. The snapshots in Figures 5.19 show that the contact surfaces prepared with the water-based release agent were relatively well-matched for all normal stresses. In contrast, the contact surfaces prepared with the oil-based release agent appeared to be mismatched. From the slices, it is observed that a mismatch in the discontinuity of specimen G_O exists that does not disappear/close with the application of additional normal stress. This mismatch is caused by a geometry mismatch between the asperities which will be discussed in more detail in section 5.4.3.2. Another difference between G_O and G_W specimens is the existence of cracks that are orthogonal to the discontinuity in the G_O specimens that were generated during loading. This is observed at normal stresses of 4 and 5 MPa (Figure 5.19). In 3 distinctly scanned G_O specimens, orthogonal cracks were generated. Additional discussion of this can be found in section 5.4.3.3.

Achieving perfectly matching contact surfaces was not possible, even for the G_W specimen. Despite considerable care taken to prepare "perfectly-matched" surfaces, it was never achieved, similar to the difficulties in preparing perfectly matched discontinuities reported by Kutter & Otto (1990) and Hencher et al. (1993). The difference between the aperture of both specimens lies in its size and connectivity (see section 5.4.3.2). Another observation is that there appears to be air bubble formation around the asperities of the G_W specimen that is not observed in the G_O specimen. These air bubbles could lead to less dense asperities that could cause a reduction in

asperity strength and result in G_W specimens having a lower surface hardness than the G_O specimens. A full 3D segmentation analysis was conducted on the scans to obtain insight into the changes in aperture and contact area with increasing normal load (section 5.4.3.2).
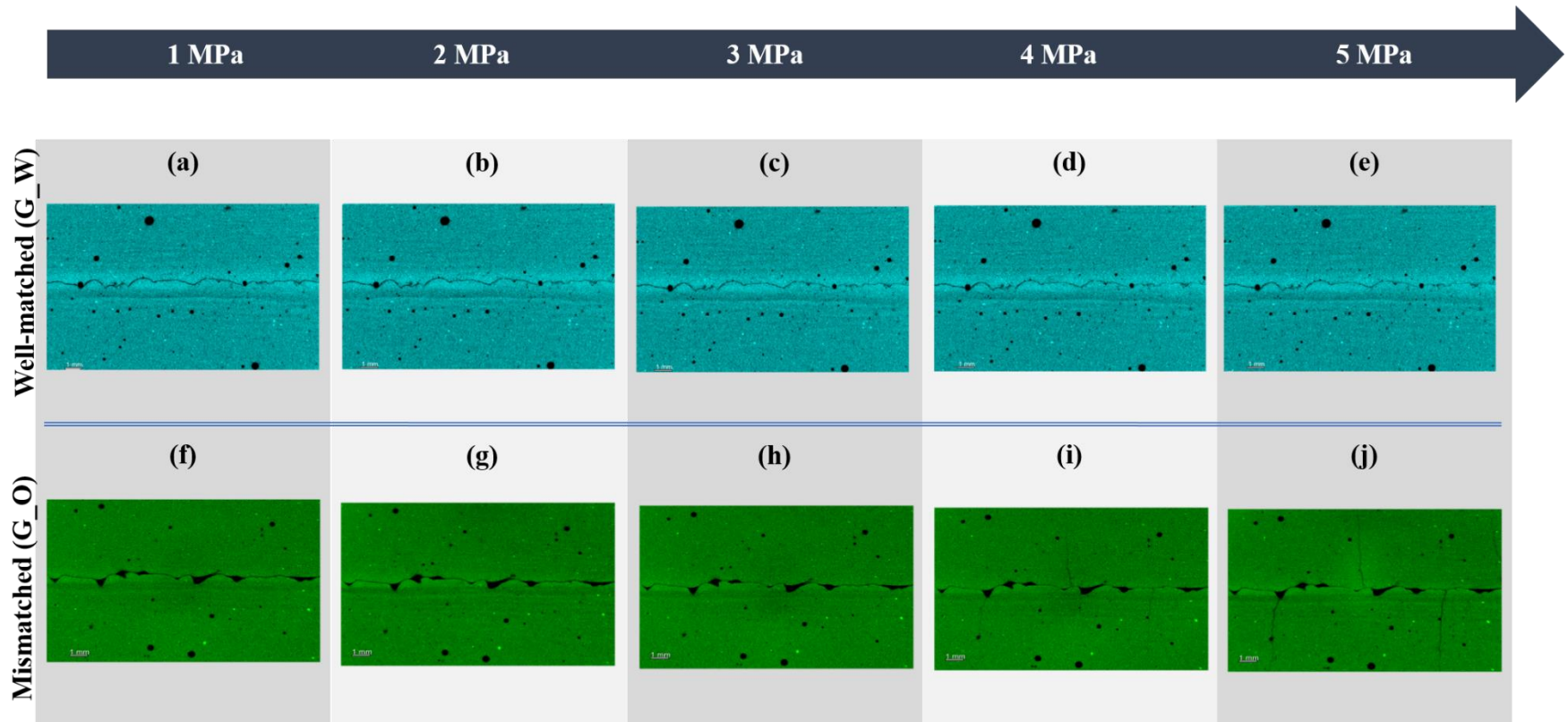
Figure 5.19. Snapshots of slices for: (a-e) G_W specimen (blue); and (f-j) G_O specimen (green), at normal stress [1-5] MPa

5.4.3.2 *Image segmentation and aperture quantification*

The following protocol was adopted to segment the fracture aperture in an unbiased manner. Figure 5.20 shows a schematic of the segmentation procedure. After normalization of the histograms of the images and adjustment of the window leveling, the images were cropped to a small area around the fracture to decrease the segmentation processing time. A built-in machine learning module in Dragonfly ORS 4.0 was employed. Before applying the module, parameters such as the training algorithm and dataset features were assigned by following these steps.

- *Masking images for training:* a couple of image slices were masked (labeled; 10 random slices) with two classes: (1) aperture in red; and (2) rock in blue, as shown in Figure 5.20. The masked images were used as the training dataset input for the model. It is important to label the images properly as this will have a direct effect on the segmented results.

- *Selecting a segmentation engine:* a segmentation engine was chosen as the "extra trees" algorithm (Geurts, P. et al., 2006; Dragonfly Documentation 2020.1). This algorithm works by dividing the data into subsets and fitting randomized decision trees, i.e., extra trees, and averages the data to avoid over-fitting and to provide accurate results. Aside from providing accurate results, an advantage of selecting extra trees as the engine is that it is computationally efficient (El-Sherbiny, B. et al., 2018). Interested readers are referred to the Dragonfly ORS documentation (2021) for more information. These decision trees are responsible for assigning each pixel in the images to the two predefined classes, i.e., aperture or rock.

- *Assigning dataset features:* Dataset features are predefined and customizable in Dragonfly ORS and represent a form of "feature criteria or image filter" that the model will be based on. Since the difference between the two classes (aperture and rock) is based on the pixel intensity, filters such as morphological, self-intensity, Otsu, and smoothing features were found to be appropriate for this application—as these features filtered the images based on the corresponding pixel intensity. The model is then trained, and the training dataset was composed of the labeled slices from step 1. It is important to note that data training is not cumulative, i.e., each time the user trains the model, a new model overwrites the previously trained one. To obtain a fair comparison between the apertures of both specimens, the same dataset features were selected for both models (G_W and G_O specimen models).

- *Model application on the complete dataset:* after choosing the parameters and training the model, the model was applied to the complete dataset (all the slices). The model outputs two regions of interest in 3D: (1) the aperture; and (2) the surrounding rock matrix, as shown in Figure 5.21, which shows a 3D view of the segmented apertures of specimens (a-e) G_W, and (f-j) G_O at normal stresses of 1-5 MPa. The images (Figure 5.21) show that the apertures in the G_O specimen are significantly larger than those in the G_W specimen.
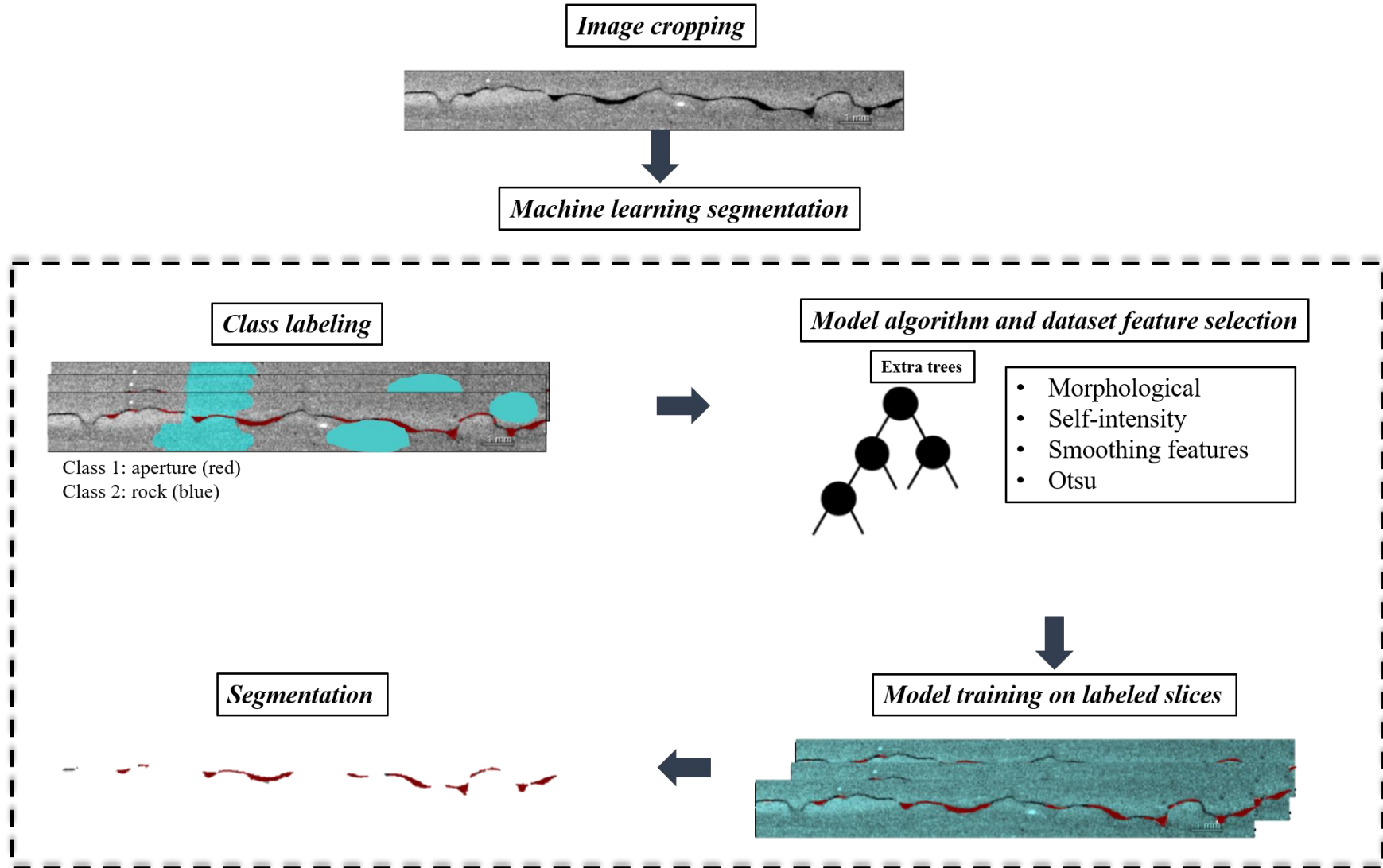
Image cropping

Machine learning segmentation

Class labeling

Class 1: aperture (red)
Class 2: rock (blue)

Model algorithm and dataset feature selection

Extra trees

- Morphological
- Self-intensity
- Smoothing features
- Otsu

Model training on labeled slices

Segmentation

Figure 5.20. Image segmentation steps

1 MPa   2 MPa   3 MPa   4 MPa   5 MPa

(a)   (b)   (c)   (d)   (e)

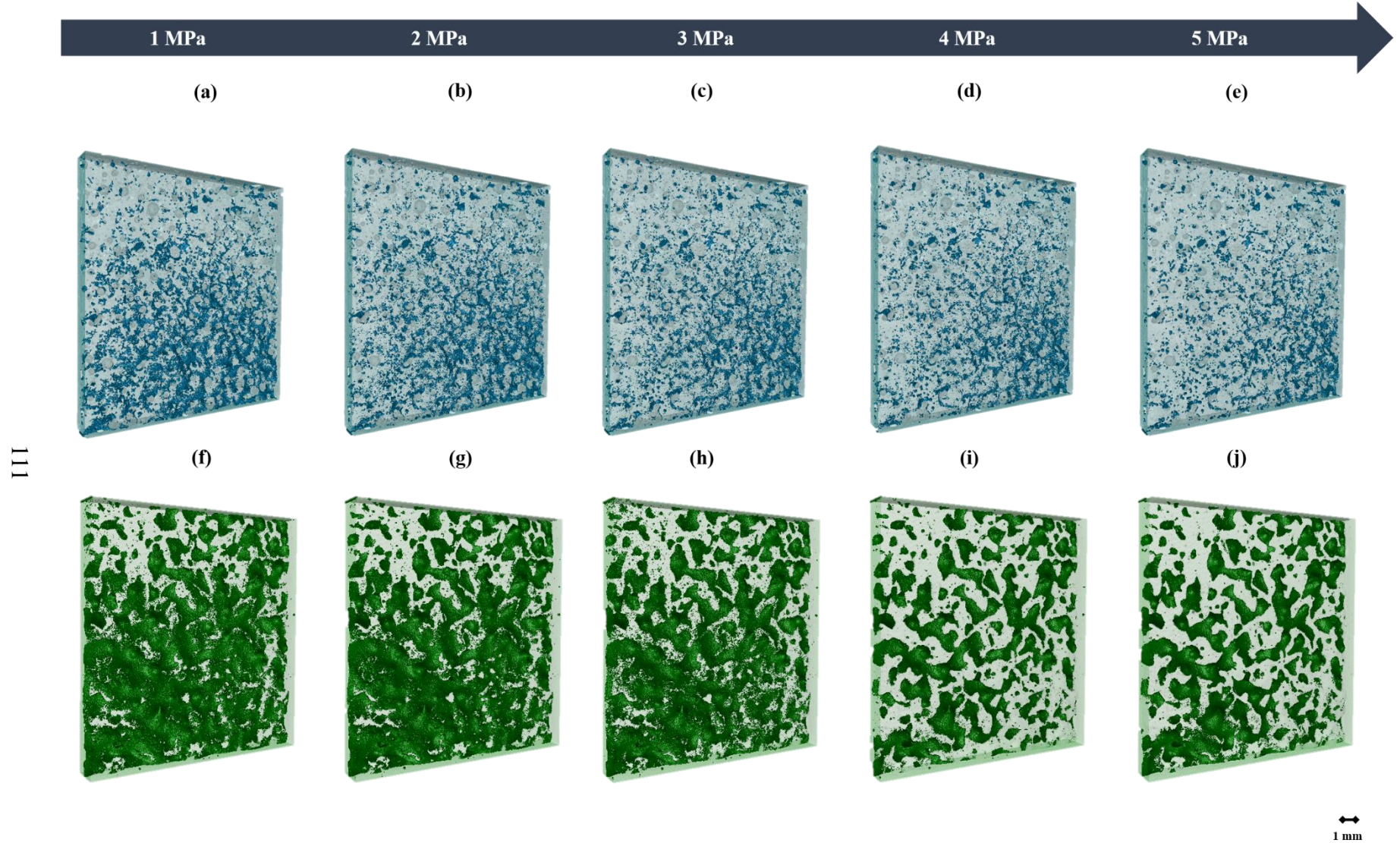(f)   (g)   (h)   (i)   (j)

1 mm

Figure 5.21. 3D segmented aperture for: (a-e) G_W; and (f-j) G_O specimens, at normal stresses of 1-5 MPa

Slices of the segmented apertures were used to quantify the apertures. The segmented images were exported from DragonFly as binary images to use with MATLAB. The quantification process adopted is summarized in Figure 5.22, and it involves: (1) importing the binary images into MATLAB; (2) looping through each column of each slice; and (3) adding the pixels corresponding to the aperture, i.e., pixel values of 1 (white regions that correspond to the aperture) in each column of each slice. This enabled a 3D reconstruction of the aperture in pixels and, after applying a calibration factor, i.e., the resolution (23 µm), a 3D reconstruction of the aperture distribution in µm, as shown in Figure 5.22 (lower image). The 3D reconstructed apertures for well-matched (G_W) and mismatched (G_O) specimens are presented in Figure 5.23 at different normal stresses.
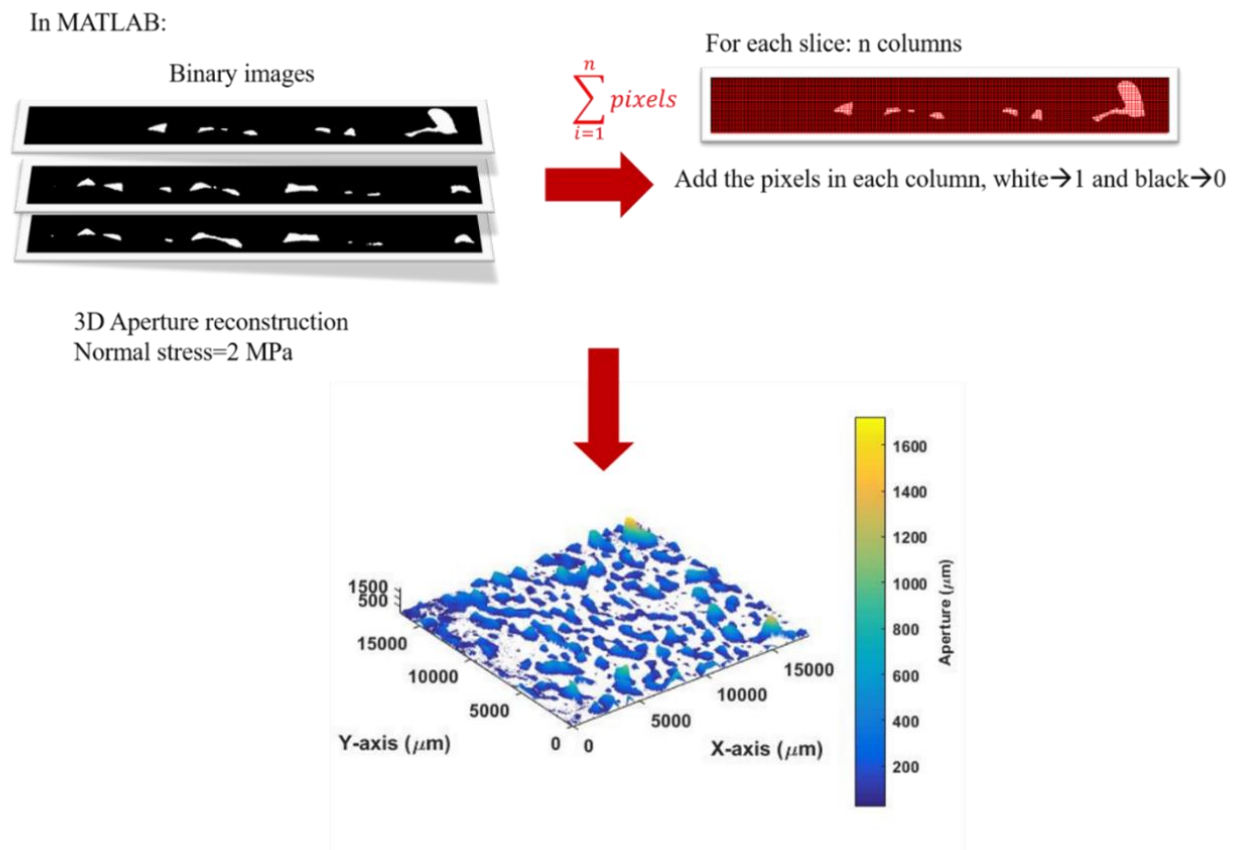

Figure 5.22. 3D aperture reconstruction and quantification in MATLAB

Figure 5.23 shows that the apertures from the G_O specimen (mismatched discontinuity) are connected at low normal stresses (1 and 2 MPa) and are quite large (~ 0.5 mm or more). As the normal stress increases to 5 MPa, the apertures become disconnected, but large apertures are still

present. This is in stark contrast to the change in apertures for the G_W specimen (well-matched discontinuity), where the apertures are quite small (mostly <150 micrometers), even at low normal stress. It is important to mention that after segmenting the aperture of G_W specimens, the air bubbles around the discontinuity were removed. The procedure illustrated in Figure 5.22 was followed to quantify the aperture.

Figure 5.24 shows the distribution of aperture for both specimens, G_W (well-matched) in solid lines and G_O (mismatched) in dashed lines, at normal stresses of 1-5 MPa. There is a distinct difference between the aperture distribution of both specimens. The aperture distribution for G_W specimens ranges between 22.89 µm and ~200 µm, whereas the distribution of G_O specimens shows apertures up to 800 µm. The large-sized voids in the aperture of the G_O specimen do not close under an increase in normal stress, as shown in Figure 5.23. This is due to a mismatch in the geometry of the asperities. From Figure 5.24, for a well-matched discontinuity specimen (G_W), the aperture distribution shifts to the left with increasing stress because of the decrease in aperture with stress and increase in the contact area. For the case of the G_O specimen, the apertures between 22-300 µm decrease with an increase in normal stress, but the larger apertures (>300 µm) are always present at all normal stresses. This is likely linked to the shape of the aperture and the mismatch in the surfaces.

From the measured apertures, a clear difference in the size and probability distribution of apertures corresponding to both specimens, G_O and G_W, is observed. The results of the segmented aperture confirm that using an oil-based release agent results in mismatched rock discontinuities and that this mismatch is always present even at normal stresses as high as 5 MPa. The aperture distributions help explain the mechanical and geophysical response of shearing a G_O specimen (Figures 5.2, 5.3, and 5.4). At low normal stress, the apertures are still connected and are larger than that at 5 MPa. The G_O specimens require additional shear displacement for the asperities to come in contact and get damaged—thus resulting in delayed point of contact and damage to the asperities. At high normal stress, the apertures in the G_O specimen are still quite large but are somewhat less connected because of an increase in contact areas. Less shear displacement is required to sustain damage—resulting in seismic precursors to shear failure in transmitted signals.
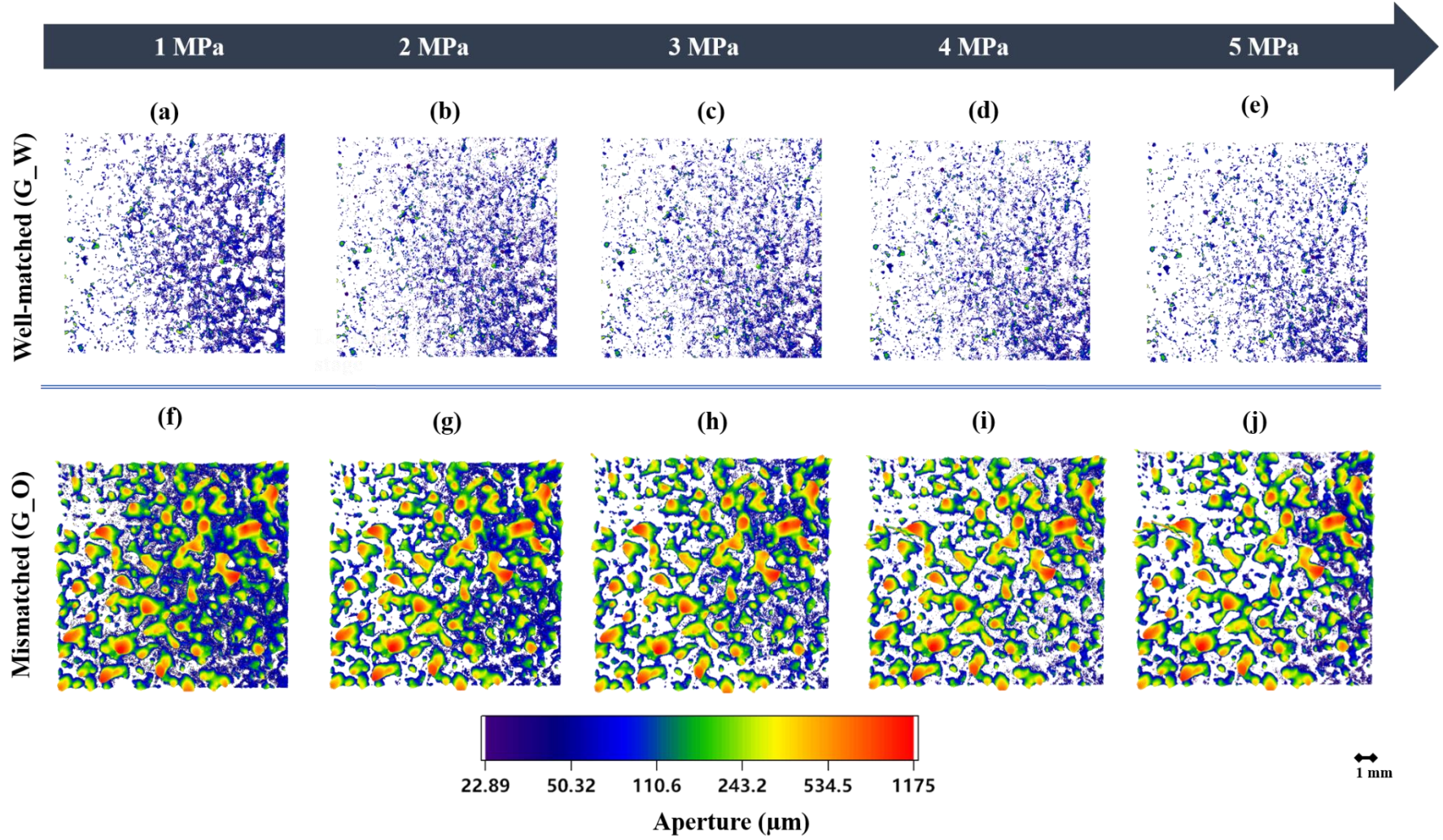
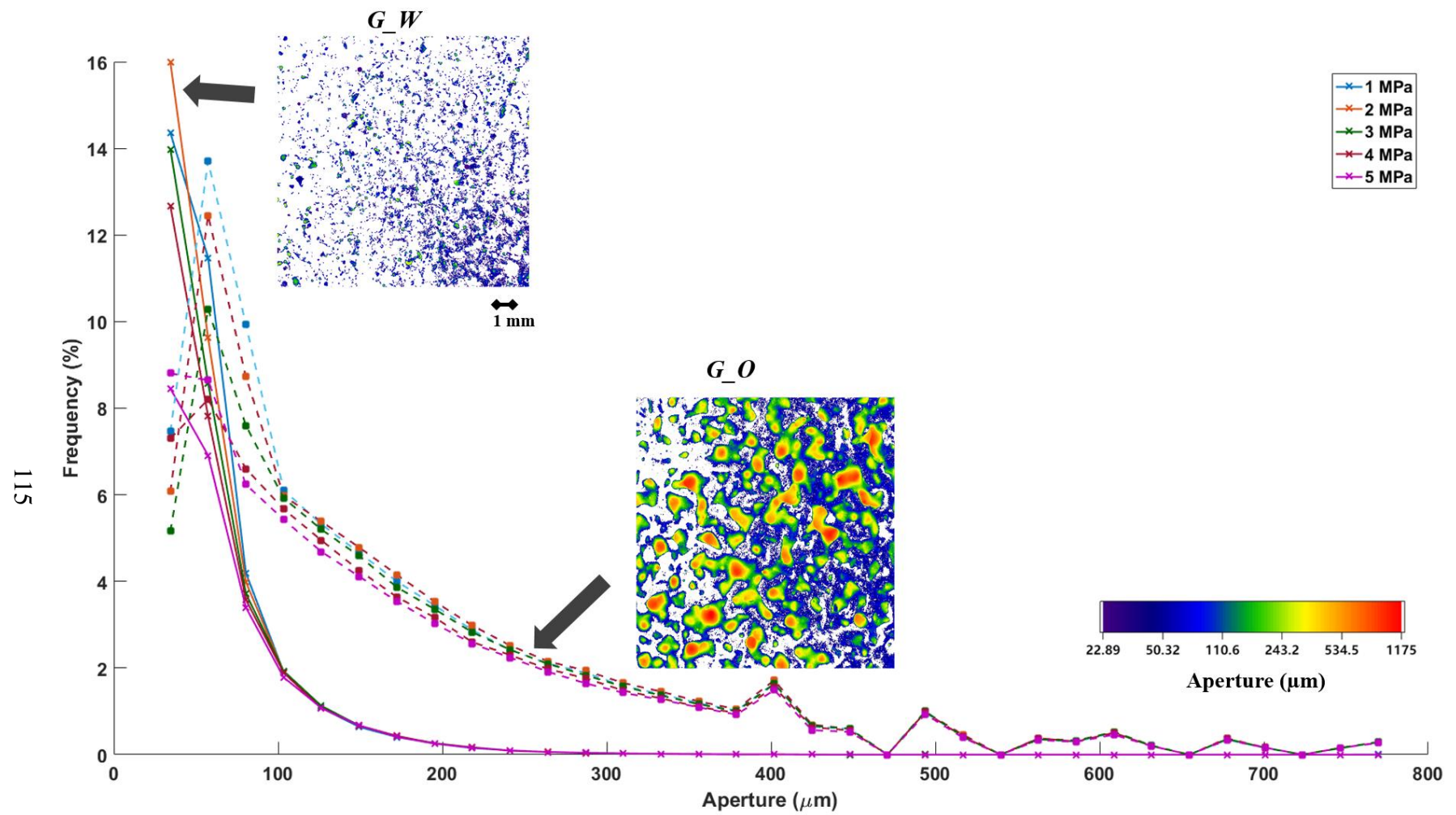Figure 5.23. Aperture quantification for: (a-e) G_W; and (f-j) G_O specimens, at 1-5 MPa normal stresses

Figure 5.24. Aperture distribution for G_O (dashed lines) and G_W (solid lines) specimens at normal stresses [1-5] MPa

5.4.3.3 *Qualitative observation: crack initiation orthogonal to the fracture:*

An interesting observation was found in 3 in-situ X-ray experiments conducted on G_O specimens and in 1 experiment conducted on G_W specimen. The observation entails the initiation of a crack perpendicular to the discontinuity. The formation of such cracks was also detected in the large-scale direct shear experiments through a sharp drop or increase in transmission recorded by transducers (Figure 3.22 in chapter 3 and Figures 5.3 and 5.4). Careful image labeling—slice by slice—was conducted to separate the crack from the voids (voids or aperture is the output of the machine learning model discussed in section 5.4.3.2). Given the complexity of the aperture distribution, this section involves a qualitative analysis only. Figure 5.25 shows: (a) a 3D view of G_O specimens, with (b) a transparent rock matrix to visualize the cracks, where two cracks were identified: 2 in the top block, and 2 in the bottom block, as shown in Figure 5.25 (b-c), respectively.
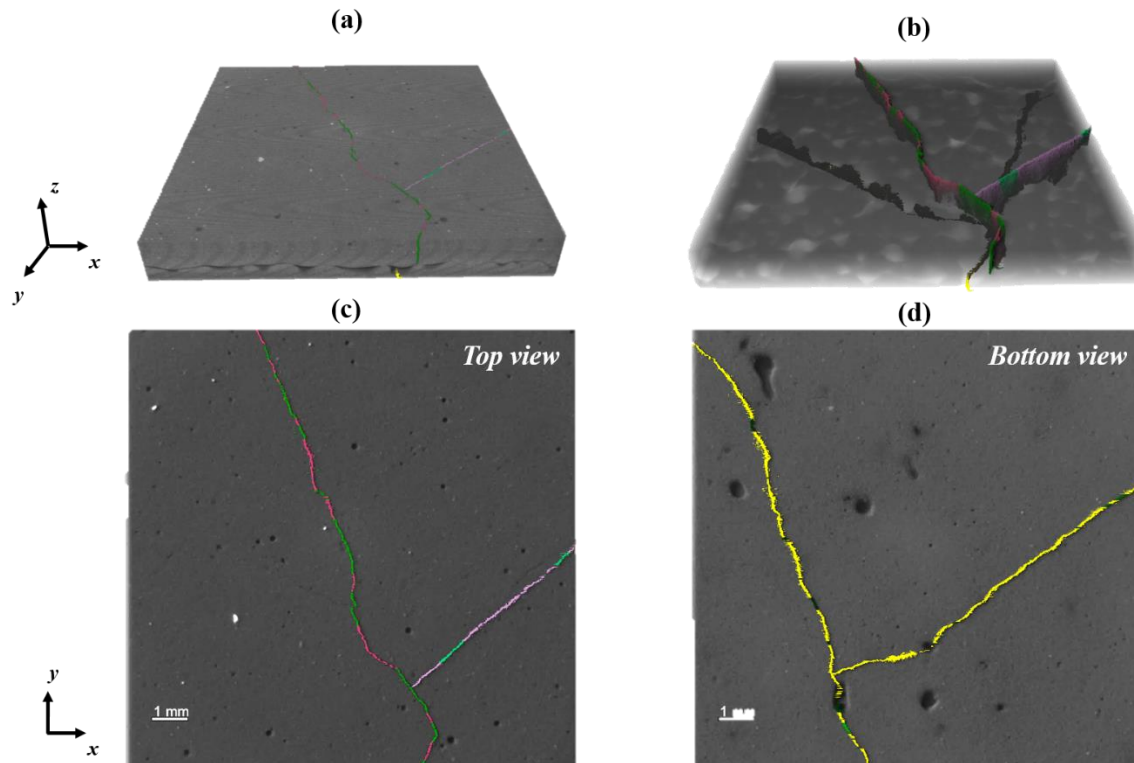
Figure 5.25. (a) 3D view of G_O specimens; (b) faded rock matrix to visualize the cracks; (c) top view of specimen G_O showing the top crack; (d) bottom view of specimen G_O showing the bottom crack

A qualitative analysis was performed to examine the preferred crack path, i.e., to answer the following question: does the crack pass through most of the voids or through the contacts of the joint? The procedure adopted for the analysis involved assigning the pixels (around the aperture) of the cracks in each slice to two main groups: (a) on voids; and (b) not on voids or on contacts. This means that for each slice, the crack is marked "on voids" if it intersects with the aperture and "on contacts" if it lies on contact regions of the rock. As mentioned in chapter 3, section 3.3.2, the initiation of a crack in a plane orthogonal to that of the discontinuity is a complex process due to the randomness and complexity of the voids and because it is not clear where the crack initiated in the y-direction (see Figure 5.25 for the coordinate system). However, a rough percentage of crack pixels that lie on the aperture is obtained to provide insight into the preferred crack path direction. Figure 5.26 presents the 3D view of the transparent rock matrix with (a) top and (b) bottom cracks identified in Figure 5.26 (b), which is flipped to show the bottom cracks; the aperture is shown in orange. The cracks are color-coded with respect to their position on the aperture, i.e., for the top cracks (Figure 5.26 (a)), green corresponds to portions of the crack that lie on contacts, and pink corresponds to portions of the crack that lie on the apertures. Similarly, for the bottom cracks (Figure 5.26 (b)), yellow represents the portions of the crack that lie on the aperture, and green denotes the portion of the crack that does not lie on the aperture.
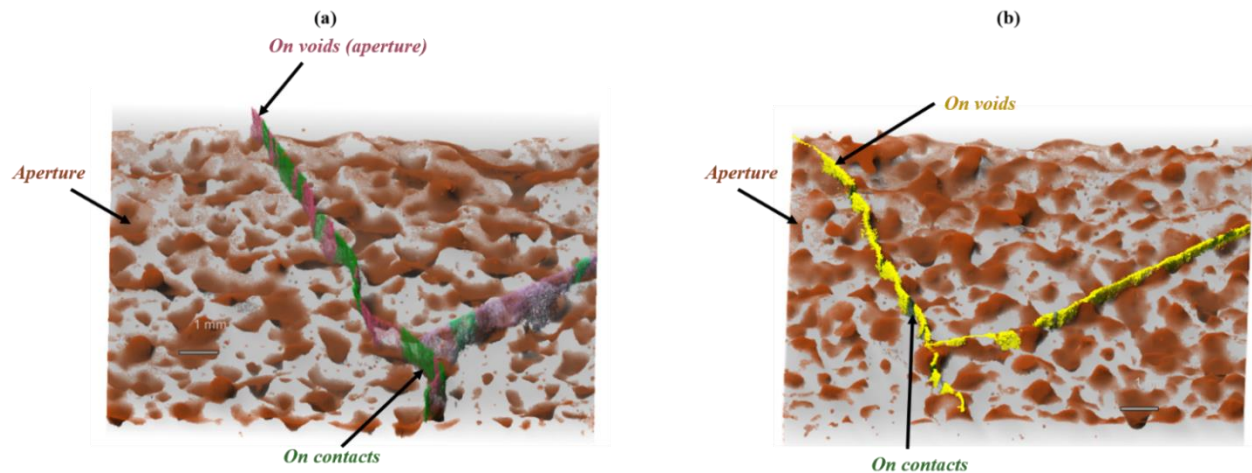

Figure 5.26. (a) top and (b) bottom 3D cracks labels on aperture of G_O specimen at normal stress of 5 MPa

To quantify the color-coded pixels, the 3D cracks were first projected on a 2D plane, i.e., XY-plane (the plane that the fracture is in, see Figure 5.25). Then, image processing using ImageJ was performed to obtain the number of pixels corresponding to each region of the crack, i.e., green and pink for top and yellow and green for bottom cracks. The procedure followed to quantify the cracks is as follows:

1. Each crack was projected on a 2D plane, i.e., XY-plane (see coordinates in Figure 5.25).
2. The projected image was then imported into ImageJ.
3. The image was then converted to 8-bit—this is a required step to be able to convert the images to binary in a later step.
4. Window leveling was then adjusted to get enough contrast between the pixel classes, i.e., on aperture and not on aperture.
5. The image was then converted into a binary image, then the white and black pixels (each corresponds to either on void or on contact class) were quantified.

This process provides only a rough estimate; there is a limitation to this analysis which is the fact that the crack is first projected on a 2D plane (XY plane in Figure 5.25); this may result in overestimating the actual number of pixels lying on voids or contacts. The qualitative results are presented in Figure 5.27 and show that for the top left crack, ~55.5 % of the pixels lie on voids (pink) while ~45.5% lie on contacts (green); for the top right crack, the percentages of pixels lying on voids and contacts were found to be ~81.1% (pink) and 18.9% (green), respectively. For the bottom right crack, 88.2% of the crack pixels lie on voids (yellow) while only 11.79% lie on contacts (green), and similarly, for the bottom left crack, the corresponding crack pixel percentages were ~89.7% on voids (yellow) and ~10.32% on contacts (green). Based on this qualitative analysis, the cracks appear to form preferentially over the voids on the joints. The crack initiation process is complex as the aperture and the contact surfaces are random, but the rough-qualitative results show that cracks have a preferential path along the voids, as opposed along contact areas.
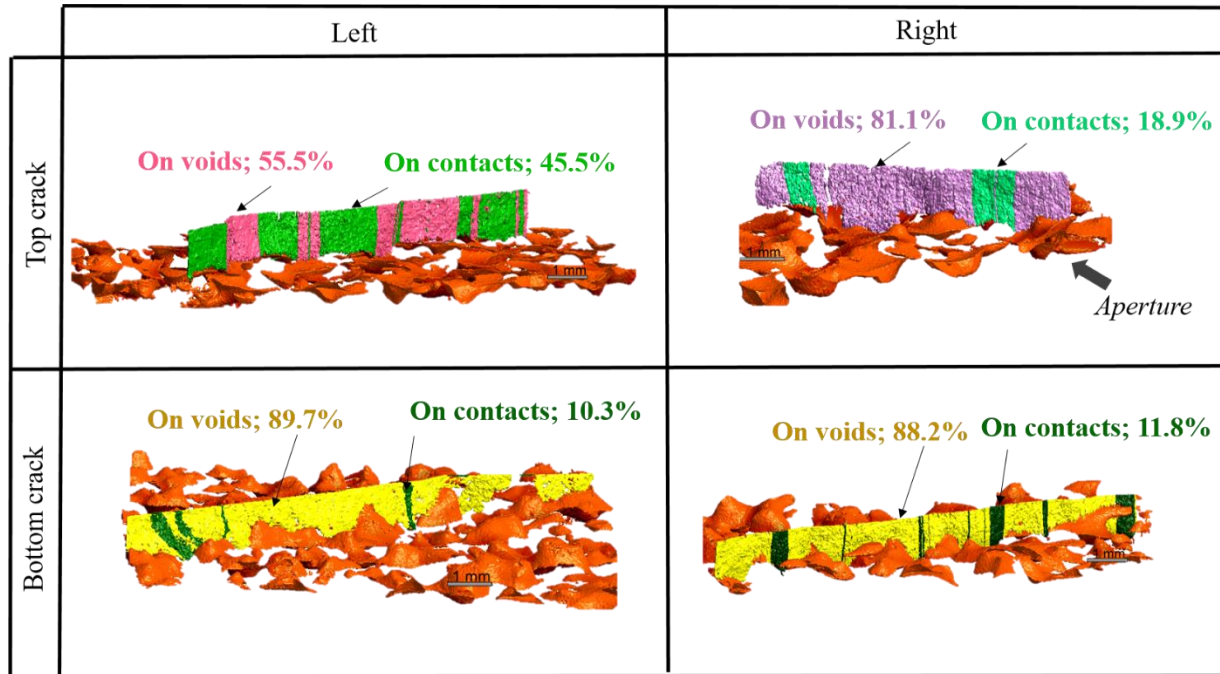
118

Figure 5.27. Qualitative analysis of orthogonal crack path on voids

5.5 Summary

The ability to detect seismic precursors to shear failure is extremely important but has only been observed on well-matched rock surfaces. It is essential to study different rock discontinuity conditions that may be present in the field, where both matched and mismatched discontinuities exist. Based on the results presented in this chapter, seismic precursors to shear failure (in the form of peaks in the normalized transmitted amplitudes) were detected for well-matched rock discontinuities at normal stresses of 2 and 5 MPa. Conversely, the ability to detect seismic precursors to shear failure on specimens with mismatched discontinuities (G_O specimens) was only possible at higher normal stress (5 MPa). Characterization of the joint surfaces prepared with water-based release agent (G_W specimen) and oil-based release agent (G_O specimen) support the hypothesis that differences in the joint conditions affect the onset of asperity damage. The micro-indentation experiments showed that surfaces prepared with an oil-based release agent were harder than those prepared with a water-based release agent for both rough (grit 36 sandpaper roughness) and smooth surfaces. The X-ray tomography data indicated a clear difference in the aperture distributions of both specimens. The oil-based release specimens tended to have

connected apertures at low normal stress and large voids that did not close under stress. Conversely, the aperture of the water-based specimen was much smaller ([23-200 µm]) than that of the G_O's specimen ([23-800µm]). The results indicated that at low normal stress, significant shear displacement is needed to increase the shear and compressional fracture specific stiffness and eventually damage the asperities, and this mechanism could take place with and without the increase in asperity micro-strength, implying that we cannot rule out which mechanism is the governing one. Findings from this chapter provide more insight into the conditions where the detection of seismic precursors to shear failure is possible and also suggest why post-peak maxima in transmission may occur.

6 CONCLUSIONS AND RECOMMENDATIONS

6.1 Introduction

Discontinuities in rock masses represent weak elements and may cause failures in slopes, excavations, and underground structures, resulting in loss of life and significant economic losses. It is necessary to find tools to monitor the evolution of failure and the shearing process of rock discontinuities. Previous studies (Hedayat et al., 2014b; 2017; 2018) successfully detected seismic precursors to shear failure of well-matched gypsum and limestone rock discontinuities at the laboratory scales. The findings from these research studies were instrumental as they highlighted the potential of using geophysical tools as telltales to shear failure of rock discontinuities. In the field, rock discontinuities may not always be perfectly matched due to physical or chemical processes that may take place. A fundamental question that this thesis aimed to answer was the following: do seismic precursors to shear failure occur when shearing rock discontinuities with different discontinuity conditions, i.e., matched, mismatched, and nonplanar—if not, then what discontinuity conditions would mask the presence of these seismic precursors to failure? This question has been answered through a combined geophysical and mechanical experimental program that integrated detailed observations in the laboratory at the meso- and micro-scales. Shear experiments on gypsum discontinuities were conducted to observe changes in compressional (P) and shear (S) waves transmitted across the discontinuity. In addition, a thorough discontinuity characterization was performed to understand the interplay between seismic wave transmission, precursory detection, and joint condition. A summary of the experimental work conducted in this research is presented in section 6.2, followed by the key findings in section 6.3, and finally, recommendations for future work in section 6.4.

6.2 Summary of the experimental work

This thesis presented the results of extensive laboratory direct shear experiments conducted on gypsum discontinuities. All the gypsum samples were prepared in the laboratory and were composed of two independent blocks; each block had a length of 152.4 mm, a width of 127 mm, and a thickness of 25.4 mm. The samples were prepared by casting one block against the other after applying a thin layer of release agent to ensure the separation of the two blocks of the

specimen after curing. The first set of experiments entailed direct shear experiments on gypsum samples with a half-cycle sine wave with an amplitude of 3.2 mm—an order of magnitude larger than the maximum asperity height—spanning the central 1/3 of the discontinuity at 1 and 2 MPa normal stresses. These experiments aimed to examine the effect of discontinuity nonplanarity on the mechanical and geophysical response using transmitted compressional (P) and shear (S) seismic signals. The second set of direct shear experiments was conducted on gypsum samples with idealized sawtooth discontinuities to systematically investigate the different modes of seismic precursors to shear failure, i.e., transmitted, reflected, and converted signals. Finally, the third set of experiments was conducted on gypsum discontinuities prepared with two release agents –water-based (created well-matched discontinuities) and oil-based (created mismatched discontinuities)— that resulted in micro-mechanical and -physical differences. These experiments aimed to determine what discontinuity conditions (with different degrees of mismatch and variations in micro-strength and -structure) could affect the detection of seismic precursors to shear failure.

6.3 Key findings

The major findings of this research work can be summarized based on the three aspects addressed in this thesis: (1) the effect of discontinuity profile, i.e., presence of a half-cycle sine wave (HCS) on the mechanical and geophysical response of gypsum discontinuities under shear, (2) precursory modes and time of appearance while shearing saw-toothed discontinuities, and (3) direct shear experiments conducted on well-matched and mismatched gypsum discontinuities (G_W and G_O specimens, respectively).

From the experiments conducted on gypsum discontinuities with a HSC wave with an amplitude of 3.2 mm, the mechanical response showed a ~ 40% increase in mean peak shear stress with respect to that of the planar discontinuity, at normal stresses of 1 and 2 MPa. Seismic wave transmission was able to detect non-uniform dilation and closure of the discontinuity through continuous transmission monitoring (even after the peak shear stress). Analysis of the signals showed an increase in transmissions at the top of the sample and a decrease in transmission at the bottom of the sample. Digital Image Correlation (DIC) results confirmed that the specimen exhibited closure at the top portion and opening at the bottom part, consistent with the seismic

response. At higher normal stress, dilation was suppressed due to increased confinement, and all transducers recorded seismic precursors to shear failure. Large-scale roughness affects the generation of precursors because it can cause non-uniform closure/dilation along the fracture plane. This suggests that multiple sensors or transmission paths would be needed to probe the behavior of different portions of a discontinuity.

Seismic precursors in the form of peaks in transmitted and converted amplitudes and troughs in the reflected amplitudes were detected by running direct shear experiments on idealized saw-toothed discontinuities. The precursors were observed at the top portion of the specimen first, i.e., where the slip initiated (detected by DIC) and then propagated across the middle and bottom part of the discontinuity. This mechanism can be thought of as a slow-motion cascade of slip failure and explains why precursory events took place progressively from the top to the middle and finally to the bottom of the discontinuity. The data showed that the reflected seismic precursors emerged first, followed by the transmitted and converted precursors. The extended displacement discontinuity theory can predict which mode will first exhibit the precursor, given the signal's frequency, the fracture-specific stiffness, and the material properties of the rock. The results indicate that monitoring the moment when precursors were first observed in the different modes may provide information about how slip propagates along a discontinuity, how close the discontinuity is to failure, and a rough estimate of fracture stiffness.

Seismic precursors to shear failure were observed in specimens prepared with a water-based release agent (G_W) with a relatively well-matched discontinuity. However, when a sample was prepared with an oil-based release agent (G_O) with a mismatched discontinuity, the peaks of the transmitted seismic signals took place after the peak shear stress for direct shear experiments conducted at a normal stress of 2 MPa. Thus, no seismic precursors were detected. At normal stress of 5 MPa, seismic precursors to shear failure were detected by shearing G_W and G_O specimens. A thorough characterization of the discontinuities was performed to understand the interplay between wave transmission, precursor detection, and differences in the discontinuity conditions for both G_O and G_W specimens. The micro-physical, -chemical, and -mechanical properties of each type of discontinuity (G_O and G_W samples) were assessed through Scanning Electron Microscopy (SEM), Electron X-ray Diffraction (EDX), micro-indentation testing, and 3D CT in-

situ X-ray scans. The following key findings were drawn from the experiments conducted on well-matched (G_W specimen) and mismatched (G_O specimen) discontinuities.

- 3D X-ray scans revealed that G_W specimens had more contact area and smaller apertures [22-300 µm] than the G_O samples [apertures 22-800 µm]. The aperture distribution of the G_W specimen showed that the apertures decreased with an increase in normal stress and the X-ray images showed an increase in the contact area. However, for the G_O samples, while the aperture in the range of [22-300 µm] decreased with increasing stress, the large apertures (>300 µm) –due to a mismatch in the geometry of the asperities—remained unchanged.

- Regarding discontinuity micro-physical, -chemical, and -mechanical characterization: SEM scans showed that G_W samples had distinct micro-gypsum needles, whereas, in the G_O samples, the needles appeared to be slightly amorphous. EDX scans showed that the surfaces prepared with oil and water-based release agents (G_O and G_W specimens) did not exhibit chemical differences. However, micro-indentation testing indicated that G_O specimens had higher hardness values than G_W specimens for smooth and rough surfaces (grit 36 sandpaper roughness). The asperities of a sample prepared with an oil-based release agent recorded a mean micro-hardness of ~ 0.4 GPa. In contrast, the asperities of the samples prepared with a water-based release agent, the mean micro-hardness was ~ 0.17 GPa. These findings imply that G_O specimens had asperities twice as strong as those of G_W specimens. Furthermore, micro-indentation on smooth discontinuities showed higher micro-hardness values (mean hardness ~ 0.3 GPa) for G_O samples than G_W samples (mean hardness ~ 0.18 GPa).

- Cracks initiating and propagating in a plane orthogonal to the discontinuities were observed for most of the uniaxial in-situ X-ray experiments conducted on G_O specimens. The generation of such cracks was also detected by the geophysical monitoring system during the direct shear experiments as a sharp drop in transmission. A qualitative analysis aimed to find the preferential crack path showed that the cracks seem to have a preferential path over the voids of a pre-existing joint, as most of the crack pixels intersected the voids as opposed to the contact area.

- The micro-physical, -chemical, -and mechanical tests showed that: (1) at a normal stress of 2 MPa, voids along the discontinuity of the G_O sample were better connected and larger than those of the G_W sample; thus, further shear displacement was required for the asperities to

achieve/increase contact and eventually incur damage; (2) the discontinuity prepared with the oil-based release agent resulted in stronger asperities, also implying that further shear displacements were needed for the asperities to be damaged. The two observations point towards a larger shear displacement to damage the asperities created with the oil-based release agent (G_O specimen).

One of the most important implications of this study is that the discontinuity conditions, i.e., micro-strength, -structure, and -contact and the normal stress applied, play a significant role in detecting seismic precursors to shear failure in transmitted seismic signals. For well-matched discontinuities (G_W specimens), seismic precursors to shear failure were detected by running direct shear experiments at 2 and 5 MPa normal stresses. Conversely, seismic precursors to shear failure were only observed at higher normal stresses for G_O specimens.

6.4 Recommendations for Future Research

This interdisciplinary research put forward new knowledge in the area of rock physics by characterizing gypsum discontinuities under shear and normal stress—at the micro and meso scales—using mechanical, geophysical, and tomographic tools. While this research provided an in-depth understanding of the conditions and types of seismic precursors to shear failure of rock discontinuities, it also paved the road for potential research that could be explored.

- It is recommended to conduct 3D X-ray in-situ direct shear experiments while using pin transducers to record the seismic response of a specimen during shearing along with the X-ray images of the void space. This would require incremental shearing steps, i.e., first, a minimal load would be applied while recording seismic and X-ray data. Then, a second loading stage, where the load is held, seismic readings and 3D X-scans would also be recorded, and so forth until the sample fails. Such experiments will enable the observation of the evolution of the damage to the asperities and could be used to evaluate the seismic response to see the onset of asperity damage at the time of precursors. This work would contribute to the understanding of the mechanism of seismic precursors.

- Based on the direct shear experiments conducted on G_W and G_O specimens, it appears that two factors may delay the onset of a precursor. These two factors were (a) discontinuity

mismatch; and (b) micro-properties, i.e., micro-strength and structure. To understand which factor governs the process, systematic direct shear experiments could be conducted on samples with idealized sawtooth discontinuities prepared with oil and water-based release agents (at normal stress of 2 MPa) to monitor seismic precursors to shear failure. Each block would be cast against a 3D printed mold based on an idealized sawtooth geometry. If the results from the experiments showed that seismic precursors to shear failure were not recorded by the sawtooth prepared with an oil-based release agent, then it seems likely that the microstructure and strength of the asperities play a more significant role.

- A mismatched discontinuity prepared in the laboratory can be viewed as a proxy of a weathered discontinuity in the field. It is thus recommended to conduct direct shear experiments on natural rock discontinuities and compare their geophysical response with the same type of rock but with an induced fracture in the laboratory. The induced fracture represents a "well-matched" discontinuity, and the naturally weathered sample represents a "mismatched" discontinuity. Prior to running the direct shear experiments, it is recommended to characterize the surfaces through SEM, EDX, X-ray scans, and laser profilometry. Such experiments are recommended to be conducted on different rock types with different weather conditions to create large variability in the data. The findings from these experiments will result in an extensive database that includes results from experiments conducted on different rock types and conditions. The extensive database collected could be used to build machine learning algorithms to develop innovatively smart techniques that help identify impending shear failure in different types of rock with various discontinuity characteristics.

- To further understand how and why cracks initiate in an orthogonal plane to the discontinuity, 3D in-situ uniaxial X-ray experiments are recommended to be performed. The experiments would entail uniaxially loading a specimen with two blocks; the first block would have a rough surface (prepared with an oil-based release agent). The second block would have a well-polished smooth surface. The specimen would be incrementally loaded, and at each loading stage, a 3D X-ray scan would be captured. These experiments would be conducted to monitor whether cracks—orthogonal to the discontinuity—would initiate—if yes, then at what loading stage and where along the discontinuity—providing

a better understanding of the mechanism of orthogonal-crack formation under normal stress. These systematic experiments could be numerically modeled to identify high-stress points, quantify the major tensile principal stresses, and compare the corresponding results with the experimental scans.

- The experimental work conducted at the laboratory scale showed that active seismic monitoring has the potential to detect seismic precursors to shear failure. It would be useful to take this work a step further and implement it in the field to solve the scale challenge. Suitable field transducers could be placed near pre-existing discontinuities in the field of a highly seismic area, and their response would be recorded every couple of hours—calibration will be needed to find the most suitable data collection rate. Such experiments could last for a long period of time—over the span of years—and the seismic response from each day would be recorded, analyzed, and compared to data collected from previous days. If these experiments were successfully scaled to the field, they would provide a foundation for potential field applications.

REFERENCES

ASTM International, 2005. ASTM E384-05: Standard Test Methodfor Microindentation Hardness of Materials. ASTM Standard.

ASTM International, 2007. ASTM E2546-07: Standard practice for instrumented indentation testing. ASTM Standard.

Bandis, S., Lumsden, A. C., & Barton, N. R. (1981, February). Experimental studies of scale effects on the shear behaviour of rock joints. In *International journal of rock mechanics and mining sciences & geomechanics abstracts* (Vol. 18, No. 1, pp. 1-21). Pergamon.

Barton, N., & Choubey, V. (1977). The shear strength of rock joints in theory and practice. *Rock Mechanics Felsmechanik Mécanique Des Roches*. https://doi.org/10.1007/BF01261801

Barton, Nicholas. (1973). Review of a new shear-strength criterion for rock joints. *Engineering Geology*. https://doi.org/10.1016/0013-7952(73)90013-6

Bobet, A. Fracture Coalescence in Rock Materials: Experimental Observations and Numerical Predictions. Sc.D. Thesis, 1997. Massachusetts Institute of Technology, Cambridge, Massachusetts.

Bobet, A., & Einstein, H. H. (1998). Fracture coalescence in rock-type materials under uniaxial and biaxial compression. International Journal of Rock Mechanics and Mining Sciences. https://doi.org/10.1016/S0148-9062(98)00005-9

Byerlee, J. (1978). Friction of rocks. Pure and Applied Geophysics PAGEOPH. https://doi.org/10.1007/BF00876528

Chen, W. Y., Lovell, C. W., Haley, G. M., & Pyrak-Nolte, L. J. (1993). Variation of shear-wave amplitude during frictional sliding. *International Journal of Rock Mechanics and Mining Sciences And*. https://doi.org/10.1016/0148-9062(93)90022-6

Cheng, F., & Haberfield, C. M. (1998). Laboratory study of the effect of drilling fluids on piles socketed into soft rock. *The Geotechnics of Hard Soils - Soft Rocks. Proceedings of the Second International Symopsium on Hard Soils-Soft Rocks, Naples, October 1998. (Two Volumes).*

Choi, M.-K. (2013). *Characterization of Fractures Subjected to Normal and Shear Stress.* Ph.D. Thesis, Lyles School of Civil Engineering, Purdue Unversity. ProQuest.

Choi, M. K., Bobet, A., & Pyrak-Nolte, L. J. (2014). The effect of surface roughness and mixed-mode loading on the stiffness ratio κ x /κ z for fractures. *Geophysics*. https://doi.org/10.1190/GEO2013-0438.1

Crawford, A. M., & Curran, J. H. (1981). The influence of shear velocity on the frictional resistance of rock discontinuities. *International Journal of Rock Mechanics and Mining Sciences And*. https://doi.org/10.1016/0148-9062(81)90514-3

Combes, J., Grossmann, A., & Tchamitchian, P. (1989). Wavelets: Time-frequency methods and phase space. The Journal of the Acoustical Society of America, 89(5), 2477–2478. https://doi.org/10.1121/1.400986

Dantas Neto, S. A., Indraratna, B., Oliveira, D. A. F., & de Assis, A. P. (2017). Modelling the Shear Behaviour of Clean Rock Discontinuities Using Artificial Neural Networks. Rock Mechanics and Rock Engineering. https://doi.org/10.1007/s00603-017-1197-z

de Pater. C. J., Groenenboom. J., van Dam. D. B. and R. Romijn. 2001. Active seismic montirong of hydraulic fractures: laboratory experiments and field applications. International Journal of Rock Mechanics Mining Science & Geomechanics Abstracts. 38/6: 777-785

De Toledo, P. E., De Freitas, M. H., & CGcol. (1993). Laboratory testing and parameters controlling the shear strength of filled rock joints. Geotechnique, 43(1), 1-19.

Demers, H., Horny, P., Gauvin, R., & Lifshin, E. (2002). WinX-ray: A new Monte Carlo program for the simulation of X-ray and charging materials. *Microscopy and Microanalysis*, *8*(S02), 1498-1499.

Dragonfly 2020.2. Object Research Systems (ORS) Inc, Montreal, Canada, 2020; software available at http://www.theobjects.com/dragonfly

Drouin, D., Couture, A. R., Joly, D., Tastet, X., Aimez, V., & Gauvin, R. (2007). CASINO V2. 42—a fast and easy-to-use modeling tool for scanning electron microscopy and microanalysis users. Scanning: The Journal of Scanning Microscopies, 29(3), 92-101.

El-Sherbiny, B., Nabil, N., El-Naby, S. H., Emad, Y., Ayman, N., Mohiy, T., & AbdelRaouf, A. (2018, March). BLB (Brain/Lung cancer detection and segmentation and Breast Dense calculation). In 2018 First International Workshop on Deep and Representation Learning (IWDRL) (pp. 41-47). IEEE.

Fecker, E., & Rengers, N. (1971). Measurement of large scale roughness of rock planes by means of profilograph and geological compass. In Proceedings symposium on rock fracture, Nancy, France (pp. 1-18).

Fischer-Cripps, A. C. (2011). Analysis of nanoindentation test data. In Nanoindentation (pp. 39-75). Springer, New York, NY.

Geurts, P., Ernst, D., & Wehenkel, L. (2006). Extremely randomized trees. Machine learning, 63(1), 3-42.

geurbi, A., Li, H., & Hedayat, A. (2021). Detection of Seismic Precursors in Converted Ultrasonic Waves to Shear Failure of Natural Sandstone Rock Joints. Rock Mechanics and Rock Engineering, 1-17.

Giachetti, A. (2000). Matching techniques to compute image motion. Image and Vision Computing. https://doi.org/10.1016/S0262-8856(99)00018-9

Gilpin, Christopher, J. Director of the Life Science Microscopy Facility at Purdue University; gilpin@purdue.edu

Goodman, R. E. (1970). The deformability of joints. In Determination of the in situ Modulus of Deformation of rock. ASTM International.

Goodman, R. E., & Ohnishi, Y. (1973). Undrained shear testing of jointed rock. Rock Mechanics Felsmechanik Mecanique Des Roches. https://doi.org/10.1007/BF01238044

Hedayat, A. (2013). *Mechanical and Geophysical Characterization of Damage in Rocks.* Ph.D. Thesis, Lyles School of Civil Engineering, Purdue Unversity. ProQuest.

Hedayat, A., Pyrak-Nolte, L. J., & Bobet, A. (2014a). Detection and quantification of slip along non-uniform frictional discontinuities using digital image correlation. Geotechnical Testing Journal, 37(5), 786-799

Hedayat, A., Pyrak-Nolte, L. J., & Bobet, A. (2014b). Precursors to the shear failure of rock discontinuities. Geophysical Research Letters. https://doi.org/10.1002/2014GL060848

Hedayat, A., & Hinton, J. (2017). Geophysical waveform's frequency attenuation as a precursor to rock shear failure. Geotechnical Special Publication. https://doi.org/10.1061/9780784480472.067

Hedayat, A., Haeri, H., Hinton, J., Masoumi, H., & Spagnoli, G. (2018). Geophysical signatures of shear-induced damage and frictional processes on rock joints. Journal of Geophysical Research: Solid Earth, 123(2), 1143-1160.

Hencher SR, Toy JP, Lumsden AC (1993) Scale-dependent shearstrength of rock joints. In: Pinto Da Cunha A (ed) Scale effects in rock masses 93; proceedings of the 2nd international workshop on scale effects in rock masses, Lisbon, Portugal, 25 June 1993. A.A. Balkema, Rotterdam, pp 233–240

Hoek, E., Carranza, C., & Corkum, B. (2002). Hoek-brown failure criterion – 2002 edition. Narms-Tac. https://doi.org/10.1016/0148-9062(74)91782-3

Hulbert, C., Rouet-Leduc, B., Johnson, P. A., Ren, C. X., Rivière, J., Bolton, D. C., & Marone, C. (2019). Similarity of fast and slow earthquakes illuminated by machine learning. *Nature Geoscience*, *12*(1), 69-74.

Indraratna, B., & Haque, A. (1997). Experimental study of shear behavior of rock joints under constant normal stiffness conditions. *International Journal of Rock Mechanics and Mining Sciences*, *34*(3-4), 141-e1.

Indraratna, B., Haque, A., & Aziz, N. (1999). Shear behaviour of idealized infilled joints under constant normal stiffness. *Geotechnique*. https://doi.org/10.1680/geot.1999.49.3.331

Indraratna, B., & Haque, A. (2000). *Shear behaviour of rock joints*. Crc Press.

Indraratna, B., Jayanathan, M., & Brown, E. T. (2008). Shear strength model for overconsolidated clay-infilled idealised rock joints. Geotechnique. https://doi.org/10.1680/geot.2008.58.1.55

Indraratna, B., Welideniya, H. S., & Brown, E. T. (2005). A shear strength model for idealised infilled joints under constant normal stiffness. Geotechnique. https://doi.org/10.1680/geot.2005.55.3.215

Indraratna, B., & Jayanathan, M. (2005). Measurement of pore water pressure of clay-infilled rock joints during triaxial shearing. *Geotechnique*. https://doi.org/10.1680/geot.2005.55.10.759

Jaeger, J. C., Cook, N. G. W., & Zimmerman, R. W. (2007). Fundamentals of rock mechanics - Fourth edition. In Tectonophysics. https://doi.org/10.1016/0040-1951(77)90223-2

Jahanian, H., & Sadaghiani, M. H. (2015). Experimental Study on the Shear Strength of Sandy Clay Infilled Regular Rough Rock Joints. Rock Mechanics and Rock Engineering. https://doi.org/10.1007/s00603-014-0643-4

Johnson, P. A., Rouet-Leduc, B., Pyrak-Nolte, L. J., Beroza, G. C., Marone, C. J., Hulbert, C., ... & Reade, W. (2021). Laboratory earthquake forecasting: A machine learning competition. Proceedings of the National Academy of Sciences, 118(5).

Kodikara, J. K., & Johnston, I. W. (1994). Shear behaviour of irregular triangular rock-concrete joints. International Journal of Rock Mechanics and Mining Sciences And. https://doi.org/10.1016/0148-9062(94)90900-8

Kulatilake, P. H. S. W., Shou, G., Huang, T. H., & Morgan, R. M. (1995, October). New peak shear strength criteria for anisotropic rock joints. In International Journal of Rock Mechanics and Mining Sciences & Geomechanics Abstracts (Vol. 32, No. 7, pp. 673-697). Pergamon.

Kutter HK, Otto F (1990) Influence of parallel and cross-joints on shear behaviour of rock discontinuities. In: Barton N, Stephansson O (eds) Rock joints, Loen, Norway, 4–6 June 1990. A.A. Balkema, Rotterdam, pp 243–250

Ladanyi B., Archambault, G. (1970): Simulation of shear behaviour of a jointed rock mass. In: Proc., 1 lth Syrup. on Rock Mechanics: Theory and Practice, AIME, New York, 105-125.

Ladanyi, B. & Archambault, G. (1977). Shear strength and deformability of filled indented joints. Proc. 1st Int. Symp. Geotechnics of Structurally Complex Formations, Capri, 317–326.

Lama, R. D., & RD, L. (1978). Influence of clay fillings on shear behaviour of joints.

Leichnitz, W. (1985). Mechanical properties of rock joints. International Journal of Rock Mechanics and Mining Sciences And. https://doi.org/10.1016/0148-9062(85)92063-7

Li, W. (2011). *Seismic Wave Propagation in Fractured Anisotropic Carbonate Rock: Experiments and Theory.* Ph.D. Thesis, Department of Physics, Purdue Unversity. ProQuest.

Li, 2011, "Seismic Wave Propagation in Fractured Anisotropic Carbonate Rock: Experiments and Theory", Ph.D. August 2011, Purdue University, West Lafayette, Indiana, 199 pages;

Li, W. Petrovitch, C. and L. J. Pyrak-Nolte, The effect of fabric-controlled layering on compressional and shear wave propagation in carbonate rock, International Journal of the Japanese Commmittee for Rock Mechanics, V. 4, no. 2, Nov 2009, pp79-85 (2009).

Modiriasari, A., Bobet, A., & Pyrak-Nolte, L. J. (2020). Seismic Wave Conversion Caused by Shear Crack Initiation and Growth. Rock Mechanics and Rock Engineering. https://doi.org/10.1007/s00603-020-02079-2

Modiriasari, A., Pyrak-Nolte, L. J., & Bobet, A. (2018). Emergent Wave Conversion as a Precursor to Shear Crack Initiation. Geophysical Research Letters. https://doi.org/10.1029/2018GL078622.

Modiriasari, A., Bobet, A., & Pyrak-Nolte, L. J. (2017). Active seismic monitoring of crack initiation, propagation, and coalescence in rock. *Rock Mechanics and Rock Engineering*, *50*(9), 2311-2325.

Mutlu, O. (2005). *Progressive failure along frictional surfaces*. Ph.D. Thesis, Lyles School of Civil Engineering, Purdue University, Proquest.

Mutlu, O., & Bobet, A. (2006). Slip propagation along frictional discontinuities. International Journal of Rock Mechanics and Mining Sciences. https://doi.org/10.1016/j.ijrmms.2005.11.012

Nakagawa, S., Nihei, K. T., & Myer, L. R. (2000). Shear-induced conversion of seismic waves across single fractures. International Journal of Rock Mechanics and Mining Sciences. https://doi.org/10.1016/s1365-1609(99)00101-x

Nolte, D. D., Pyrak-Nolte, L. J., Beachy, J., & Ziegler, C. (2000). Transition from the displacement discontinuity limit to the resonant scattering regime for fracture interface waves. International journal of rock mechanics and mining sciences, 37(1-2), 219-230.

Pan, B., Qian, K., Xie, H., & Asundi, A. (2009). Two-dimensional digital image correlation for in-plane displacement and strain measurement: A review. Measurement Science and Technology. https://doi.org/10.1088/0957-0233/20/6/062001

Papaliangas T., Lumsden A. C., Hencher S. R. and Mano- lopoulou S. Shear strength of modelled filled rock joints. Rock Joints; Proc. Int. Symp. on Rock Joints, Loen, Norway (N. Barton and O. Stephansson, Eds), pp. 275-282. Balkema, Rotterdam (1990).

Papaliangas, T., Hencher, S. R., Lumsden, A. C., & Manolopoulou, S. (1993, April). The effect of frictional fill thickness on the shear strength of rock discontinuities. In International Journal of Rock Mechanics and Mining Sciences & Geomechanics Abstracts (Vol. 30, No. 2, pp. 81-91). Pergamon.

Patton, F. D. (1966). Multiple modes of shear failure in rock. 1st ISRM Congress 1966.

Phien-Wej, N., Shrestha, U. B., & Rantucci, G. (1991). Effect of infill thickness on shear behavior of rock joints. In International symposium on rock joints (pp. 289-294).

Pyrak-Nolte, L. J, de Pater, C. J. and J. Jocker , Seismic Monitoring of Fracture Formation, 2005. Paper Number 05- 869, Alaska Rocks 2005, The 40th U.S. Symposium on Rock Mechanics (USRMS): Rock Mechanics for Energy, Mineral and Infrastructure Development in the Northern Regions, held in Anchorage, Alaska, June 25-29, 2005.

Pyrak-Nolte, L. J., Myer, L. R., & Cook, N. G. W. (1990). Transmission of seismic waves across single natural fractures. Journal of Geophysical Research. https://doi.org/10.1029/JB095iB06p08617

Pyrak-Nolte, Laura J. (2018). Fracture specific stiffness. In Science of Carbon Storage in Deep Saline Formations: Process Coupling across Time and Spatial Scales. https://doi.org/10.1016/B978-0-12-812752-0.00014-9

Rouet-Leduc, B., Hulbert, C., Lubbers, N., Barros, K., Humphreys, C. J., & Johnson, P. A. (2017). Machine learning predicts laboratory earthquakes. *Geophysical Research Letters*, *44*(18), 9276-9282.

Saeb, S., & Amadei, B. (1992). Modelling rock joints under shear and normal loading. International Journal of Rock Mechanics and Mining Sciences And. https://doi.org/10.1016/0148-9062(92)93660-C

Savic. M. 1995. Ultrasonic Scattering from a Hydraulic Fracture: Theory, Computation and Experiment. Ph.D. Thesis. Delft University of Technology

Scholz, C. H., Sykes, L. R., & Aggarwal, Y. P. (1973). Earthquake prediction: A physical basis. Science. https://doi.org/10.1126/science.181.4102.803

Schoenberg, M. (1980). Elastic wave behavior across linear slip interfaces. Journal of the Acoustical Society of America. https://doi.org/10.1121/1.385077

Schreier, H., Orteu, J. J., & Sutton, M. A. (2009). Image correlation for shape, motion and deformation measurements: Basic concepts, theory and applications. In Image Correlation for Shape, Motion and Deformation Measurements: Basic Concepts, Theory and Applications. https://doi.org/10.1007/978-0-387-78747-3

Scuderi, M. M., Marone, C., Tinti, E., Di Stefano, G., & Collettini, C. (2016). Precursory changes in seismic velocity for the spectrum of earthquake failure modes. Nature Geoscience. https://doi.org/10.1038/ngeo2775

Singh, H. K., & Basu, A. (2016). Shear behaviors of 'real' natural un-matching joints of granite with equivalent joint roughness coefficients. Engineering Geology. https://doi.org/10.1016/j.enggeo.2016.07.004

Singh, H. K., & Basu, A. (2018). A comparison between the shear behavior of 'real'natural rock discontinuities and their replicas. Rock Mechanics and Rock Engineering, 51(1), 329-340.

Skinas, C. A., Bandis, S. C., & Demiris, C. A. (1990). Experimental investigations and modelling of rock joint behaviour under constant stiffness. In International symposium on rock joints (pp. 301-308).

Sutton, M. A., Yan, J. H., Tiwari, V., Schreier, H. W., & Orteu, J. J. (2009). The effect of out-of-plane motion on 2D and 3D digital image correlation measurements. Optics and Lasers in Engineering. https://doi.org/10.1016/j.optlaseng.2008.05.005

Swan, G. (1983). Determination of stiffness and other joint properties from roughness measurements. Rock Mechanics and Rock Engineering, 16(1), 19-38.

Swan, G., & Zongqi, S. (1985). Prediction of shear behaviour of joints using profiles. Rock Mechanics and Rock Engineering, 18(3), 183-212.

Tang, Z. C., & Wong, L. N. Y. (2016). New criterion for evaluating the peak shear strength of rock joints under different contact states. Rock Mechanics and Rock Engineering, 49(4), 1191-1199.

Thirukumaran, S., & Indraratna, B. (2016). A review of shear strength models for rock joints subjected to constant normal stiffness. *Journal of Rock Mechanics and Geotechnical Engineering*, *8*(3), 405-414.

Whitcomb, J. H., Garmany, J. D., & Anderson, D. L. (1973). Earthquake prediction: Variation of seismic velocities before the san francisco earthquake. Science. https://doi.org/10.1126/science.180.4086.632

Worthington et al., 2007 -- Worthington, M. The compliance of macrofractures. The Leading Edge. 1118-1122. September. 2007)

Xia, C. C., Tang, Z. C., Xiao, W. M., & Song, Y. L. (2014). New peak shear strength criterion of rock joints based on quantified surface description. Rock Mechanics and Rock Engineering, 47(2), 387-400.

Xu Shao Xie, Wang Biquan, & Zhang Guangyue. (1981). The foreshock sequence of Haicheng earthquake and earthquake swarm - the use of foreshock sequences in earthquake prediction. Acta Seismologica Sinica.

Zhao, J. (1997). Joint surface matching and shear strength. Part A: joint matching coefficient (JMC). International Journal of Rock Mechanics and Mining Sciences & Geomechanics Abstracts. https://doi.org/10.1016/S0148-9062(96)00062-9.

APPENDIX A. SUPPORTING EXPERIMENTS FOR CHAPTER 3

Supporting experiments for the data presented in chapter 3 are included in Appendix A. Seismic data from repeatability experiments for samples with HCS=3.2 mm at 1, and 2 MPa are presented in Figures A.1 and A.2 for (a) top, (b) middle, and (c) bottom transducers, respectively. Similar to the plots presented in the thesis, the figures show the normalized transmitted amplitudes recorded by transducers as a function of shear displacement or time, and the secondary y-axis plots the shear stress.
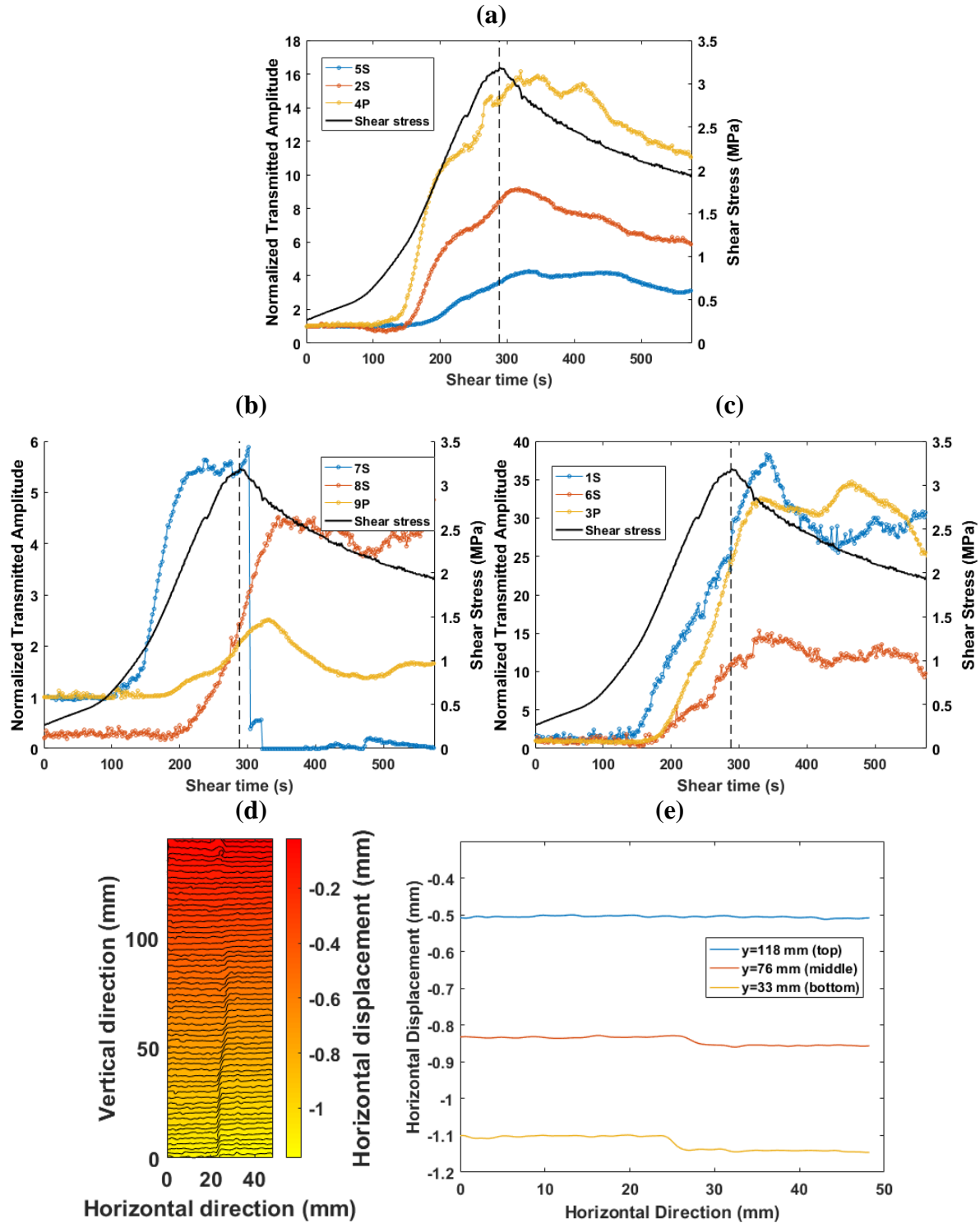
Figure A.1. Normalized transmitted amplitude of a specimen with HCS=3.2 mm, for (a) top, (b) middle, and (c) bottom transducers; the secondary y-axis plots shear stress as a function of shearing time; at normal stress of 1 MPa; horizontal (d) contour and (e) cross-sections from the top, middle, and bottom portions of the specimen
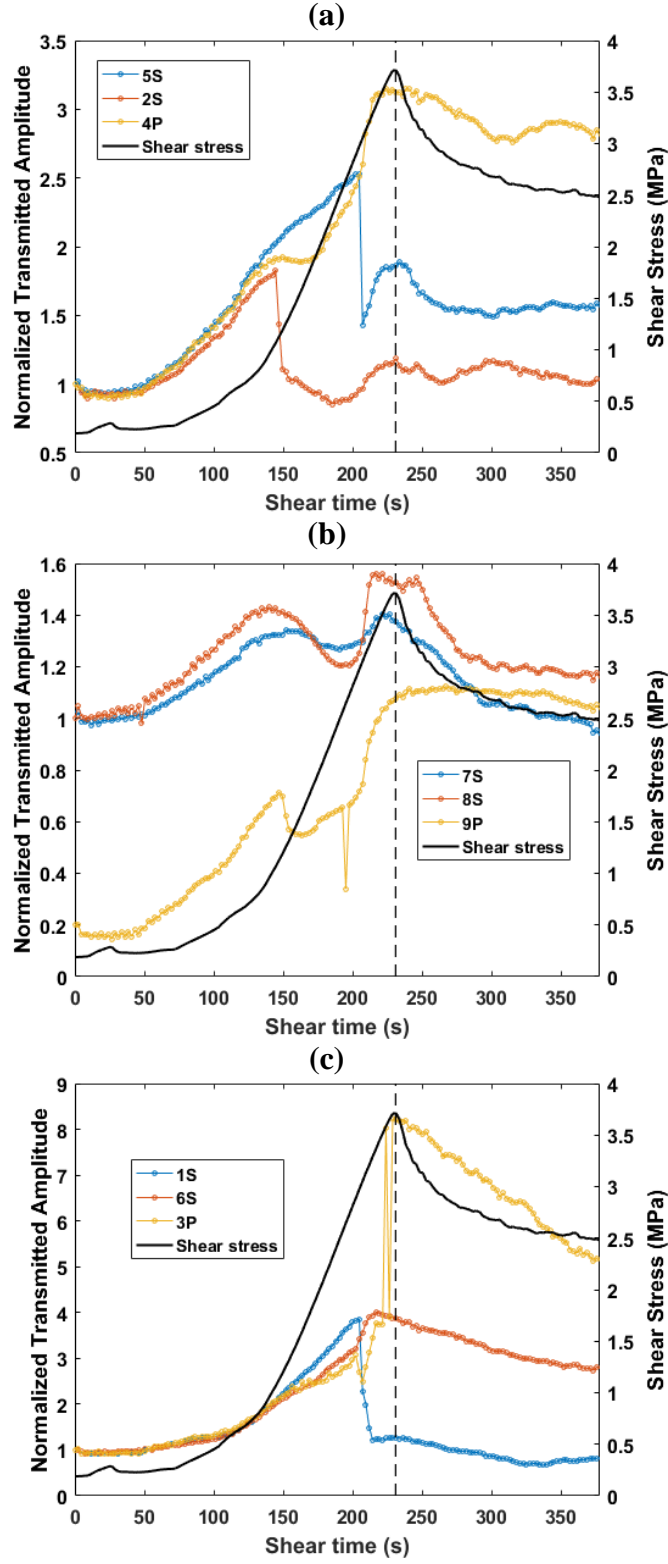
Figure A.2. Normalized transmitted amplitude of a specimen with HCS=3.2 mm, for (a) top, (b) middle, and (c) bottom transducers; the secondary y-axis plots shear stress as a function of shearing time; at normal stress of 2 MPa

APPENDIX B. SUPPORTING EXPERIMENTS FOR CHAPTER 4

Data corresponding to all transducers for the experiment presented in Chapter 4 (Figures B.1, B.2, and B.2, for top, middle, and bottom transducers, respectively). The data for the repeatability experiment are presented in Figures B.4, B.5, and B.6 for top, middle, and bottom transducers, respectively.
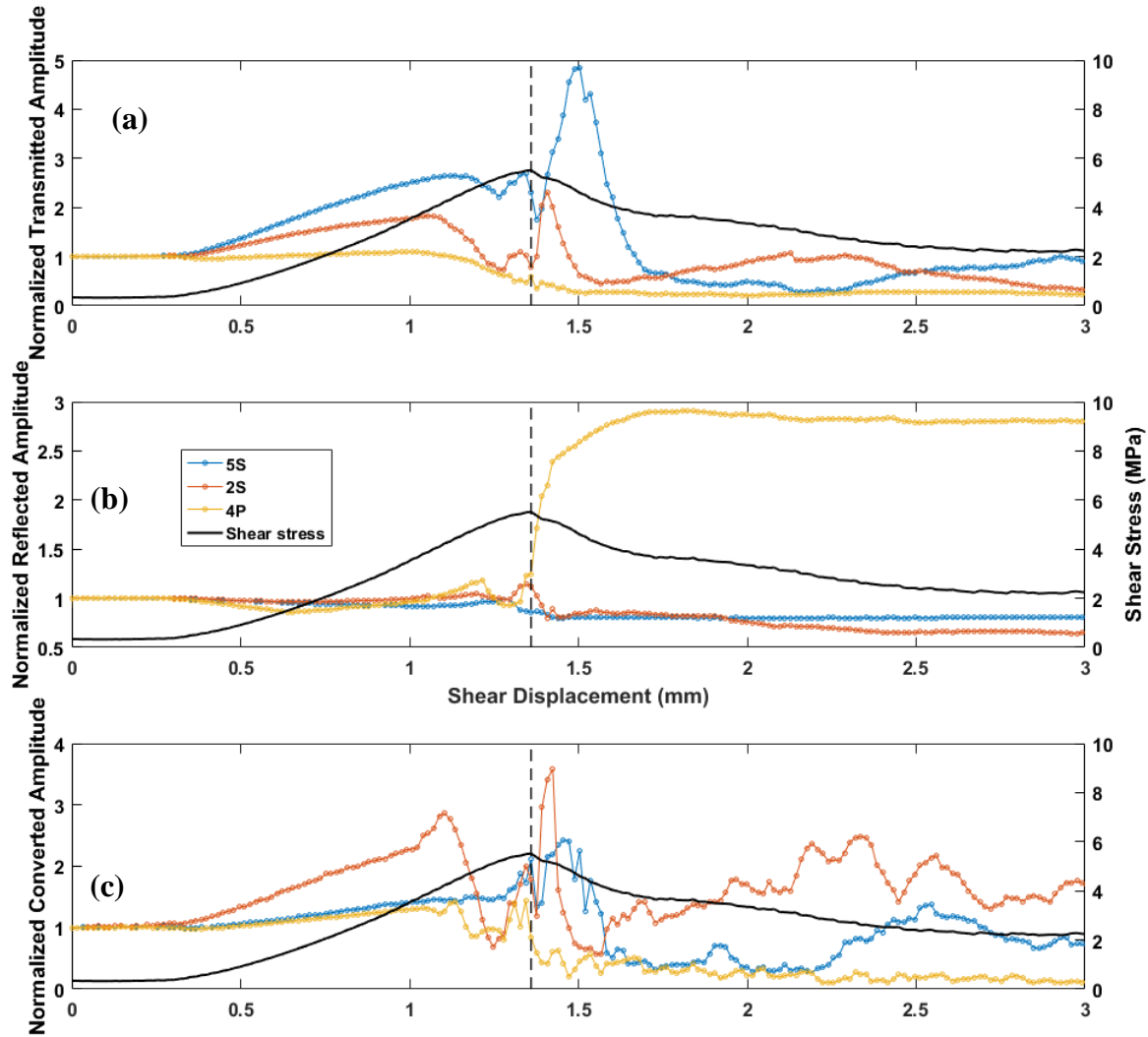
Figure B.1. Normalized (a) transmitted, (b) reflected, and (c) converted amplitude as a function of shear displacement for top transducers; the secondary y-axis plots the shear stress; at a normal stress of 2 MPa
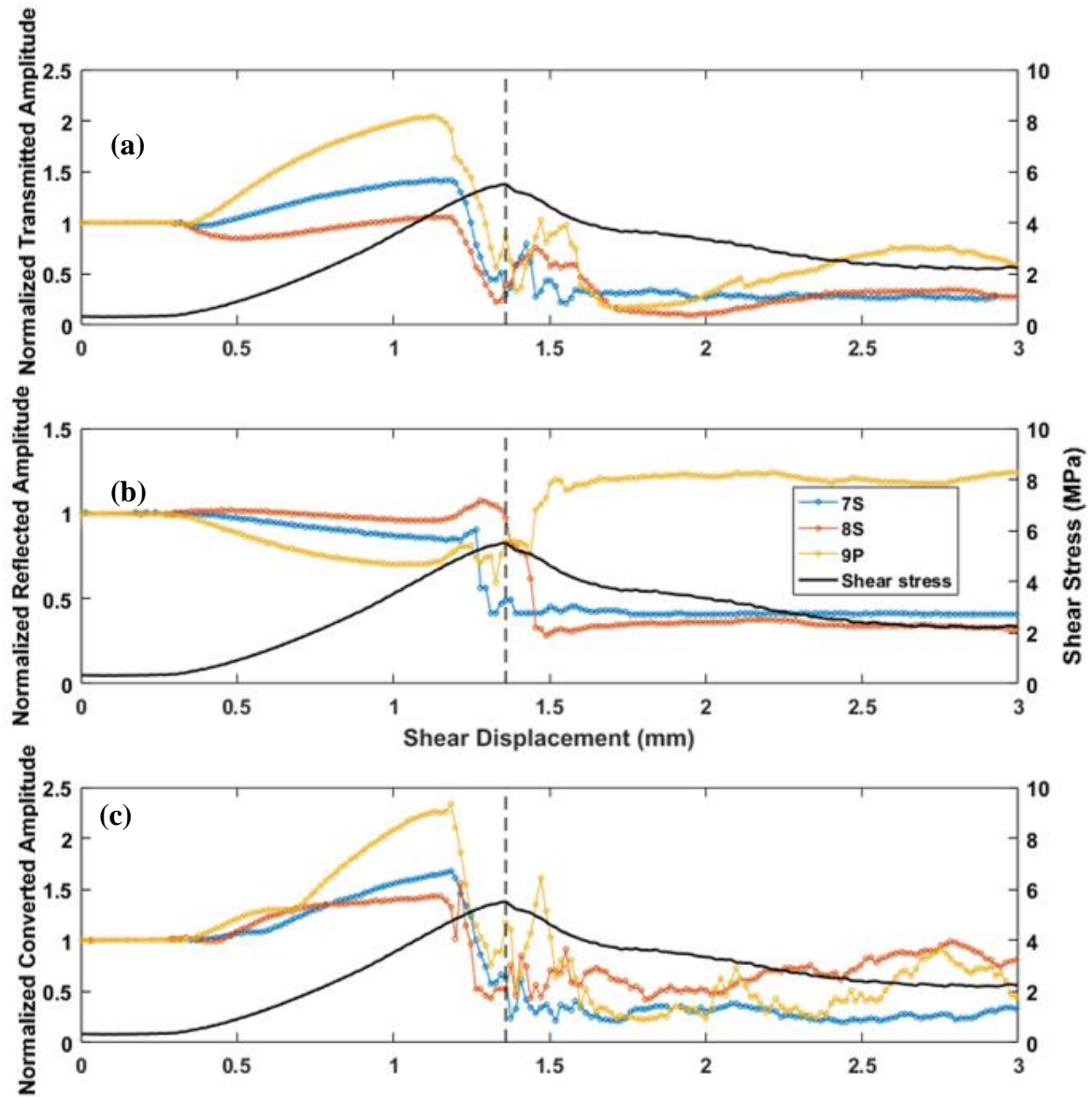
Figure B.2. Normalized (a) transmitted, (b) reflected, and (c) converted amplitude as a function of shear displacement for middle transducers; the secondary y-axis plots the shear stress; at a normal stress of 2 MPa
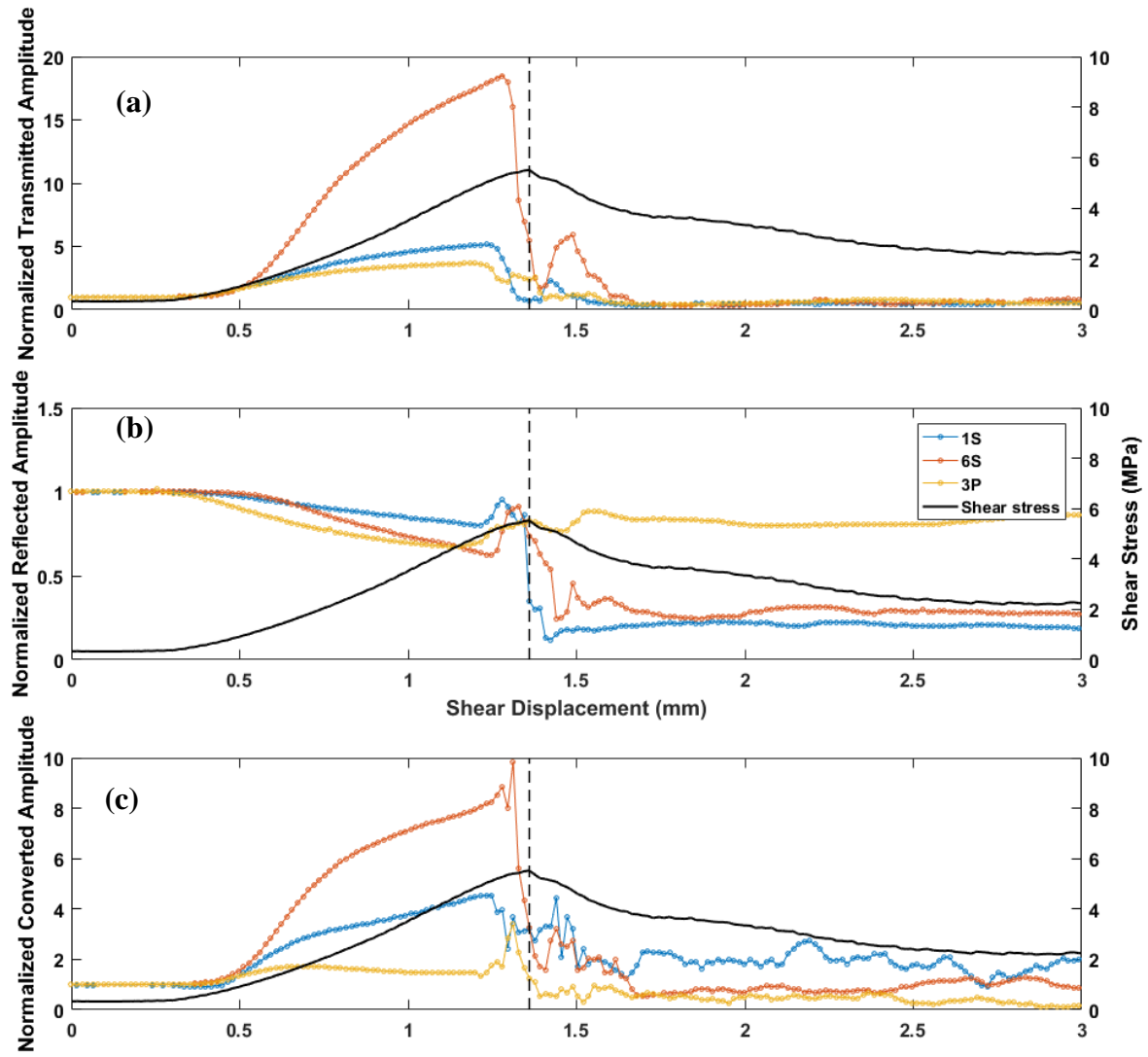
Figure B.3 Normalized (a) transmitted, (b) reflected, and (c) converted amplitude as a function of shear displacement for bottom transducers; the secondary y-axis plots the shear stress; at a normal stress of 2 MPa
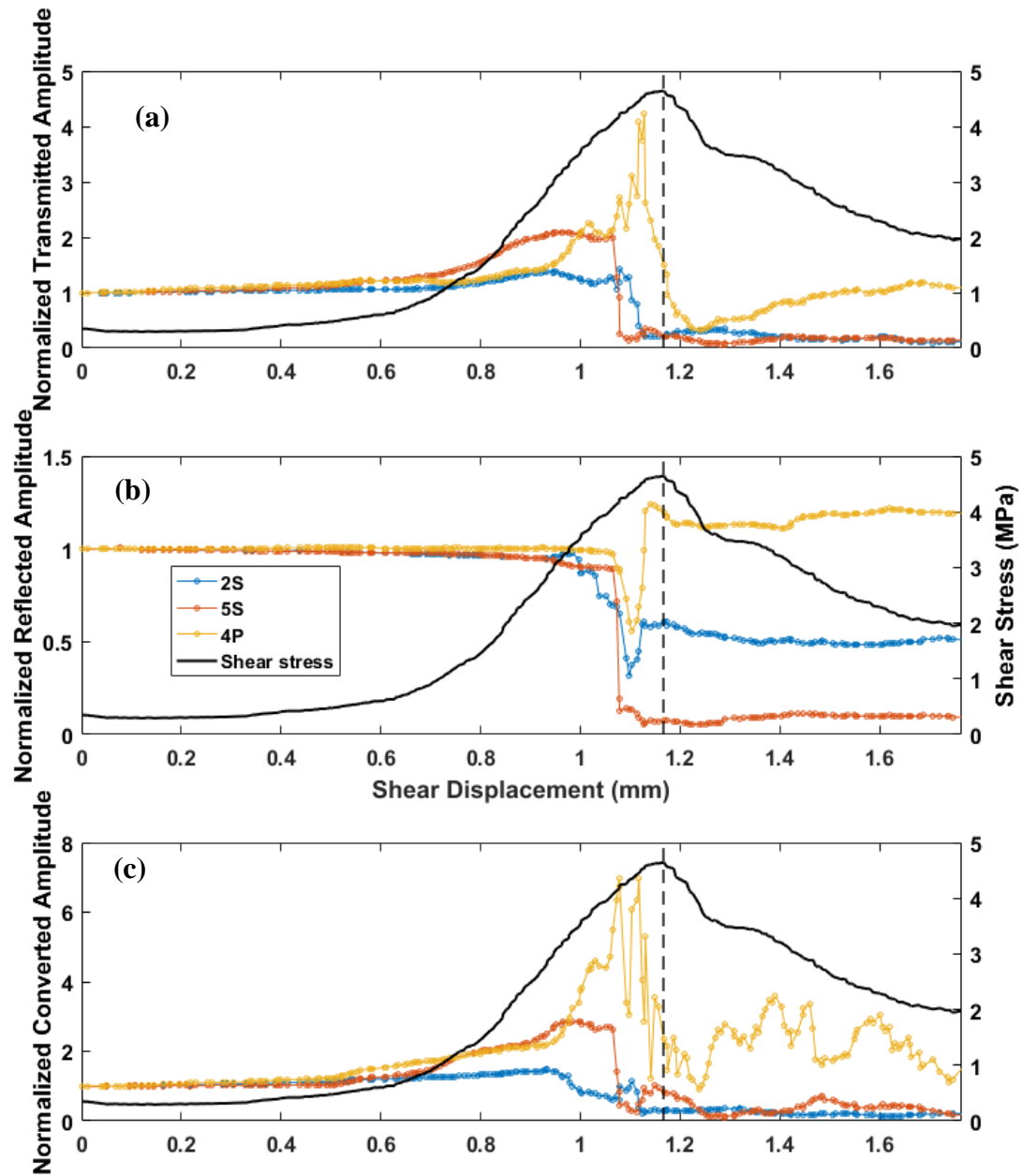
Figure B.4. Normalized (a) transmitted, (b) reflected, and (c) converted amplitude as a function of shear displacement for top transducers; the secondary y-axis plots the shear stress; at a normal stress of 2 MPa
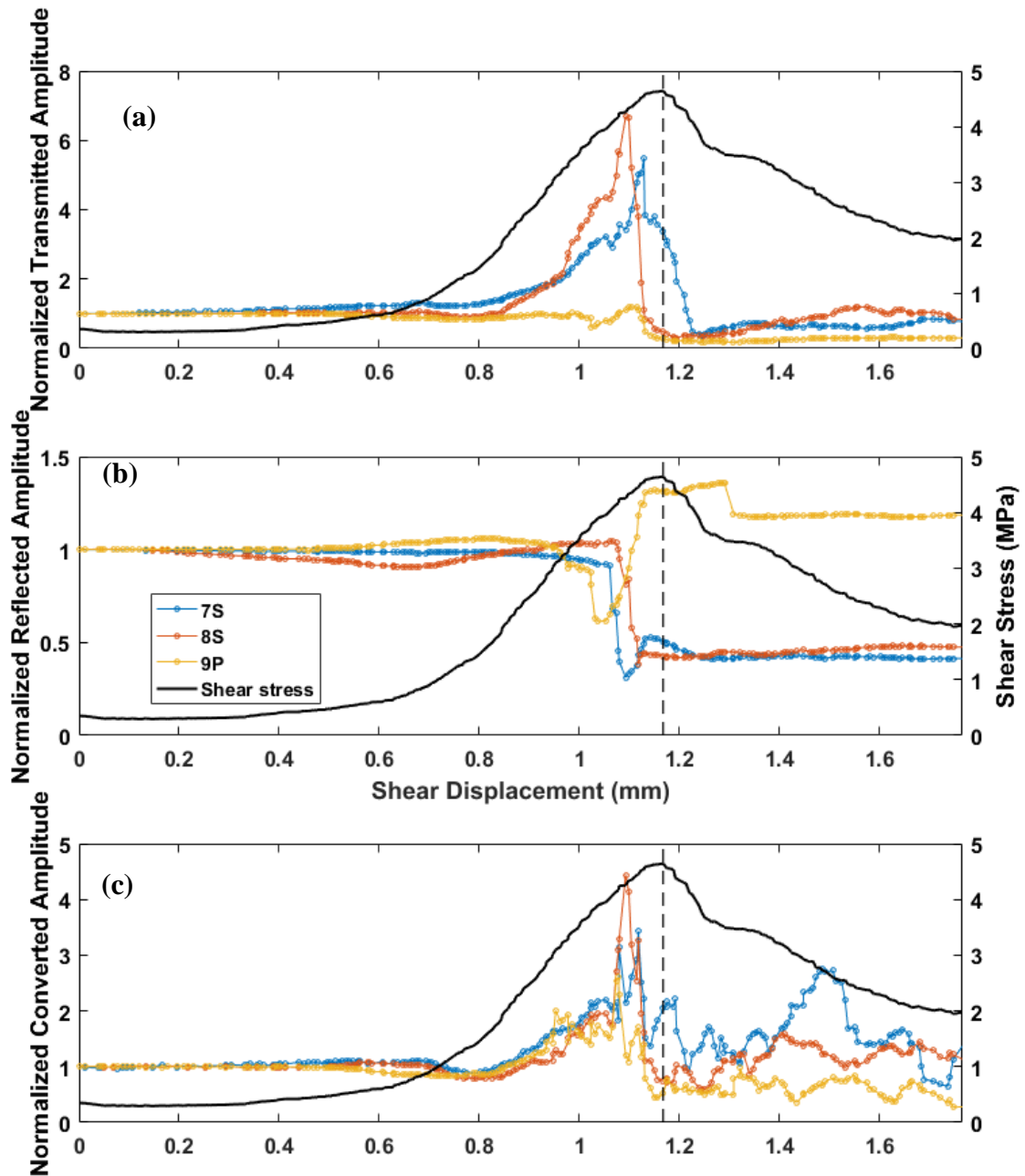
Figure B.5. Normalized (a) transmitted, (b) reflected, and (c) converted amplitude as a function of shear displacement for middle transducers; the secondary y-axis plots the shear stress; at a normal stress of 2 MPa

143
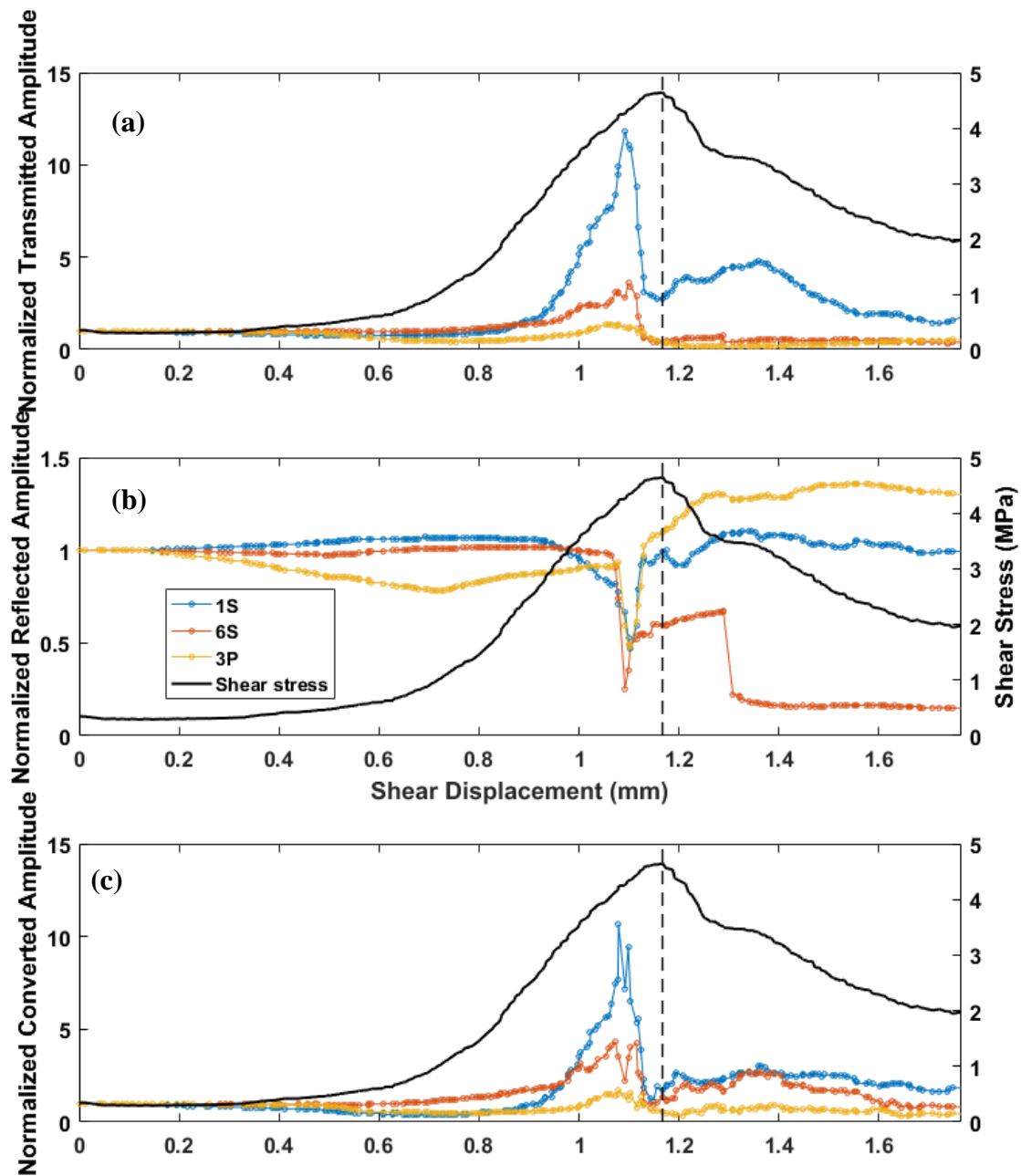
Figure B.6. Normalized (a) transmitted, (b) reflected, and (c) converted amplitude as a function of shear displacement for bottom transducers; the secondary y-axis plots the shear stress; at a normal stress of 2 MPa

APPENDIX C. SUPPORTING EXPERIMENTS FOR CHAPTER 5

The repeatability experiments conducted on samples prepared with water and oil-based release agent (G_W and G_O specimens) at 2 and 5 MPa are presented in this section.

(a)
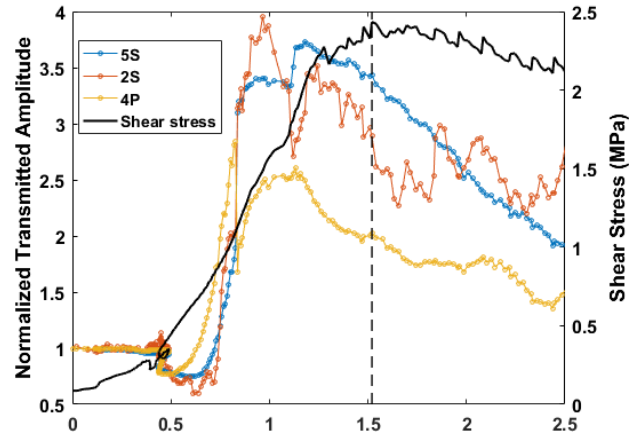
(b)
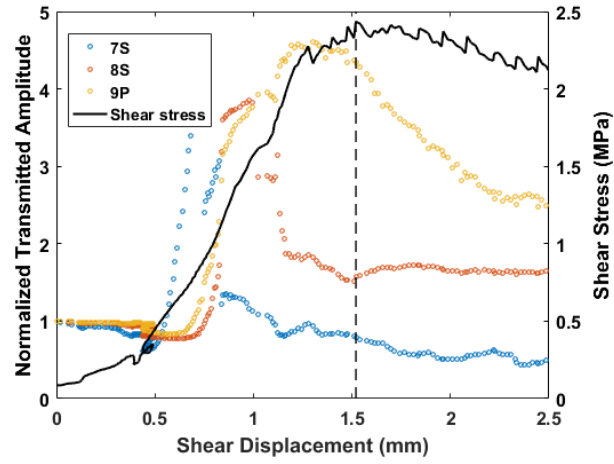
(c)
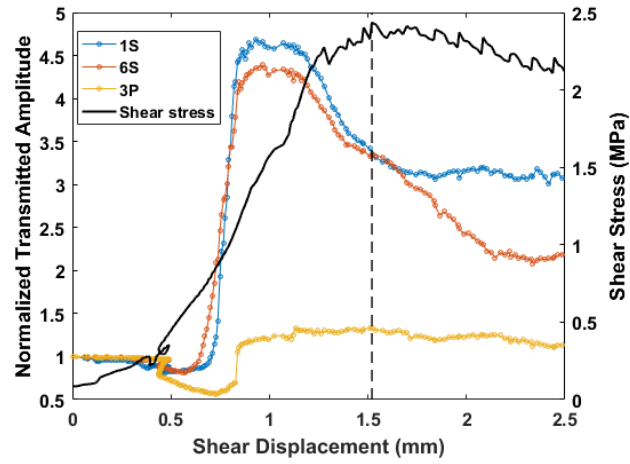
Figure C.1. Normalized transmitted amplitude for (a) top, (b) middle, and (c) bottom transducers for a G_W specimen sheared at 2 MPa normal stress

146
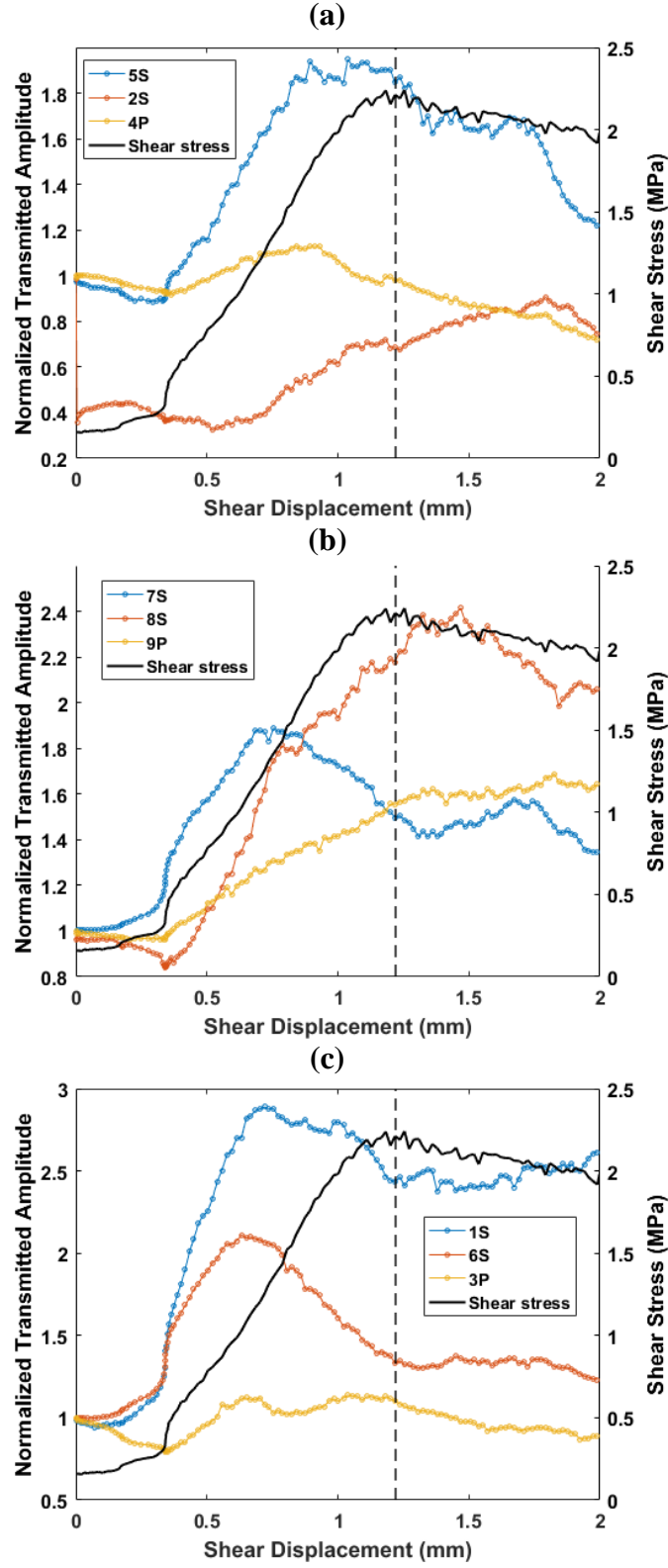
Figure C.2. Normalized transmitted amplitude for (a) top, (b) middle, and (c) bottom transducers for a G_W specimen sheared at 2 MPa normal stress
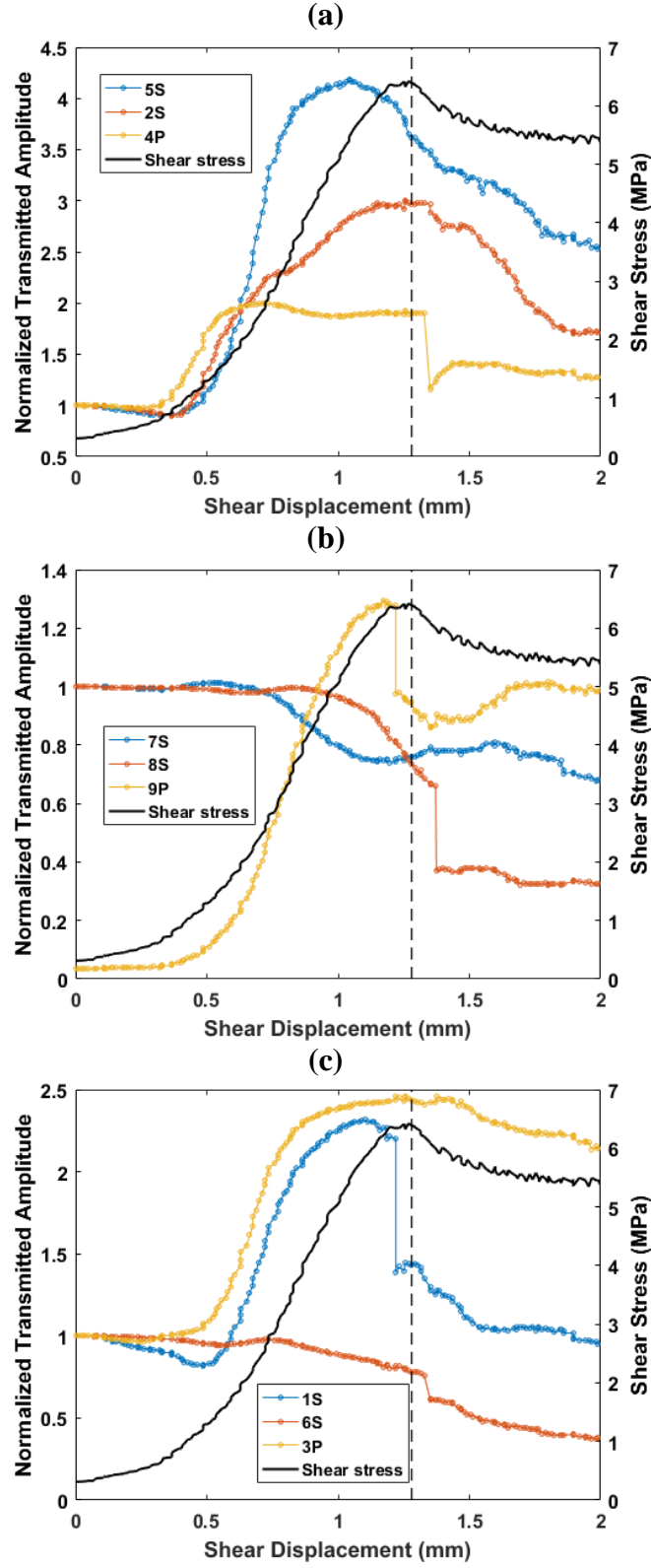
Figure C.3. Normalized transmitted amplitude for (a) top, (b) middle, and (c) bottom transducers for a G_W specimen sheared at 5 MPa normal stress
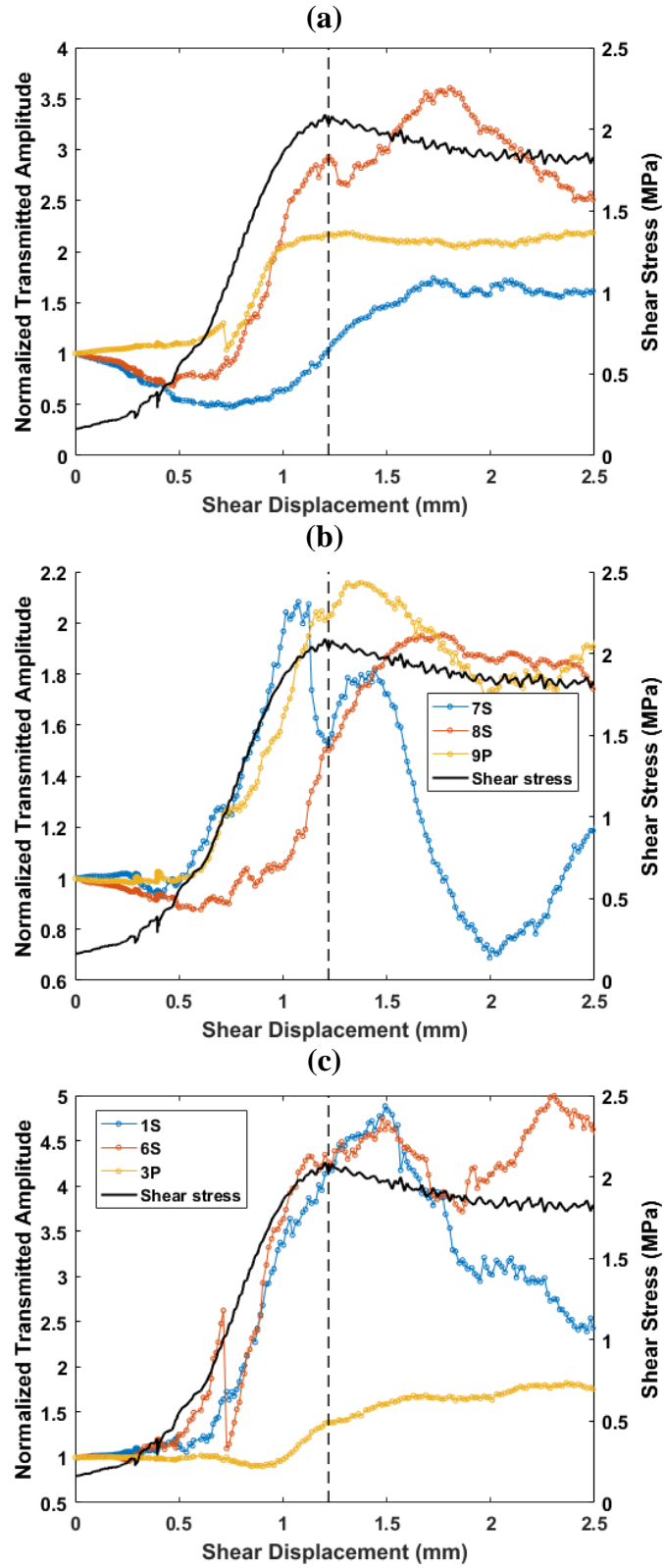
Figure C.4. Normalized transmitted amplitude for (a) top, (b) middle, and (c) bottom transducers for a G_O specimen sheared at 2 MPa normal stress
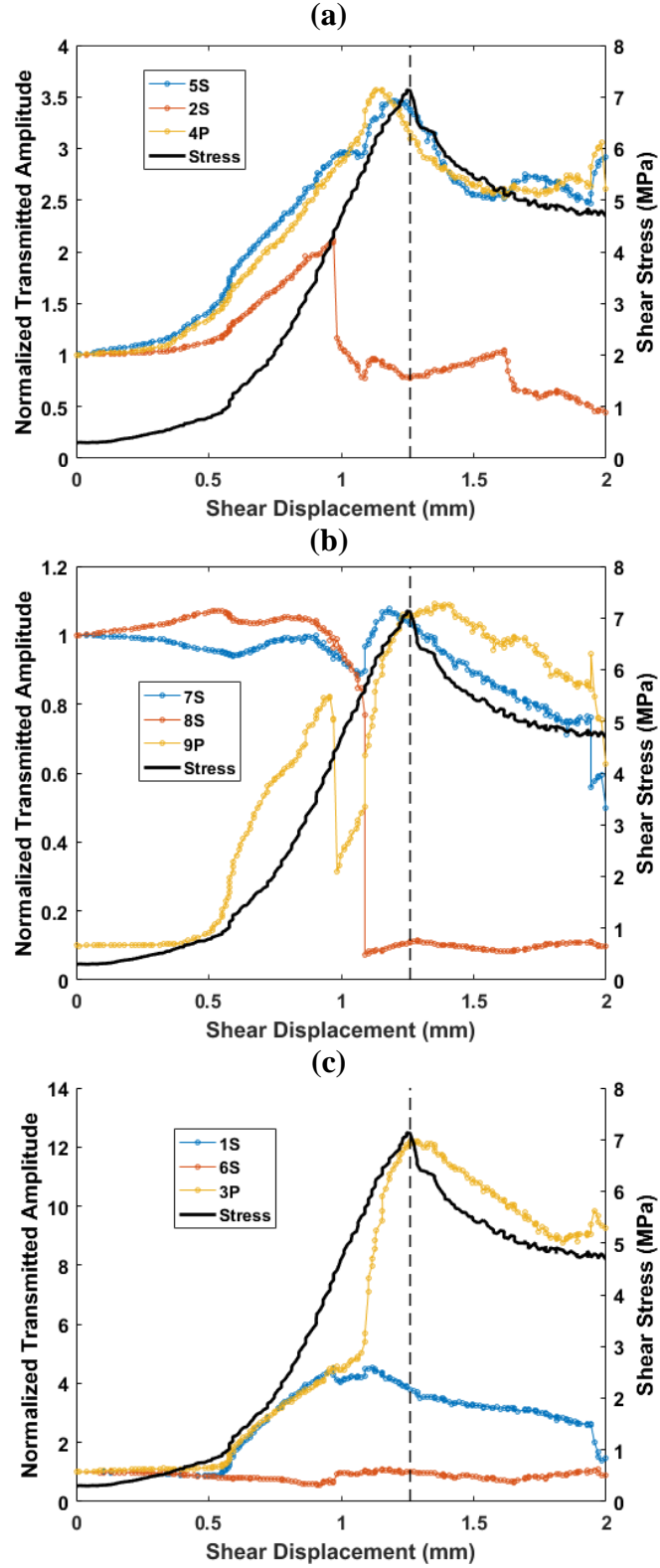
Figure C.5. Normalized transmitted amplitude for (a) top, (b) middle, and (c) bottom transducers for a G_O specimen sheared at 5 MPa normal stress
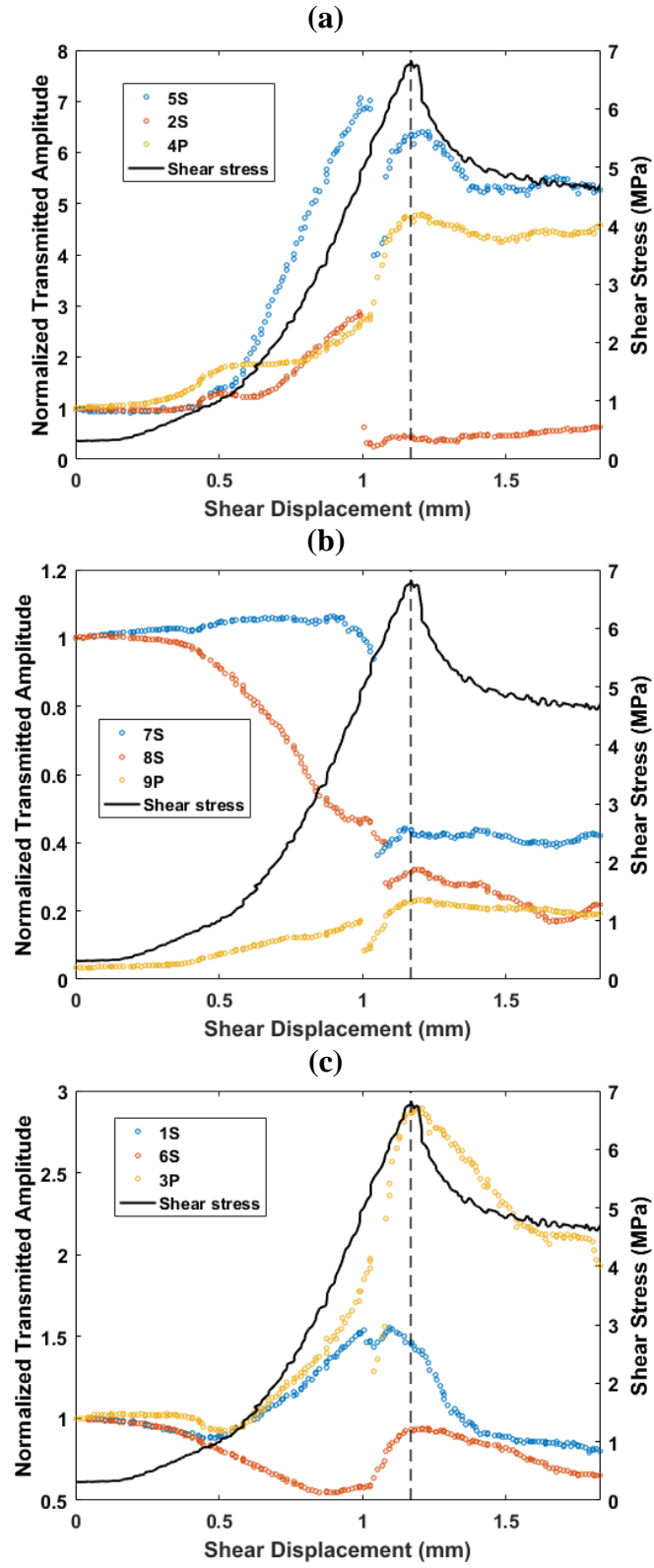
Figure C.6. Normalized transmitted amplitude for (a) top, (b) middle, and (c) bottom transducers for a G_O specimen sheared at 5 MPa normal stress

APPENDIX D. SUPPLEMENTARY MATERIAL FOR CHAPTER 5

Images of "failed" to separate G_O specimens due to insufficient amount of release agent applied are presented in Figure D.1.
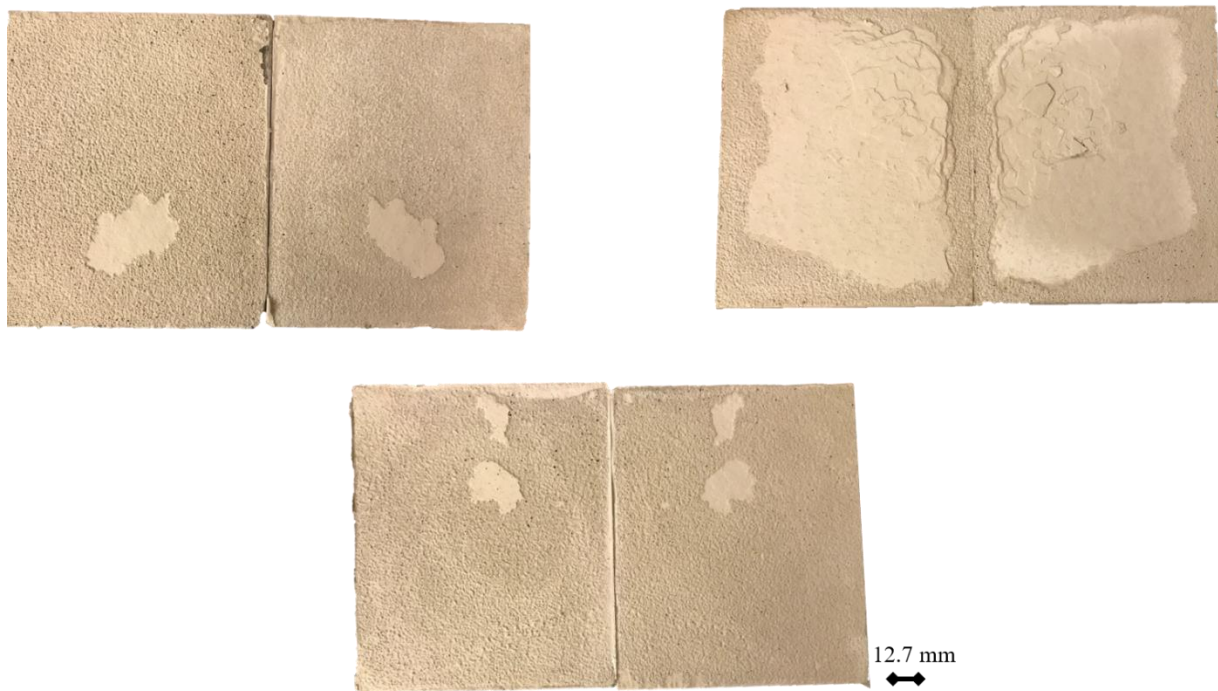
Figure D.1. "Failed to separate" G_O specimens due to insufficient amount of release agent

APPENDIX E. SEM AND EDX COMPLETE DATASET

SEM scans for a surface prepared with oil and water-based release agents are included in this Appendix (Figure E.1-E.8). EDX data for all the spectra obtained are also included in this appendix (Figure E.9).
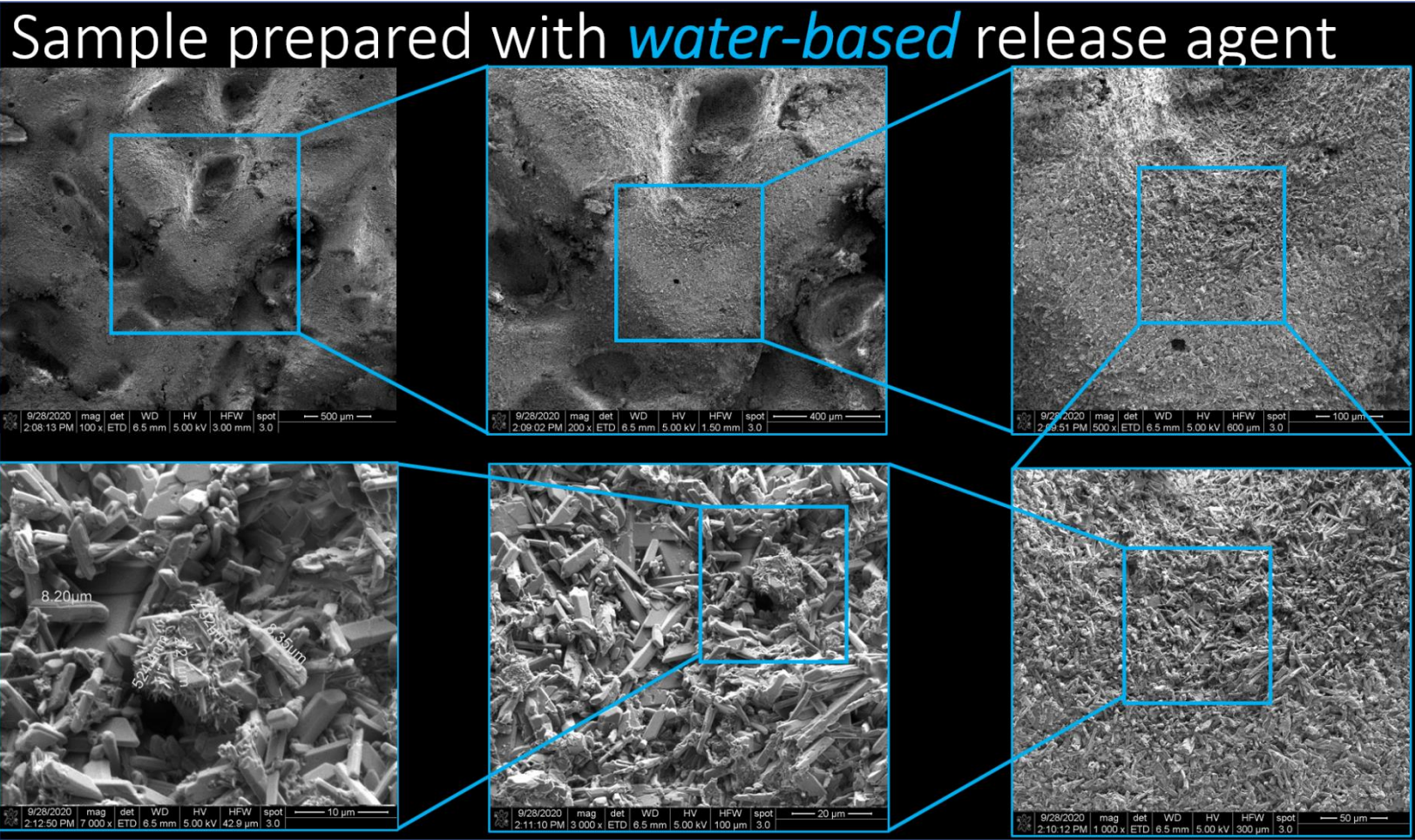
Figure E.1. SEM scans on a rough surface (grit 36 roughness) prepared with the water-based release agent
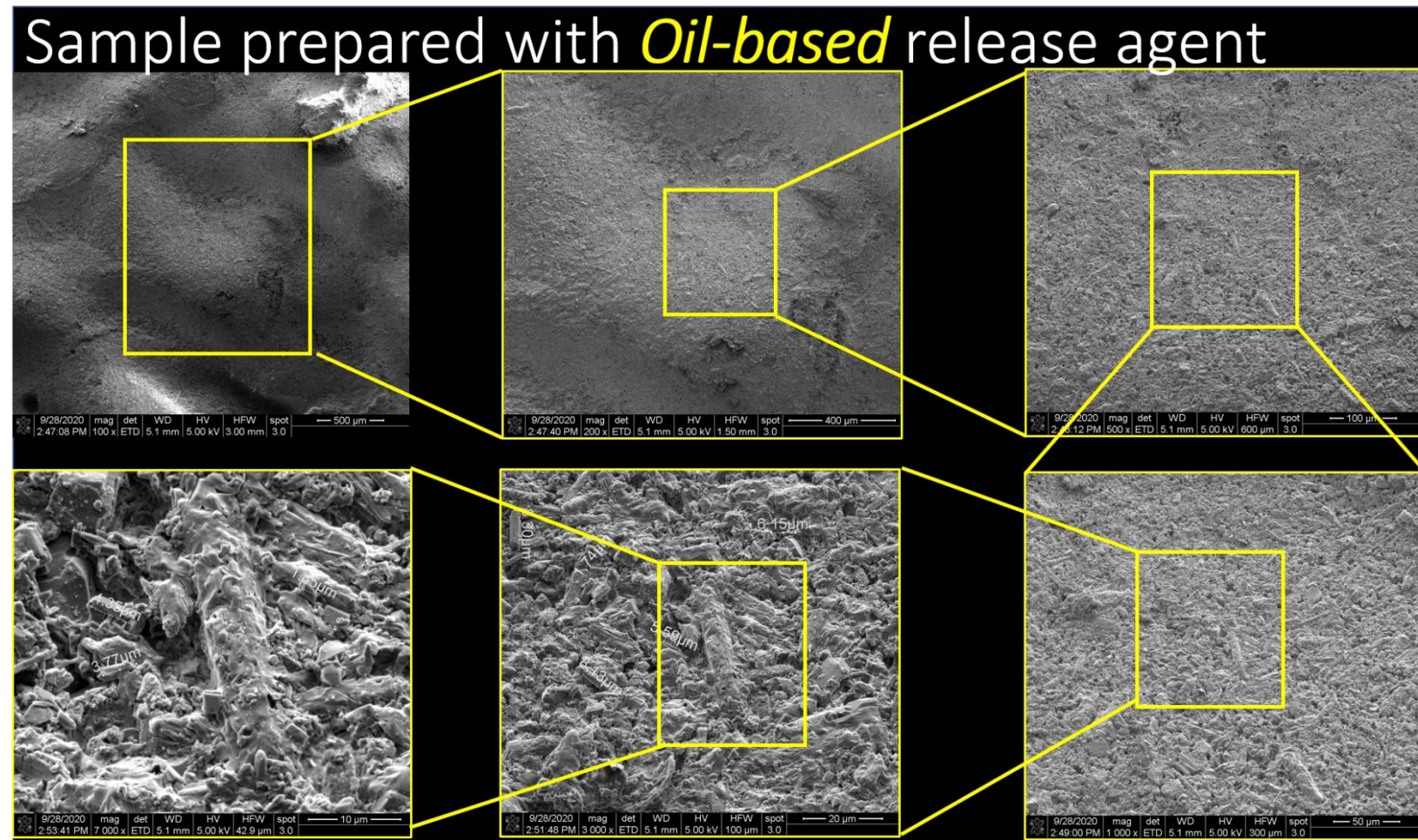
Figure E.2. SEM scans on a rough surface (grit 36 roughness) surface prepared with the oil-based release agent
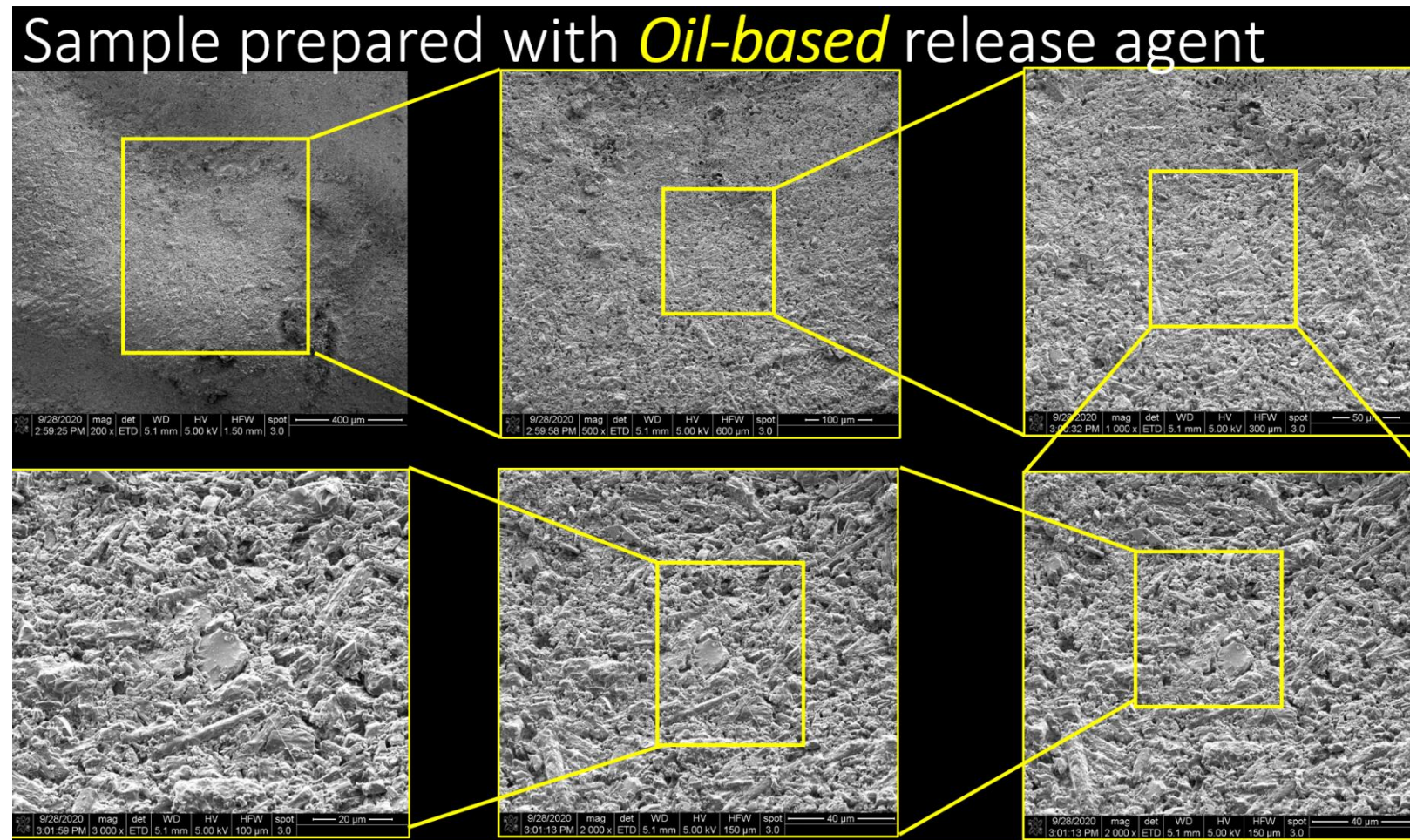
Figure E.3. SEM scans on a rough surface (grit 36 roughness) prepared with the oil-based release agent
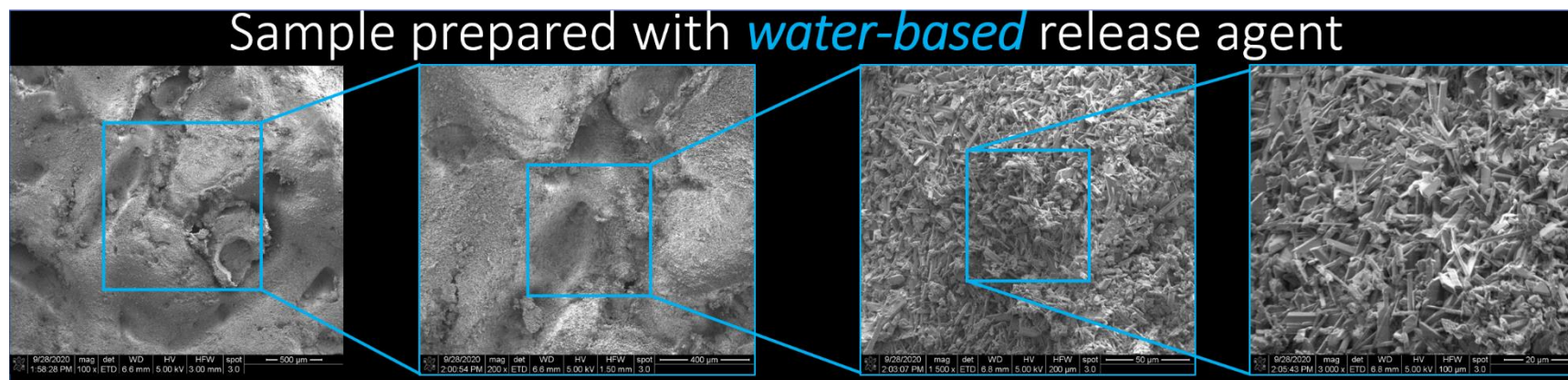
Figure E.4. SEM scans on a rough surface (grit 36 roughness) prepared with the water-based release agent
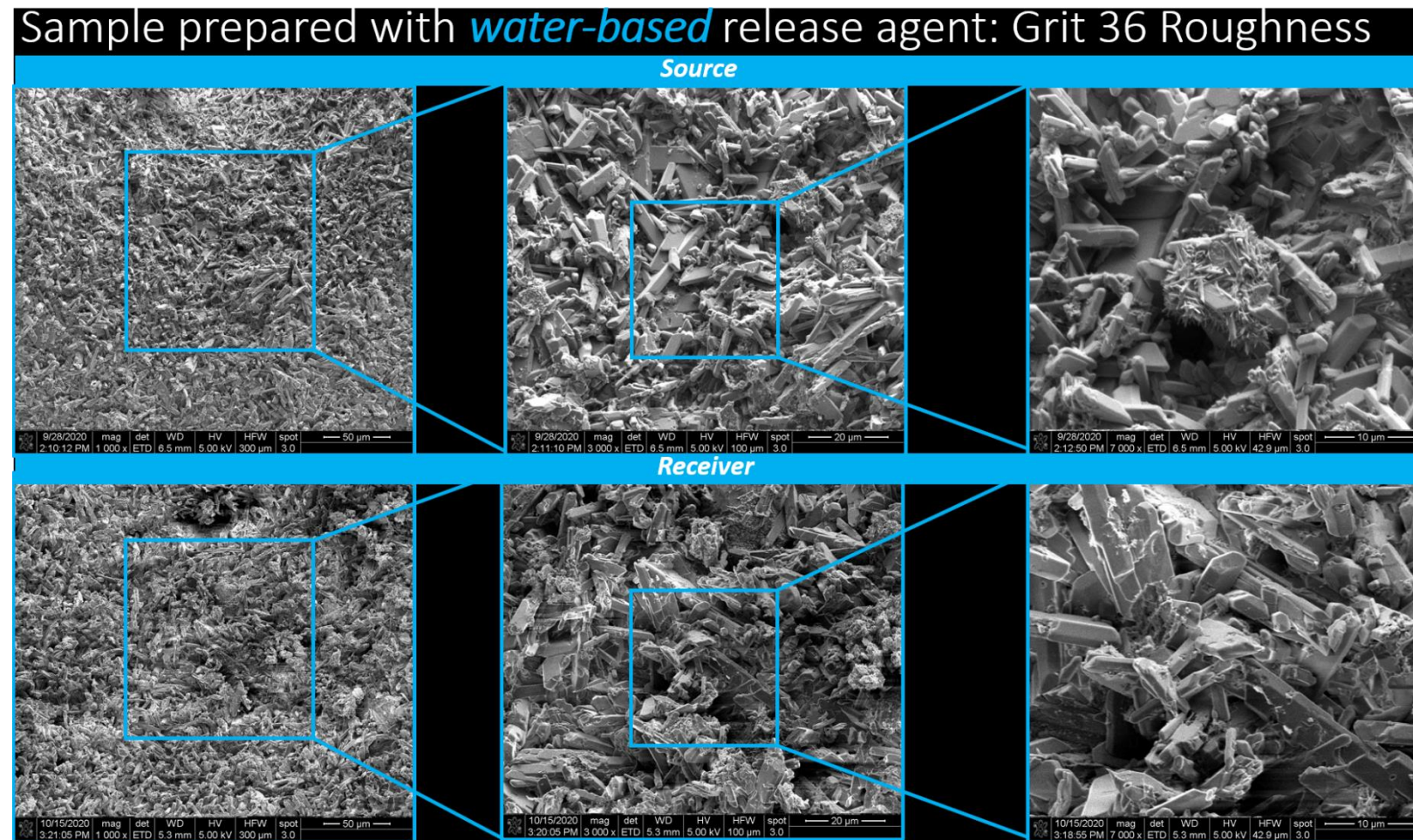
Figure E.5. SEM scans on a rough surface (grit 36 roughness) prepared with the water-based release agent
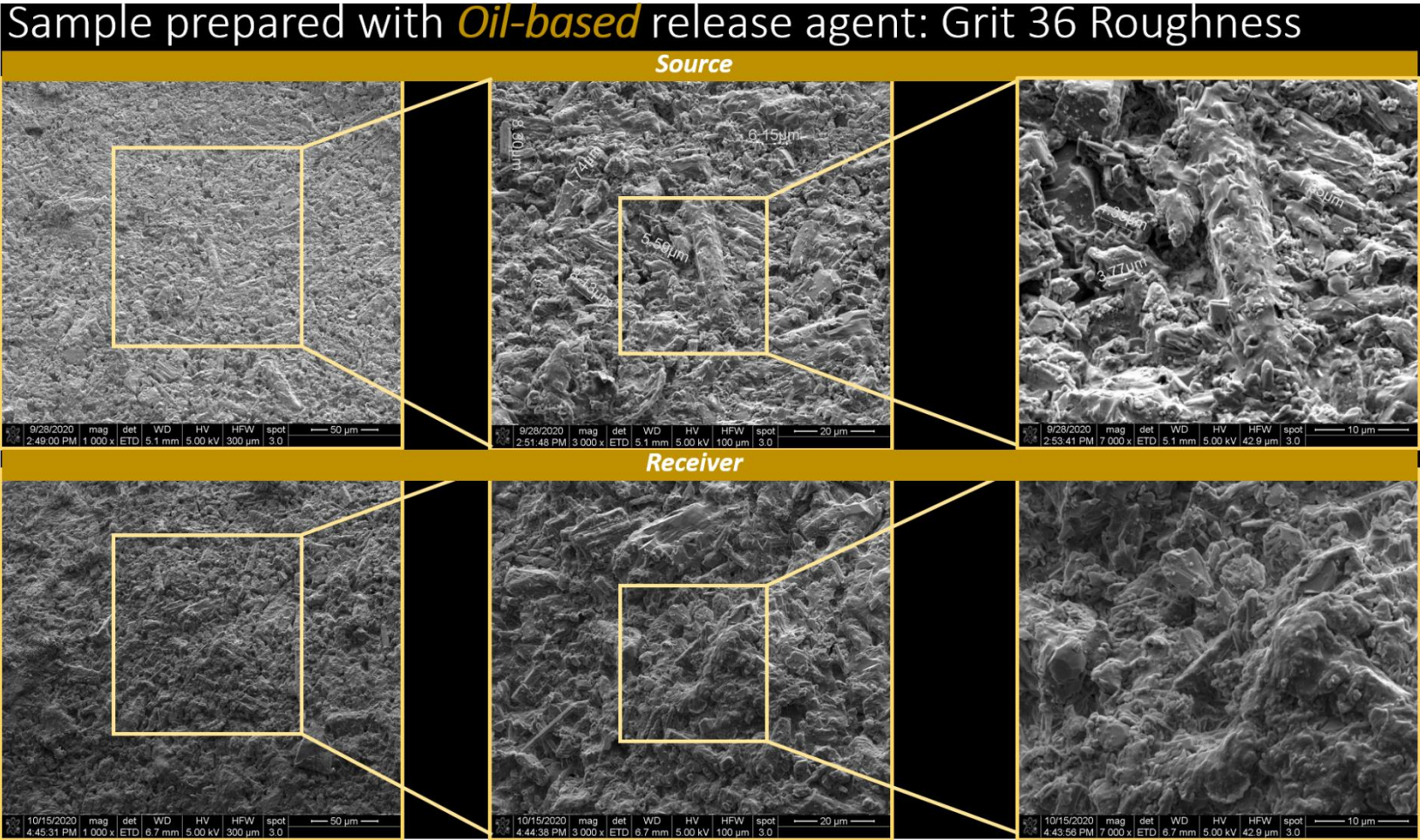
Figure E.6. SEM scans on a rough surface (grit 36 roughness) prepared with the oil-based release agent
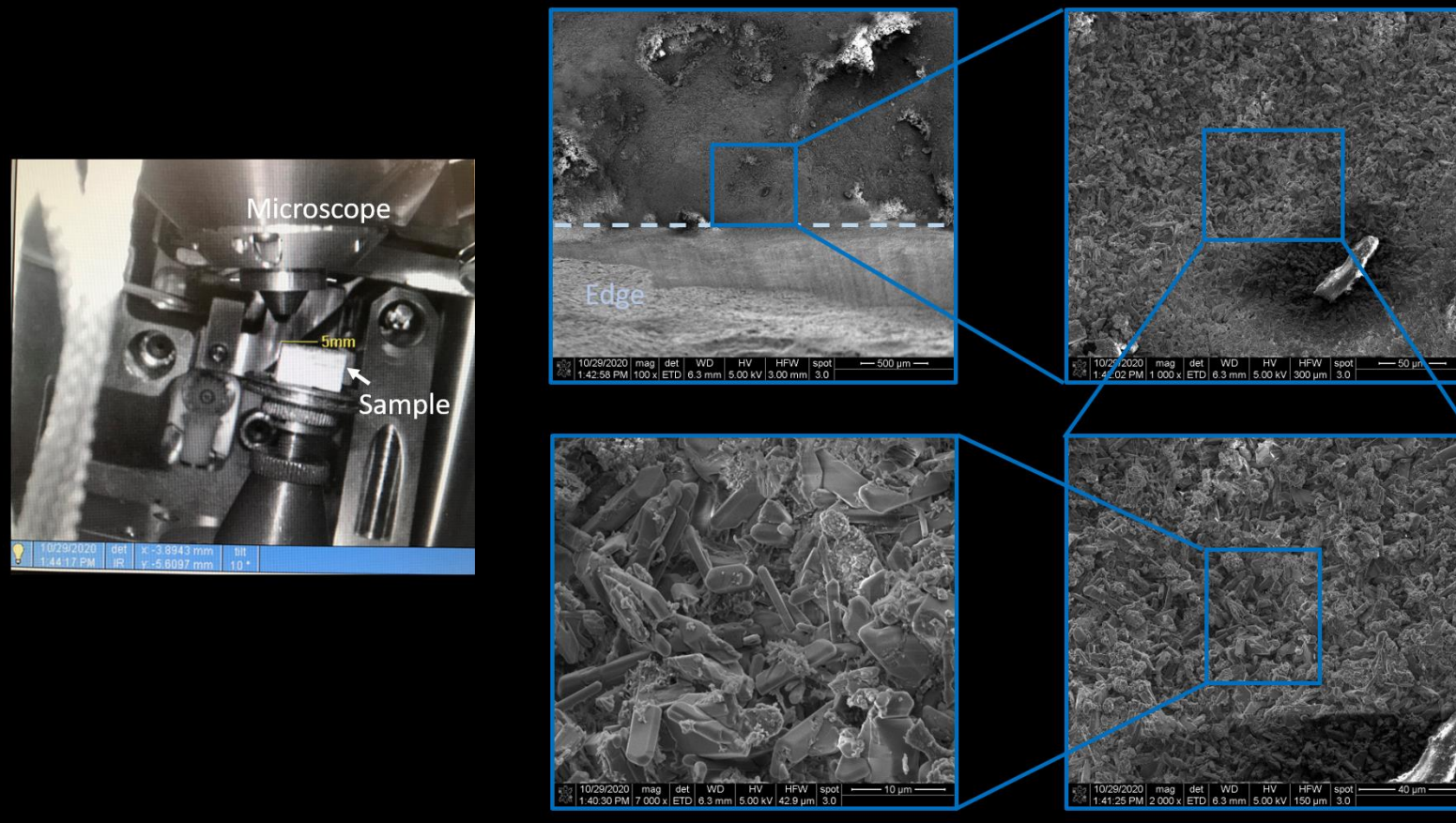
Figure E.7. SEM scans on a rough surface (grit 36 roughness) prepared with water-based release agent imaging the edge
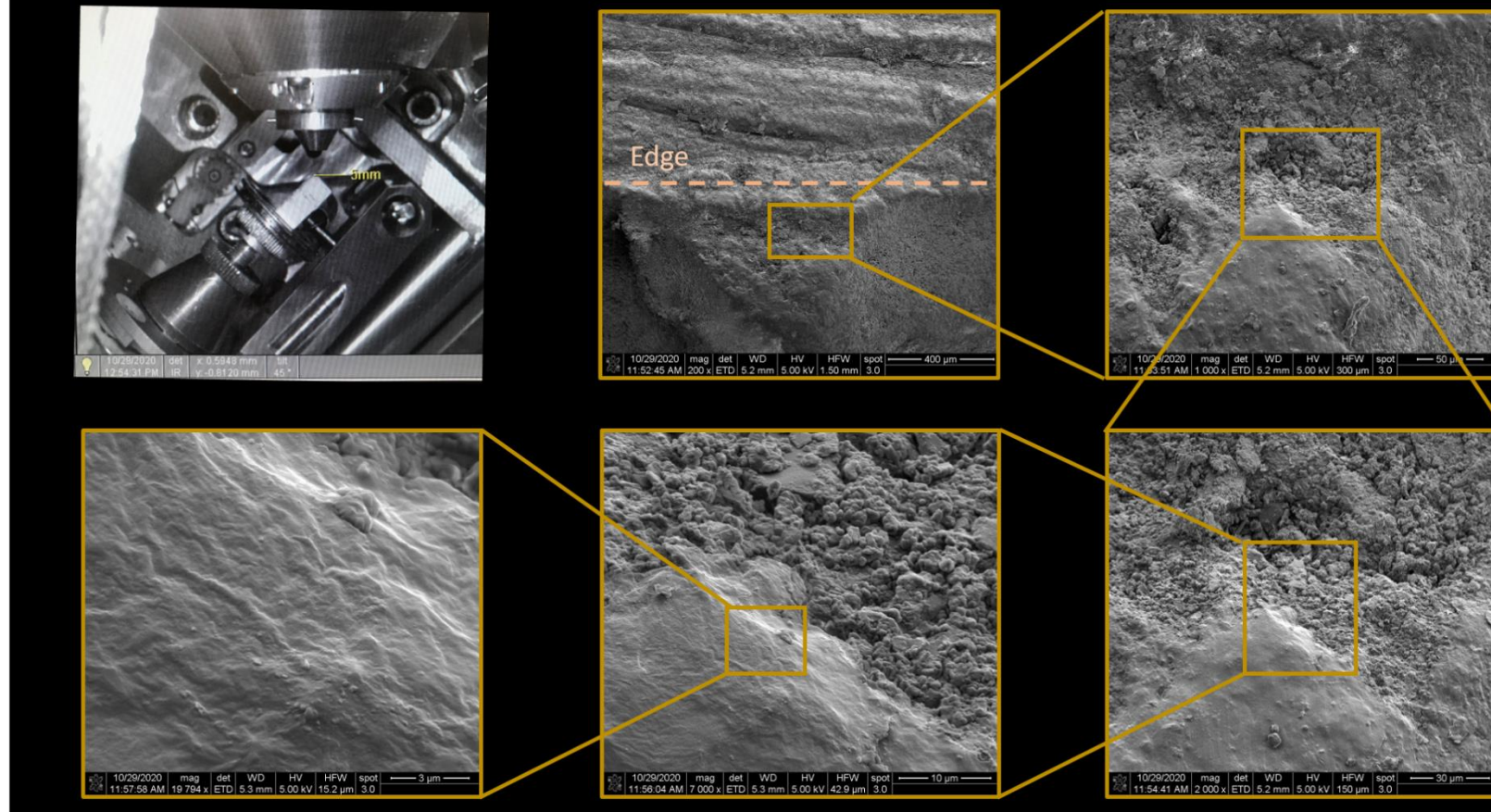
Figure E.8. SEM scans on a rough surface (grit 36 roughness) prepared with an oil-based release agent, imaging the edge
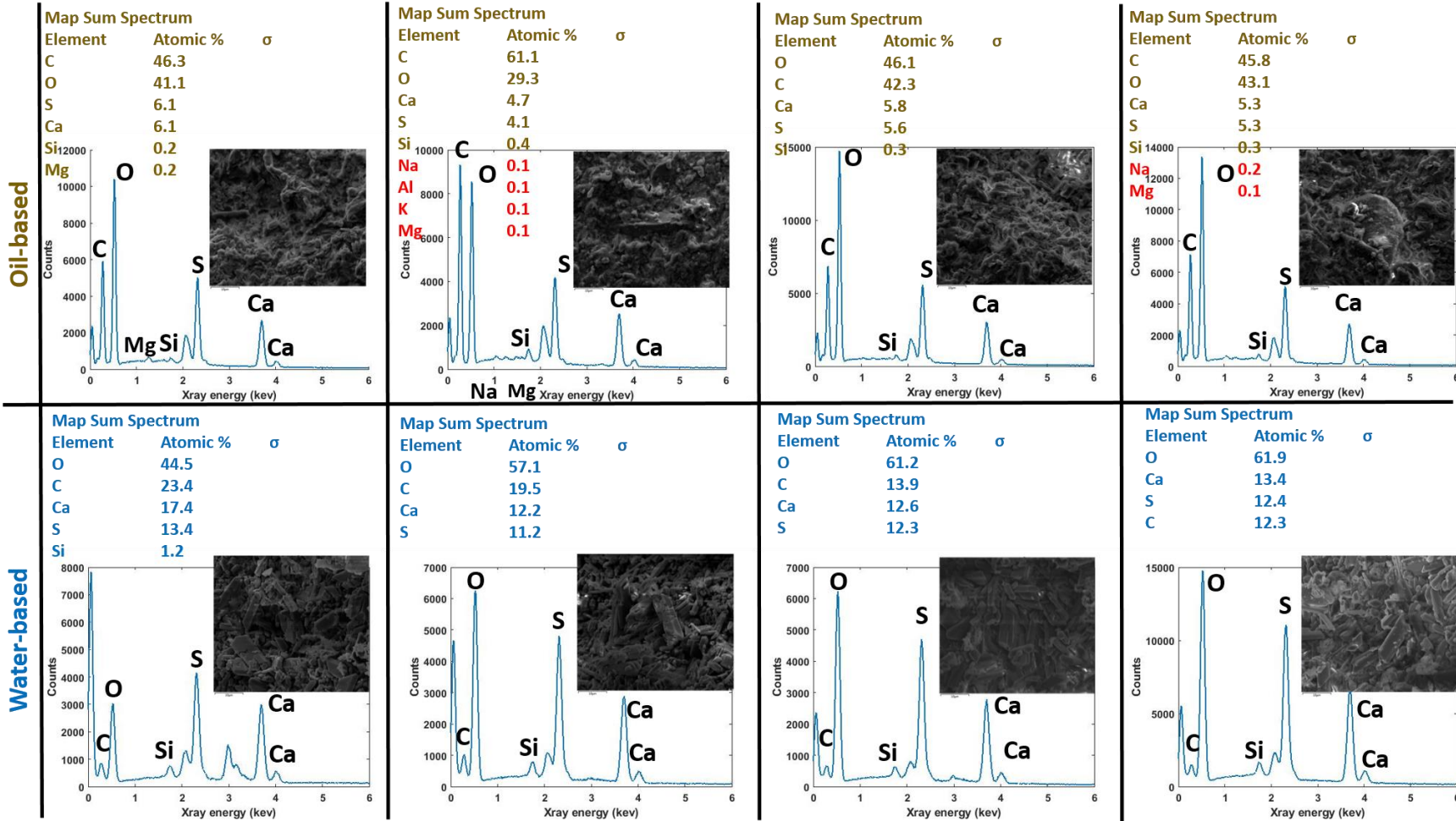
Figure E.9. Full dataset of all the EDX spectra obtained for surfaces prepared with oil-based release agent (top row) and water-based release agent (bottom row)

APPENDIX F. XRAY SCANS REPEATABILITY EXPERIMENTS

The repeatability experiments conducted on imaging fractures of G_O (Figures F.1-F.4) and G_W (Figures F.5 and F.8) specimens are presented in this appendix.

1 MPa 2 MPa 3 MPa 4 MPa 5 MPa

3D Reconstruction

(a) (b) (c) (d) (e)

Aperture quantification

(f) (g) (h) (i) (j)

22.00 48.75 108.0 239.3 530.3 1175
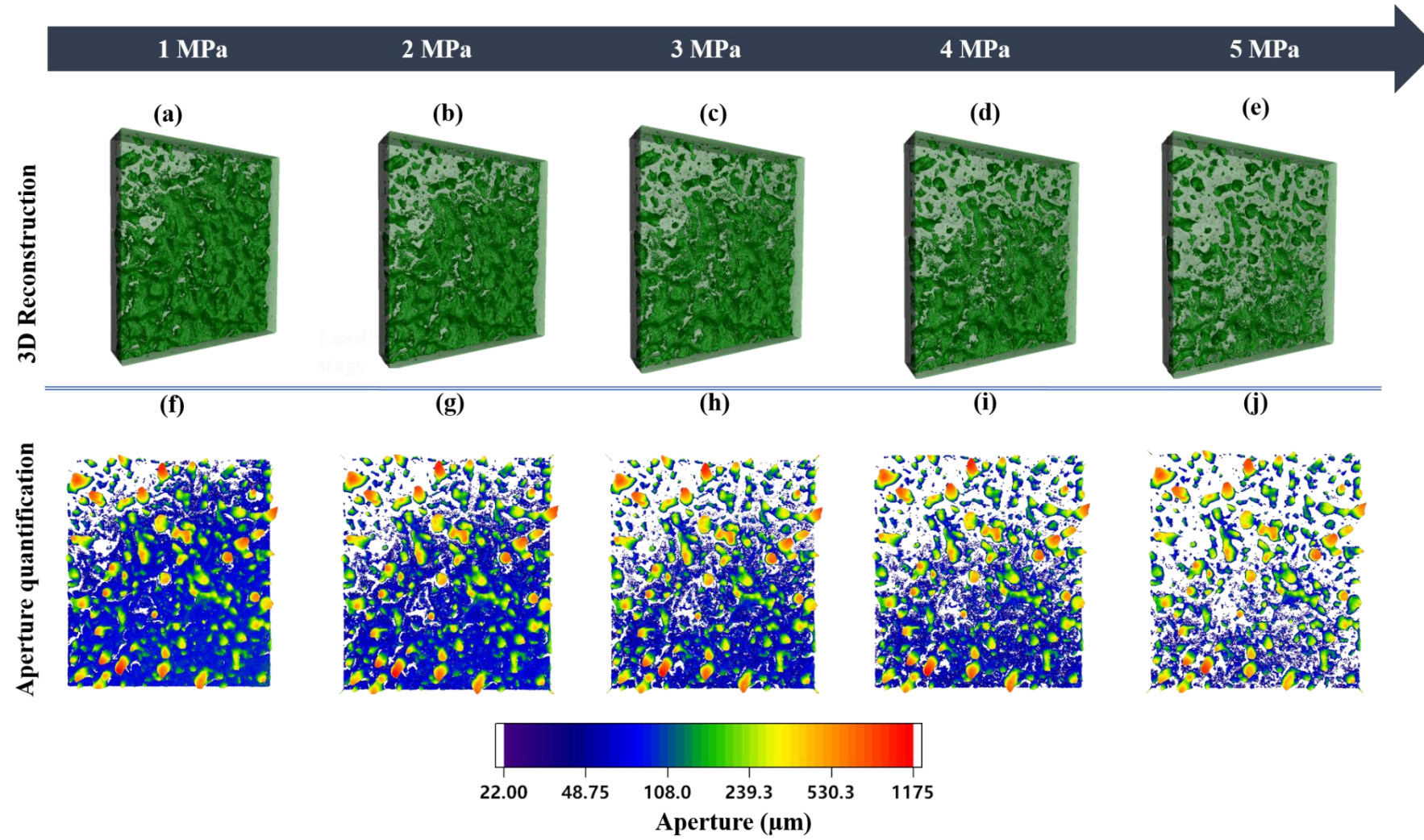
Aperture (µm)

Figure F.1. 3D segmented aperture for: (a-e) G_O; and (f-j) quantified aperture, at normal stresses of 1-5 MPa
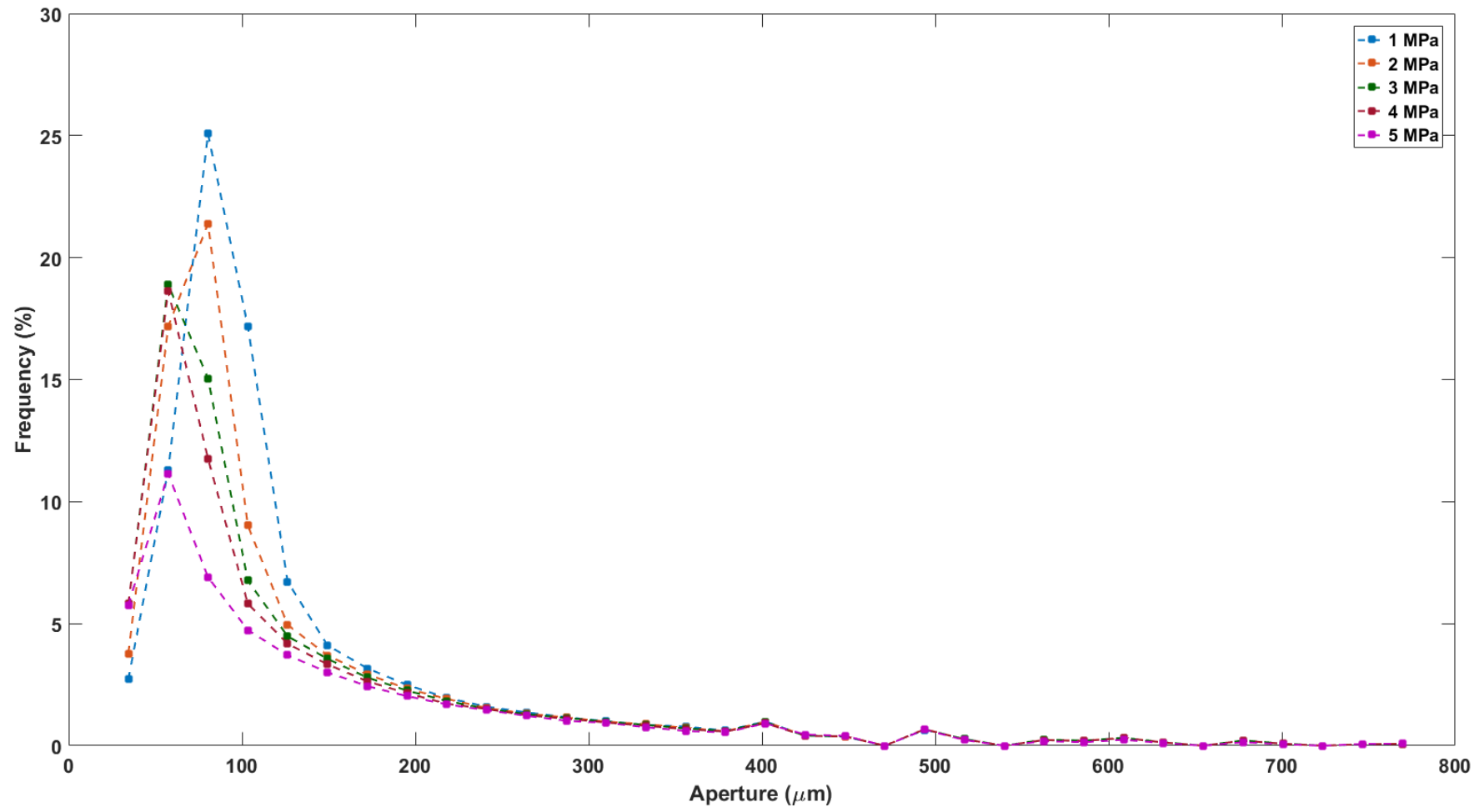
Figure F.2. Aperture distribution for specimen G_O presented in Figure F.2 at normal stresses of 1-5 MPa
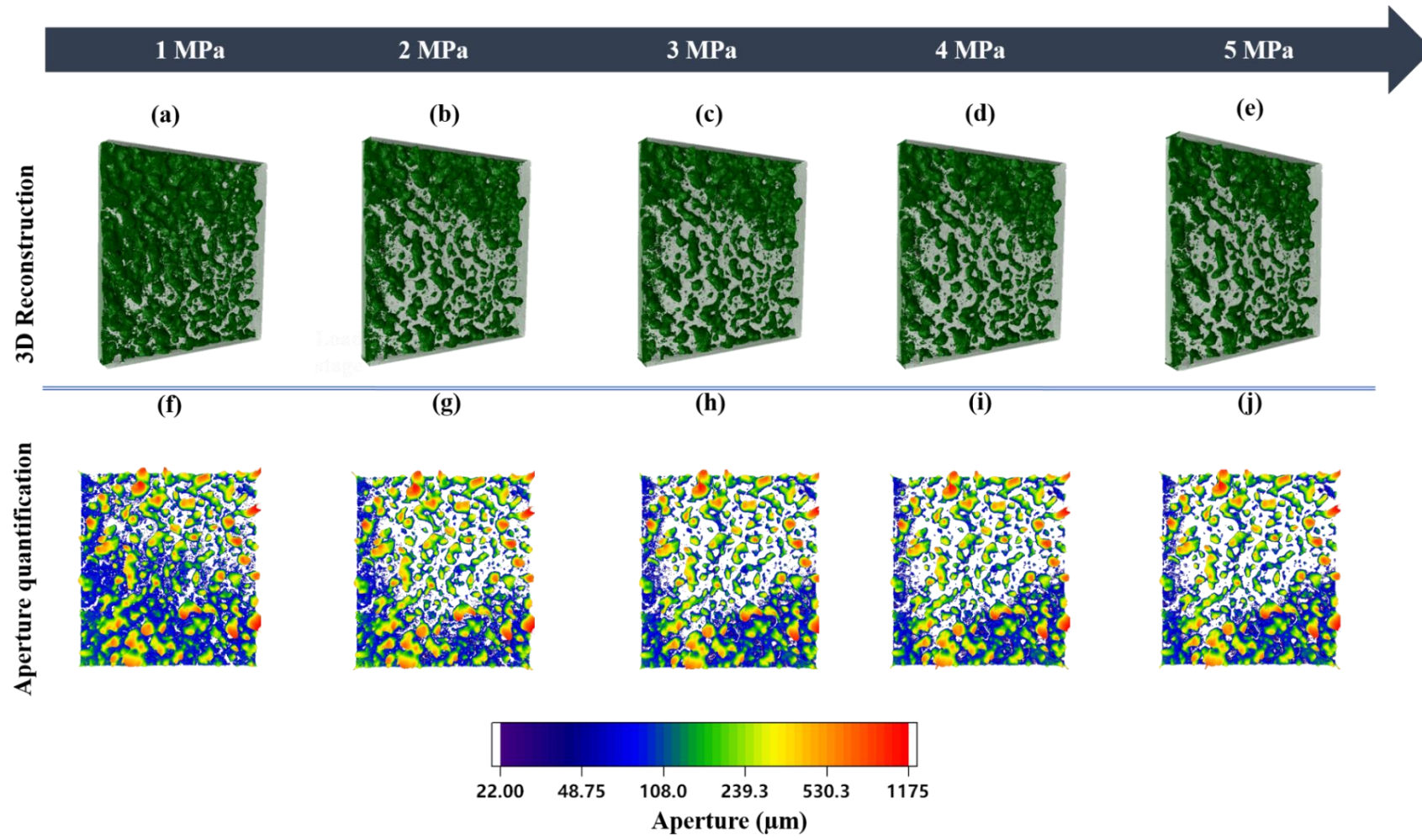
Figure F.3. 3D segmented aperture for: (a-e) G_O; and (f-j) quantified aperture, at normal stresses of 1-5 MPa
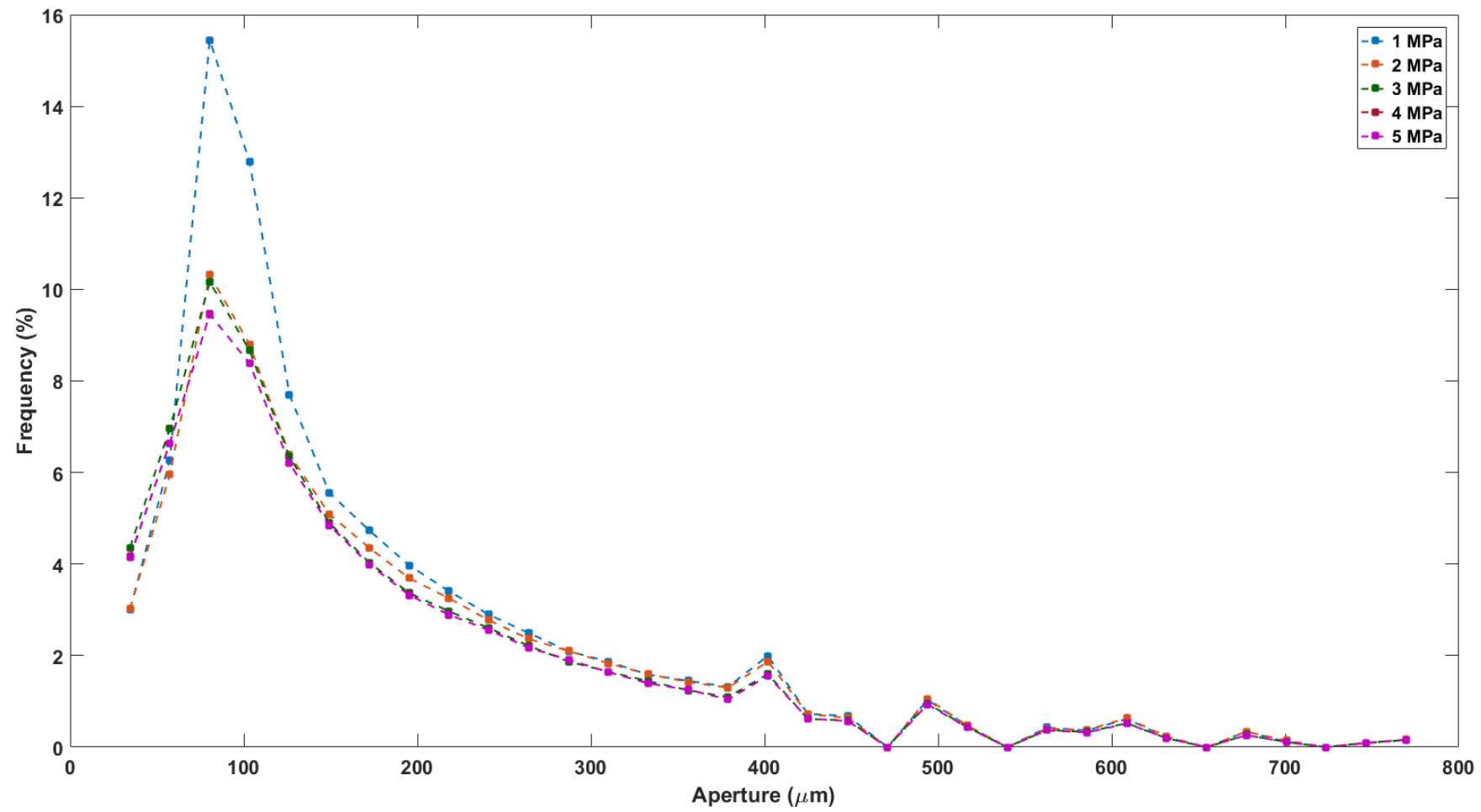
Figure F.4. Aperture distribution for G_O specimen presented in Figure F.3
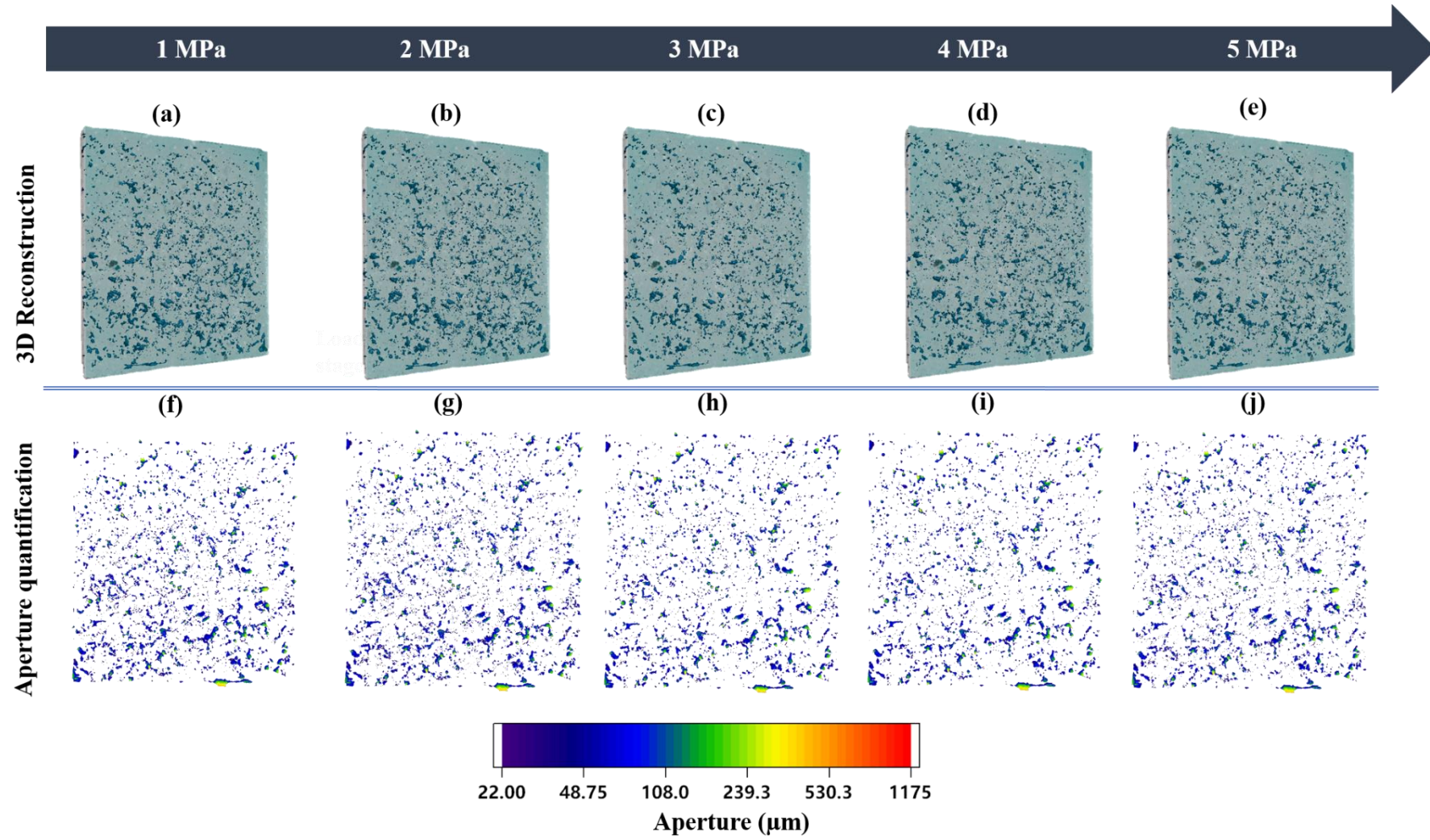
Figure F.5. 3D segmented aperture for: (a-e) G_W; and (f-j) quantified aperture, at normal stresses of 1-5 MPa
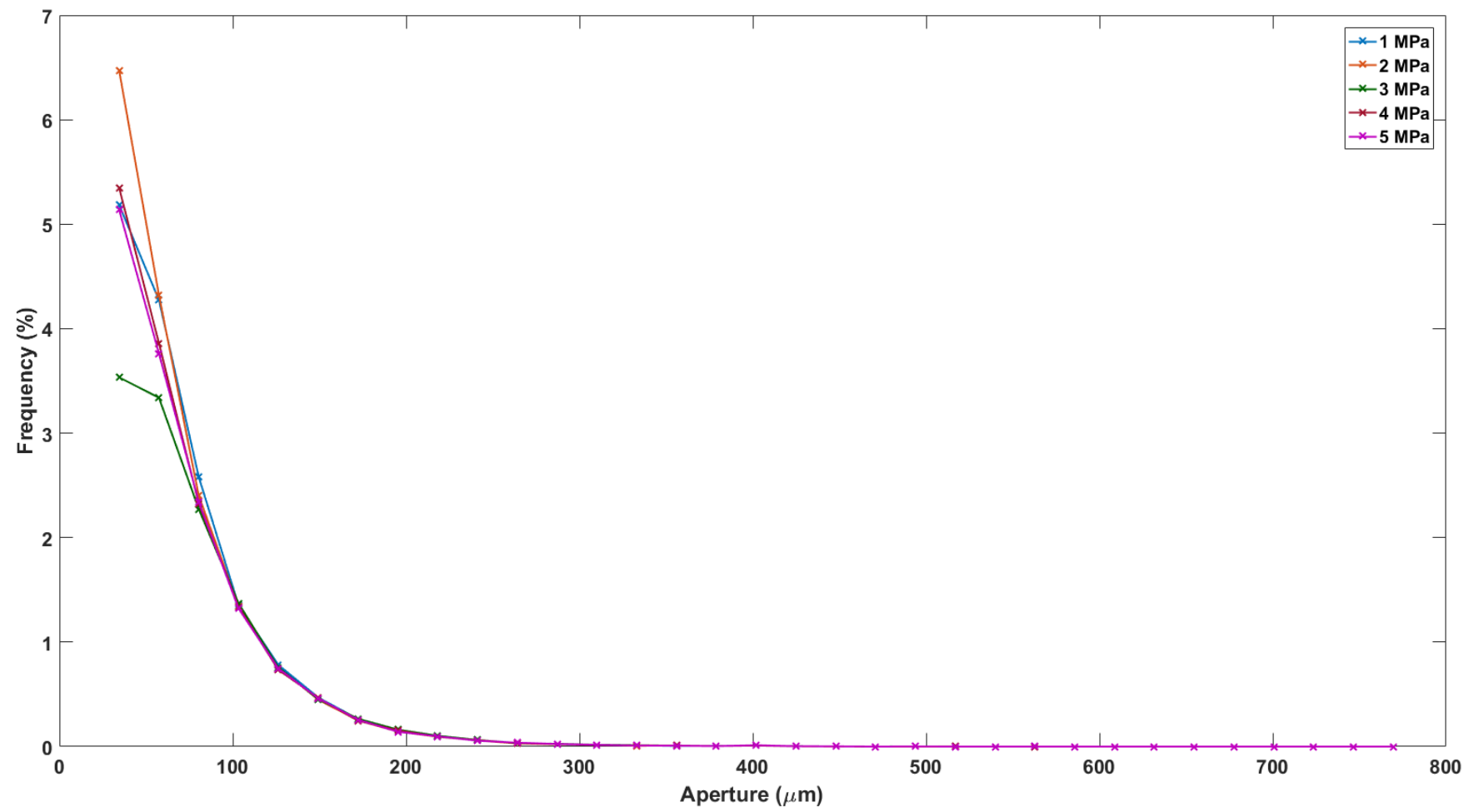
Figure F.6. Aperture distribution for G_O specimen presented in Figure F.5
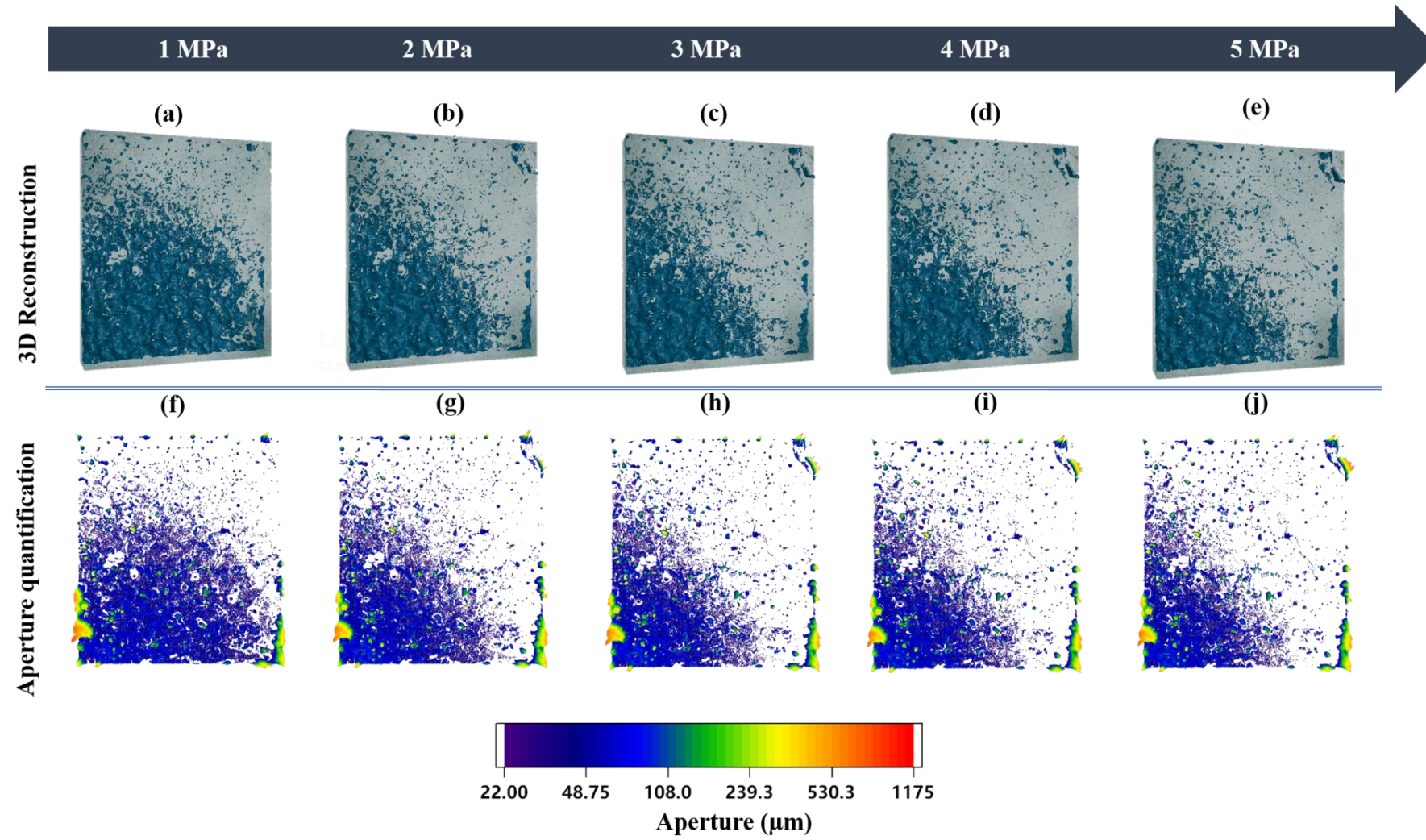
Figure F.7. 3D segmented aperture for: (a-e) G_W; and (f-j) quantified aperture, at normal stresses of 1-5 MPa
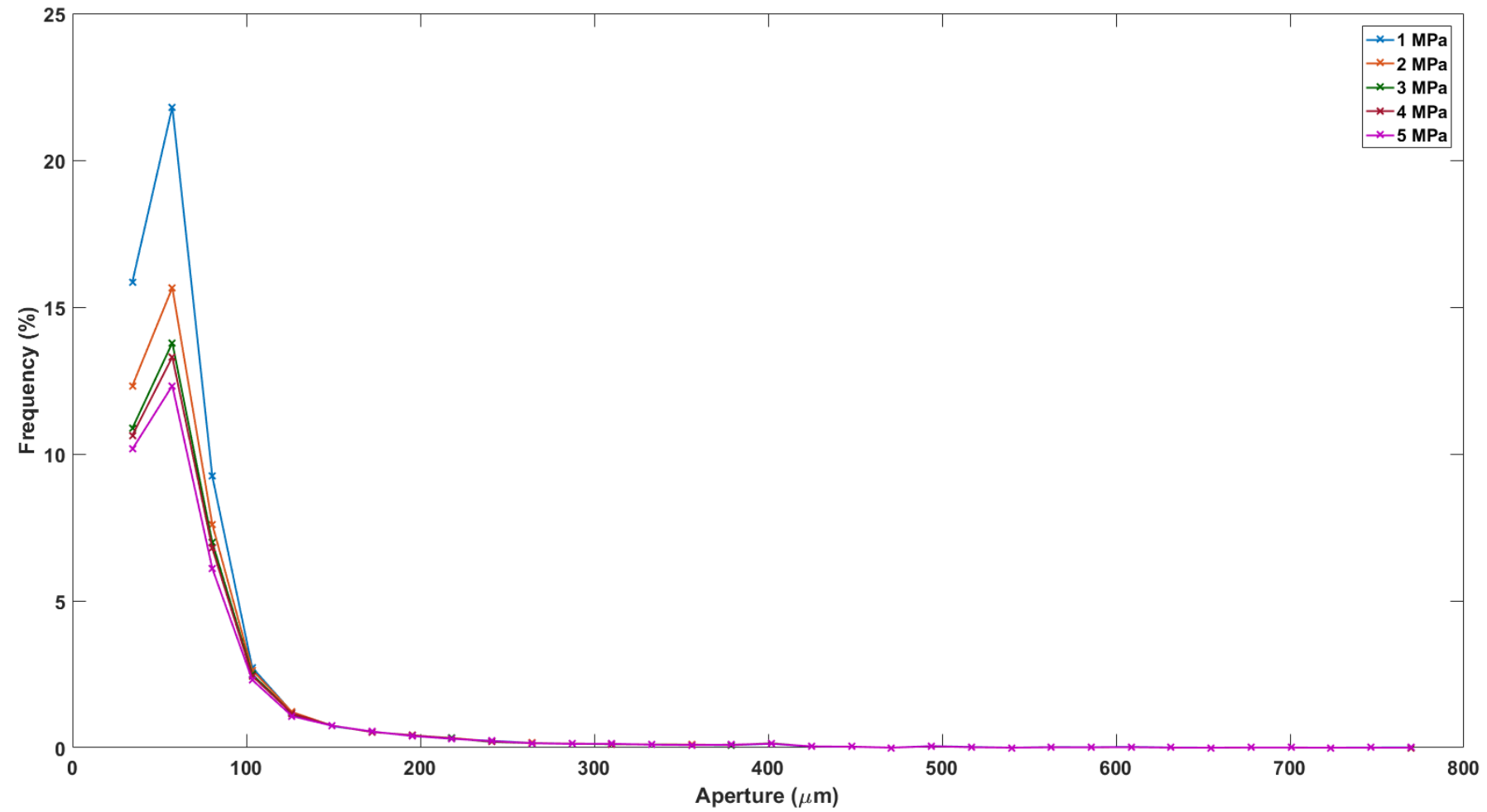
Figure F.8. Aperture distribution for G_O specimen presented in Figure F.7

APPENDIX G. REFLECTED SIGNALS FOR G_W & G_O SPECIMENS

This appendix includes the corresponding reflected data for G_W and G_O specimens presented in chapter 5, in Figures G.1, G.2 for specimen G_W and G.3, G.4 for G_O specimen, sheared at normal stresses of 2 and 5 MPa, respectively.
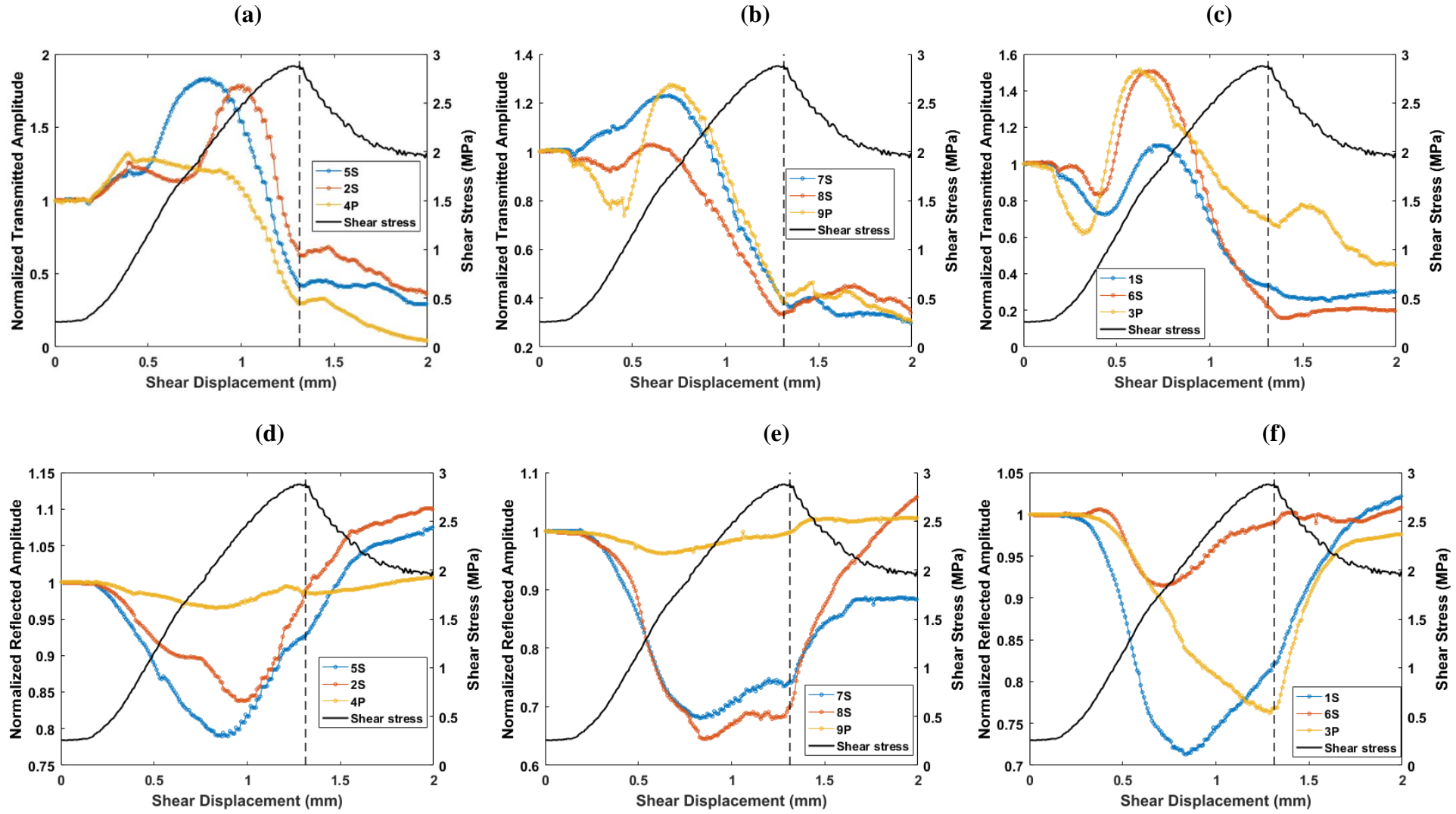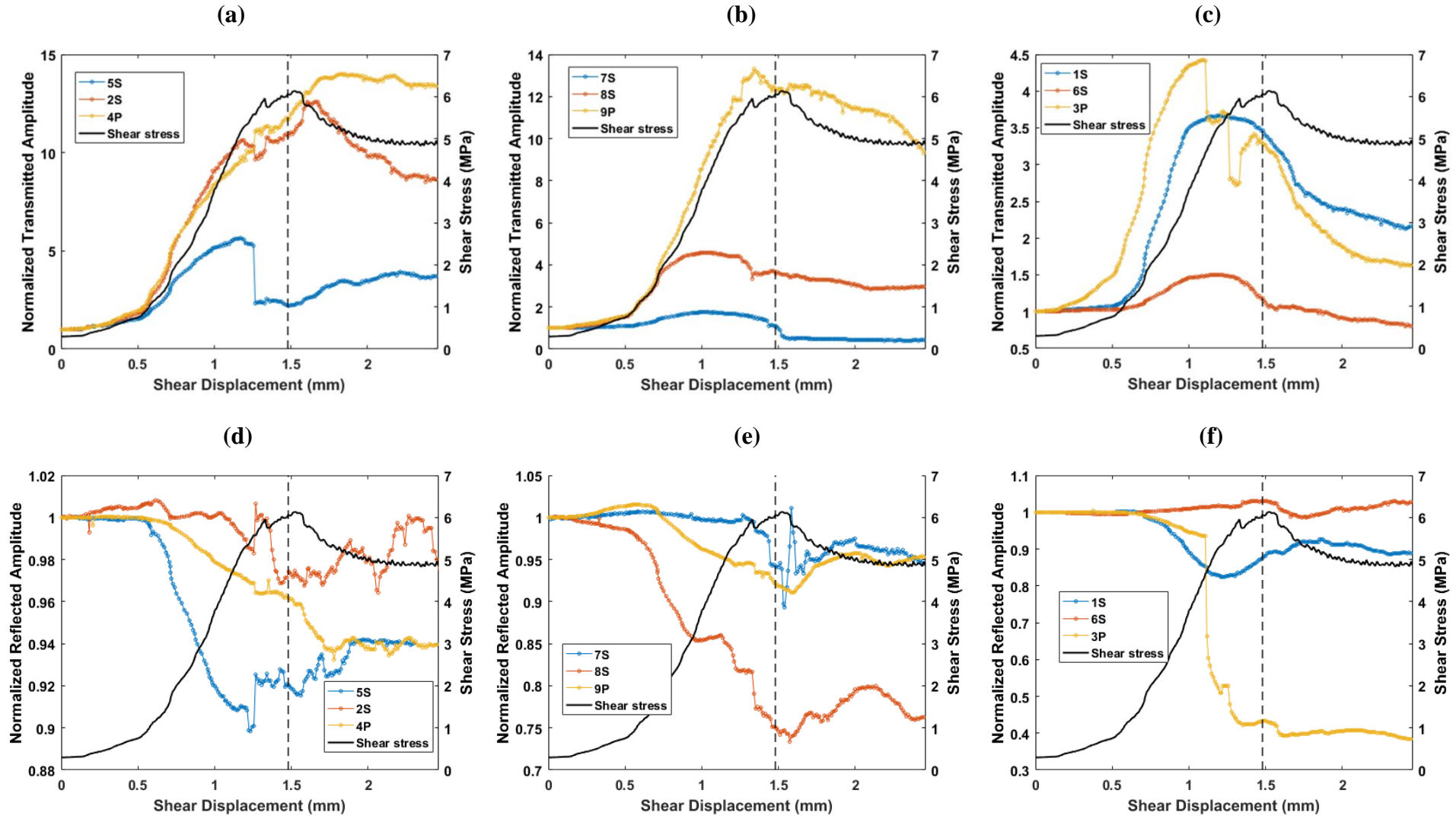
Figure G.1. Normalized transmitted amplitude for specimens prepared with water-based release agent (top row) and reflected (bottom row for (a & d) top, (b & e) middle, and (c & f) bottom transducers; the secondary y-axis plots the shear stress; at normal stress = 2 MPa
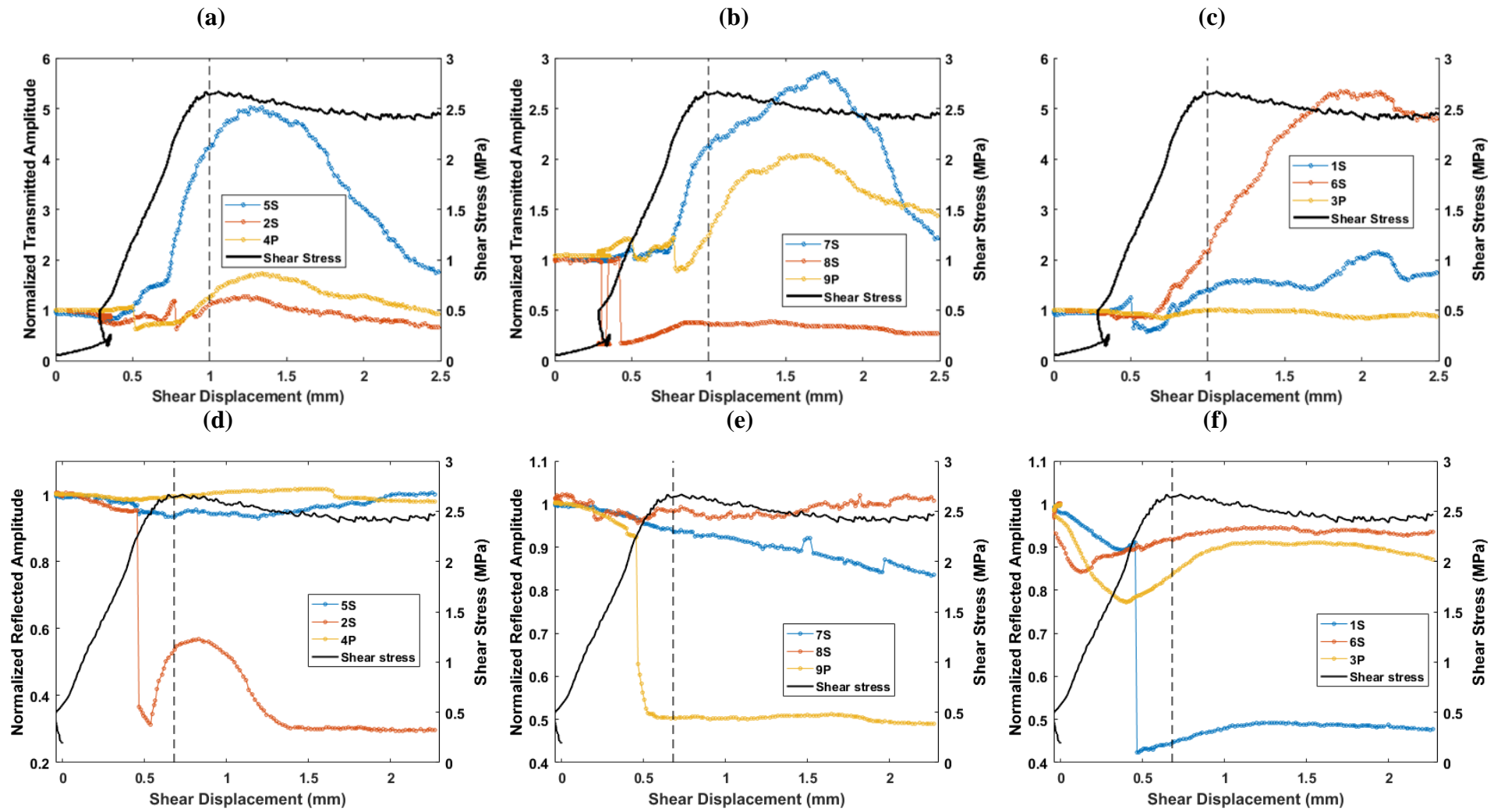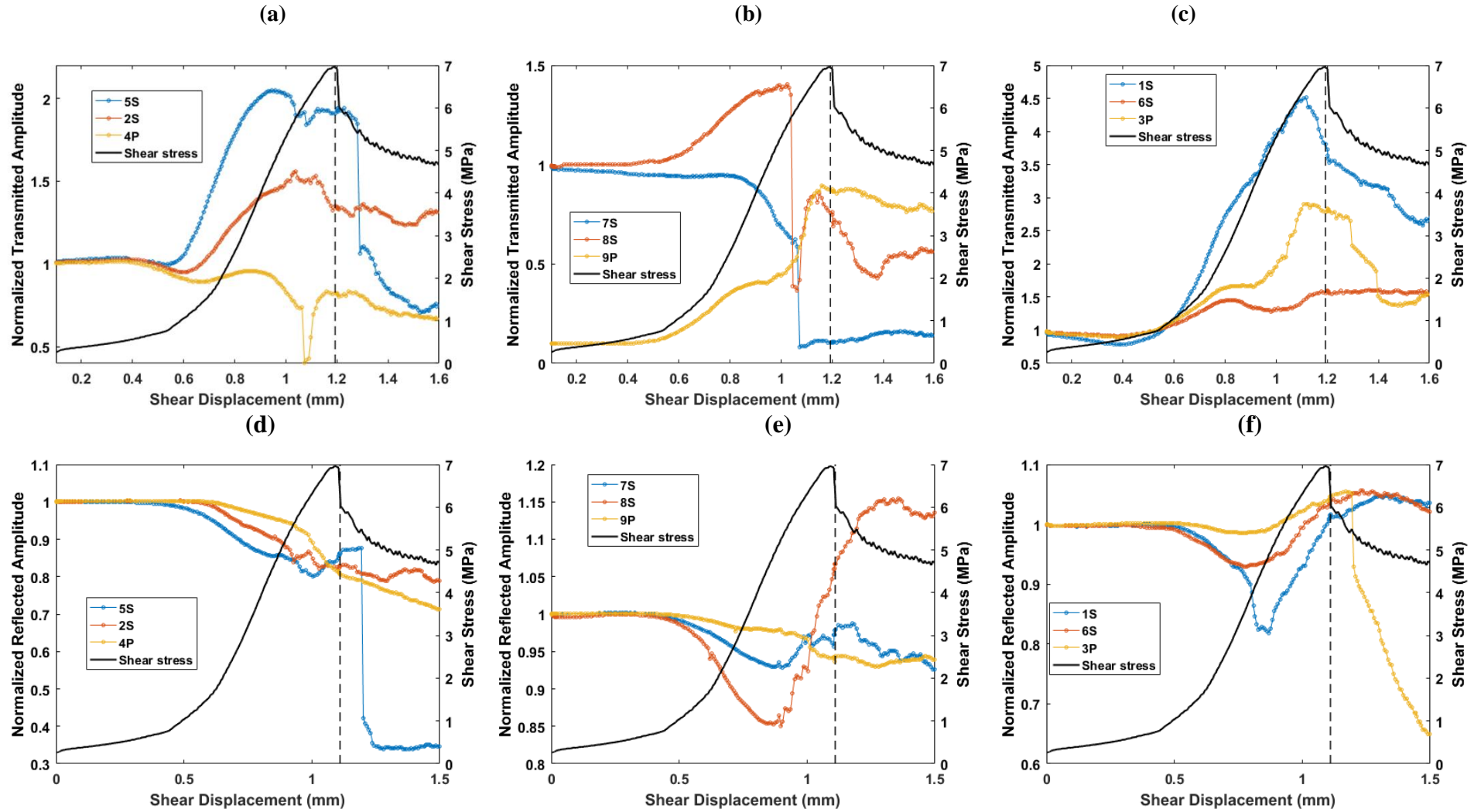
Figure G.2. Normalized transmitted amplitude for specimens prepared with oil-based release agent (top row) and reflected (bottom row for (a & d) top, (b & e) middle, and (c & f) bottom transducers; the secondary y-axis plots the shear stress; at normal stress = 2 MPa

Figure G.3. Normalized transmitted amplitude for specimens prepared with water-based release agent (top row) and reflected (bottom row for (a & d) top, (b & e) middle, and (c & f) bottom transducers; the secondary y-axis plots the shear stress; at normal stress = 5 MPa

Figure G.4. Normalized transmitted amplitude for specimens prepared with oil-based release agent (top row) and reflected (bottom row for (a & d) top, (b & e) middle, and (c & f) bottom transducers; the secondary y-axis plots the shear stress; at normal stress = 5 MPa

APPENDIX H. DIRECT SHEAR EXPERIMENTS ON INFILLED DISCONTINUITIES

Introduction

Rock discontinuities in the field are not always clean as they may contain debris and fill transported by weathering, chemical processes, and/or fluids. It is important to understand how filled discontinuities behave when subjected to shear. For this reason, direct shear laboratory experiments were performed on filled discontinuities. The experiments were conducted on gypsum discontinuities with embedded fill (partially filled) in the asperities

Proppant (infill material)

Proppant brand "Interprop Hybrid" from Saint Gobain was selected as the fill material because of its high strength with a crush resistance of 4% at a stress of 86.2 MPa, i.e., only 4% of the grains are crushed when subjected to a stress of 86.2 MPa. 2D X-ray scans were conducted to understand the physical characteristics of the proppant. The scans were performed using a Zeiss Xradia 510 Versa X-ray Microscope (XRM) at the Physics Department at Purdue University. A high resolution (15 µm/pixel) and a low resolution (1 mm/pixel) scans were conducted as shown in Figure H.1 (a-b), respectively. The energy and power of the scans were 160 kV and 10W, respectively. The sample was placed between the source and the detector with source and detector distances of 100 mm and 300 mm, respectively. The scans had an exposure time of 1 second for 3201 projections, 0.4x magnification factor, bin size of 2, and no filter was used (air). Voxel size was 15 µm and 1 mm for high- and low-resolution scans, respectively.
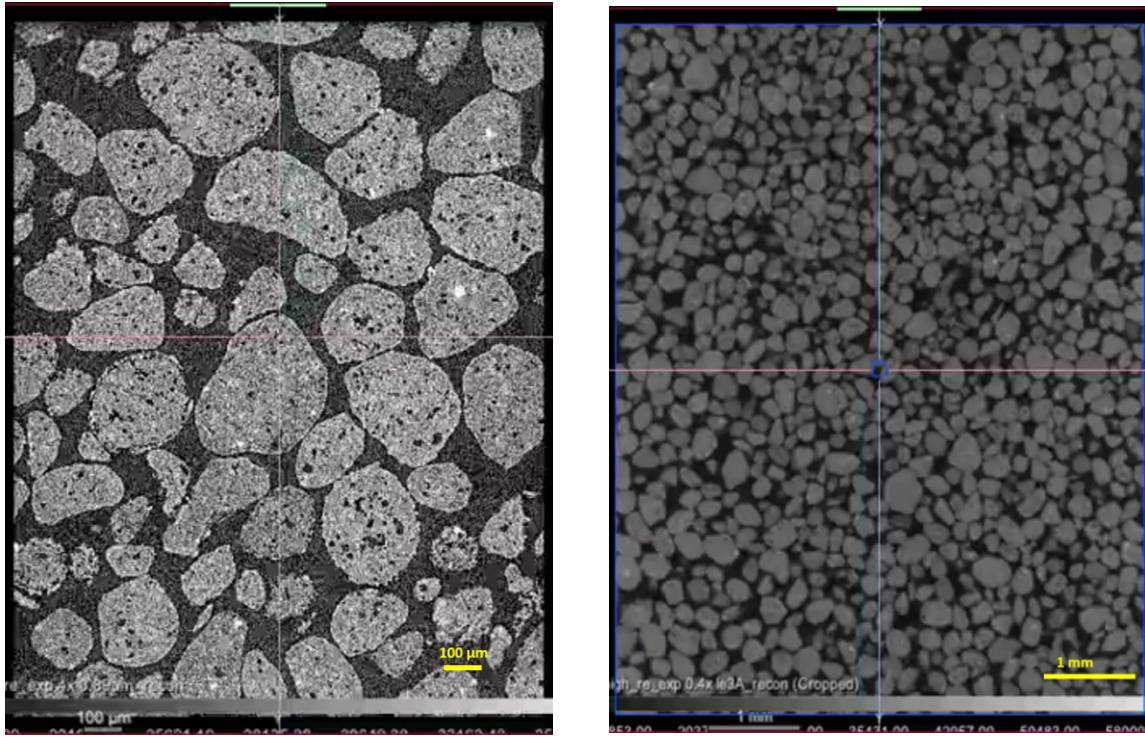
Figure H.1. Xray 2D (a) high resolution scan (15 µm/pixel); (b) low resolution scan (1 mm/pixel)

Figure H.1 (a-b) shows that the particles of the proppant exhibit different shapes and are not perfectly round. Figure H.1 (a) also shows that the particles are porous.

Sieve analysis was conducted to obtain the particle size distribution of the proppant and to characterize its gradation. Figure H.2 shows a graph of the particle size distribution. Based on the sieve analysis data, the average particle size diameter was 0.25 mm (D_{50}). To find the proppant's gradation, the uniformity coefficient (C_u) and the coefficient of curvature (C_c) were computed from D_{10}, D_{30}, and D_{60} values obtained from the particle size distribution.

$$C_u = \frac{D_{60}}{D_{10}} = \frac{0.2792\ mm}{0.1855\ mm} = 1.47 \qquad C_c = \frac{D_{30}{}^2}{D_{10} \times D_{60}} = \frac{(0.2316)^2}{0.1855 \times 0.2792} = 1.06$$

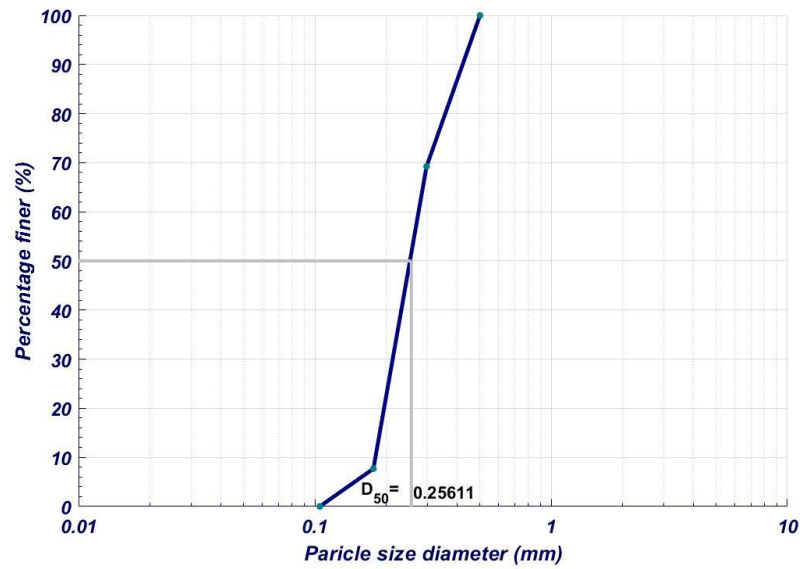Based on the computed coefficients C_u and C_c, the proppant was classified as poorly graded sand.

Figure H.2. Particle size distribution

A pycnometer was used to measure the proppant's density. Figure H.3 (a) shows an image of the pycnometer with the proppant placed in the sample chamber. The sample was pressurized with ten cycles of helium gas from a helium tank with a pressure of 151.69 kPa. Figure H.3 (b) shows the measured density for each cycle along with the variation in temperature. The mean density of the proppant was found to be ~3.33 g/cm^3.
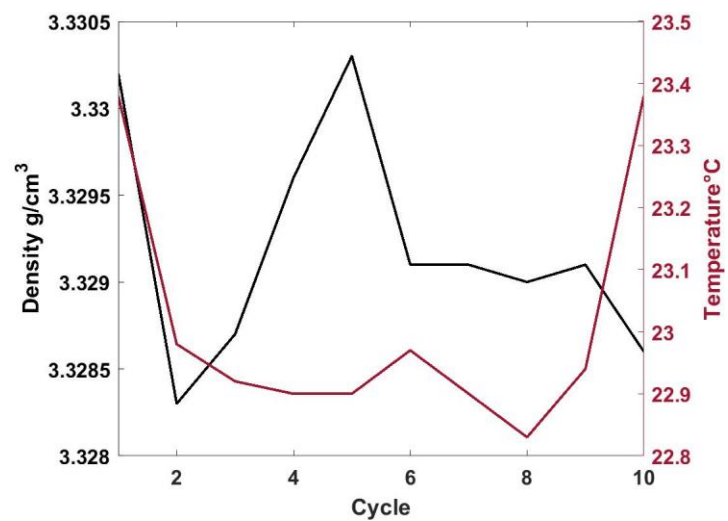

Figure H.3. (a) pycnometer used to measure proppant density; (b) density measured

179

This section presents the experiments conducted on samples with thick fill in the discontinuities (thickness~0.46 mm).

Sample preparation

Gypsum samples with rough discontinuities (roughness of girt 36 sandpaper) were prepared following the same procedure presented in section 3.2 of chapter 3; however, these samples were prepared using the oil-based mold release agent (Duogard). The proppant was spread on the discontinuity of one of the gypsum blocks, also using sieve number 50 (0.297 mm opening). Figure H.4 shows the sample prepared before prior to running the experiment.
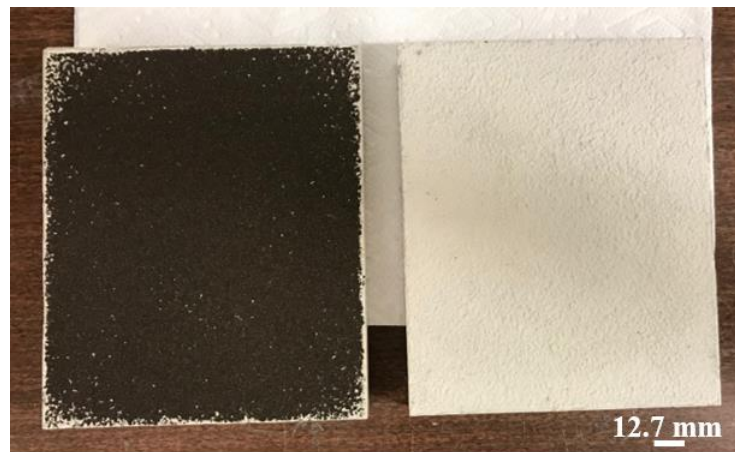
Figure H.4. Infilled discontinuity sample (before shearing)

Direct Shear Experimental Results

Mechanical response:

Direct shear experiments with infilled discontinuities were conducted in the laboratory at a normal stress of 2 MPa. Figure H.5 shows the shear stress curves of representative direct shear experiments conducted on clean and infilled discontinuities. The shear stress curve corresponding to an infilled discontinuity (marron) is different than the curve that corresponds to a clean (black) one; the curve corresponding to a clean discontinuity reaches a peak (2.01 MPa), then drops. On the other hand, the shear stress curve associated with an infilled discontinuity reaches a peak (1.57 MPa), but the post-peak drop is smaller. The presence of the infill in the discontinuity results in a ~ 21.8% reduction in shear strength.
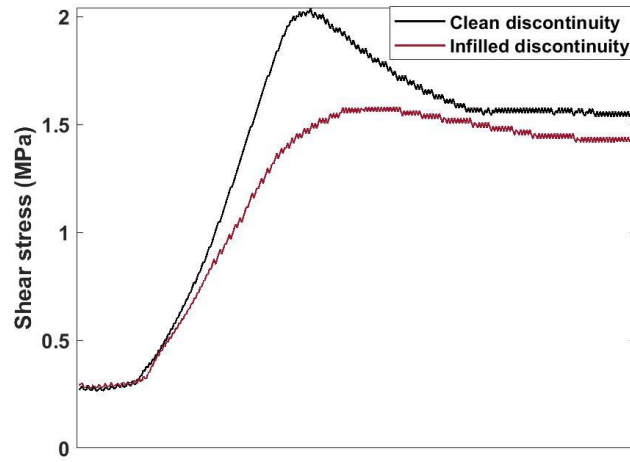
Figure H.5. Shear stress curves for clean and infilled discontinuities at a normal stress of 2 MPa

Geophysical response:

Figure H.6 shows the normalized transmitted and reflected amplitude as a function of shear displacement for transducers probing the top, middle, and bottom 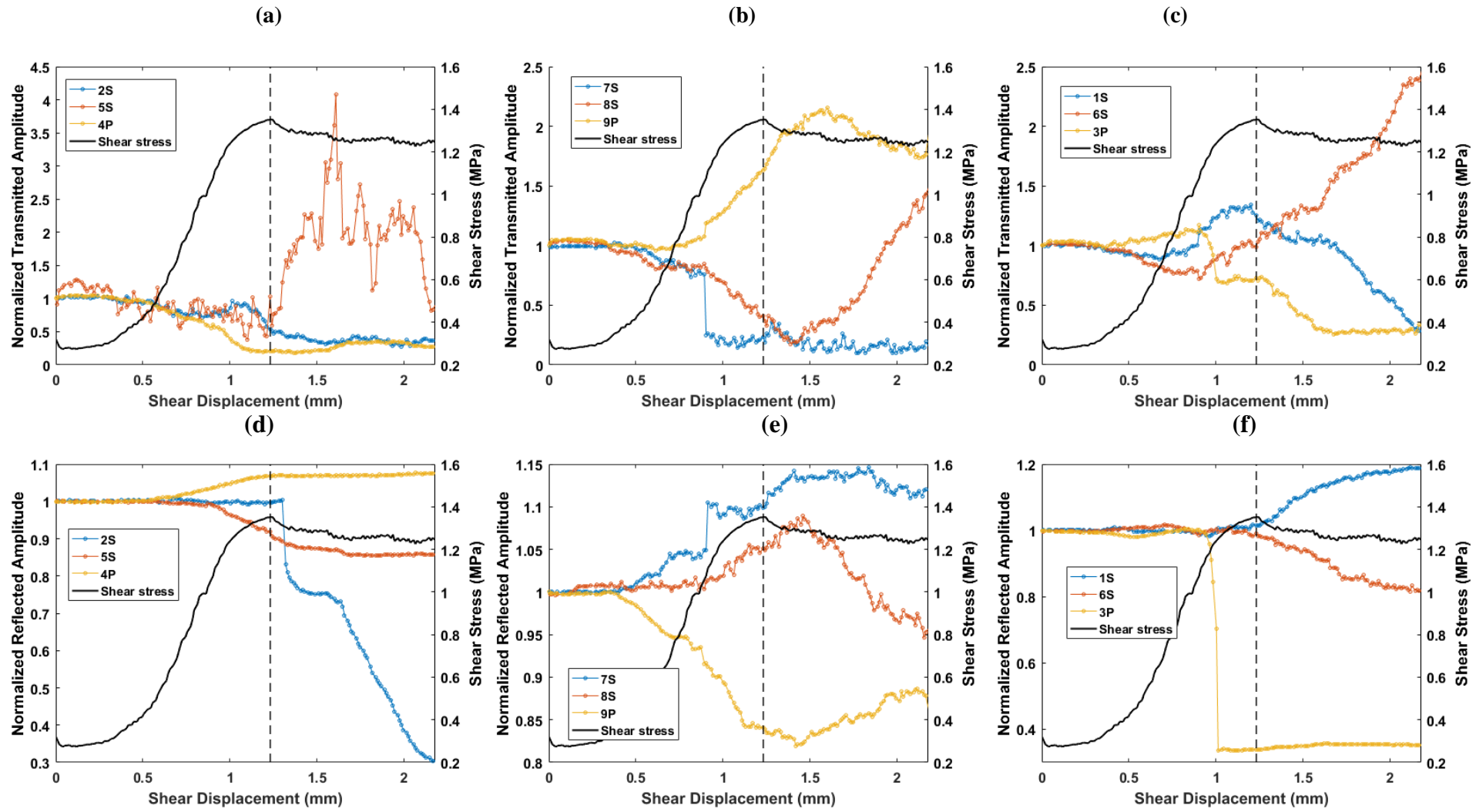portion of the specimen sheared at a normal stress of 2 MPa. Similarly, Figure H.7 shows normalized transmitted and reflected amplitude as a function of shear displacement for transducers probing the top, middle, and bottom portion of another specimen sheared at a normal stress of 2 MPa.

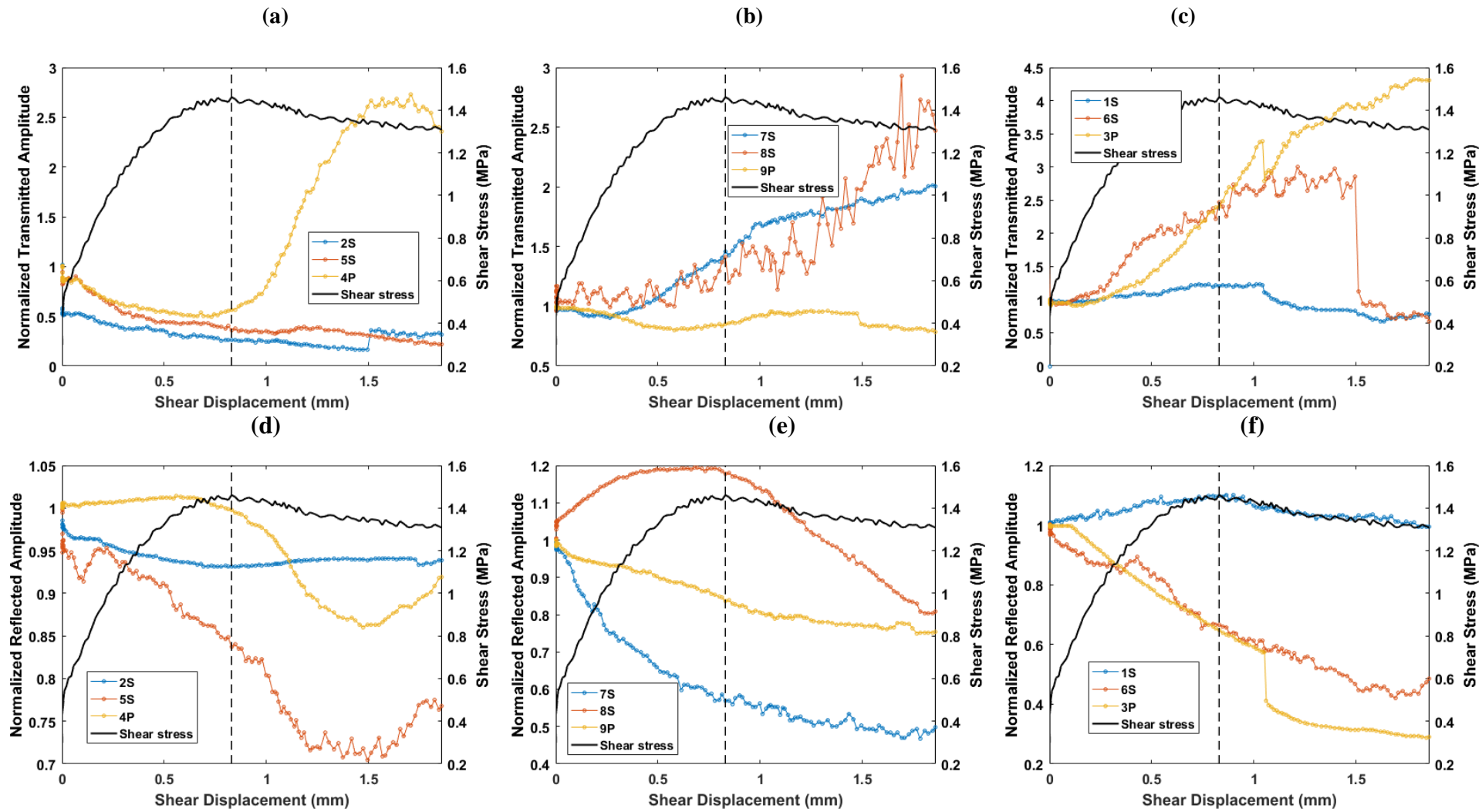Figure H.6. Normalized transmitted amplitude for an infilled specimen sheared at a normal stress of 2 MPa

Figure H.7. Normalized transmitted amplitude for an infilled specimen sheared at a normal stress of 2 MPa

Direct shear experiments on gypsum samples with embedded infilled discontinuities

Direct shear experiments on proppant-filled discontinuities were conducted in the laboratory. The experiments were conducted on samples with partially filled discontinuities, i.e., proppant embedded in discontinuities and rock to rock contact exists.

Sample preparation

Two types of samples with proppant-embedded discontinuities were prepared, following a process similar to that described in section 3.2 in Chapter 3. Sandpaper with grit 36 was used to create the rough interface. The two samples differed in the type of mold release agent applied on the first block before casting the second block. A water-based (2418 Dow corning release emulsion) and an oil-based (Duogard) release agent were used to prepare the two types of samples, i.e., GE_W (water-based) and GE_O (oil-based), respectively. Once the two halves of the specimen were prepared, using one of the halves as the mold for the other half, the proppant was placed on one of the blocks. This was done by depositing the proppant using a sieve number 50 (0.297 mm opening) placed at the height of 50.8 mm above the gypsum block. This process was adopted following a trial-and-error procedure. After the proppant was deposited, the two gypsum blocks were assembled and subjected to a 2 MPa normal stress for 2 hours. Afterward, the two blocks were separated, and excess proppant was brushed off. Figure H.8 shows a sample with embedded proppant prior to testing. Note that most of the embedded proppant is on the block shown to the right in Figure H.8.

Figure H.8. Sample embedded with proppant in the discontinuity GE_W

Figure H.9 and H.10 show the normalized transmitted amplitude of transducers probing the (a) top, (b) middle, and (c) bottom portion of the specimen. The normalized reflected amplitudes are also plotted for (d) top, (e) middle, and (f) bottom portion of the specimen, at a normal stress of 2 MPa. A similar experiment on a specimen prepared with a water-based release agent with embedded infill sheared at a normal stress of 2 MPa is presented in Figure H.11.
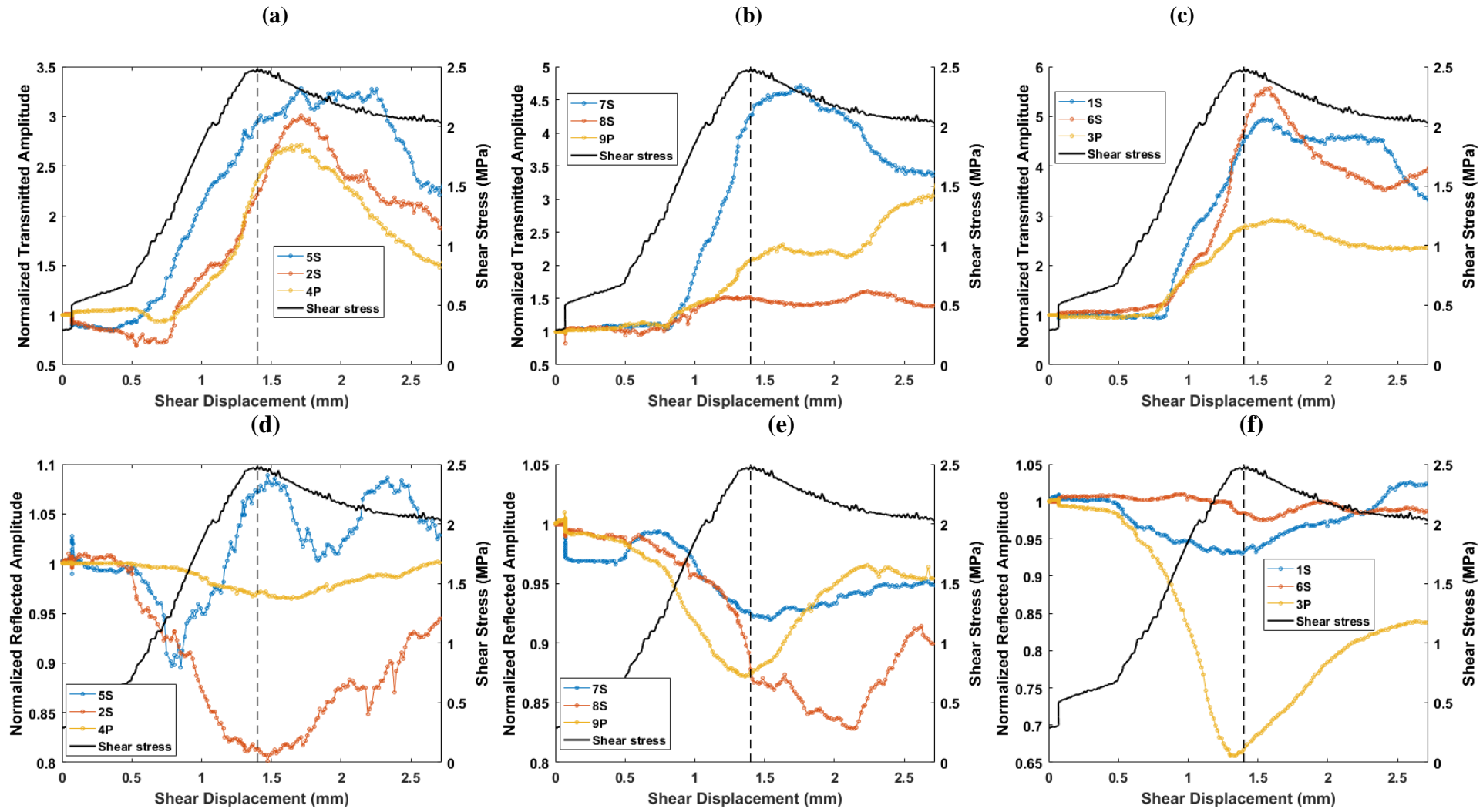
Figure H.9. Normalized transmitted amplitude for a partially infilled specimen (oil-based release agent) sheared at a normal stress of 2 MPa (GE$_O$)
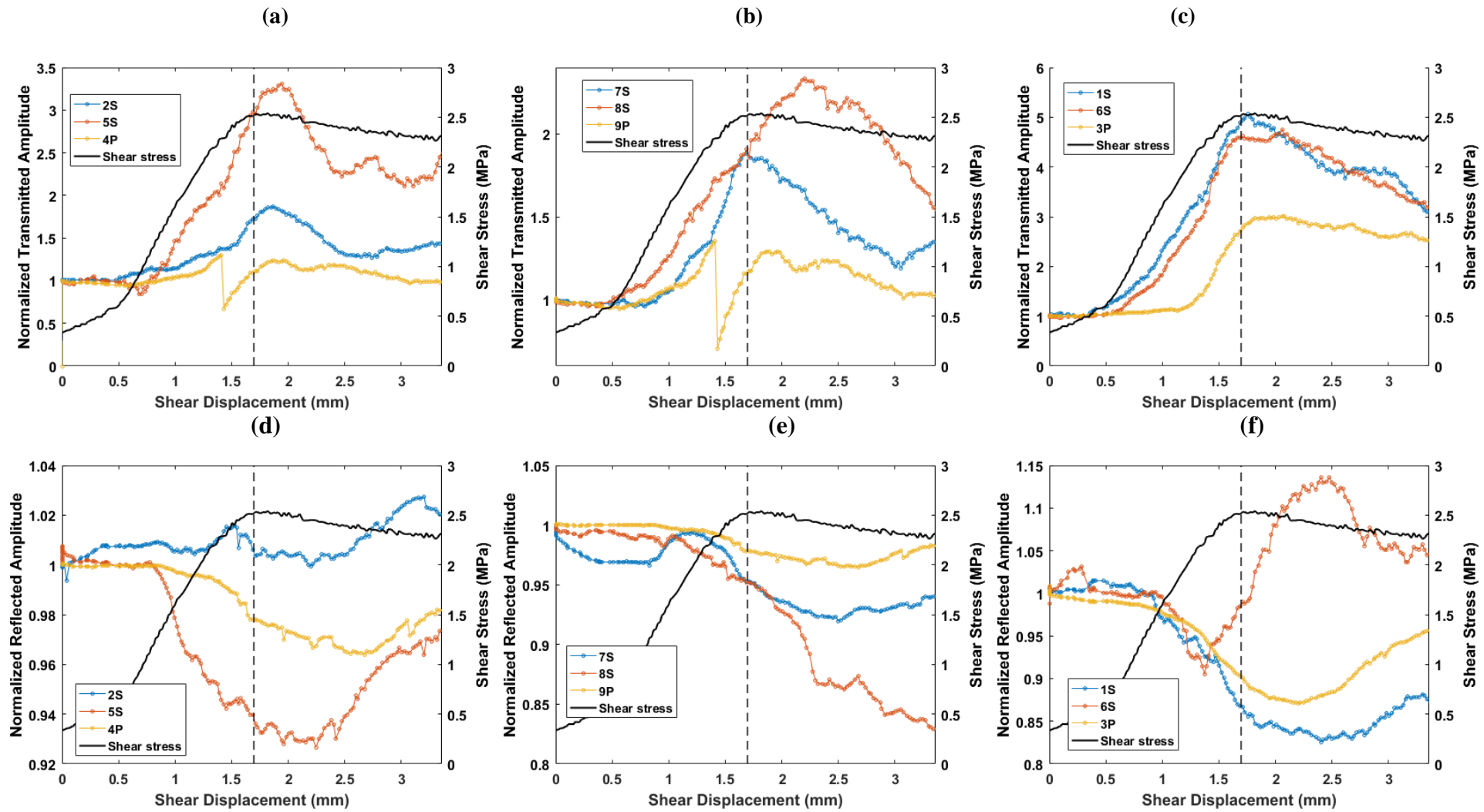
Figure H.10. Normalized transmitted amplitude for a partially infilled specimen (oil-based release agent) sheared at a normal stress of 2 MPa (GE$_O$)
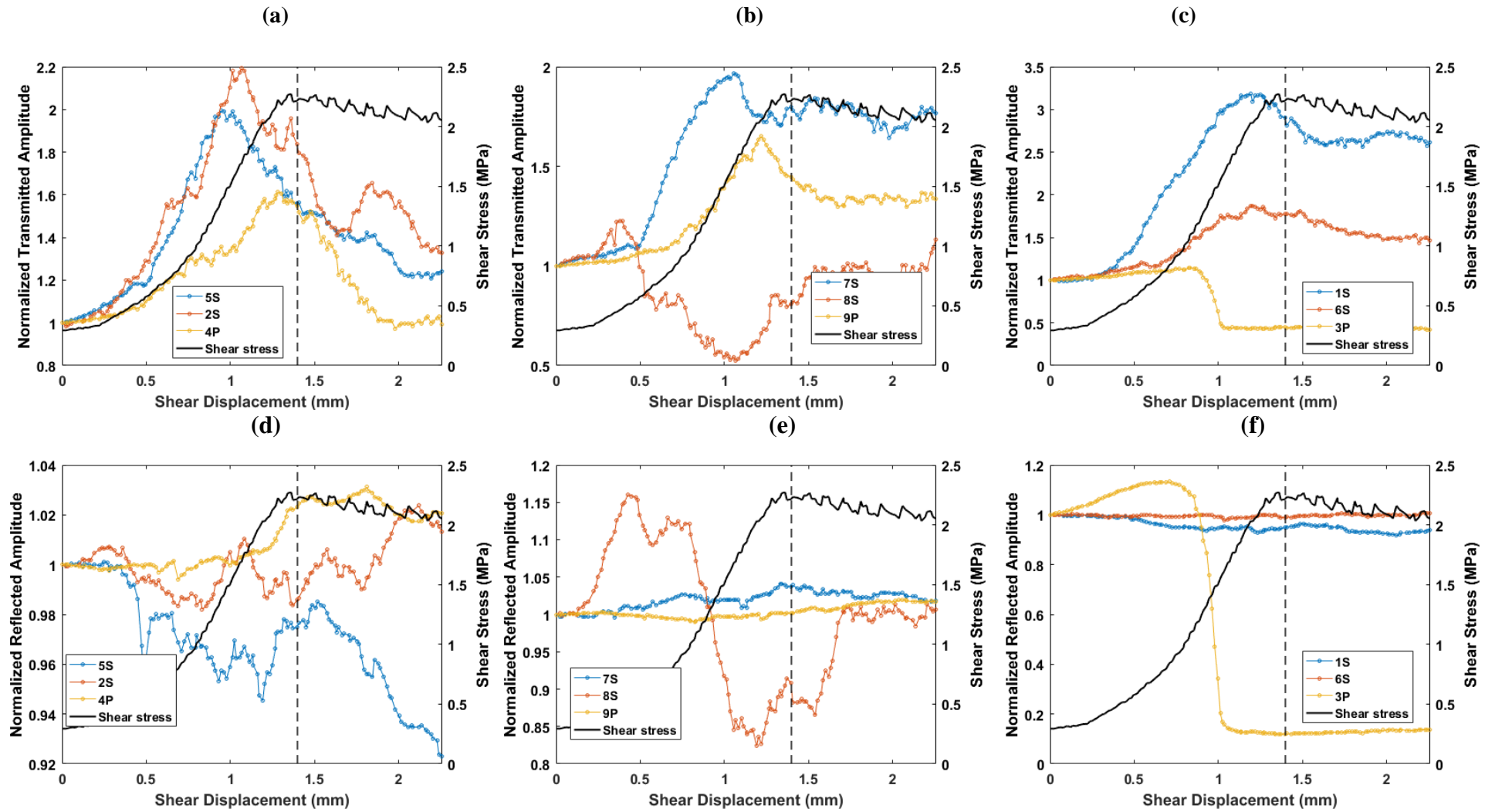
Figure H.11. Normalized transmitted amplitude for a partially infilled specimen (water-based release agent) sheared at a normal stress of 2 MPa (GE$_W$)

Characterizing the fill-asperity interaction in an infilled discontinuity

The asperity-proppant interaction during shearing is complex due to the gradation and shape of the proppant particles. Direct shear experiments with a thick layer of proppant (0.49 mm thickness) were conducted and resulted in inconclusive conclusions, presented in Figures H.6 and H.7. For this reason, X-ray in-situ loading experiments were conducted to analyze and observe the asperity-proppant interaction under normal stress.

Xray in-situ loading experiments on infilled discontinuities

A schematic of the sample used for the X-ray imaging is shown in Figure H.12 (a), and a scan of the sample is shown in Figure H.12 (b). The sample was composed of two independent prismatic blocks with a perfectly matched discontinuity prepared following the same procedure described in Section 3.2 of Chapter 3. Each gypsum block had the following dimensions: 25 mm in length, 20 mm in width, and 6 mm in height.
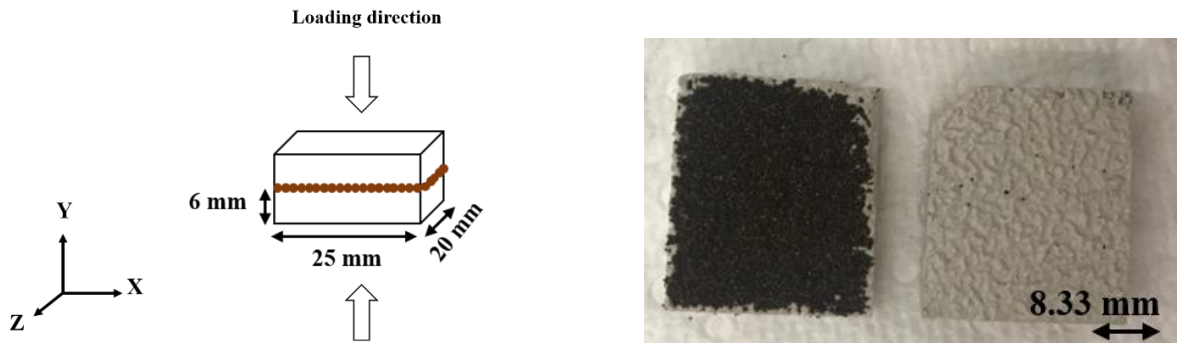

Figure H.12.(a) schematic of the sample scanned using X-ray tomography; (b) image of the sample with proppant
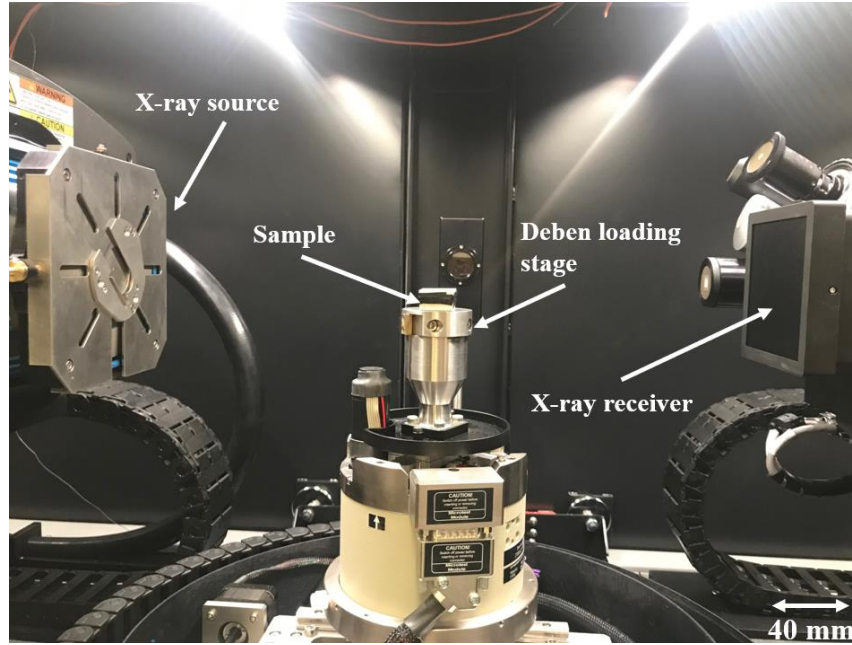
Figure H.13. X-ray in-situ machine setup

The sample in Figure H.12 was scanned using a 3D X-ray microscope (XRM), Model Zeiss Xradia 510 Versa. As shown in Figure H.13, the sample was placed on a Deben CT5000 loading stage, positioned between the X-ray source and receiver. The sample was loaded in the normal direction (y-direction), as shown in Figure H.12 (a), and was scanned at 4 distinct stages at a loading rate of 0.1 mm/min. Figure H.14 shows the normal stress versus time plot. The three loading stages are *A* (0.25 MPa), *B* (2 MPa), *C* (5 MPa), and an unloading stage *D* (0.25 MPa). The scans were conducted with a resolution of 17 µm/pixel. The energy and power of the scans were 160 kV and 10W, respectively. The sample was placed between the source and the detector with source and detector distances of 100 mm and 300 mm, respectively. The scans had an exposure time of 1 second for 3201 projections, 0.4x magnification factor, bin size of 2, and no filter was used (air). Voxel size was 17 µm. After the test, the collected XRM images were post-processed using Objective Research Systems (ORS) Dragonfly 4.0 software to reconstruct the 3D geometric scans of the sample.
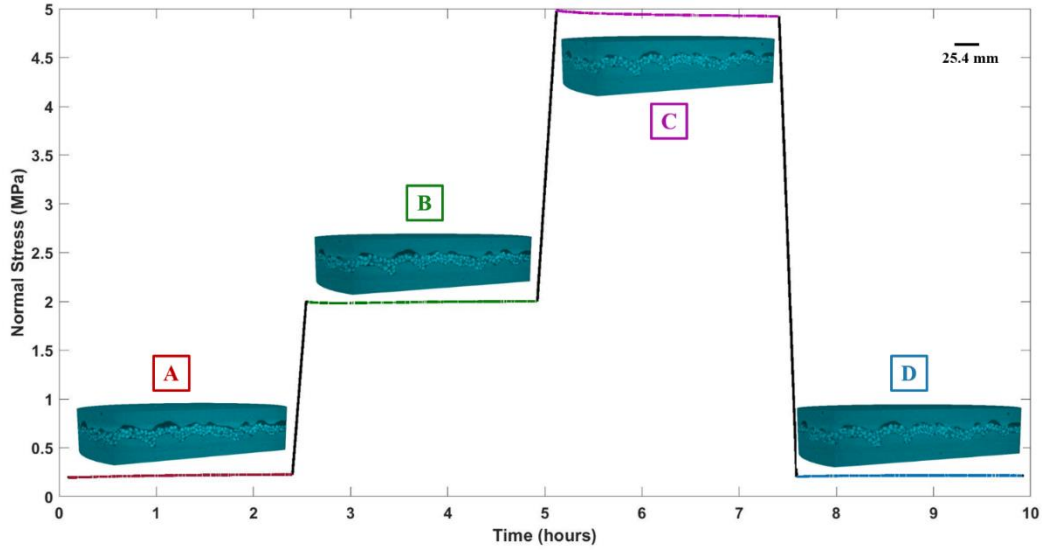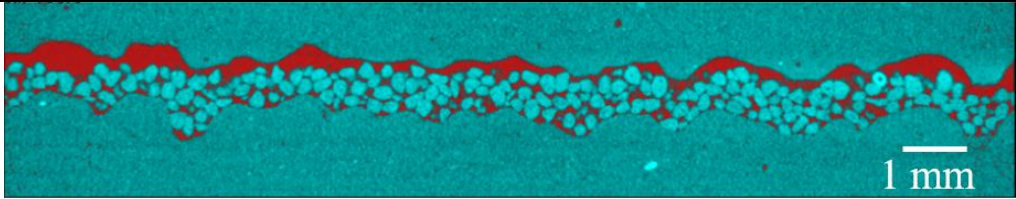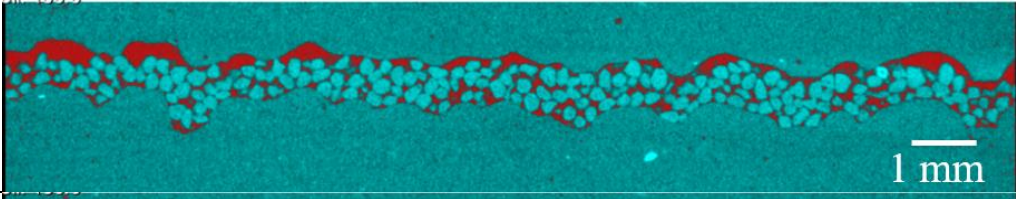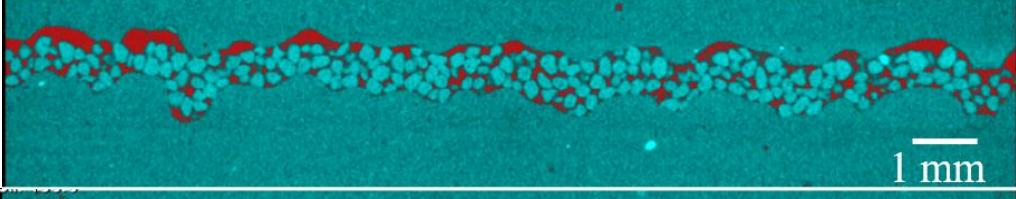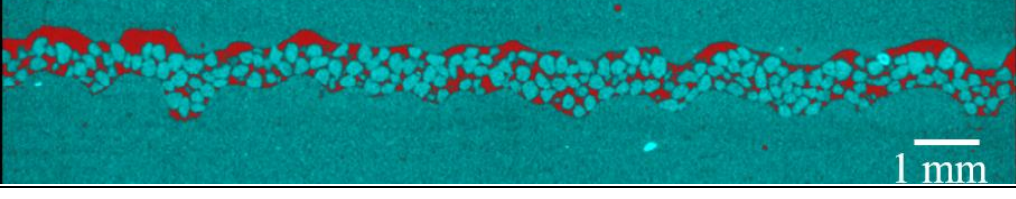
Figure H.14. Normal stress versus time for in-situ 3D XRM scanning

A slice through the 3D reconstructed scan at each stage is presented in Figure H.14. At loading stage **A** (0.25 MPa), the proppant particles filled the asperities' undulations of the bottom gypsum block, and voids were observed because of a mismatch at the interface created by the presence of the fill. As the sample was loaded up to normal stress of 2 and 5 MPa (stages **B** and **C**, respectively), the volume of voids decreased because of an increase in normal stress. At the unloading stage (stage **D** normal stress = 0.25 MPa), the sample did not return to its original configuration (stage **A**). 3D image analysis was conducted using the Dragonfly software to quantify the volume of voids. First, the image was segmented based on voxel intensity to isolate the voids (air-filled regions shown in Table H.1). Then, the volume of voids was computed for each loading stage. As the normal stress increased from 0.25 MPa (stage **A**) to 5 MPa (stage **B**), the volume of voids decreased from 1.73×10^{11} µm³ to 1.58×10^{11} µm³ (an 8.67 % decrease of the original volume of voids) and was further reduced to 1.05×10^{11} µm³ (a 39.3 % decrease of the original volume of voids) at a normal stress of 5 MPa. Interestingly, at the unloading stage (**D**), which has the same normal stress as loading stage **A**, the volume of voids did not rebound to the initial volume, i.e., to 1.73×10^{11} µm³. This is indicative of compaction of the proppant, which suggests that the proppant's grains may move and rearrange during loading.

Table H.1. Computed volume of voids for each loading stage for the in-situ XRD loading experiment

Stage	Normal stress (MPa)	Snapshot	The volume of voids ($\times 10^{11}$ μm^3)	Percentage decrease in volume of voids (with respect to stage A)
A	0.25		1.73	0
B	2		1.58	8.67 %
C	5		1.05	39.3 %
D	0.25 (unload)		1.19	31.2 %

VITA

Hala El Fil completed her bachelor's and Master of Civil Engineering degrees at the American University of Beirut in May 2016 and August 2017, respectively. She came to the United States in August 2017 and joined the graduate program at Purdue University. After earning her Ph.D., she will join Exponent Inc. as an associate. Her research interests include rock mechanics, applied geophysics, and fracture mechanics.